UNIVERSITÄT DER BUNDESWEHR MÜNCHEN

Fakultät für Elektrotechnik und Informationstechnik

Tomographic Two-Color-Pyrometry of the Wire Arc Spray Process regarding Particle Temperature and in-flight Particle Oxidation

Stefan Kirner

Vollständiger Abdruck der von der Fakultät für Elektrotechnik und Informationstechnik der Universität der Bundeswehr München zur Erlangung des akademischen Grades eines

Doktor Ingenieur

(Dr.-Ing.)

genehmigte Dissertation.

1. Gutachter:	Prof. Dr.-Ing. Jochen Schein Universität der Bundeswehr München
2. Gutachter	Prof. Dr.-Ing. habil. Thomas Klassen Helmut-Schmidt-Universität – Universität der Bundeswehr Hamburg
Vorsitzender des Promotionsausschusses:	Prof. Dr.-Ing. Klaus Landes Universität der Bundeswehr München

Die Dissertation wurde am 23.06.2017 bei der Universität der Bundeswehr München eingereicht und durch die Fakultät für Elektrotechnik und Informationstechnik am 03.04.2018 angenommen. Die mündliche Prüfung fand am 25.04.2018 statt.

Danksagung

Diese Dissertation entstand während meiner Tätigkeit als wissenschaftlicher Mitarbeiter am Institut für Plasmatechnik und Mathematik an der Universität der Bundeswehr München. Obwohl die Erstellung einer Dissertation ein „Privatvergnügen“ und eine Einzelarbeit ist, kann dies nicht ohne Hilfe aus dem Institut und der Familie gelingen. Deshalb möchte ich mich im Folgenden bei allen bedanken, die mich dabei auf irgendeine Weise unterstützt haben.

Zunächst möchte ich Professor Jochen Schein für die Überlassung des interessanten Themas und die stetige Unterstützung vor und während meiner Promotion danken. Durch sein Vertrauen in meine Arbeit und seine unerschütterliche Rückendeckung hat er mir die Möglichkeit gegeben, Projekte in vielen unterschiedlichen Gebieten der Plasmatechnik zu bearbeiten, zu präsentieren und zu verteidigen. Durch diese bestmögliche Ausbildung wurde ich hervorragend auf den Einstieg in die Industrie vorbereitet und konnte ab der ersten Arbeitswoche nicht nur durch fachliches Wissen überzeugen.

Außerdem möchte ich mich bei seinem Vorgänger, Professor Klaus Landes, bedanken. Er hat mich auf meinem Weg zur Promotion ständig begleitet und stand mir mit Rat und Tat zur Seite. Es war eine Ehre für mich, dass er die Betreuung meiner Bachelorarbeit und meiner Diplomarbeit übernommen hat und jetzt letztendlich durch die Übernahme des Vorsitzes bei der Verteidigung meiner Promotion auch beim vorerst letzten Schritt meiner akademischen Karriere dabei ist.

Bei Professor Thomas Klassen bedanke ich mich für die Übernahme des Koreferats.

Eine weitere Person, die entscheidend an meinem Werdegang beteiligt war, ist Dr. Günter Forster – der Meister „Yoda“, die gute Seele des Labors. Ohne seine fachliche Hilfe, seine aufmunternden Worte und seine schier unerschütterliche Geduld wäre ich wahrscheinlich in so manchem Motivationstief versunken und hätte meine Arbeit nicht vollendet. Er war es, der mich überhaupt erst auf die Idee zu promovieren gebracht hat und seiner stetigen Unterstützung ist es zu verdanken, dass diese Arbeit fertiggestellt wurde.

Dr. Stephan Zimmermann alias „Zimbo“ danke ich für die Hilfe bei der Durchführung der LDA- und DPV-Messungen. Zimbo stand mir immer mit guten Ratschlägen zur Seite und konnte mir bei vielen elektronischen und messtechnischen Problemen weiterhelfen. Dr. Jochen Zierhut alias Jozi sage ich Danke für die vielen interessanten Gespräche beim Mittagessen, die mir einen Einblick in industrielles und kundennahes Arbeiten gegeben haben. Ein besonderer Dank gilt auch Dr. Karsten Hartz-Behrend, der durch seine straffe Projektkoordination immer dafür gesorgt hat, dass ich den Blick für das Wesentliche nicht verliere.

Meinen promovierenden „Mitstreitern“ Marina und Marvin Kühn-Kauffeldt, Mathias Pietzka, Stefan Eichler und Matthias Bredack danke ich für die freundschaftliche Zusammenarbeit und die Unterstützung bei dem ein oder anderen fachlichen Problem. Unvergesslich bleiben die regelmäßigen Schweißlabor-Kaffeerunden, bei denen über z.T. abstruse physikalische Theorien philosophiert wurde (dI/dt - Schallmauer).

Ein außerordentlicher Dank gilt meinem Laborkumpel Michal Szulc. Mit ihm habe ich so manche Überstunde geschoben, um ausufernde Versuchspläne durchzuarbeiten und somit anfangs aussichtlose Projekte doch noch zu retten. Sein großes fachliches Wissen im Bereich der Plasmatechnik und seine Gabe, sich immer und überall für andere Zeit zu nehmen, sind eine Bereicherung für das gesamte Institut.

Ein weiterer Dank gilt der Instituts-Werkstatt unter der Leitung von Ulrich Bayrle. Ihre präzise Arbeitsweise und ihr fachliches Wissen auf dem Gebiet der Mechanik haben so manchen unmöglich erscheinenden Versuchsaufbau möglich gemacht. Neben ihrer hervorragenden Arbeit haben sie mit viel Witz und Spaß für ein lockeres und angenehmes Arbeitsklima gesorgt.

Außerdem danke ich Silva Schein für die Anfertigung der vielen Schliffe sowie Cornelia Budach und Dagmar Bergel für die Hilfe bei der Überwindung so mancher bürokratischen Hürde.

Meiner Familie möchte ich für alles danken. Danke Mama und Papa, dass ihr mich immer und bei allem unterstützt habt. Egal, welchen Weg ich eingeschlagen habe, auf euch konnte ich mich verlassen.

Der größte Dank gilt meiner lieben Frau Carmen. Durch ihre unerschütterliche Rückendeckung und ihre motivierende Art hat sie einen erheblichen Anteil am Gelingen dieser Arbeit. Ich weiß, dass du in den letzten Jahren viel für mich zurückstecken musstest und hoffe, dass ich dir das irgendwann zurückgeben kann. Ich danke dir auch für meinen letzten Motivationsschub – Maja und Antonia. Die Geburt unserer wunderbaren Töchter hat so manches arbeitstechnische Problem relativiert und mir eine gelassenere Sicht auf die Dinge gelehrt. Ihr drei seid der Grund, weshalb ich die Promotion erfolgreich abgeschlossen habe. Danke!

Abstract

Thermal spraying methods are processes which provide high energy for the melting and atomizing of powder, rod or wire shaped feedstock materials that are finally applied to a substrate. The coating can improve surface properties, such as wear resistance and corrosion protection of mechanical components, and add functional properties. In addition to a careful substrate preparation, the physical properties of the coating particles are decisive for the quality of the coating. Temperature, size, rate and velocity represent the classical quantities, which can be measured in situ using various diagnostics.

Since many industrially used coating methods, such as for example wire arc spraying, are used under atmospheric conditions, another quality-determining parameter is the degree of oxidation. This particle property cannot be measured by established diagnostics and must therefore be qualitatively derived from the above mentioned quantities or subsequently be measured by means of destructive methods (microsections, EDX, etc.).

For these reasons the aim of this work is the development and testing of a diagnostic for the in-flight measurement of particle oxidation.

This innovative measurement method detects the entire particle plume from different directions using a 2D two-color-pyrometry and allows the calculation of spatially resolved three-dimensional temperature and intensity distributions based on a tomographic evaluation method. By additionally using measurements of the particle velocities (Laser-Doppler-Anemometry) and particle sizes (Particle Shape Imaging) the surface emissivity of the particles along the spraying direction can be calculated, which in turn allows quantitative conclusions on the degree of particle oxidation.

Investigations on the wire arc spraying process have shown that the particle plume can be assumed to be optically thin and is thus suited for emission tomography. In addition, particle oxidation degrees could be measured which tend to correlate well with oxide contents in finished coatings. Especially in the case of using nitrogen as atomizing gas, the oxide content in the layer can be predicted very well with the aid of the in-flight measured emissivities.

Kurzfassung

Bei thermischen Beschichtungsverfahren handelt es sich um Prozesse, die hohe Energie zum Aufschmelzen und Zerstäuben von Grundmaterial, das pulver-, stab- oder drahtförmig vorliegt, zur Verfügung stellt. um dieses letztendlich auf ein Substrat auftragen zu können. Durch die Beschichtung können Oberflächeneigenschaften, wie z. B. Verschleiß- und Korrosionsschutz von mechanischen Bauteilen, verbessert und funktionelle Eigenschaften hinzugefügt werden. Ausschlaggebend für die Qualität einer Schicht sind neben einer sorgfältigen Substratpräparation die physikalischen Eigenschaften der Beschichtungspartikel. Temperatur, Größe, Rate und Geschwindigkeit stellen die klassischen Größen dar, die mit Hilfe diverserer Diagnostiken in situ gemessen werden können.

Da viele industriell angewendete Beschichtungsverfahren, wie beispielsweise das Lichtbogendrahtspritzen, unter Atmosphäre angewendet werden, ist eine weitere qualitätsbestimmende physikalische Größe der Oxidationsgrad der Partikel. Diese Partikeleigenschaft kann von keiner bekannten etablierten Diagnostik gemessen werden und muss folglich von den zuvor genannten Größen qualitativ abgeleitet oder im Nachhinein mit Hilfe von destruktiven Methoden (Schliffbild, EDX, etc.) ermittelt werden.

Aus diesen Gründen ist das Ziel dieser Arbeit die Entwicklung und Erprobung einer Diagnostik zur in situ Messung der Partikeloxidation.

Bei dieser innovativen Messmethode wird der gesamte Partikelstrahl aus unterschiedlichen Richtungen mit Hilfe einer 2D Zwei-Farben-Pyrometrie erfasst. Basierend auf einer tomografischen Auswertemethode, werden ortsaufgelöste dreidimensionale Temperatur- und Intensitätsverteilungen berechnet. Durch die zusätzliche Messung der Partikelgeschwindigkeiten (Laser-Doppler-Anemometrie) und -größen (Particle Shape Imaging) kann der Oberflächenemissionsgrad der Partikel entlang der Spritzachse berechnet werden, die wiederum quantitative Rückschlüsse auf den Oxidationsgrad der Partikel zulässt.

Die Untersuchungen am Lichtbogendrahtspritzprozess haben gezeigt, dass der Partikelstrahl als optisch dünn angenommen werden kann und folglich für die Emissionstomografie geeignet ist. Außerdem konnten Partikeloxidationsgrade gemessen werden, die gut mit in Schichten gemessenen Oxidgehalten korrelieren. Besonders bei der Verwendung von Stickstoff als Zerstäubergas kann der Oxidgehalt in der Schicht mit Hilfe der in situ gemessenen Emissionsgrade sehr gut vorhergesagt werden.

1 Introduction

In 2011 the term Industry 4.0 was used for the first time by Kagermann et al. [1] in order to describe the industrial change that takes place in German industry. They even go so far to say that Industry 4.0 is the fourth industrial revolution, after the application of mechanical production facilities using water and steam power, the introduction of mass production using electrical power and the automation by means of electrical and information technology [2]. Industry 4.0 describes the networking of all human and mechanical participants on the value chain of a product form the development to the recycling [2]. Apart from the progressing automation, intelligent control and decision mechanism are applied in order to optimize and control the industrial production in real time [1]. Due to the extensive funding provided by the "Bundesministerium für Bildung und Forschung" Industry 4.0 is on everyone lips and a popular new field of research. However, there are also critical voices saying for example,

> *"We may not have known it was called Industry 4.0, but we've been doing it for years."*
>
> **Heinz Jörg Fuhrmann, CEO of Salzgitter** [3]

Also in thermal spraying the meaning of Industry 4.0 is nothing new, since the automation and networking of processes is an important research topic that has been pursued for years. One example is the control of the wire arc spray process using artificial neuronal networks [4]. Such control methods are indispensable for the automation and may be an important step to keep away workers from the spraying chamber with its harmful ultrafine particle fumes [5]. Even in the case that the manual operating of thermal spray processes is unavoidable, information technology could be a possibility to improve the process in real time and support workers. The institute for "Plasmatechnik and Mathematik" at the "Universität der Bundewehr München" for example plans a research project, in which conceivable uses of a head-mounted display will be investigated. This intelligent system should help the worker to plan the coating task, support him during the spraying process by means of real-time monitoring and log the measured data in order to facilitate the quality control [6].

The prerequisite for all these developments is a fundamental understanding of the process and the coating quality determining parameters. Since the most influencing parameters are the in-flight properties of the particles, most of the available diagnostics for thermal spraying are developed in order to measure particle velocity, size, rate or temperature. Other properties like for example the oxidation can only be derived from these results and be qualitatively evaluated.

Before the need of developing an innovative diagnostic for the in-flight oxidation measurement can be formulated more precise, a detailed overview of existing thermal spraying processes, of the coating formation and of established particle diagnostics is given in the next chapters.

1.1 Thermal spraying – State of the art

In Europe the expression thermal spraying is standardized by DIN EN 657 [7]. According to this definition thermal spraying is a group of coating processes in which metallic or nonmetallic feedstock is partly or completely molten, atomized and finally sprayed on a pretreated substrate surface. For this purpose special equipment and peripheral devices are necessary in order to provide energy, feedstock, gas and other additional media. Figure 1 shows the principle setup for thermal spraying.

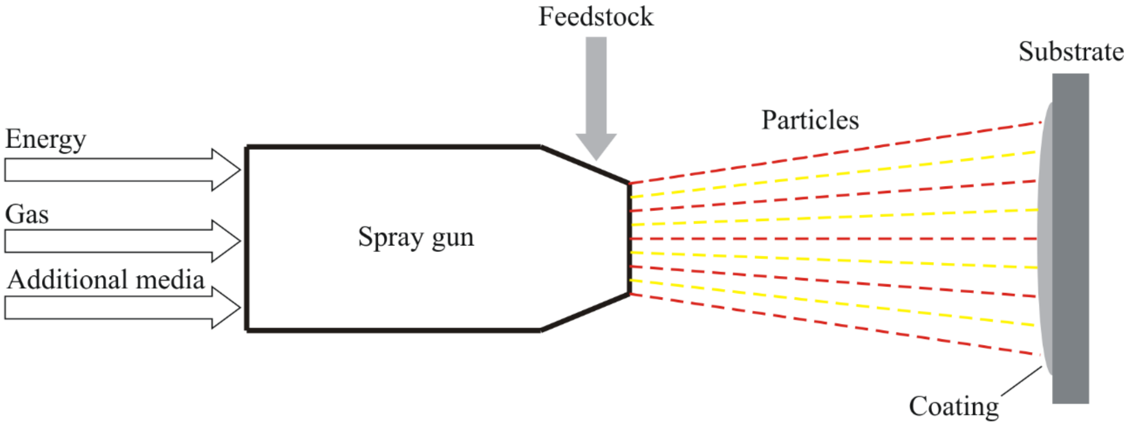

Figure 1: Principle setup for thermal spraying, consisting of a spray gun that is supplied with energy, gas and additional media (cooling water, ...) in order to melt and atomize the feedstock. The resulting particles are accelerated and sprayed on a pretreated substrate.

By coating the surfaces of components they can be improved according to functional performance, wear resistance, life time and production costs [8]. This is possible because base materials which are easy to work and more economical are coated with high performance materials [9]. The feedstock used for thermal spraying is usually in the form of powder, wires or rods [10] and is made of metals, alloys, ceramics, or cermets [9]. The classification of coating techniques can according to [11] be done by coating thickness and substrate temperature. As Figure 2 shows, thermal spraying covers a wide range of coating thicknesses and substrate temperatures and can consequently be used for many different applications.

A current example that combines many of the above listed advantages is the coating of engine cylinder bores. In this application the cylinder bores of aluminum or magnesium engines are thermally sprayed in order to reduce friction and to decrease fuel consumption [12, 13]. By applying the thermal sprayed coating directly on the cylinder bores it is no longer necessary to put in iron liners and consequently an additional weight reduction can be achieved, besides the reduction due to the use of aluminum or magnesium as engine base material [14]. In addition the process related porosities, exposed by honing, serve as oil reservoir and thus are the source for decreased friction [13]. The thermal spray processes that can be used for this special application are high velocity oxygen fuel (HVOF) spraying [12], atmospheric plasma spraying (APS) [12, 13, 15] and wire arc spraying [12–14].

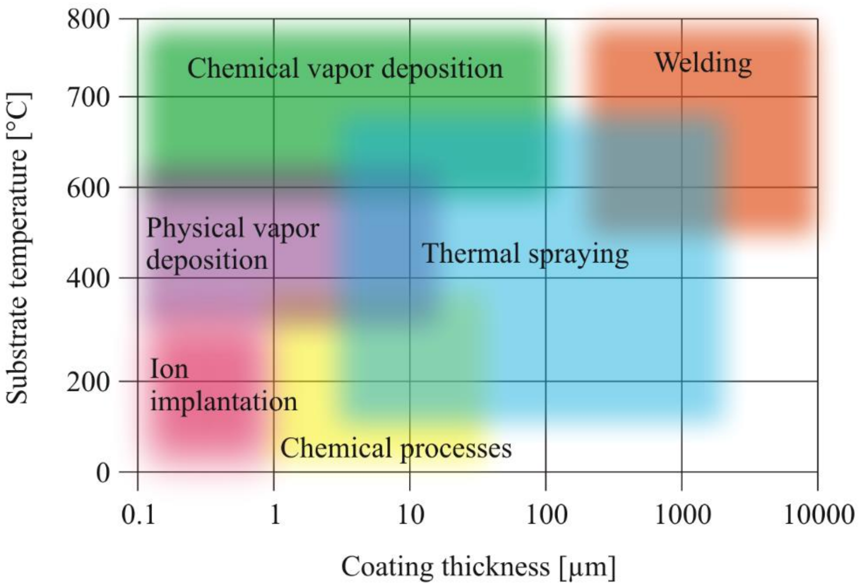

Figure 2: Classification of thermal spraying among other coating processes regarding coating thickness and substrate temperature. Adopted from [11].

In the next chapter a classification of the different thermal spraying processes is done and the most important ones are presented in detail. Additionally the evaluation of thermal sprayed coatings is discussed and an overview about the most important particle diagnostics is given.

1.1.1 Process overview

The “established” literature divides the thermal spray processes into combustion and electric discharge techniques [8, 10, 16, 17]. The two techniques differ only in the way how the energy for fusing the feedstock is provided.

A special thermal spray process that cannot be assigned to one of the both classifications is cold-gas spraying. Responsible is the type of energy input to the particles. At cold spraying the unmolten particles are accelerated with a high velocity cold gas stream. As soon as the particles strike the substrate they are immediately slowed down and the high kinetic energy is transformed to thermal energy leading to plastic deformation and coating generation. [18, 19]

The first “real” documented thermal spray process was invented by Max Ulrich Schoop at the beginning of the 20th century [20]. This nowadays called flame spraying process is – as the name indicates – a combustion process whereby a flame created by burning acetylene and oxygen serves as heat source. The feedstock, usually provided as wire, is fed axially into the flame and the resulting molten particles are atomized by a surrounding stream of compressed air. [8]

A more sophisticated form of the flame spray process is the high velocity oxygen fuel (HVOF) spraying. In contrast to usual flame spraying the combustion of oxygen and a gaseous or liquid fuel takes place in a separate chamber. The injection in this chamber is done with high pressures and high gas flows (e.g. 0.55 to 0.83 MPa, 28 l/h kerosene and 61400 l/h oxygen: “WokaJet-

410” from the company “Oerlikon metco” [21]) so that the resulting flame expands supersonically through a long Laval nozzle. The feedstock is injected as powder into the flame, depending on the construction either axial or radial. [22]

One of the most variable spraying techniques concerning the choice of feedstock material is plasma spraying. This electric discharge process provides high gas temperatures and velocities and is usually operated with inert gas, which in turn prevents oxidation [16]. The main feature of every plasma torch is at least one electric arc that is struck between a cathode and an anode. In the case of the simplest setup the cathode is a pointed tungsten cylinder and the anode a tungsten coated copper tube that serves as nozzle at once. The process gas flowing between cathode and anode is heated by the arc and leaves the gun through the nozzle as plasma jet [23, 24]. Depending on the setup the powdery feedstock is injected internal axial, internal radial or external radial [16]. Regarding the number of anodes and cathodes and their arrangement many different torch setups are commercially available. The constructions range from simple one-cathode/one-anode guns and three-cathode/one-anode [25, 26] guns to one-cathode/three-anodes guns [27] and one cathode/five anodes guns [28].

Another process that can be added to the electric discharge techniques is the wire arc spray process. The principle setup is presented in Figure 3.

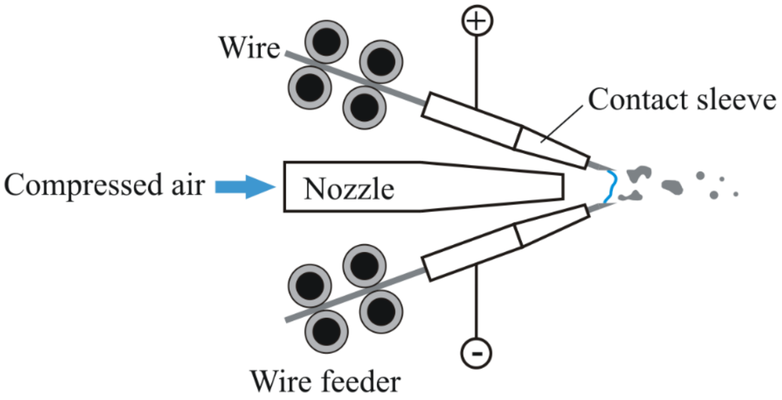

Figure 3: Principle setup of the wire arc spray process, consisting of a nozzle, a current source, two contact sleeves, two wire feeder and two conductive wires serving as feedstock.

It consist of two conductive wires that are continuously fed towards each other under fixed angle. Using contact sleeves the wires are connected to a current source and because of the potential difference an electric arc is struck in the gap between the wires. The hot arc melts the wire tips and with the help of a high velocity gas flow the molten material is atomized. Finally the detached particles are accelerated towards the substrate where they generate a layer. In general a constant voltage dc power supply is used as current source and due to the high gas flow rates and the related costs compressed air is used as atomizing gas. [8, 29]

Since the wires function as electrodes and feedstock at the same time the melting of the complete coating material is guaranteed and consequently high coating efficiencies can be reached. This advantage leads unavoidably to a problem that is topic of many research works. Due to the different arc attachment on cathode (constricted) and anode (diffuse) the melting of the wires and therefore the particle generation differs [30, 30, 31]. This asymmetric melting behavior results in different temperature, velocity and size distributions between particles detached form the cathode and particles detached form the anode [32–35]. Another negative effect concerning the particle generation is the periodic fluctuation and re-ignition of the arc caused by the periodic removal of the molten material [35]. Liao et al. [36] showed for example that because of the fluctuations there are bimodal particle distributions both for the cathode wire and the anode wire. An interesting approach to solve this problem is the use of pulsed current controlling the arc movement [37].

All these research studies about wire arc spraying show that the particle generation is influenced by many process parameters and that the resulting particles can vary with respect to temperature, velocity and size. For this reason the wire arc spray process is an ideal measurement object for particle diagnostics and is used in this work to test the developed tomographic two-color-pyrometry.

1.1.2 Formation of thermal sprayed coatings

Every formation of thermal sprayed coatings starts with the particles generated from the feedstock. In the case of wire- or rod-shaped feedstock there are process related less unmolten particles presents than in the case of powdery feedstock [8]. The atomized particles are transported by a stream of gas, whose influences they are exposed to during their flight time. If the thermal spray process is performed in atmosphere the particles are additionally influenced by the surrounding air and the oxygen, respectively [38]. Since the temperature of the particles is above the melting point oxidation takes place very fast using metallic feedstock. In order to clarify the influence of the temperature on the oxidation, the Arrhenius law [39, 40] presented in Equation 1.1 can be used.

$$k = Ae^{\frac{-E_a}{RT}} \tag{1.1}$$

Using this equation the rate k of a chemical reaction with the activation energy E_a can be calculated. Besides the activation energy the rate depends on the gas constant R, the temperature T and the frequency factor A. Whereby A takes the number of collisions with the correct geometry into account [39] and is in turn slightly temperature dependent [8]. To illustrate the significant influence of the temperature on the oxidation of metal particles, the factor $\exp\left(-E_a/RT\right)$ for iron depending on the temperature is presented in Figure 4. Therefore the activation energy of iron $E_a = 246.8\ \mathrm{kJ/mol}$ validated by Wilson et al. [41] is used. As we can see by increasing the temperature from 1850 K to 2150 K, the oxidation rate increases approximately by one order of magnitude

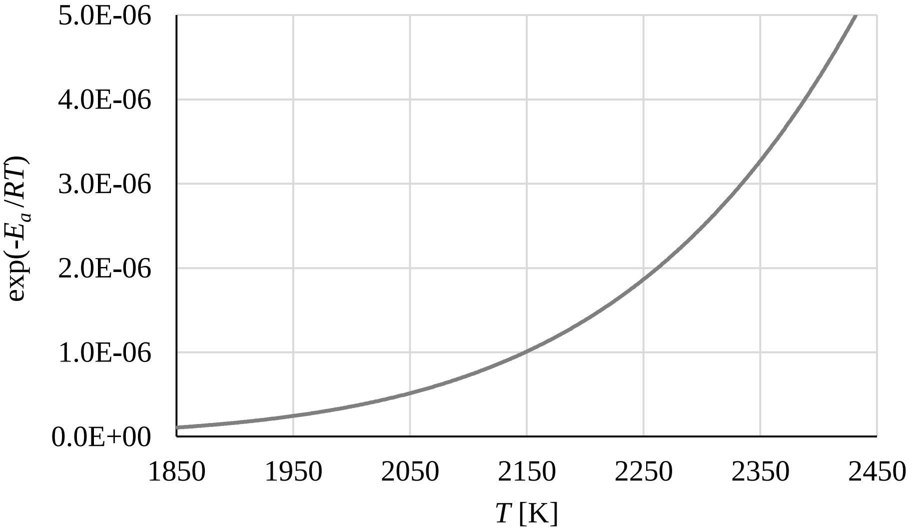

Figure 4: Proportional factor $\exp(-E_a/RT)$ *for the calculation of the iron oxidation rate depending on the temperature T. For the calculation* $E_a=246.8$ *kJ/mol validated by Wilson et al.* [41] *was used. R stands for the gas constant.*

Oxidation always occurs at the surface of a material and propagates inside through diffusion of metal and oxygen into the oxide layer [41, 42]. However Deshpande et al. [43] and Espie et al. [44] determined that there are both: a thin oxide sheet on the surface of the particles and oxide inclusions within the particles. Responsible for the oxide fractions within the particles is convective movement of the liquid oxides and metals resulting in continuous mixing [8, 43–45]. Regarding small particles this effect may lead to complete oxidation as can be seen in the cross section presented in Figure 5.

The first molten particles that strike the substrate surface spread over and fill out the free spaces of the surface. Consequently it is important to clean and to roughen the substrate surface in order to achieve a good adhesion [8]. The cooling of the particles happens very fast because of the great mass of the substrate compared to the particles and thus the impact of the following particles takes place on a solid underground [46]. Through the continuously impact and flattening of the particles a lamellar structure is formed. The principle setup of a thermal sprayed coating is presented in Figure 5 on the left side. For comparison on the right side of Figure 5 a cross section of a wire arc sprayed coating is illustrated. Besides the lamellar structure of the feedstock, porosity, oxides and unmolten particles can be seen. The oxides are present in form of so called oxide strings [16], solidified oxide droplets and oxide trapped inside the particles [43]. As Li et al. [47] investigated for HVOF spraying of MCrAlY material there is, besides the in-flight-oxidation, a second oxidation mechanism leading to oxide strings. This so called post-impact oxidation is caused by the oxidation of the flattened particle surfaces taking place until the next particles strike. The porosity within the coating occurs among other things because of material shrinkage on cooling, unmolten or pre-solidified particles, poor intrasplat cohesion and cracking [16].

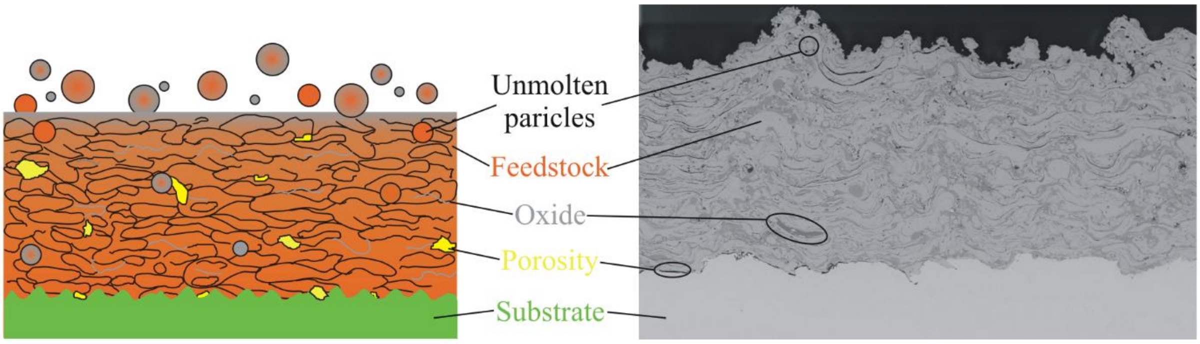

Figure 5: Left: Schematic drawing of a thermal sprayed coating. Right: Cross section of a wire arc sprayed coating. Both images show the typical structure consisting of a substrate, feedstock material, oxides, porosity and unmolten particles.

Since the intention of the diagnostic developed in this work is the measurement of the particle temperature and the in-flight oxidation, the particle parameters influencing the oxidation and the corresponding trends are summarize in Table 1. In the next chapter the most important particle diagnostic techniques and the commercially available systems are presented.

Table 1: Particle parameters influencing the oxidation and the relating reasons.

	Trend	**Particle oxidation**	**Reason**
Particle temperature	↗	↗	Arrhenius law 1.1
Particle size	↗	↘	Lower surface area to volume ratio [16]
Particle velocity	↗	↘	Reduced dwell time [16]

1.1.3 Particle diagnostics

Particle diagnostics used for thermal spray processes may be classified into passive and active diagnostics. According to this definition the passive systems only observe the particles whereas active diagnostics need an external light source interacting with the particles and evaluate the blocked and the reflected light, respectively.

One of the simplest ways to determine for example particle velocities can be realized using digital cameras and applying the time-of-flight method. In this technique a CCD or CMOS camera acquires images of the spray plume, whereby the exposure time is chosen in a way that the flying particles leave bright traces on the images. With the help of the trace length determined using image processing methods, the image scale and the adjusted exposure time the velocity of single particles can finally be calculated. It is obvious that this method can only be applied to thermal spray processes that generate luminous particles. Matz et al. [48] for example used the PVI-system from the company “Zierhut Messtechnik GmbH” to investigate the influence of the nozzle setup on particle velocities in wire arc spraying.

Another particle diagnostic using a digital camera is the SprayWatch from the company “Oseir” [49]. Compared to the PVI this system additionally enables the measurement of particle temperatures applying the principle of two-color-pyrometry. To acquire particle images at two different wavelength bands two small stripes of the CCD sensor are covered with different filters. In order to combine velocity and temperature measurement the camera records an image with short exposure time followed by an image with long exposure time. The short exposed image (part without filter in front) shows the typical particle traces and can be evaluated by means of the time-of-flight method. The long exposed image (double-stripe part) is used to calculate particle temperatures by means of two-color-pyrometry. Additionally the SprayWatch can be transformed to an active diagnostic by applying a high power pulsed laser diode module called HiWatch. This option enables the measurement of non-luminous particles such as cold-sprayed particles [50, 51].

Vattulainen et al. [52] present another possibility to measure particle velocities and temperatures using a single camera. In their setup a custom double mirror is used to record the flying particles at two different wavelength bands. The first surface of the mirror reflects radiation in the visible band the second surface in the near-IR band. The resulting images show two overlapping traces for each particle that can in turn be evaluated by means of the time-of-flight method and two-color-pyrometry.

The PVI as well as the SprayWatch and the diagnostic developed by Vattulainen et al. [52] are easy to handle and to adjust but because of the projection of the spray plume on single two dimensional sensors the information in direction of observation gets lost. As a consequence one velocity component of the particle trajectories is missing and no statements can be made about the three dimensional expansion of the spray plume.

In [53] a new measurement technique is suggested in order to remedy this lack of information by using several cameras positioned around the spray plume simultaneously acquiring images with short exposure times. With the help of image processing methods and a so called sinus-fit the position and the three dimensional trajectories of single particles can be calculated. The principle setup for the so called tomographic particle localization and velocity measurement is presented on the left side of Figure 6. An example for a measured particle trajectory distribution is shown on the right side.

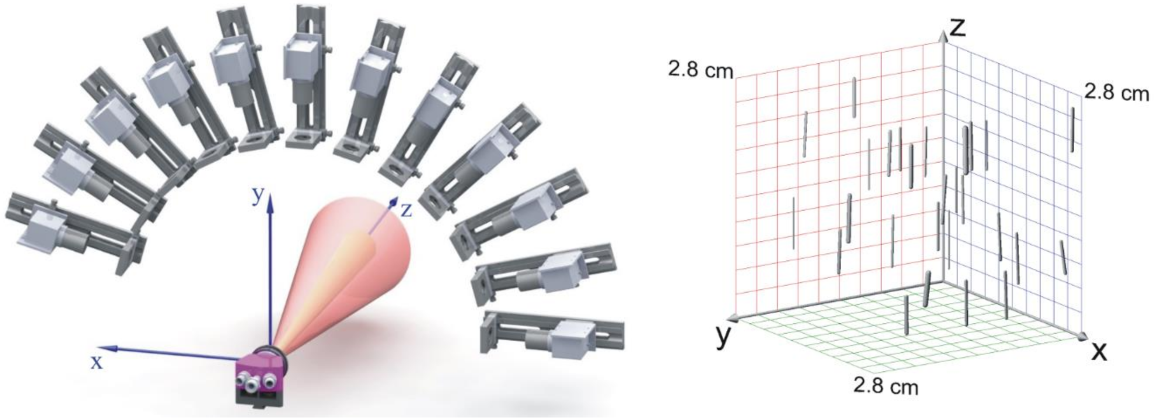

Figure 6: Principle setup for tomographic particle localization and velocity measurement (left) and an example for a particle trajectory distribution (right) measured with this diagnostic. Both adopted from [53].

Another passive particle diagnostic is the DPV-system from the company “Tecnar”. The function of this diagnostic is well described in [54–57] and can be explained based on Figure 7. The particles flying through the measurement volume of the DPV are projected onto the entrance of a fiber, which in turn is covered with a two-slit photomask. The optical signal is parallelized and divided with the help of a lens and a dichroitic mirror. Using two interference filters with different central wavelengths and two lenses the signal is projected onto photodetector 1 and photodetector 2.

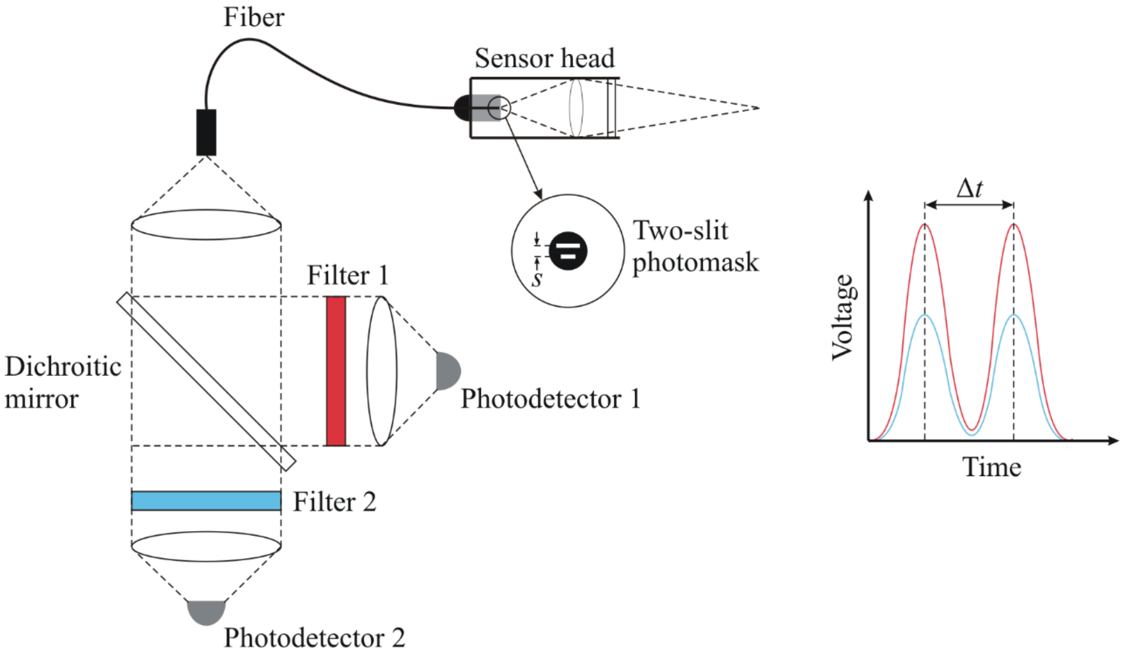

Figure 7: Schematic drawing of the DPV setup and the voltage signals received from the photodetectors. According to [54, 55].

On the right side of Figure 7 the signals received by the two photodetectors are illustrated. As can be seen the signals generated by one particle show two peaks, which in turn can be used to determine the time Δt needed to cover the distance s between the two slits. The particle velocity is finally given by $v_P = M_i \cdot s/\Delta t$, where M_i stands for the image scale of the sensor head. For the determination of the particle temperatures again the principle of two-color-pyrometry is used, whereby the assumption is made that the particles behave like gray bodies meaning that their emissivities are independent on the wavelength. With the help of the temperature and the energy detected in one channel the particle diameter can be calculated assuming spherical particles and doing an energy correction for particles that are not fully seen in both slits [57]. Because for this method the emissivity of the particles has to be known, a complex calibration of the DPV has to be performed using a powder with known size distribution [54, 55].

Since the measurement time of the DPV is, due to the small measurement volume ($1.4\,\mathrm{mm}^2 \times 1.9\,\mathrm{mm}$ [55]) and the single particle detection, relatively long, the company “Tecnar” also offers the diagnostic Accuraspray intended for the control of industrial thermal spray applications [56]. The principle setup (see Figure 8) of this diagnostic consist of a lens, two single fibers and two photodetectors (PD_1 and PD_2) with different interference filters in front.

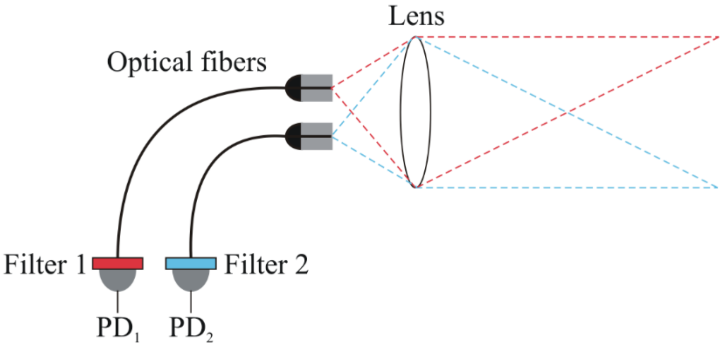

Figure 8: Schematic drawing of the Accuraspray setup for the detection of particle ensemble velocities and temperatures (According to [56]*).*

The optical setup is designed in a way that each fiber covers a large measurement volume of about $3\times3\times20\,\mathrm{mm}^3$ [56] and consequently many particles are observed at the same time[56]. As long as almost all particles fly through each measurement volume, the voltage signals received of the photodetectors are equal but time-shifted. This time-of-flight determined by doing the cross-correlation of the two signals [56] and the distance between the two measurement volumes are used to calculate an average velocity of the particle ensemble. The temperature determination again is based on two-color-pyrometry and provides only average data, too. Further no particle diameters can be estimated due to the particle ensemble measurement technique of the diagnostic. In contrast to the DPV the Accuraspray is additionally equipped with a CCD camera that offers the possibility to analyze the appearance of the spray plume regarding for example its position, width or intensity [55].

Like the CCD camera of the Accuraspray the Particle Flux Imaging (PFI) [58, 59] from the company “Zierhut Messtechnik GmbH” characterizes the entire spray plume and does not measure single particle properties. The diagnostic is based on a CCD camera that acquires images with long exposure time (320 ms [58]) and approximates the smoothed emission of the spray plume with ellipses. Because of the quickly available information of the whole spray plume and the low technical effort (only one single camera, no calibration), this diagnostic is perfectly qualified for online control of thermal spray processes. Hartz-Behrend et al. [4] for example applied the PFI as sensor in order to control the wire arc spray process using artificial neural networks. For research purposes the PFI is not suitable, since selected particle properties have to be known in order to be able to identify the parameters influencing for example the coating formation.

An example for an active particle diagnostic based on digital cameras is the Particle Image Velocimetry (PIV). In this method two consecutive laser flashes illuminate the measurement volume of the diagnostic and the camera acquires either two single images or one double-exposed image synchronized with the laser. The images are evaluated using particle tracking, auto-correlation or cross-correlation methods in order to calculate the spatial distance between matching particle pairs. By means of known exposure time a two dimensional particle trajectory field can finally be determined. [60]

The disadvantage of measuring only two velocity components can be solved by tomographic 3D-PIV [61]. Here three dimensional particle distributions are reconstructed by means of tomography using several images simultaneously recorded form different directions. The three dimensional trajectory distribution again is calculated with the help of 3D cross-correlation and the known exposure time.

A more complex technique to measure particle velocities is the Laser Doppler Anemometry (LDA). This laser based diagnostic adopted from experimental fluid mechanics is usually applied for point wise velocity measurement of a flow using tracer particles [62, 63]. Since in the case of thermal spraying “tracer particles” are process related present anyway and their properties are of particular interest concerning coating formation, the transfer of LDA is obvious. The principle setup of an LDA-system designed for thermal spray applications is shown in Figure 9 on the left side. This setup already used for the measurement of particle velocities during the plasma-spray process [64] was developed by Mayr [65] and Reusch [66], and is also used in this work. On the right side of Figure 9 an enlargement of the measurement volume including the wave, velocity and observation direction vectors is shown. The measurement volume is generated by crossing two laser beams under the angle Θ. In the crossing zone an interference pattern develops that interacts with the flying through particles. The scattered light is collected by a lens and projected onto a photo multiplier, which in turn generates a voltage signal. Since the particle sizes in thermal spraying range from several µm up to some 10 µm the scattering mechanisms occurring are Mie-scattering and normal optical reflection, refraction and diffraction [66]. The simplest way to explain the LDA is the interference fringe model that is strictly speaking only valid for particles smaller than the distance between two maxima in the interference fringe pattern. For this reason the Doppler-model according to [66] is used for the explanation of the measurement principle.

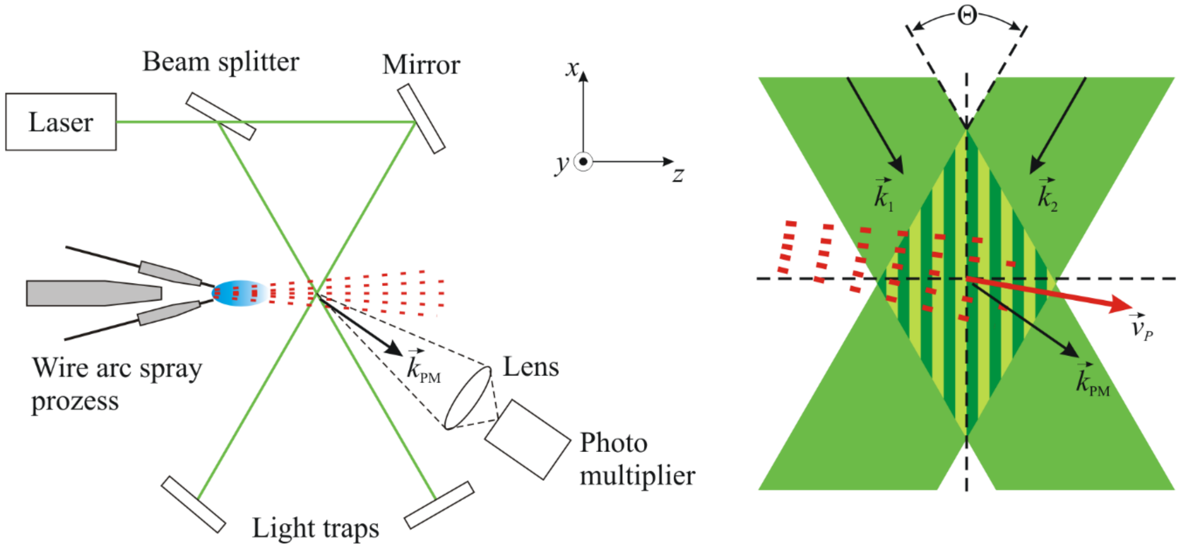

Figure 9: Schematic drawing of the Laser Doppler Anemometry setup (left) and an enlargement of the measurement volume including the wave, velocity and observation direction vectors necessary for the derivation of the Doppler-model. According to [64]

In the Doppler-model the frequency $f_{P,i}$ that a particle with the velocity $\vec{v}_P$ sees from the laser beams 1 and 2, can be calculated according to the Doppler-effect as follows:

$$f_{P,i} = f_L \cdot \left(1 - \frac{\vec{v}_P \cdot \vec{e}_i}{c}\right) \quad \text{for } i = 1, 2 \tag{1.2}$$

where f_L is the laser frequency, c the speed of light and $\vec{e}_i$ the direction of the corresponding wave vector $\vec{k}_i = 2\pi/\lambda_L \cdot \vec{e}_i$. With the help of the particle frequency the Doppler shifted frequencies $f_{PM,i}$ seen by the stationary photo multiplier can be determined using Equation 1.3

$$f_{PM,i} = \frac{f_{P,i}}{1 - \frac{\vec{v}_P \cdot \vec{e}_{PM}}{c}} = \frac{f_L}{1 - \frac{\vec{v}_P \cdot \vec{e}_{PM}}{c}} \cdot \left(1 - \frac{\vec{v}_P \cdot \vec{e}_i}{c}\right) \quad \text{for } i = 1, 2 \tag{1.3}$$

Since the scattered light from the laser beams 1 and 2 is superimposed and the photo multiplier is too slow to measure the laser frequency, only the Doppler-difference frequency f_D can be observed.

$$f_D = f_{PM,2} - f_{PM,1} = \frac{f_L}{1 - \frac{\vec{v}_P \cdot \vec{e}_{PM}}{c}} \cdot \frac{\vec{v}_P}{c} \cdot (\vec{e}_1 - \vec{e}_2) \tag{1.4}$$

As velocities of thermal spray particles are much smaller than the speed of light ($|\vec{v}_P|/c \ll 1$), Equation 1.4 can be simplified as follows:

$$f_D = \frac{f_L}{c} \cdot \vec{v}_P \cdot \left(\vec{e}_1 - \vec{e}_2\right) \qquad 1.5$$

This equation is independent on the observation direction $\vec{e}_{PM}$. Using $f_L = c/\lambda_L$ and calculating $\left(\vec{e}_1 - \vec{e}_2\right)$ with the geometrical relations in Figure 9, f_D is given by

$$f_D = \frac{1}{\lambda_L} \cdot v_{P,x} \cdot 2\sin\left(\frac{\Theta}{2}\right) \qquad 1.6$$

Finally the velocity component in x-direction can be determined by solving Equation 1.6 for $v_{P,x}$ and extracting f_D out of the voltage signal measured with the photo multiplier. Besides particle velocities also particle rates dn/dt can be measured using LDA. The limitations of the presented LDA-diagnostic are the determination of only the velocity component that is perpendicular to the fringe pattern and the point wise measurement technique. The disadvantage of missing velocity components can be solved through applying an additional pair of crossing laser beams, whose interference pattern is turned 90° compared to the first one [62]. However, the point wise measurement remains and consequently the time consuming scanning of a measurement pattern is necessary in order to achieve three dimensional information of the spray plume.

Another laser based method to measure particle velocities and rates is the Laser-Two-Focus (L2F) diagnostic. L2F in principle works like a light barrier, whereby the scattered light of particles flying through the measurement volumes of two focused laser beams is measured. By using the distance between the two laser points and the measured time delay, the particle velocity component perpendicular to the laser beams can be determined.

All above mentioned diagnostics, except the DPV, are not able to measure the particle size. Even the DPV only derives the size from measured particle emissions, whereby a complex calibration procedure is necessary and spherical particles are assumed. A diagnostic that enables the direct determination of the particle size is the Phase Doppler Anemometry (PDA). The setup of this diagnostic is similar to the LDA setup, with the sole difference that a second detector (lens & photo multiplier) positioned under a different elevation angle additionally observes the measurement volume. If the particles are spherical both detectors measure the same LDA-burst time shifted. This time is equal to a phase difference, which in turn is proportional to the radius of the particles. In summary the PDA enables the point wise measurement of single particle velocities and sizes, whereby the particles have to be spherical. [67]

A diagnostic for size measurement independent of the shape of the particles is the Particle Shape Imaging (PSI). The development of this innovative thermal spraying diagnostic is documented in [68, 69]. The principle setup (see Figure 10) consist of a laser, a beam splitter and an optic.

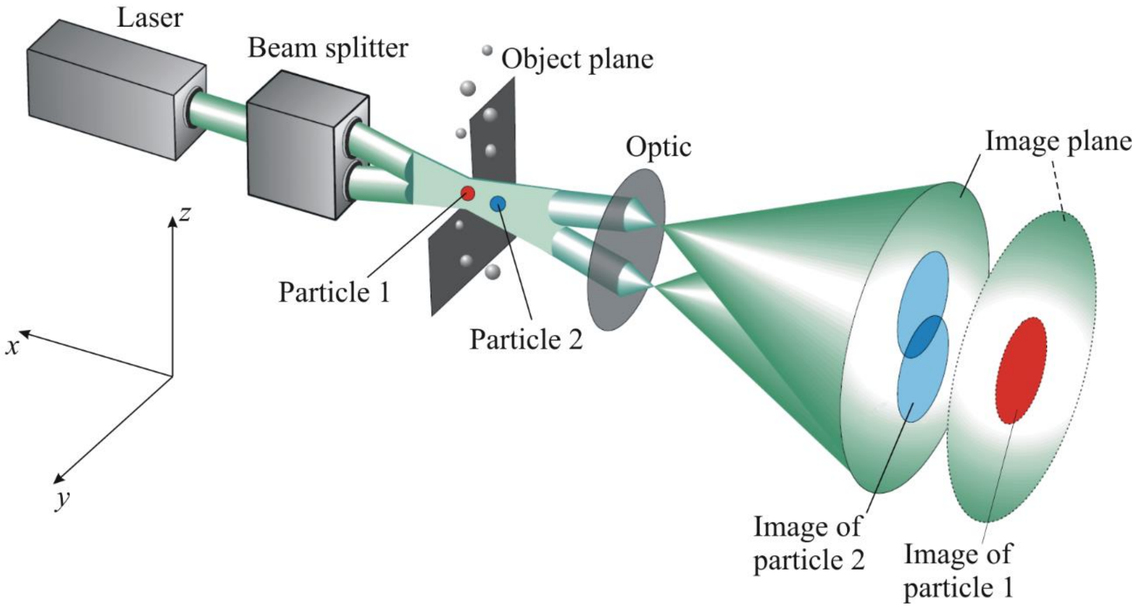

Figure 10: Principle setup of the Particle Shape Imaging (PSI), consisting of a laser, a beam splitter and an optic. Adopted from [68].

The beam splitter optic divides the laser beam into two single rays that are crossed in the measurement volume. Opaque particles flying through the measurement volume shadow the laser light and are projected to the image plane. The imaging optic is chosen in a way that high magnifications are reached (~24 using a mirror lens [68], ~27 using a lens system [69]) and consequently even small particles (>10 µm) can be detected. Since the particles are fast the detector has to be able to acquire images with short exposure times (5 ns to 200 ns) in order to avoid motion blur. To guarantee sufficient sensitivity despite the short exposure times, an image intensifier has to be used as detector. As it can be seen in Figure 10 only the particles directly positioned in the image plane (particle 1) are projected one times to the image plane. Particles located before or behind the object plane can due to the two laser beams be seen twice in the image plane. With the help of the distance between the double projections the particle position within the measurement volume can be determined. Furthermore the particles can be observed from two different directions, what in turn allows conclusions concerning the particle shape and size. By applying a trigger system even particle velocities and rates can be determined. [68–70]

Since it would be desirable to measure all particle properties at once, it is obvious to combine the above mentioned particle diagnostics. Fincke et al. [71] for example developed a diagnostic allowing the simultaneous point wise determination of particle sizes, velocities, rates and temperatures. For this purpose a setup was designed that includes LDA, two-color-pyrometry and size measurements, whereby the size determination is based on the measurement of absolute scattered laser light. By using this combination of diagnostics important results concerning the plasma particle interaction could be obtained.

After the comprehensive explanation of the particle diagnostics used in industry and in research and development, in the next chapter the reasons are discussed, why further research on this topic is still necessary. For a better overview the known diagnostics and their measured quantities are summarized in Table 2.

Table 2: Summary of the known particle diagnostics and their measured quantities (v: particle velocity, s: size, T: particle surface temperature, dn/dt: particle rate). The geometrical dimension of the results are listed, too.

Diagnostic	***v***	***s***	***T***	***dn/dt***	**Dimension**	**Comment**
PVI	✓	✗	✗	✗	2D	
SprayWatch	✓	✗	✓	✗	2D	
Vattulainen [52]	✓	✗	✓	✗	2D	
Kirner [53]	✓	✗	✗	✗	3D	
DPV	✓	✓	✓	✓	0D	
Accuraspray	✓	✗	✓	✗	0D	Particle ensemble measurement
PFI	✗	✗	✗	✗	2D	Qualitative evaluation of the whole spray plume
PIV	✓	✗	✗	✗	2D	Possibility of 3D measurement
LDA	✓	✗	✗	✓	0D	
L2F	✓	✗	✗	✓	0D	
PDA	✓	✓	✗	✓	0D	
PSI	✗	✓	✗	✓	0D	
Fincke [71]	✓	✓	✓	✓	0D	

1.2 Need of further research

Besides the adhesion and the porosity, the oxide content is one of most important factors influencing the quality of metallic thermal sprayed coatings. Negative effects of oxides included in coatings are for example decreased hardness or decreased cohesion between splats leading to reduced toughness and cracking [72, 73]. However, there are not only disadvantages, oxides may also increase the bonding to the substrate [72] or improve the resistance to compressive loading [74]. Since in-flight oxidation of the particles mainly contributes to the oxide content [43, 44, 72] the in-situ measurement of particle properties is indispensable for process control and evaluation. As it can be seen on the basis of Table 1 the velocity as well as the size and the temperature of the particles influence the in-flight oxidation. Consequently all three parameters have to be known in order to draw reliable conclusions concerning the degree of oxidation. As it can be seen in Table 2 there are only two diagnostics that are able to measure all necessary particle parameters at once. On the one hand the DPV requiring a complex calibration and on the other hand the experimental setup of Fincke et al. [71] designed for research. Of course also other methods could be combined, but it is obvious that in any case a point by point measurement is necessary to get the velocity, the size and the temperature. And in order to achieve spatial resolved data of the whole spray plume the time consuming scanning of a measurement pattern is unavoidable. Furthermore even determined particle velocities, sizes and temperatures only allow qualitative or comparing statements regarding the oxidation, since it is very difficult to estimate the chemical influence of the process gas and the surrounding environment.

For these reasons, the aim of this work is the development of a diagnostic enabling the quantitative determination of particle in-flight oxidation along the spraying direction. The idea behind this innovative measurement technique is based on two-color-pyrometry. By observing the spray plume at two different wavelength bands and assuming gray body behavior an average surface temperature can be calculated. With the help of the known temperature and the intensities measured at one of the two wavelength bands, finally the change in emissivity caused by oxidation can be estimated. Further particle parameters that are needed as input for the model are measured with established diagnostics.

The recording and evaluation of the raw data is done by means of tomography. Through the combination of two-color-pyrometry and tomography three dimensional intensity and temperature distributions can be determined. The application of tomography on a thermal spray plume consisting of opaque particles is a completely new approach. In the past tomographic measurement techniques in thermal spraying have only been used for the investigation of plasma jets [75, 76].

2 Two-color-pyrometry

The two-color-pyrometry is an optical method for the contactless measurement of surface temperatures of solid bodies. In this measuring procedure the radiation of an object is observed at two different narrow wavelength regions and it is assumed that the emissivities of the surface at these two wavelengths are approximately similar. For the physical understanding of two-color-pyrometry the theoretical bases of thermal radiation have to be known. In the following chapter these are summarized and explained.

2.1 Theoretical bases of thermal radiation and two-color-pyrometry

The thermal radiation coming up against a body interacts in three different ways. It is partially reflected by the surface (reflectivity ρ), partially absorbed by the body (absorptivity α) and partially transmitted through the body (transmissivity τ). Since the incident radiation has to be the sum of the interacting radiation, the following relation can be written:

$$\alpha + \tau + \rho = 1 \qquad 2.1$$

The thermal radiation of bodies has been described for the first time by Gustav Kirchhoff [77]. He showed that the radiation absorbed by a body in thermal equilibrium is emitted in the same scale. This legality can be expressed by the absorptivity α and the emissivity ε:

$$\alpha = \varepsilon \qquad 2.2$$

A special king of radiation is the so called black body radiation. A black body absorbs the whole incident radiation, so that τ and ρ are equal zero and it follows for α and ε:

$$\alpha = \varepsilon = 1 \qquad 2.3$$

Josef Stefan [78] and Ludwig Boltzmann [79] discovered the dependence of the thermal radiated power of a black body on the temperature. They postulated that the power P emitted over the whole wavelength region by the surface A of a black body is the product precisely of this surface, the Stefan-Boltzmann-constant σ and the fourth power of the absolute temperature T of the black body.

$$P = \sigma A T^4 \qquad 2.4$$

The first one describing the thermal radiation in dependence on the temperature and the wavelength was Wilhelm Wien [80]. The Wien distribution law[81] exactly describes the spectrum of the thermal radiation of a black body for short wavelengths, however for long wavelengths the law does not fit experimental data. The spectral exitance depending on the temperature T and the wavelength λ can be calculated using Equation 2.5 [81].

$$M_{\lambda s}(\lambda,T)=\frac{C_1}{\lambda^5}\frac{1}{\exp\left(\frac{C_2}{\lambda T}\right)} \tag{2.5}$$

Where $C_1=2\pi hc^2$, $C_2=hc/k$, h is Planck's constant, c is the speed of light and k is the Boltzmann constant. The discrepancy in the Wien distribution law for long wavelengths could be solved by Planck's law. This law, postulated by Max Planck in the year 1900, describes the spectral exitance $M_{\lambda s}$ of a black body depending on his temperature T at a single wavelength λ [82–84]:

$$M_{\lambda s}(\lambda,T)=\frac{C_1}{\lambda^5}\cdot\frac{1}{\exp\left(\frac{C_2}{\lambda T}\right)-1} \tag{2.6}$$

Figure 11 shows spectral exitance curves for different black body temperatures dependent on the wavelength. It can be seen, that the maximum of the exitance is shifted to smaller wavelengths with increasing temperature. The wavelength λ_{max} wherein the spectral exitance $M_{\lambda s}$ of a black body with the temperature T reaches the maximum can be determined using Wien's displacement law [85]:

$$\lambda_{max}=\frac{2897.8}{T}\,[\mu\text{m}\cdot\text{K}] \tag{2.7}$$

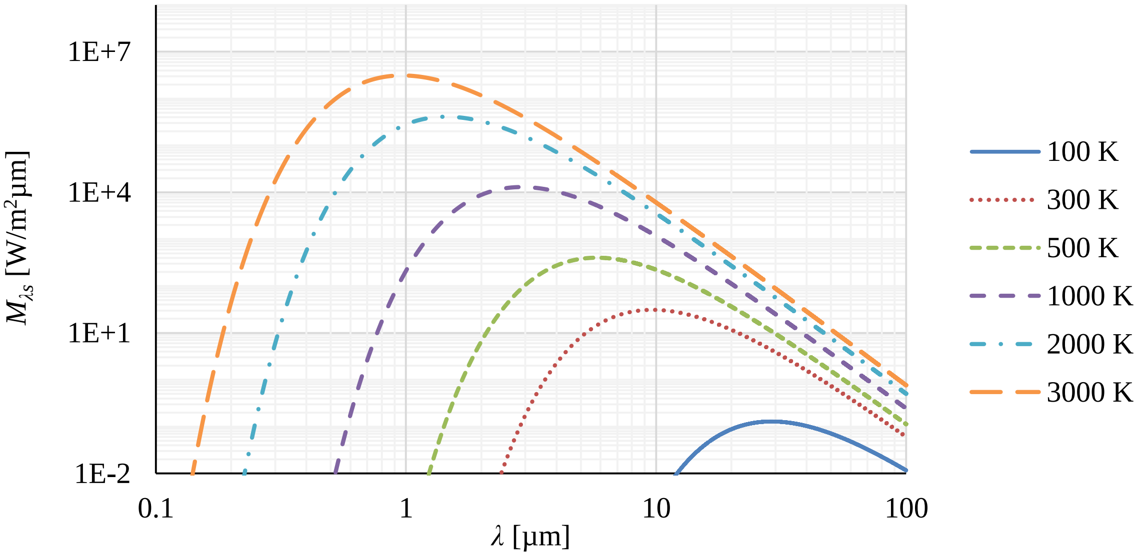

Figure 11: Spectral exitance curves for different black body temperatures in dependence of the wavelength.

A black body is idealized and does in reality not exist in this form. The behavior of a black body surface can e.g. be approximated by a narrow opening of a cavity in a metal cylinder [85]. For real bodies the absorptivity, the transmissivity, the reflectivity and the emissivity depend on the direction, the wavelength, the temperature [86] and on surface properties like e.g. roughness [87]. Figure 12 shows the principle behavior of the black, gray and real body emissivity depending on the wavelength. As we can see, the emissivity of a black body is constant and equals one, the emissivity of a gray body is also constant, but since the transmissivity and the reflectivity are not equal zero, the emissivity is smaller than one. The real body emissivity is also smaller than one and in general changes with the wavelength and the temperature. Accordingly for a real body the spectral exitance has to be multiplied by the emissivity to get the spectral radiant exitance $M_\lambda(\lambda,T)$:

$$M_\lambda(\lambda,T)=\varepsilon(\lambda,T)\cdot M_{\lambda s}(\lambda,T) \qquad 2.8$$

Since it is difficult and sometimes impossible to measure the emissivity, it is necessary to use a measurement method for the determination of the surface temperature that works independently on this parameter. The most important technique used in industry and research is the two-color-pyrometry. In the following chapters the principle of two-color-pyrometry and the technical realization in the context of this work are explained.

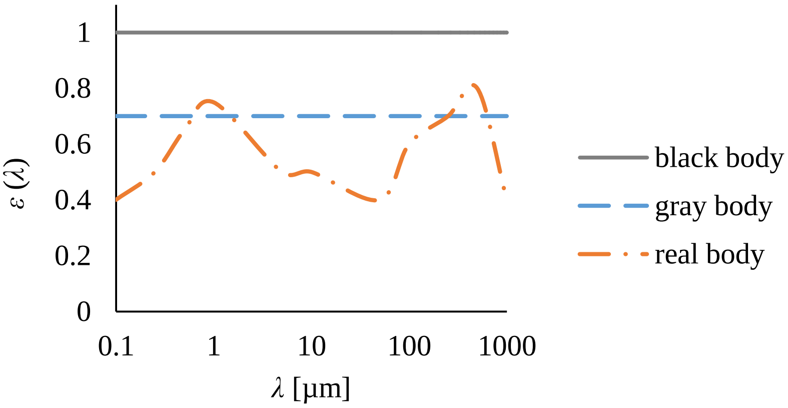

Figure 12: Principle emissivities of a black, a gray and a real body depending on the wavelength.

The basic principle of the two-color-pyrometry is the observation of the measurement object at two different wavelengths λ_1 and λ_2. For each wavelength the spectral radiant exitance has to be calculated and divided by each other, resulting in the quotient Q:

$$Q(T)=\frac{\varepsilon(\lambda_1,T)\cdot M_{\lambda s}(\lambda_1,T)}{\varepsilon(\lambda_2,T)\cdot M_{\lambda s}(\lambda_2,T)} \qquad 2.9$$

By the assumption that the observed object behaves like a gray body it follows

$$\varepsilon(\lambda_1, T) = \varepsilon(\lambda_2, T) \qquad 2.10$$

and consequently the emissivities in Equation 2.9 can be canceled. The remaining Equation 2.11 for the determination of the quotient Q just depends on the temperature T.

$$Q(T) = \frac{\lambda_2^5 \cdot \left(\exp\left(\frac{C_2}{\lambda_2 \cdot T} \right) - 1 \right)}{\lambda_1^5 \cdot \left(\exp\left(\frac{C_2}{\lambda_1 \cdot T} \right) - 1 \right)} \qquad 2.11$$

Because Equation 2.11 cannot directly be solved for T, measured intensity quotients have to be compared with quotients calculated with Equation 2.11.

2.2 Technical realization

In the following chapters the technical realization of the two-color-pyrometry is discussed. Particularly the setup, the selection of the components, the optical properties, the temperature calculation method and the calibration of the system are presented in detail.

2.2.1 Experimental setup

The principle setup of the two-color-pyrometer is shown in Figure 13 and was already used in similar form for the measurement of tungsten cathode temperatures [88]. It consists of two cameras, two lenses and a beam splitter integrated in a positioning device. The beam splitter divides the incident light in equal parts and different interference filters in front of each camera enable the observation of the measurement object at two different wavelengths. To guarantee precise overlapping of the two images the beam splitter can be positioned with micrometer screws and the cameras are rotatable. The usage of cameras as detectors enables two dimensional measurement and consequently the acquisition of temperature images.

For the diagnostic presented in this work the camera “pixelfly VGA” from the company “PCO AG” is selected. The advantages and disadvantages using this camera are, besides the interference filter and beam splitter selection, discussed in Chapter 2.2.2. The lenses used have a fixed focal length of 25 mm and an adjustable focal number reaching from 1.4 to 16. The optical properties of the two-color-pyrometer are presented in Chapter 2.2.3. Depending on which wire arc spraying parameter set is used, neutral density filters can additionally be placed in front of each camera. Furthermore the cameras are synchronized via the “exposure” output of camera 1 and the “trigger” input of camera 2.

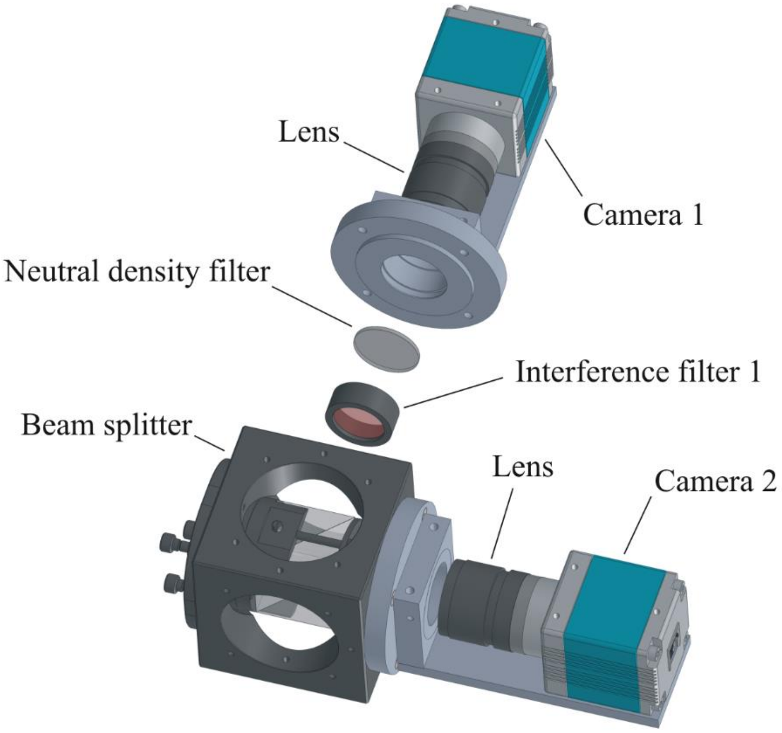

Figure 13: Principle setup of the Two-Color-Pyrometry consisting of two cameras, two lenses and a beam splitter. In front of each camera an interference filter is positioned (central wavelength filter 1: 800 nm, filter 2: 900 nm and FWHM=10 nm both).

2.2.2 Camera, interference filter and beam splitter selection

In this work a tomographic particle diagnostic based on two-color-pyrometry is presented. In the case of tomographic temperature measurements (see Chapter 3) the radiation of many particles is collected over a long time (>1 s) to obtain smooth images of the spray plume. Since the length of the exposure time has to be long, there is always enough light reaching the sensor of the camera and consequently no special requirements concerning the quantum efficiency q_e are necessary. To guarantee good image quality, the temperature compensated camera "pixelfly VGA" with high linearity (non linearity < 2 %) from the company "PCO AG" is chosen. This camera offers exposure times up to 65 s and is equipped with a CCD-Sensor (640x480 Pixels) with a dynamic range of 12 bit. The quantum efficiency dependent on the wavelength is shown in Figure 14. [89]

For the selection of the interference filters different aspects have to be considered. Gathers [90] demonstrated with his simulations that the error for the two-color-pyrometry, due to the assumption of constant emissivities, can be minimized using filters with peak intensity wavelengths widely separated and located on the blue side of the maximum of the spectral exitance. Since no secured information about the thermal properties of the used feedstock (material number 1.5125 [91]) is available, the properties of iron are used below. This is justifiable since 97.493 % of the wire consists of iron [91]. Thus the surface temperature of the observed liquid droplets range from the melting point of iron (1811 K [92]) to the boiling point of iron (3073 K [93]) and accordingly the spectral exitance maxima calculated with Wien's displacement law (see Equation 2.7) from 1600 nm to 943 nm. Consequently the peak intensity wavelengths of the two used interference filters have to be smaller than 943 nm. The bandwidth of the filters plays according to Gathers [90] no significant role. To maximize the signal received by the cameras, the spectral exitance has to be measured at wavelengths close to the spectral maximum (943 nm) of the lowest expected temperature and in a region, where the camera has adequate quantum efficiencies. For comparison the spectral exitance for a black body temperature of 1811 K is shown in Figure 15.

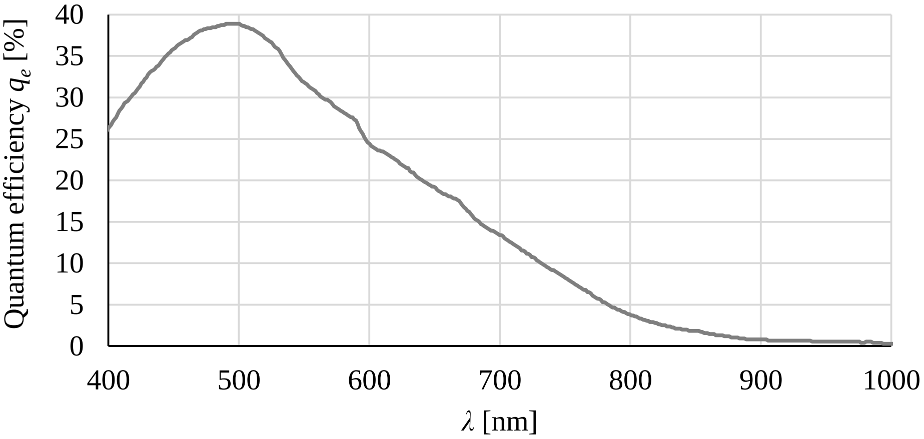

Figure 14: Quantum efficiency of the camera "pixelfly" from the company "PCO AG" [89].

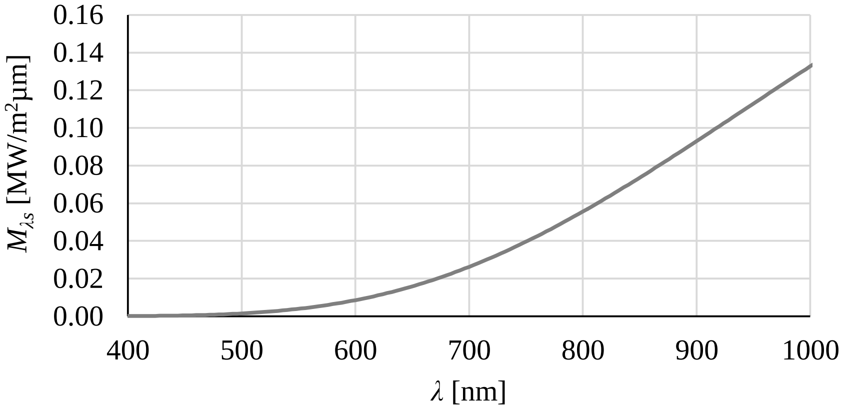

Figure 15: Spectral exitance for a black body temperature of 1811 K (melting point of iron).

The wavelength range, in which the camera receives the maximum thermal radiation emitted by the particles can be determined by multiplying the spectral radiance $M_{\lambda s}$ by the quantum efficiency q_e of the camera. Figure 16 for example shows the product of the spectral exitance trace for a temperature of 1811 K (see Figure 15) and the camera sensitivity curve (see Figure 14) dependent on the wavelength. As aforementioned there are no special demands on the quantum efficiency of the "pixelfly" camera therefore the wavelength range to be considered for the interference filter selection is chosen between 750 nm and 900 nm.

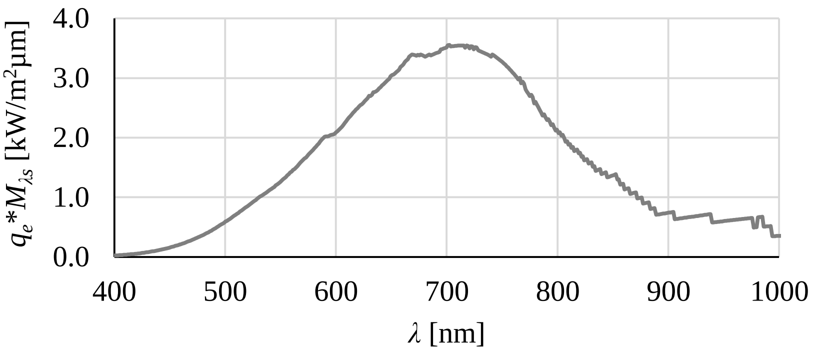

Figure 16: The spectral exitance for a temperature of 1811 K multiplied by the quantum efficiency curve of the "pixelfly" camera.

Furthermore on the one hand the separation of the central wavelengths has to be small to minimize the error caused by the gray body assumption and on the other hand large to minimize the temperature uncertainty caused by measurement errors. For these reasons interference filters with the peak intensity wavelengths $\lambda_1 = 800\,\text{nm}$ and $\lambda_2 = 900\,\text{nm}$ are chosen. In addition the filters have a *FWHM*-value (Full Width at Half Maximum) of 10 nm. The transmission curves of the used filters f_1 [94] and f_2 [95] depending on the wavelength are shown in Figure 17. Since the manufacturer curves are not individually measured for every single filter and the curves may differ due to fabrication tolerances, the wavelength dependent transmission is determined using a quartz halogen lamp and the spectrometer "MC-UV/NIR" from the company "TranSpec". To be able to calculate the transmission curves the spectrum of the lamp is measured both without and with filter between spectrometer input and lamp. Through dividing the spectrum without filter by the spectrum with filter the real transmission curves can be determined (see Figure 17).

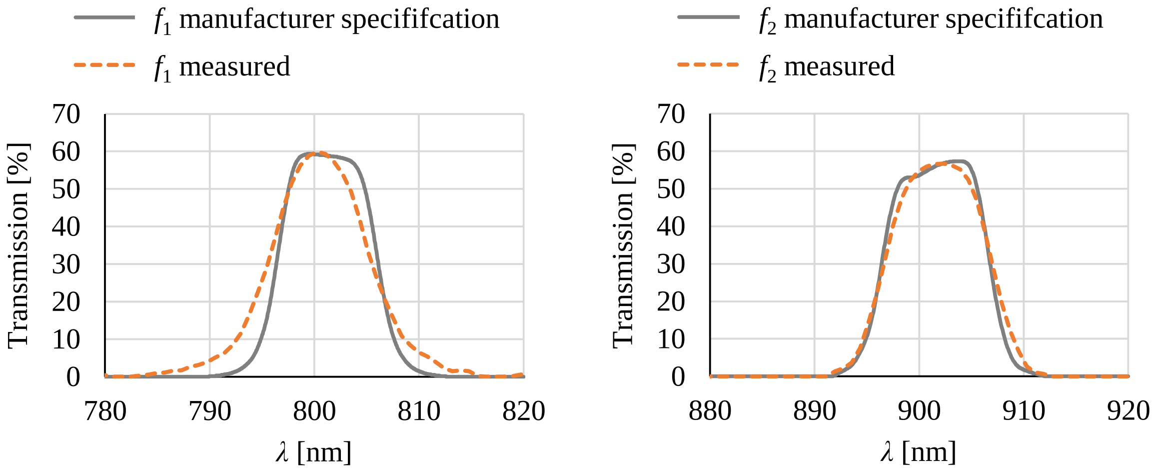

Figure 17: Left: Transmission curves of the interference filter f_1 with peak intensity wavelength at 800 nm and FWHM=10 nm (adopted from [94], *and measured). Right: Transmission curves of the interference filter f_2 with peak intensity wavelength at 900 nm and FWHM=10 nm (adopted from* [95] *and measured).*

The measurement error E_{GB} caused by the gray body assumption is defined by the ratio of the temperature error ($T_{real} - T_{measured}$) and the measured temperature [96]. For the following considerations the Wien approximation (see Equation 2.7) has to be solved for T resulting in Equation 2.12 and for the determination of $T_{measured}$ the ration $\varepsilon_2 / \varepsilon_1$ has to be set one. Furthermore it is assumed that the transmission curves of the interference filters are Dirac functions.

$$T = \frac{C_2 \left(\frac{1}{\lambda_2} - \frac{1}{\lambda_1} \right)}{\ln\left(\frac{M_{\lambda s,1}}{M_{\lambda s,2}} \cdot \frac{\varepsilon_2}{\varepsilon_1} \cdot \frac{\lambda_1^5}{\lambda_2^5} \right)} \tag{2.12}$$

The resulting Equation 2.13 [96, 97] (see derivation in the Appendix A.1) for E_{GB} only depends on the emissivities, the real temperature T_{real} and the two central wavelengths λ_1 and λ_2 of the interference filters.

$$E_{GB} = \frac{T_{real} - T_{measured}}{T_{measured}} = \frac{T_{real} \cdot \ln\left(\frac{\varepsilon(\lambda_1, T_{real})}{\varepsilon(\lambda_2, T_{real})} \right)}{C_2 \cdot \left(\frac{1}{\lambda_1} - \frac{1}{\lambda_2} \right)} \tag{2.13}$$

Taking the emissivities of liquid iron at 800 nm $\varepsilon(800\,\text{nm}, 1811\,\text{K}) = 0.3788$ and at 900 nm $\varepsilon(900\,\text{nm}, 1811\,\text{K}) = 0.3687$ calculated according to Watanabe et al. [98], the error due to gray body assumption is $E_{GB} = 2.42\,\%$.

For the calculation of the temperature uncertainty caused by measurement errors the spectral exitances in Equation 2.12 are approximated by the corresponding measured intensities I and the ratio of the emissivities is set one:

$$T = \frac{C_2 \left(\frac{1}{\lambda_2} - \frac{1}{\lambda_1} \right)}{\ln\left(\frac{I_1}{I_2} \cdot \frac{\lambda_1^5}{\lambda_2^5} \right)} \tag{2.14}$$

The temperature error ΔT can be estimated through the first order terms of a Taylor series as long as the variations ΔI_1 and ΔI_2 of the measured intensities are small [99, 100]:

$$\Delta T = \frac{\delta T}{\delta I_1} \Delta I_1 + \frac{\delta T}{\delta I_2} \Delta I_2 \tag{2.15}$$

Equation 2.16 [96] (see Appendix A.1) presents the solution of Equation 2.15. It describes the relative temperature error $\left|\Delta T / T\right|$ dependent on the temperature T, the measured intensities, their variations and the central wavelengths λ_1 and λ_2.

$$\left|\frac{\Delta T}{T}\right| = \left|\frac{T\lambda_1\lambda_2}{C_2\left(\lambda_2-\lambda_1\right)}\right| \cdot \left(\frac{\Delta I_1}{I_1}+\frac{\Delta I_2}{I_2}\right) \qquad 2.16$$

As Equation 2.16 shows the measurement uncertainties ($\Delta I_1 / I_1$ and $\Delta I_2 / I_2$) are amplified by a factor that only depends on the temperature and the wavelengths of the used interference filters. Choosing a wide separation of the central wavelengths decreases this factor and consequently the relative temperature error, too. For the used interference filters (800 nm and 900 nm) and the expected temperatures (1811 K to 3073 K) the factor is between 0.9062 and 1.5378. Assuming a worst case measurement uncertainty of $\Delta I = 50\,\text{counts}$ per pixel and an 80 % utilization of the dynamic range (“pixelfly” 12 bit) the temperature error ranges from 2.77 % to 4.69 %.

The last optical element that has to be chosen carefully is the beam splitter. Therefore a cube optimized for the NIR region from the company “QIOPTIQ” with an edge length of 30 mm is chosen. The beam splitter has a broadband antireflective-coating “ARB 2 NIR”, that guarantees residual reflections smaller than 0.5 % in a wavelength region between 750 nm and 1050 nm [101]. This special kind of coating is necessary to avoid multiple reflections between the sensor surface and the beam splitter surface (see Figure 13).

2.2.3 Optical properties

The sector of the spray plume that can be analyzed using the two-color-pyrometer depends on the measurement volume of the diagnostic. Particles in this volume appear in focus on the acquired images and can be correctly evaluated. As Figure 18 shows, the dimension of the measurement volume depends on the depth of field (*DOF*), the width *W* and the height *H* of the object plane (green).

A point light source positioned in the object plane of a lens is exactly imaged to the image plane or to be more precise to the sensor of the camera. If the source is moved out of focus it appears as round spot, the so called circle of confusion (CoC). As long as the size of the CoC is smaller than a pixel the image appears as if the object would be located in the object plane. Consequently for the calculation of the *DOF* the diameter of the CoC has to be smaller than the edge length of a pixel [102, 103].

The dimension of the *DOF* is restricted by the near limit D_N and the far limit D_F relating to the position of the lens. According to [103–106] D_N, D_F and *DOF* can be calculated using Equation 2.17, 2.18 and 2.19. The limits depend on the object distance S_o, the focal distance f, the f-Number N and the diameter d_c of the circle of confusion.

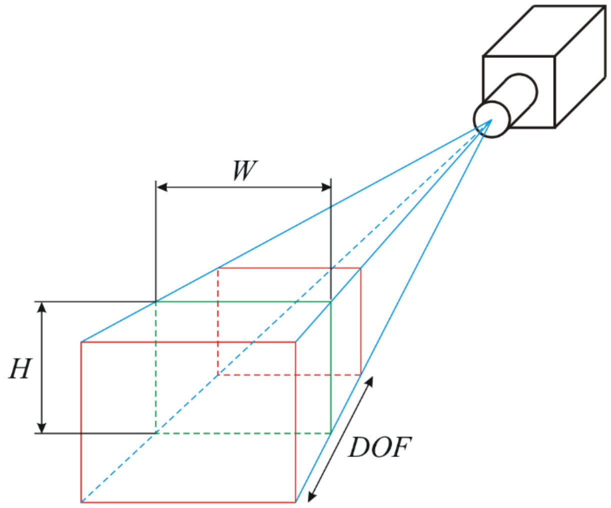

Figure 18: Measurement volume of the two-color-pyrometer dependent on the depth of view (DOF) and the object plane dimensions (green).

$$D_N = \frac{S_o f^2}{f^2 + Nd_c(S_o - f)} \tag{2.17}$$

$$D_F = \frac{S_o f^2}{f^2 - Nd_c(S_o - f)} \tag{2.18}$$

$$DOF = D_F - D_N \tag{2.19}$$

The diagram in Figure 19 presents the *DOF* dependent on the object distance for the “pixelfly” camera. The *DOF* in the diagram is calculated for the focal length $f = 25\,\text{mm}$, the f-Number $N = 16$ and the circle of confusion diameter $d_c = 9.9\,\mu\text{m}$ (edge length of a pixel [89]). As can clearly be seen, the *DOF* increases with increasing object distance.

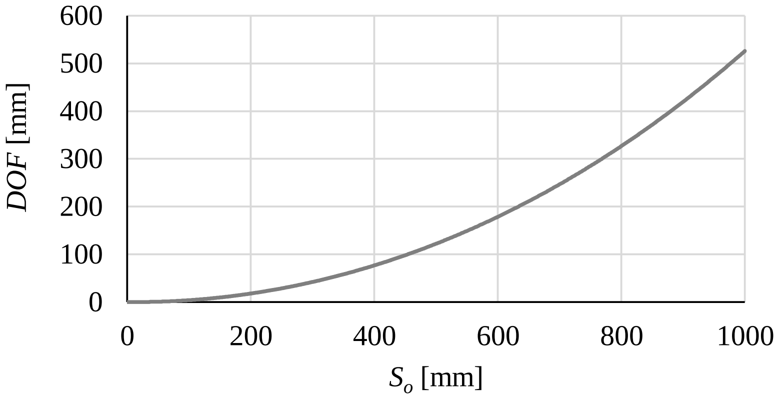

Figure 19: Depth of field (DOF) dependent on the object distance S_o for the “pixelfly”.

The calculated *DOF* for the object distance of the experimental setup (see Chapter 3.3.1) is listed in Table 3. The width W and the height H of the object plane are dependent on the resolution $w \times h$, the pixel edge length d_c, the object distance S_0 and the focal length f. The dimensions can be calculated using Equation 2.20 and 2.21. In addition they are listed in Table 3, too.

$$W = w \cdot d_c \cdot \frac{S_o - f}{f} \qquad 2.20$$

$$H = h \cdot d_c \cdot \frac{S_o - f}{f} \qquad 2.21$$

As it can be seen in Figure 18 the width and the height of the measurement volume changes outside the object plane. In order to estimate if this distortion can be neglected the following calculations are necessary. Figure 20 shows the geometrical relations for an object G positioned directly in the object plane S_o (green) and in the near limit D_N of the *DOF* (red).

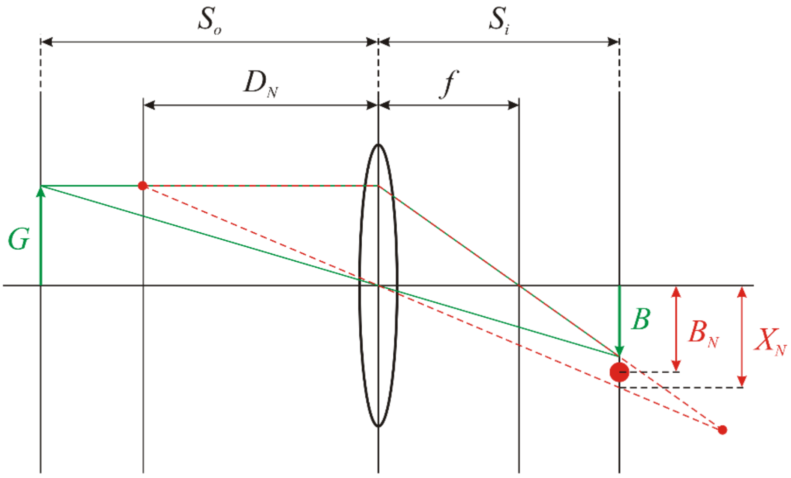

Figure 20: Optical imaging of an object G exactly located in the object plane S_0 and of the same object located in the near DOF limit D_N, whereat the image distance S_i (sensor position) is constant. B_N presents the blurred image and B the image in focus.

If the object is positioned in the object plane it is projected to the image plane S_i and the size B of the image can be determined using Equation 2.22.

$$B = G \frac{S_i}{S_0} \qquad 2.22$$

The same object located in the near limit of the *DOF* namely is perceived to be in focus but is stretched in the image plane S_i compared to the image B. In order to be able to calculate the extension B_N of the blurred image, the distance X_N (see Figure 20) has to be determined with the following equation:

$$X_N = S_i \frac{G}{D_N} \tag{2.23}$$

With the help of X_N and B it follows for B_N:

$$B_N = \frac{B + X_N}{2} \tag{2.24}$$

Finally the relation of B_N to B can be determined using Equation 2.25.

$$\frac{B_N}{B} = \frac{1}{2}\left(1 + \frac{S_o}{D_N}\right) \tag{2.25}$$

To get the relation of B_F to B only D_N in Equation 2.25 has to be replaced by D_F. All results concerning the measurement volume of the experimental setup presented in this chapter are listed in Table 3.

Table 3: Important optical properties of the experimental setup dependent on the pixel edge length of the "pixelfly" camera, the resolution of the camera and the object distance S_0.

Pixel edge length [µm]	9.9
Resolution $w \times h$	640×480
Object distance .. [mm]	625
Object plane width W **[mm]**	152.06
Object plane height H **[mm]**	114.05
Near limit of the depth of field D_N **[mm]**	542.50
Far limit of the depth of field D_F **[mm]**	737.08
Depth of field ***DOF*** **[mm]**	194.58
B_N/B	1.08
B_F/B	0.92

The values in the last two rows show that objects located in the near and far limit of the depth of field are enlarged for 8 % and minimized for 8 %, respectively. This geometrical error may be negligible since the expansion of the measurement object (spray plume) is significantly smaller than the *DOF* (see Chapter 3.3.2).

2.2.4 Temperature calculation

The real intensities I_1 and I_2 detected by the cameras with the two different interference filters in front can be calculated using Equation 2.26 and 2.27.

$$I_1(T) = K_1 \cdot \int_{\lambda_s}^{\lambda_e} q_e(\lambda) \cdot f_1(\lambda) \cdot \varepsilon(\lambda, T) \cdot M_{\lambda s}(\lambda, T)\, d\lambda \quad \text{with } \lambda_{s/e} = \lambda_1 \mp 2 \cdot FWHM \qquad 2.26$$

$$I_2(T) = K_2 \cdot \int_{\lambda_s}^{\lambda_e} q_e(\lambda) \cdot f_2(\lambda) \cdot \varepsilon(\lambda, T) \cdot M_{\lambda s}(\lambda, T)\, d\lambda \quad \text{with } \lambda_{s/e} = \lambda_2 \mp 2 \cdot FWHM \qquad 2.27$$

Therefore the camera quantum efficiency q_e and the transmission curves of the filters f_1 and f_2 have, besides the spectral radiant exitance, to be taken into account. Since the transmission curves of the filters are not a Dirac function, the integral with respect to λ on the interval λ_s to λ_e has to be formed. Furthermore calibration factors K_1 and K_2, that include different uncertainties, are necessary. One of the main problems responsible for the need of calibration factors is the use of manufacturer data concerning the transmission curves of the filters (see Figure 17) and the quantum efficiency of the camera (see Figure 14). As the exchange of the components with nominally the same characteristic has shown, there is a large deviation and the manufacturer data may only be used for reference. Further problems that have to be taken into account are possible shifts of the central wavelengths caused by a tilt of the interference filters [107] and the wavelength dependent reflection and transmission curves (50 % ± 3 % [108]) of the beam splitter. Since the results of the integrals of Equation 2.26 and 2.27 indicate the emitted power per square meter and the measured intensities are dimensionless quantities, the calibration factors K_1 and K_2 must have the unit $\mathrm{m^2/W}$.

As already mentioned in Chapter 2.1 the assumption is made that the observed objects behave like grey bodies and consequently the emissivities equal one and only depend on the temperature:

$$\varepsilon(\lambda, T) = \varepsilon(T) \qquad 2.28$$

By forming the quotient of I_1 and I_2 the emissivities can be canceled so that the resulting Equation 2.29 only depends on the temperature, whereas the quotient of the calibration factors can be written as $K = K_1 / K_2$.

$$Q(T)=\frac{I_1(T)}{I_2(T)}=K\cdot\frac{\int_{\lambda_s}^{\lambda_e} q_e(\lambda)\cdot f_1(\lambda)\cdot M_{\lambda s}(\lambda,T)d\lambda}{\int_{\lambda_s}^{\lambda_e} q_e(\lambda)\cdot f_2(\lambda)\cdot M_{\lambda s}(\lambda,T)d\lambda} \tag{2.29}$$

Because from f_1, f_2 and q_e only single values and no functions are available, the integrals in Equation 2.29 cannot be solved and have to be approximated with the so called Riemann sum [109]. The quotient Q dependent on T can finally be calculated using Equation 2.30.

$$Q(T)=K\cdot\frac{\sum\limits_{i=-2\cdot FWHM/\Delta\lambda}^{2\cdot FWHM/\Delta\lambda} q_e(\lambda_1+i\cdot\Delta\lambda)\cdot f_1(\lambda_1+i\cdot\Delta\lambda)\cdot M_{\lambda s}(\lambda_1+i\cdot\Delta\lambda,T)\cdot\Delta\lambda}{\sum\limits_{i=-2\cdot FWHM/\Delta\lambda}^{2\cdot FWHM/\Delta\lambda} q_e(\lambda_2+i\cdot\Delta\lambda)\cdot f_2(\lambda_2+i\cdot\Delta\lambda)\cdot M_{\lambda s}(\lambda_2+i\cdot\Delta\lambda,T)\cdot\Delta\lambda} \tag{2.30}$$

The constant step size $\Delta\lambda$ has to be chosen small in order to minimize the error. The evaluation of the data has shown that a step size of $\Delta\lambda=0.5\,\text{nm}$ is sufficient for a good approximation of the integrals. Figure 21 shows the quotient Q dependent of the temperature T calculated for the transmission curves f_1 and f_2, the quantum efficiency q_e of the “pixelfly” camera and a calibration factor of $K=0.1828$.

In order to determine a 2D-temperature distribution, the intensities measured by camera 1 have to be divided by the ones measured by camera 2 (Q_m). As Equation 2.30 cannot be solved for the temperature, the measured quotients Q_m on position x and y of the quotient image have to be compared with the calculated quotient $Q(T)$ in order to determine the measured temperature $T_m(x,y)$. If $Q(T)$ is equal $Q_m(x,y)$ it follows $T_m(x,y)=T$.

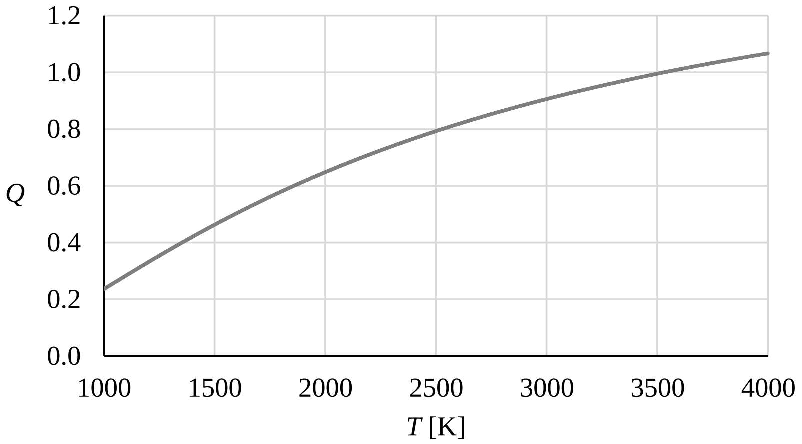

Figure 21: Quotient Q dependent on the temperature T calculated for the transmission curves f_1 and f_2, the quantum efficiency qe of the “pixelfly” camera, a calibration factor of $K = 0.1828$ and a step size of $\Delta\lambda = 0.5$ nm.

2.2.5 Calibration of the two-color-pyrometer

For the estimation of the calibration factor K the miniature quartz halogen lamp “L7390A” (tungsten filament) and a precision current source with four different levels are used. To be able to calibrate the two-color-pyrometer the temperatures of the lamp for the four current values have to be known. Therefore the spectra of the four levels (Figure 22) are measured using the spectrometer “Aryelle” from the company “LBS-Berlin”.

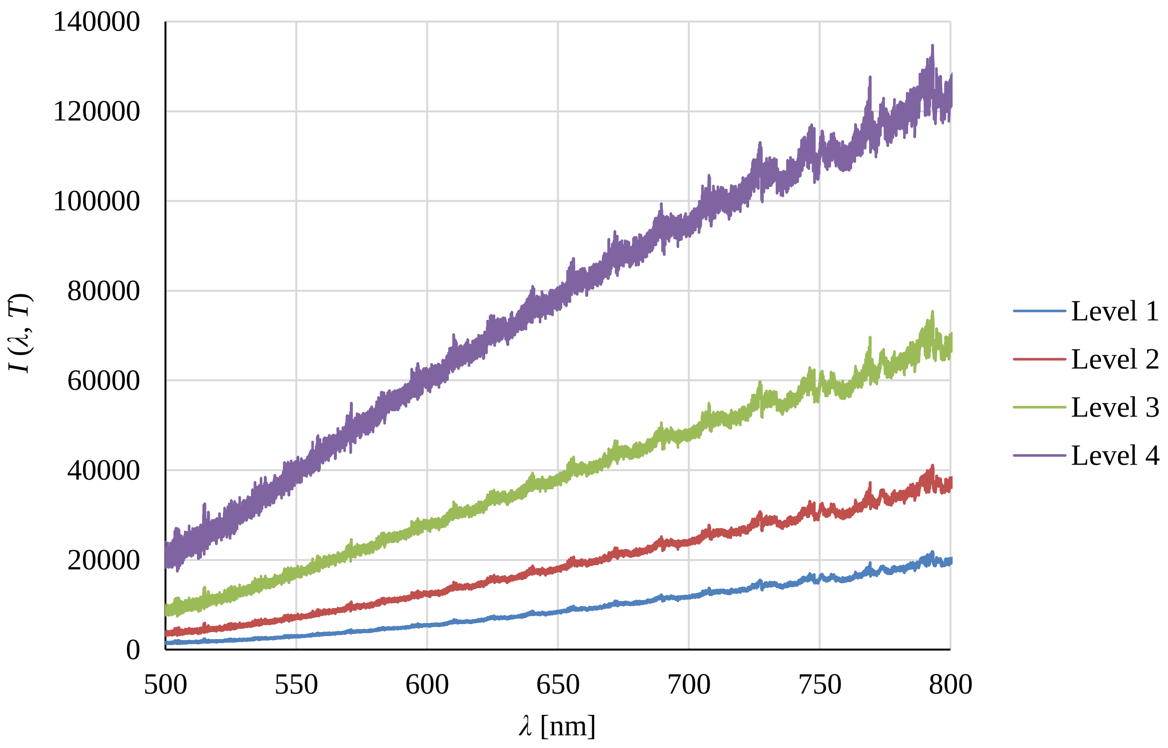

Figure 22: Spectra of the miniature halogen lamp at four different current levels measured with the spectrometer “Aryelle”

The dimensionless recorded spectral intensity $I(\lambda)$ of the lamp can be described by the following equation:

$$I(\lambda, T) = k_0 \cdot \varepsilon(\lambda, T) \cdot M_{\lambda s}(\lambda, T) \qquad 2.31$$

In this connection k_0 [m³W^{-1}] is a proportional factor that takes the geometrical dependence of the radiation into account and $\varepsilon(\lambda, T)$ is the emissivity of the lamp (tungsten filament). As the results of Dmitriev et al. [110] and Larrabee et al. [111] in Figure 23 show, the emissivity of tungsten for the estimated temperatures (2000 K – 3000 K) and the observed wavelength region (500 nm – 800 nm) is almost constant. Thus $\varepsilon(\lambda, T)$ and k_0 can be summarized to the proportional factor H_T [m³W^{-1}]. From Equation 2.6 and 2.31 it finally follows for $I(\lambda, T)$:

$$I(\lambda,T) = H_T \cdot \frac{C_1}{\lambda^5} \cdot \frac{1}{\exp\left(\frac{C_2}{\lambda \cdot T}\right) - 1} \tag{2.32}$$

The unknown parameter H_T and T in this equation are determined by fitting Equation 2.32 to the N measured discrete values $I_i(\lambda_i, T)$ by means of the least-square method. Therefore the sum of square residuals R is calculated:

$$R = \frac{1}{2} \cdot \sum_{i=1}^{N} \left(I_i(\lambda_i, T) - H_T \cdot \frac{C_1}{\lambda_i^5} \cdot \left(\exp\left(\frac{C_2}{\lambda_i \cdot T}\right) - 1 \right)^{-1} \right)^2 \tag{2.33}$$

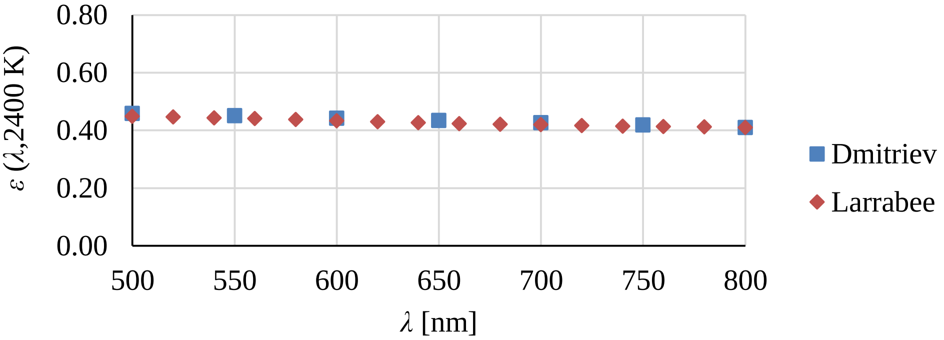

Figure 23: Emissivity of tungsten for 2400 K dependent on the wavelength measured by Dmitriev et al. [110] *and Larrabee et al.* [111].

Since Equation 2.33 is a non-linear least-square problem, the Levenberg-Marquardt (LM) algorithm is used for the calculation of the parameter vector $\boldsymbol{p} = (H_T, T)$ [112]. For this iterative technique the Jacobian Matrix $\boldsymbol{J}$ of $I(\lambda, T)$ has to be determined (see Equation 2.34):

$$\boldsymbol{J} = \frac{\delta \boldsymbol{I}}{\delta \boldsymbol{p}} = \begin{pmatrix} \frac{\delta I(\lambda_1, T)}{\delta H_T} & \frac{\delta I(\lambda_1, T)}{\delta T} \\ \vdots & \vdots \\ \frac{\delta I(\lambda_i, T)}{\delta H_T} & \frac{\delta I(\lambda_i, T)}{\delta T} \\ \vdots & \vdots \\ \frac{\delta I(\lambda_N, T)}{\delta H_T} & \frac{\delta I(\lambda_N, T)}{\delta T} \end{pmatrix} \tag{2.34}$$

with

$$\frac{\delta I(\lambda_i, T)}{\delta H_T} = \frac{C_1}{\lambda_i^5} \cdot \frac{1}{\exp\left(\frac{C_2}{\lambda_i \cdot T}\right) - 1} \tag{2.35}$$

and

$$\frac{\delta I(\lambda_i,T)}{\delta T}=H_T\cdot\frac{C_1\cdot C_2}{\lambda_i^6\cdot T^2}\cdot\exp\left(\frac{C_2}{\lambda_i\cdot T}\right)\cdot\left(\exp\left(\frac{C_2}{\lambda_i\cdot T}\right)-1\right)^{-2} \qquad 2.36$$

At the beginning of the LM method the starting point $\boldsymbol{p_0}=(H_{T_0},T_0)$ has to be chosen. Subsequently in every iteration step the correction vector $\boldsymbol{\delta_p}=(\Delta H_T,\Delta T)$, that minimizes the sum *R* of square residuals, has to be found. To get $\boldsymbol{\delta_p}$ the following system of linear equations has to be solved:

$$\left(\boldsymbol{J}^T\boldsymbol{J}+\mu\boldsymbol{E}\right)\cdot\boldsymbol{\delta_p}=\boldsymbol{J}^T\boldsymbol{\varepsilon} \qquad 2.37$$

with μ as damping term, ***E*** as identity matrix and $\boldsymbol{\varepsilon}=\left(I_1-I(\lambda_1),\dots,I_i-I(\lambda_i),\dots,I_N-I(\lambda_N)\right)$ as error vector. In Equation 2.37 $\boldsymbol{J}^T\boldsymbol{J}$ can be combined to $\boldsymbol{N}$ and $\boldsymbol{J}^T\boldsymbol{\varepsilon}$ to $\boldsymbol{F}$ and it follows:

$$\left(\boldsymbol{N}+\mu\boldsymbol{E}\right)\cdot\boldsymbol{\delta_p}=\boldsymbol{F} \qquad 2.38$$

so that

$$\Delta T=\frac{\left(F_2-F_1\cdot\frac{N_{21}}{N_{11}+\mu}\right)}{N_{22}+\mu-\frac{N_{12}\cdot N_{21}}{N_{11}+\mu}}\quad\text{and}\quad\Delta H_T=\frac{F_1-N_{12}\cdot T_1}{N_{11}+\mu}. \qquad 2.39$$

The algorithm has to be repeated until the chosen abort criterion is fulfilled. The used starting points and parameters are presented in the following listing of the complete algorithm:

1. Choosing starting point $\boldsymbol{p_0}$ (for all calculations $H_{T_0}=1\,\mathrm{m^3W^{-1}}$ and $T_0=10000\,\mathrm{K}$ was chosen)
2. Calculation of R_{old}, ***N*** and ***F*** using $\boldsymbol{p_{old}}$ and Equation 2.33 - Equation 2.37
3. Choosing damping term μ (for all calculation $\mu=1$ was chosen)
4. Calculation of $\boldsymbol{\delta_p}$ using ***N***, ***F***, $\boldsymbol{p_{old}}$ and Equation 2.39
5. Calculation of $\boldsymbol{p_{new}}=\boldsymbol{p_{old}}+\boldsymbol{\delta_p}$ and R_{new} using $\boldsymbol{p_{new}}$
6. If $R_{new}>R_{old}$ then double μ, $R_{old}=R_{new}$ and go to step 4
   If $R_{new}<R_{old}$ then $\boldsymbol{p_{old}}=\boldsymbol{p_{new}}$, $R_{old}=R_{new}$ and go to step 3
7. The iterations from step 3 to step 6 are done until $R_{new}=R_{old}$ (local minimum of the sum of square residuals *R* is reached)

The diagram in Figure 24 shows the evolution of H_{Tnew} and T_{new} for the spectrum of level 1 dependent on the iteration step. The trends of the graphs indicate the convergence of the algorithm and show that there is no significant change after 8 iterations.

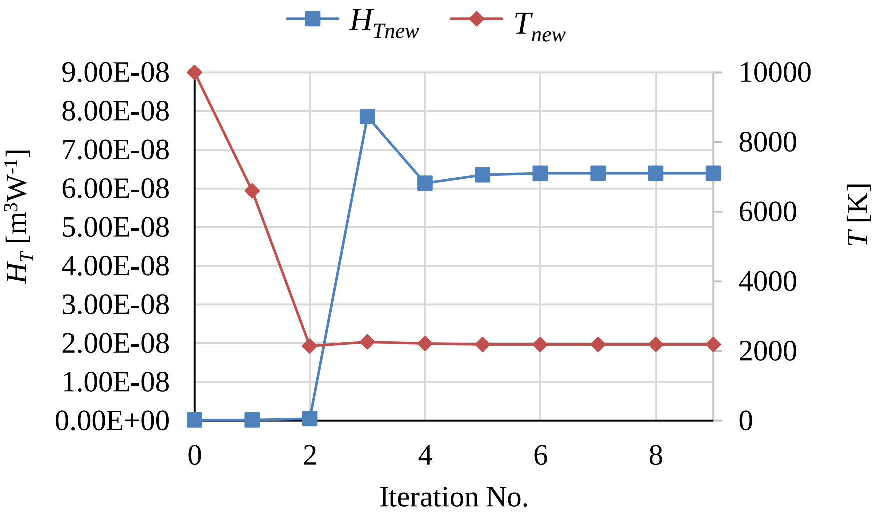

Figure 24: Convergence of the parameters H_{Tnew} and T_{new} for the fit to the lamp spectrum measured at current level 1 after nine iterations.

In Table 4 the calculated temperatures T_{ref} and proportional factors H_T for the four levels are listed. At level 1 the algorithm was canceled after 11 iterations, at level 2 after 14 iteration, at level 3 after 20 iterations and at level 4 after 19 iterations.

Table 4: Calculated temperatures T_{ref} and proportional factors H_T for the four different current levels of the halogen lamp.

Level	**Current [A]**	T_{ref} [K]	H_T [m^{3}W^{-1}]
1	4.82	2190	$6.39 \cdot 10^{-8}$
2	5.42	2351	$6.82 \cdot 10^{-8}$
3	6.11	2530	$7.34 \cdot 10^{-8}$
4	6.92	2723	$8.12 \cdot 10^{-8}$

The example in Figure 25 shows the measured spectrum (blue) of the halogen lamp at current level 1 and the corresponding calculated spectrum (red). It can be seen that Equation 2.32 using the calculated parameters of Table 4 is a good approximation for the measured values.

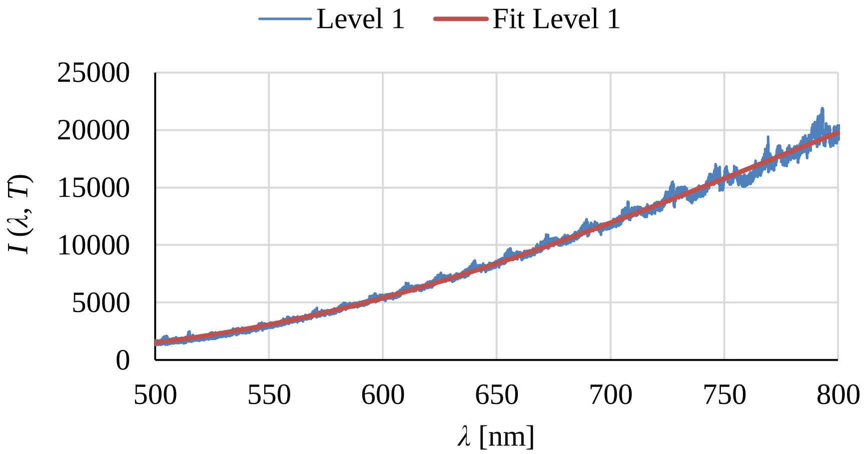

Figure 25: Measured spectrum (blue) $I_i(\lambda_i, T)$ *of the miniature halogen lamp at current level 1 and the corresponding calculated spectrum (red)* $I(\lambda_i, T)$

As the two-color-pyrometer enables two dimensional measurements and consequently the complete camera sensors are used, the calibration has to be done for every pixel. Responsible therefore is the dependence of the transmittance and the reflectance of the beam splitter cube on the incidence angle of light [113] and the reduction of the image brightness from the periphery towards the center due to natural and optical vignetting [114, 115]. For this reason an experimental setup, as shown in Figure 26, was arranged that consists of a holder for the two-color-pyrometer and a device to move the calibration lamp. The vertical movement is done by a hand driven linear axle and the horizontal movement by a stepper driven linear axle.

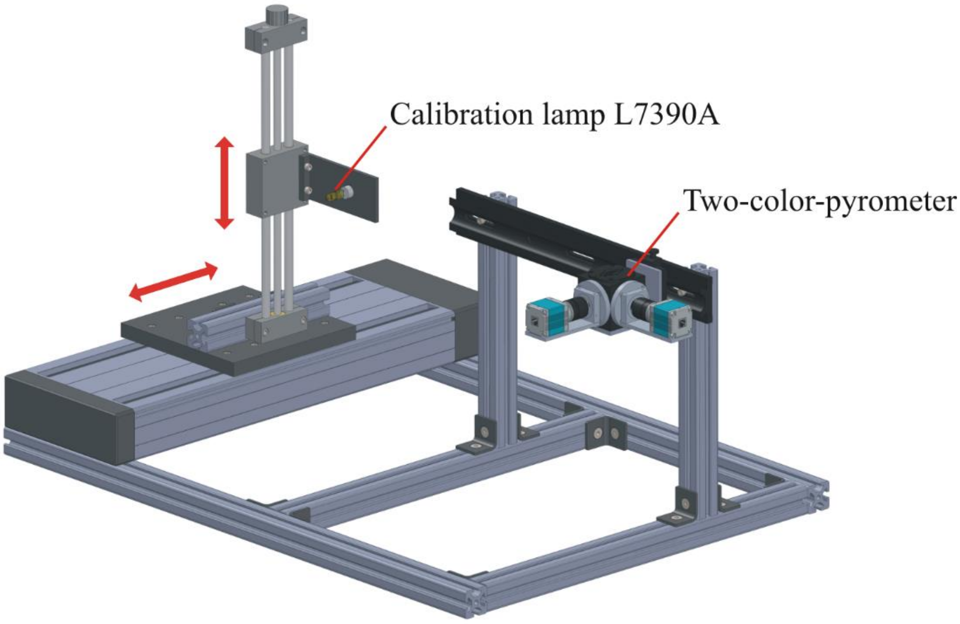

Figure 26: Experimental setup for the calibration of the two-color-pyrometer, consisting of the calibration lamp that can be moved horizontal and vertical using a stepper motor driven axle and a hand driven linear axle.

By moving the stepper driven axle with high velocity and acquiring an image with long exposure time, the moving lamp appears as straight stripe on the camera sensor. A constant lamp velocity throughout the object plane of the two-color-pyrometer is reached, by setting the start and end point 20 cm before and after the position where the lamp goes into the measurement volume and leaves the measurement volume. This ensures that the acceleration and brake ramps are completed in time. Since the particles of the spray plume are less bright using nitrogen as atomizing gas instead of compressed air, different neutral density filters have to be mounted in front of the two-color-pyrometer and consequently the calibration has to be performed for both cases. The neutral density filter combinations for the two different setups are, besides the calibration levels, velocities and exposure times, listed in Table 5.

Table 5: Neutral density filter (OD: optical density) combinations used for the two different atomizing gases and the corresponding calibration levels, lamp velocities and exposure times.

Atomizing gas	**ND filter camera 1**	**ND filter camera 2**	**ND filter for both**	**Level**	**v_L [cm/min]**	**t_E [s]**
Compressed air	OD = 2.0	OD = 0.4	OD = 0.6	4	600	5
Nitrogen	OD = 2.0	OD = 0.4	-	1	900	3

In Figure 27 typical images of the moving calibration lamp recorded with camera 1 (800 nm filter, receives transmitted light) and camera 2 (900 nm filter, receives reflected light) are presented. In Figure 28 the maxima of all columns are plotted against the *y*-coordinate. The diagrams of the column maxima show that the measured lamp intensities are not constant in *y*-direction, although the velocity and the lamp current have not been changed. To get the dependence along the *x*-direction, too, many single pictures of the moving lamp are acquired,

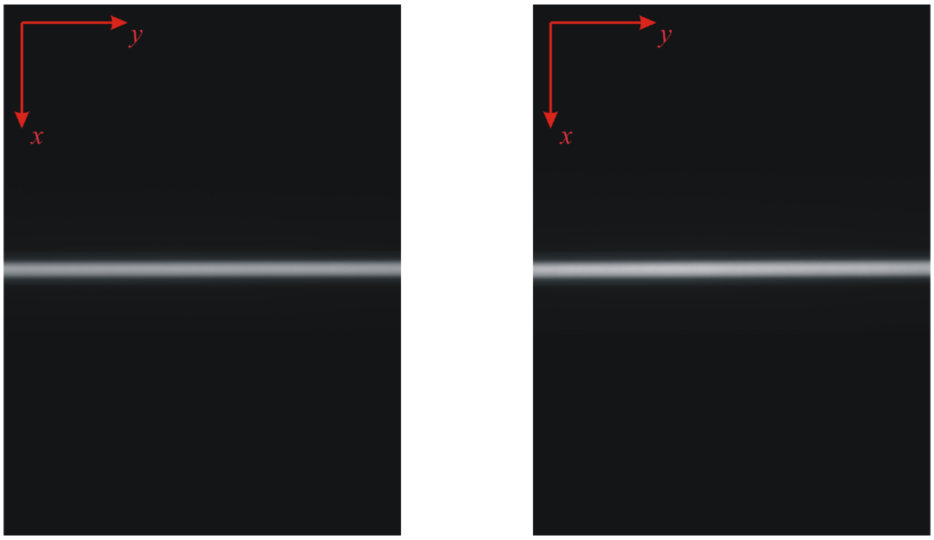

Figure 27: Images of the moving calibration lamp (level 4, compressed air) recorded with camera 1 (left, 800 nm interference filter) and camera 2 (right, 900 nm interference filter).

whereby the lamp position in *x*-direction is previously changed. The result is a series of pictures on which the stripe moves top down. The distance between two following stripes is approximately 10 pixels. In order to get a reference intensity for every pixel of the sensor, the missing values in *x*-direction are calculated through linear interpolation between two adjacent intensities.

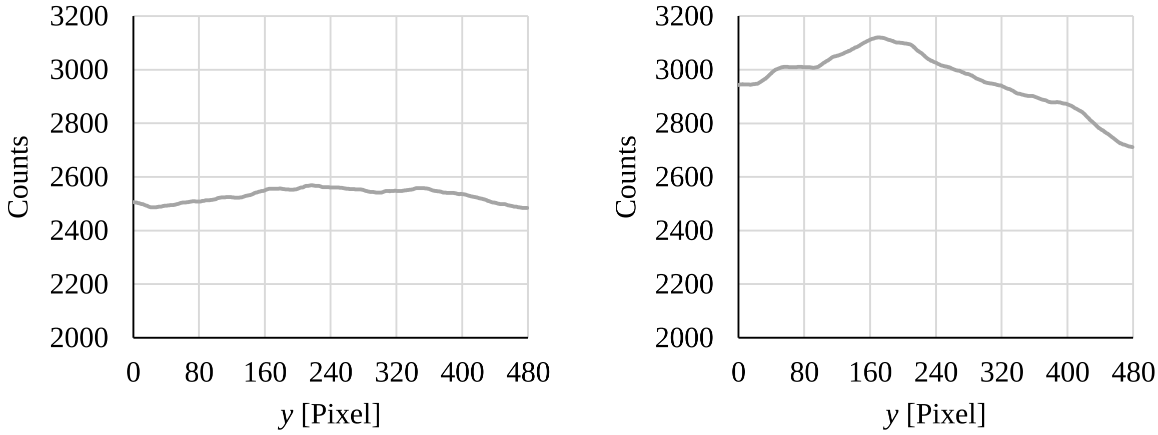

Figure 28: Maxima for all columns of the stripe images presented in Figure 27 (left: camera 1, right: camera 2) plotted against the y-coordinate.

An example for such a calculated intensity field can be seen in Figure 29. It belongs to camera 1 and was determined using the calibration setup for compressed air. According to Table 5 the lamp level was set to 4, the velocity to 600 cm/min and the exposure time to 5 s.

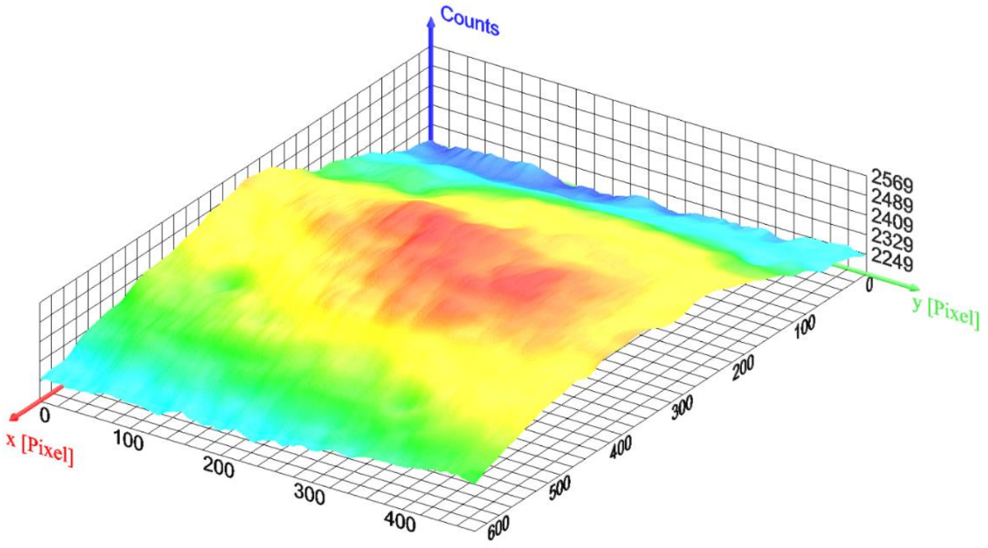

Figure 29: Intensity field of camera 1, calculated using a series of stripe pictures. The calibration setup for compressed air was used (lamp level 4, velocity 600 cm/min, exposure time 5 s).

To achieve the same sensitivity for every pixel of camera 1 and camera 2, correction matrices are determined. For this purpose average reference values $I_{ref,1}$ and $I_{ref,2}$ over 10 x 10 pixels located in the middle of the intensity fields are calculated and subsequently the value of every pixel is divided by the corresponding reference value (camera 1: $I_{ref,1}$ and camera 2: $I_{ref,2}$). In Figure 30 the correction factor matrix for camera 1 calculated using the intensity field in Figure 29 is presented. The intensity fields and the corresponding correction factor fields for camera 2 and for the two-color-pyrometer setup used for nitrogen are shown in the Appendix A.1.

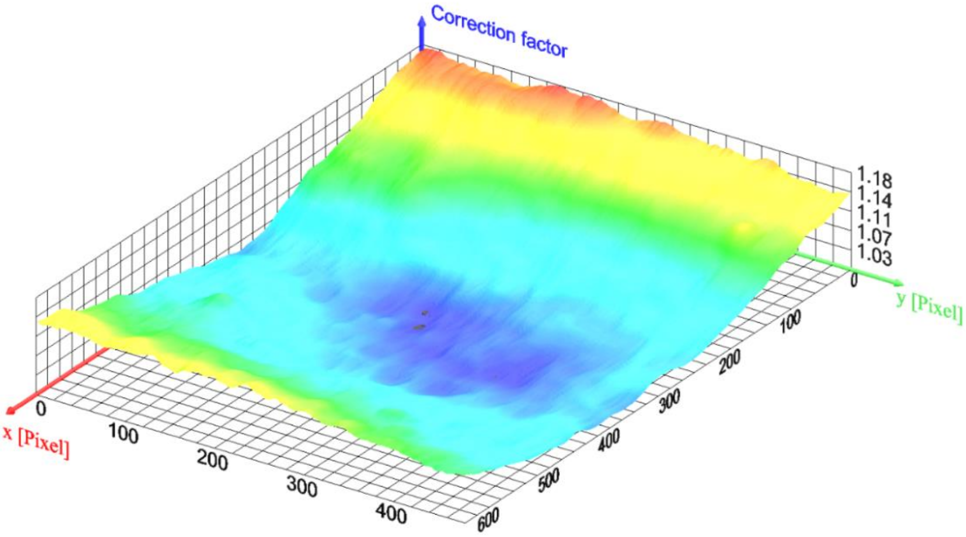

Figure 30: Correction factors for camera 1, calculated using the intensity field in Figure 29 and the average intensity $I_{ref,1}$ located in the middle of the intensity field.

Because of the per-element multiplication of the raw images by the correction factor matrices before the temperature determination, it is sufficient to calculate a single calibration factor K that is valid for the complete quotient image (see Chapter 2.2.4). For this purpose Equation 2.30 has to be solved for K, and T has to be set to T_{ref} according to the used calibration level (see Table 4). Furthermore $Q\left(T_{ref}\right)$ is given by the ratio of $I_{ref,1}$ and $I_{ref,2}$. The final expression for the determination of the calibration factor is summed up in Equation 2.40.

$$K = \frac{I_{ref,1}}{I_{ref,2}} \cdot \frac{\sum\limits_{i=-2\cdot FWHM/\Delta\lambda}^{2\cdot FWHM/\Delta\lambda} q_e\left(\lambda_2 + i\cdot\Delta\lambda\right)\cdot f_2\left(\lambda_2 + i\cdot\Delta\lambda\right)\cdot M_{\lambda s}\left(\lambda_2 + i\cdot\Delta\lambda, T\right)\cdot\Delta\lambda}{\sum\limits_{i=-2\cdot FWHM/\Delta\lambda}^{2\cdot FWHM/\Delta\lambda} q_e\left(\lambda_1 + i\cdot\Delta\lambda\right)\cdot f_1\left(\lambda_1 + i\cdot\Delta\lambda\right)\cdot M_{\lambda s}\left(\lambda_1 + i\cdot\Delta\lambda, T\right)\cdot\Delta\lambda} \qquad 2.40$$

In Table 6 the calibration factors for the two-color-pyrometer setups used for compressed air and nitrogen are listed.

Table 6: Calculated calibration factors for the compressed air setup and the nitrogen setup.

Atomizing gas	**Level**	**Calibration factor K [m^2/W]**
Compressed air	**4**	0.1828
Nitrogen	**1**	0.1236

3 Tomographic measurement of the temperature distribution

In order to obtain a 3D temperature distribution of the spray plume, the two-color-pyrometer has to be combined with a tomographic recording and evaluation technique. The fundamentals of tomography and the technical realization, including the experimental setup and the data processing, are explained in the following chapters. Furthermore the requirements on the wire arc spray plume, that have to be fulfilled to enable tomographic investigations, are discussed. For convenience the fundamentals of tomography are discussed on the basis of a single cross section of the measurement object.

3.1 Fundamentals of tomography

The aim of tomography is the reconstruction of three dimensional objects using two-dimensional distributions of measured values acquired from different directions. The foundations for tomography were laid by the mathematician Johann Radon in 1917 with the Radon-Transformation [116, 117]. With his work [118] he proved the existence of a projection value $p(\phi,i)$ that can be calculated through integrating a function $f(x,y)$ along a straight line $L_{\phi,i}$. As long as $f(x,y)$ is steady and becomes zero within a circle with endless radius it follows:

$$p(\phi,i)=\int_{L_{\phi,i}} f(x,y)ds \qquad 3.1$$

As illustrated in Figure 31, $L_{\phi,i}$ is defined by the angle ϕ between the straight line and the x-axis and the distance i to the center point.

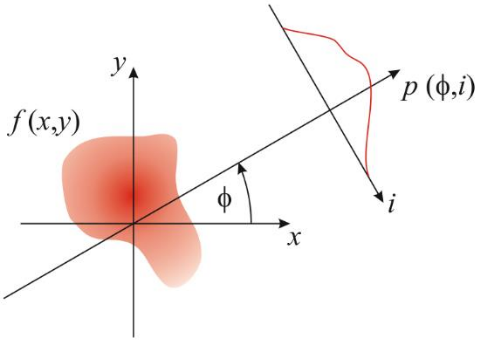

Figure 31: Principle of the Radon-transformation: Calculation of a value p through integrating a function f(x,y) along a straight line given by the angle ϕ and the distance i.

For the generation of the projection values two different acquisition methods that depend on the properties of the observed object, can be used. The first one, that is well-known from Computed Tomography (CT) in human medicine, is the so called transmission tomography (see Figure 32 left). Here the object is illuminated with an X-ray source and the transmitted light is projected onto a detector [116]. In contrast, for emission tomography no additional light source is necessary. The precondition for this is an object that is luminous and optically thin. A schematic drawing of such an object is shown in Figure 32 on the right side. Optically thin means that light emitted from any place can leave the object without being absorbed [119, 120] and consequently information of the whole object receives the detector. Since the particles are luminous and the radiation carries the temperature information, only emission tomography can be considered for the wire arc spray process. The optical depth of the spray plume is discussed in Chapter 3.2.

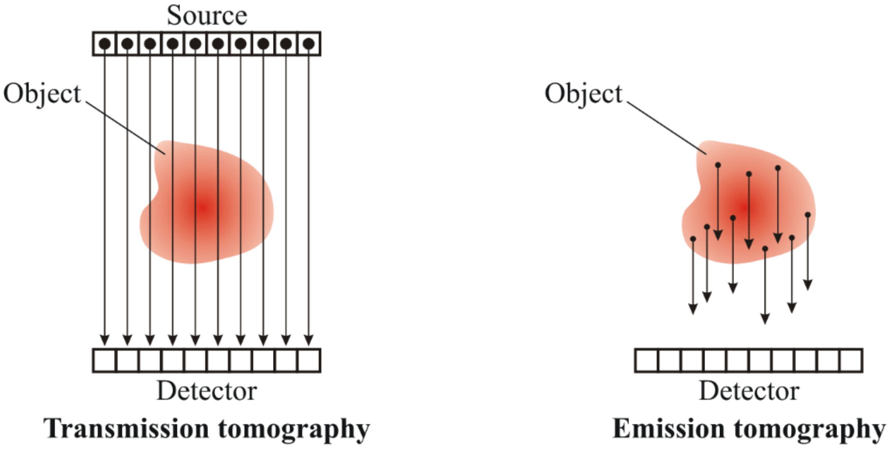

Figure 32: Principle methods for the tomographic projection generation. Left: object is illuminated and the transmitted light is projected onto the detector. Right: optically thin and luminous objects can be projected onto the detector without external light source.

To be able to solve the inverse problem of Equation 3.1 and to compute $f(x,y)$, many projections from different directions are necessary (see Figure 33).

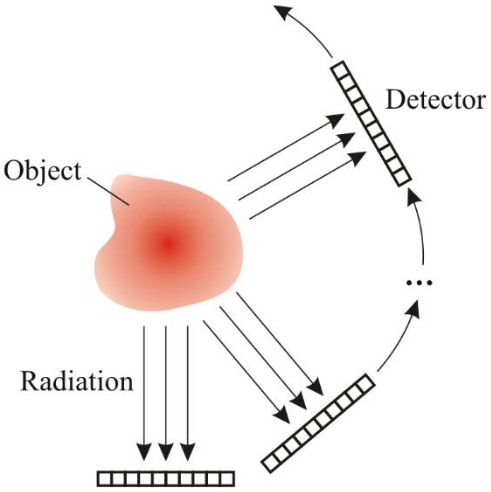

Figure 33: Tomographic acquisition technique: The detector has to be moved around the object and images have to be recorded in defined angle steps.

For this reason the detector has to be moved around the object and an image has to be acquired in every angle step $\Delta\phi$. To avoid recording of redundant information, the last measurement position should be at an angle of $180° - \Delta\phi$. Consequently the number of projection directions k is given by Equation 3.2:

$$k = \frac{180°}{\Delta\phi} \qquad 3.2$$

Since the used detector (CCD-Sensor) measures discrete spatial values (pixels), it is obvious to divide the cross section into cells, too. Figure 34 shows the discretization of the projections and the cross section, including all variables and parameters necessary to describe the mathematical problem.

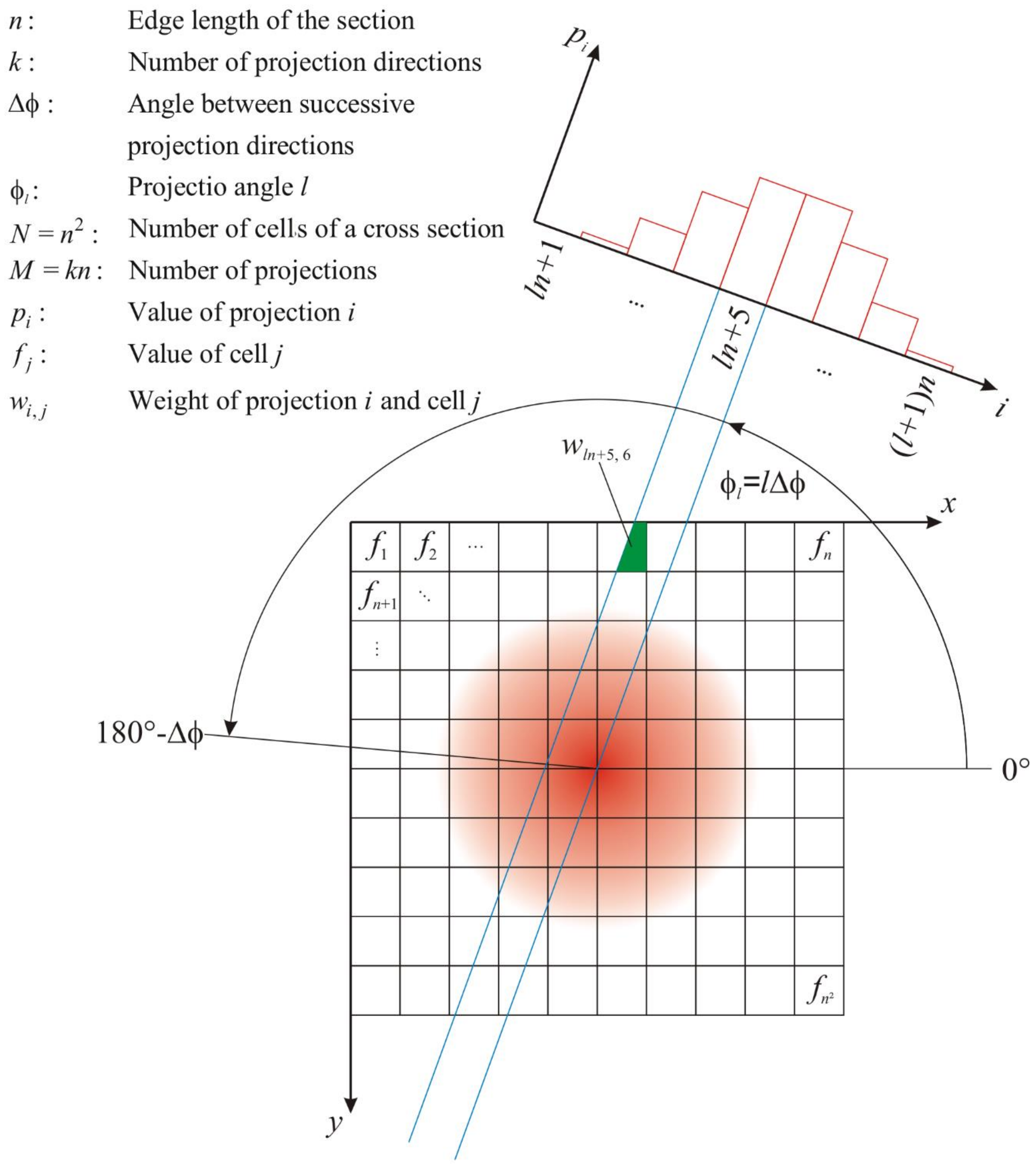

Figure 34: Discretization of the projections and the cross section including all necessary variables and parameters for the mathematical description of the inverse reconstruction problem.

To discretize the function $f(x,y)$ a quadratic grid with an edge length of n cells is applied. The $N = n^2$ resulting values f_n are used to calculate the $M = k \cdot n$ projection values p_i, which number depends on the projection direction number l ($\phi_l = l \cdot \phi_l$) and the edge length n of the quadratic grid. For the determination of p_i all sub-areas of the cells, that relate to the corresponding beam (blue lines in Figure 34), have to be taken into account. Therefore for every projection i the N weights $w_{i,j}$ have to be known. They can be calculated using Equation 3.3

$$w_{i,j} = \frac{\text{sub-area of cell } j \text{ relating to projection } i}{\text{area of cell } j} \tag{3.3}$$

As an example the weight $w_{ln+5,6}$ is marked green in Figure 34. An detailed description for the systematic calculation of the weights is given in [121]. The value of a single projection value can finally be determined with Equation 3.4.

$$p_i = \sum_{j=1}^{N} w_{i,j} \cdot f_j \quad \text{for } i = 1 \ldots M \tag{3.4}$$

By summarizing the M projections to the column vector

$$\vec{p} = (p_1, \ldots, p_M)^{\mathrm{T}} \tag{3.5}$$

the N values f_j to the column vector

$$\vec{f} = (f_1, \ldots, f_N)^{\mathrm{T}} \tag{3.6}$$

and the weights to the $M \times N$ matrix

$$\boldsymbol{W} = \begin{pmatrix} w_{1,1} & \cdots & w_{1,N} \\ \vdots & \ddots & \vdots \\ w_{M,1} & \cdots & w_{M,N} \end{pmatrix} \tag{3.7}$$

the set of linear equations (see Equation 3.4) can be expressed as presented in Equation 3.8:

$$\begin{gathered} \vec{p} = \boldsymbol{W} \vec{f} \\ \text{with } \vec{p} \in \mathbb{R}^M, \boldsymbol{W} \in \mathbb{R}^{M \times N} \text{ and } \vec{f} \in \mathbb{R}^N \end{gathered} \tag{3.8}$$

Since the aim of tomography is the reconstruction of the cross section and the distribution $f(x,y)$, respectively, Equation 3.8 has to be solved for the vector $\vec{f}$. The direct solution is only possible if $M = N$ and if the inverse of $\boldsymbol{W}$ exists. But even if this conditions are fulfilled, the resolution of the cross section is usually high and consequently $\boldsymbol{W}$ is large so that the direct inversion places high demands on the processing power of computers [116]. Because of these reasons, iterative methods are used to calculate the vector $\vec{f}$. In this work the so called algebraic reconstruction technique (ART) is applied to solve the tomographic problem. This iterative ART is based on the Kaczmarz's method [122] and can be written as follows:

$$\vec{f}^{(m)} = \vec{f}^{(m-1)} - \frac{\vec{w}_i \vec{f}^{(m-1)} - p_i}{\vec{w}_i (\vec{w}_i)^{\mathrm{T}}} (\vec{w}_i)^{\mathrm{T}} \quad \text{for } i = 1 \ldots M \qquad 3.9$$

The derivation of this equation is well defined in [116]. In every iteration step m the previous cross section values $\vec{f}^{(m-1)}$ are corrected M-times using the projections p_i and the corresponding rows $\vec{w}_i$ of the weight matrix $\boldsymbol{W}$. The structure of the vector $\vec{w}_i$ is presented in Equation 3.10.

$$\vec{w}_i = \left(w_{i,1}, w_{i,2}, \ldots, w_{i,N} \right) \qquad 3.10$$

Through applying the iterative ART it became possible to reconstruct cross sections with high resolution and satisfactory convergence after a few iterations. The relatively fast convergence of the algorithm could only be achieved by rearrangement of the projection indices i in one iteration step m. It is well known in literature [123] that large angles between projections used for the ART are good for the performance of the algorithm. Exemplary results for the convergence are shown in Chapter 3.3.2.

As already mentioned at the beginning of this chapter the mathematical fundamentals of tomography are only explained for the reconstruction of a single cross section using one column of the CCD-sensor. But through stacking the cross sections calculated for all columns, a 3D-distribution of the observed object can be created.

3.2 Properties of the wire arc spray plume regarding tomography

The tomographic two-color-pyrometry presented in this work is developed to determine three dimensional intensity and particle temperature distributions of the wire arc spray plume. Therefore long exposure times are necessary to guarantee a sufficiently high number of particles on every position of the spray plume. The resulting images (see Figure 40) are very smooth and can be used for the tomographic reconstruction.

As mentioned in the previous chapter tomography is usually performed by screening an object with an X-ray source and measuring the percentage that is not absorbed. Another way to do tomography is the so called emission tomography. To be able to apply this method the observed object has to be luminous and optically thin. Plasma jets for example used for thermal spraying fulfill these requirements and have successfully been investigated using optical emission tomography. Landes et al. [76] for example proved the triple symmetry of a “TRIPLEX II” torch and Hlína et al. [75] calculated time resolved three dimensional plasma temperature distributions.

In this work the measurement object is the spray plume of the wire arc spray process and the fast moving particles, respectively. Since the particles are molten steel droplets, they are opaque and only the light emitted from the surface can be measured. Remedy for this problem is provided by observing no single particles but an ensemble of particles. By integrating over a long time (>1 s) it should be guaranteed that a sufficient number of particles flies through every point of the measurement volume so that the acquired smooth 2D images reflect statistical particle distributions.

In addition it is necessary that the light emitted from the particles receives the detector without being shadowed by other particles. To be able to prove this condition the parameter optical thickness τ can be introduced. This dimensionless quantity is usually used to express the radiation losses in a medium. According to [124] the relation between the source intensity I_{tot} and the received intensity I_{rec} can be written as follows:

$$I_{rec} = I_{tot} \cdot e^{-\tau} \tag{3.11}$$

In the case of the particle plume I_{tot} is the radiation of all particles sent to the detector and I_{rec} is the radiation that is received by the detector. To be able to do tomographic reconstructions the wire arc spray plume has to be optically thin ($\tau \ll 1$ [119, 120]).

For the determination of τ, spatially resolved particle rates measured by Laser Doppler Anemometry, mean particle velocities measured by the DPV and mean particle sizes measured by Particle Shape Imaging are used. Figure 35 for example shows a particle rate cross section of the spray plume located 70 mm in front of the wire tips. The process parameters were set to 28.9 V, 4 m/min and 4 bar. Compressed air was used as atomizing gas.

An observation channel divided into equal-sized cubes is used in order to estimate the amount of shadowed particles. In Figure 35 an example for such a channel is marked (white squares) and in Figure 36 above three of these cubes and the transiting particles are enlarged in a principle drawing. With the help of the spatially-resolved particle rates, the total number of particles per second dN_n / dt flying through the area of the nth white square in z-direction can be calculated. As shown in Figure 36 above it is assumed that all particles go through the cubes one after the other and consequently the time $t_{P,n}$ between two following particles for channel n can be calculated as follows:

$$t_{P,n} = \left(\frac{dN_n}{dt} \right)^{-1} \tag{3.12}$$

Since the particle velocity variation in the *xy*-plane is negligible and the particle size cannot be measured spatially-resolved, it is assumed that all particles have the same velocity $\vec{v}_P$ and the same radius r_P. Furthermore only the velocity in z-direction $v_{P,z}$ can be measured using the DPV and consequently $v_{P,x}$ and $v_{P,y}$ have to be negligible, too.

The timing of the particle movement is presented in Figure 36 below. The diagram shows a time line for every cube presented in Figure 36 above. Whereby a high pulse, whose length Δt_P is given by Equation 3.13, represents the appearance of a particle.

$$\Delta t_P = \frac{2\, r_P}{v_{P,z}} \tag{3.13}$$

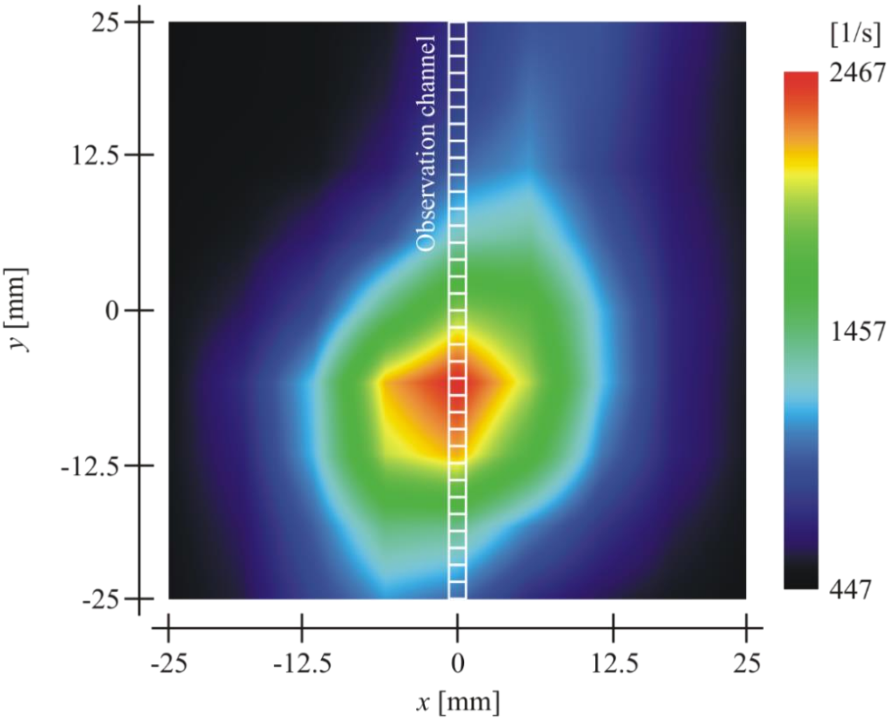

Figure 35: Spatially resolved particle rates measured by Laser Doppler Anemometry (see Chapter 5.4). Cross section of the spray plume located 70 mm in front of the wire tips. Process parameters: 28.9 V, 4 m/min, 4 bar and compressed air.

The dashed frame marked in the diagram shows the observation window. Its length is given by the duration of stay of the particles in the cubes and can be calculated by Equation 3.14 using the cube edge length l_C and the particle velocity $v_{P,z}$.

$$t_C = \frac{l_C}{v_{P,z}} \tag{3.14}$$

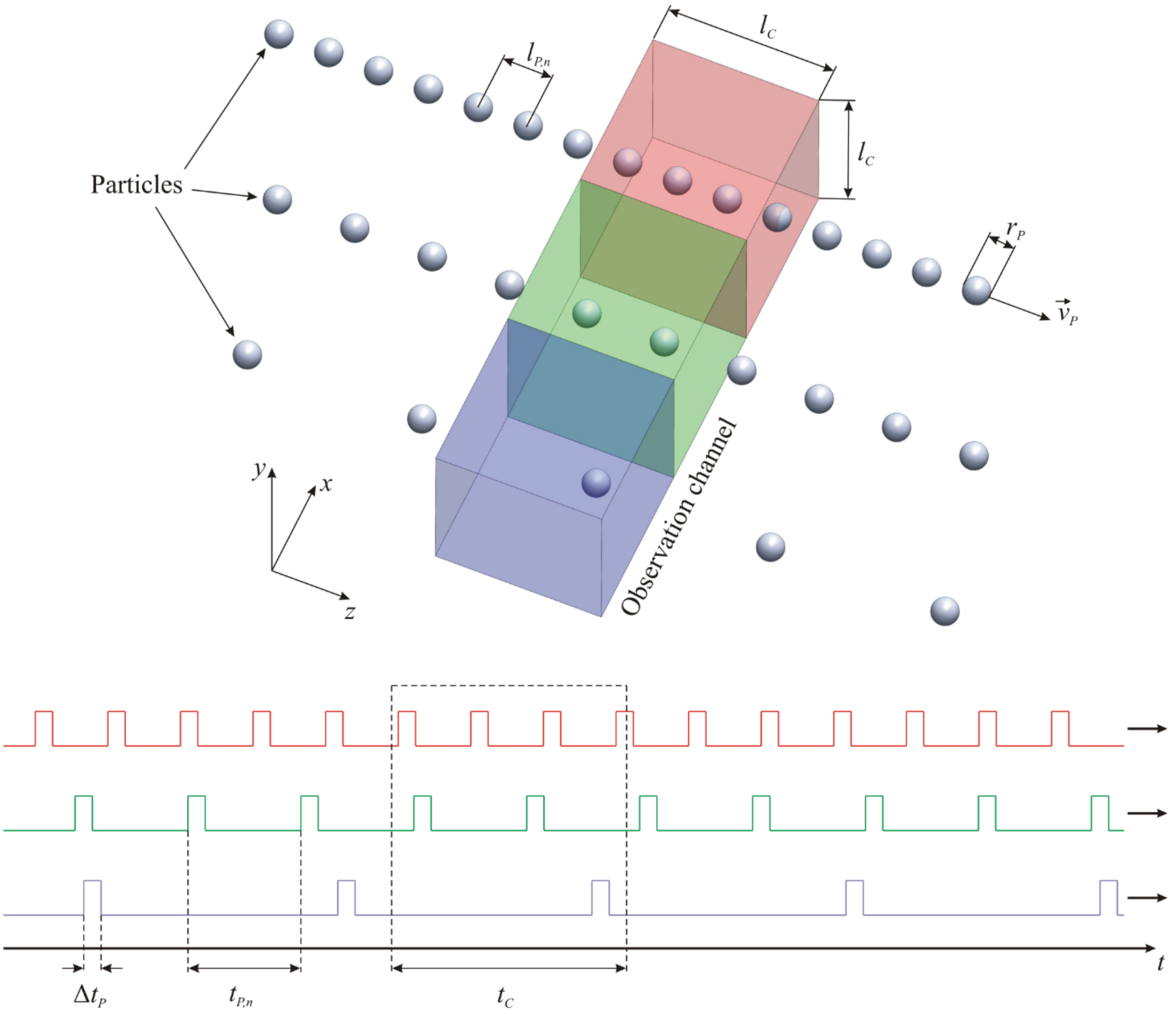

Figure 36: Above: Principle drawing of three cubes taken of the observation channel and the corresponding transiting particles. Below: Temporal connections of the transiting particles illustrated in a diagram with marked observation window (dashed frame).

By moving the time lines with small time steps Δt through the stationary observation window, the total emitted intensity I_{tot} can be calculated and the probably absorbed intensity I_{abs} can be estimated. It has to be taken into account that all particles located in previous cubes and all particles located in the same cube overlap the actual observed particle with a certain probability. This probability may be expressed by Equation 3.15.

$$L_{PC} = \frac{\pi\, r_P^2}{l_C^2} \tag{3.15}$$

The factor L_{PC} describes the percentage of the observation channel side that is shadowed by a particle with the radius r_P.

For the example presented in Figure 36 the total intensity of the particles located in the observation channel is given by $I_{tot} = 6 \cdot I_0$ and the absorbed intensity can be calculated as follows:

$$I_{abs} = \underbrace{L_{PC} \cdot I_0}_{\text{1st particle in green cube}} + \underbrace{2 \cdot L_{PC} \cdot I_0}_{\text{2nd p. in green cube}} + \underbrace{3 \cdot L_{PC} \cdot I_0}_{\text{1st p. in red cube}} + \ldots + \underbrace{5 \cdot L_{PC} \cdot I_0}_{\text{3rd p. in red cube}} \qquad 3.16$$

Since it is assumed that all particles in one cross section of the spray plume have the same temperature and emissivity, the intensity emitted by all of them is equal and can be expressed with I_0. Finally the optical thickness can be determined through calculating the received intensity I_{rec} and solving Equation 3.11 for τ:

$$\tau = \ln\left(\frac{I_{tot}}{I_{tot} - I_{abs}}\right) \qquad 3.17$$

The principle structure of the implemented algorithm is illustrated with the help of the program flow chart in Figure 120 (Appendix A.2). As it can be seen in Figure 37 the algorithm converges and the resulting optical depth is independent of the chosen edge length of the observation channel cubes. Detailed results are presented in Chapter 6.5 and are discussed in Chapter 7.

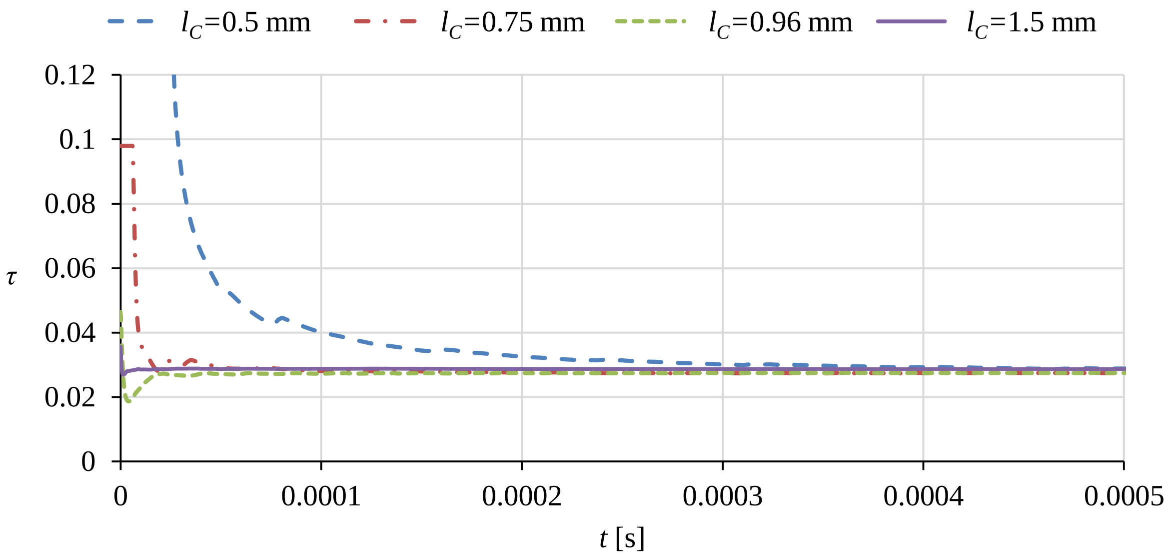

Figure 37: Optical depths calculated using the developed algorithm and the LDA results shown in Figure 35. The observation channel is located at x=0 and its edge length is varied.

3.3 Technical realization

To be able to apply the tomographic evaluation technique presented in Chapter 3.1, an adequate experimental setup is required for the acquisition of the raw data. Furthermore these images have to be pre-processed in order to calculate three dimensional intensity distributions and in the next step three dimensional temperature distributions. In the following chapters the experimental setup and the complete data processing are explained in detail.

3.3.1 Experimental setup

A CAD-drawing of the experimental setup used for the tomographic image acquisition is presented in Figure 38. The two-color-pyrometer module described in Chapter 2.2 is mounted onto a rotating disk using an optical rail to extant the object distance to 625 mm. The rotation of the ball bearing mounted disk is enabled by a mechanism consisting of a gear while, a shaft and a stepper motor. The spray gun has to be located in such a way that the particles fly through the whole in the middle of the disk and the gear wheel.

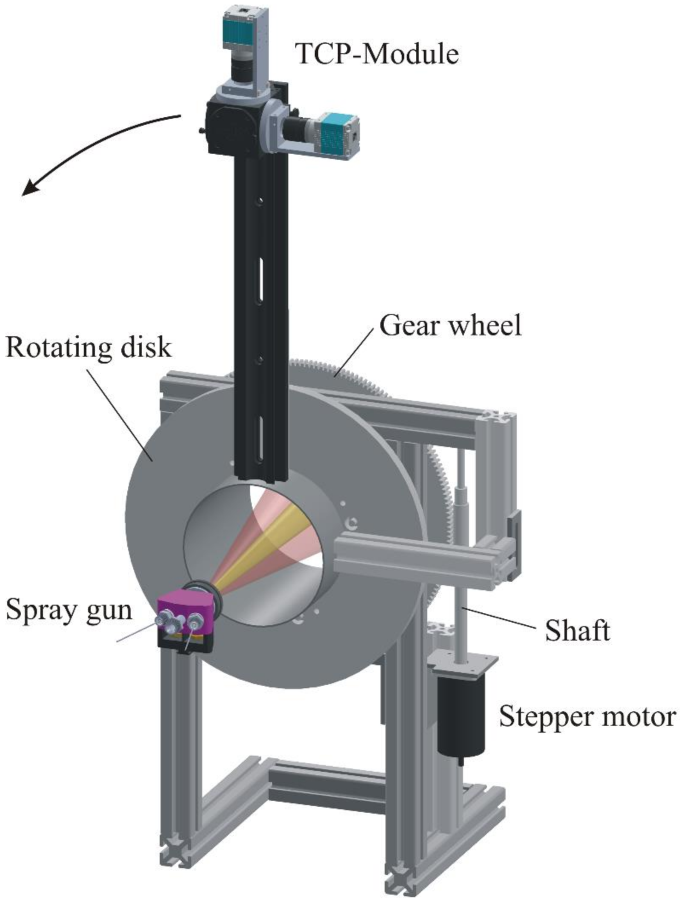

Figure 38: CAD-drawing of the experimental setup used for the tomographic measurements. The setup consists of a TCP-Module mounted onto a rotating disk via an optical rail. The disk is driven by a mechanism consisting of a gear wheel, a shaft and a stepper motor. The wire arc gun is positioned in such a way, that the spray plume goes through the whole in the middle of the rotating disk.

During a measurement the module is moved around the spray plume in 3° steps. According to Equation 3.2 $k = 60$ images are made by the two cameras. To avoid vibrations the rotation speed is kept low and after reaching the next position the diagnostic waits for a delay of 1 second before acquiring the next images. In addition the two cameras are synchronized by connecting the “exposure” output of camera 1 to the “trigger” input of camera 2.

In order to measure the temperature distribution and the particle oxidation over a wide range of the spray plume, the tomographic setup shown in Figure 38 is located on three different positions. The resulting measuring regions are presented in Figure 39. The overlapping of the zones can on the one hand be used as evidence for the continuity of the diagnostic and on the other hand to smooth the measured curves. As already mentioned the distance between the diagnostic and the middle of the pray plume is 625 mm. In Chapter 2.2.3 the measurement volume has already been discussed in detail and it has been shown that the width W of the object plane in z-direction is 114 mm. Furthermore the first measurement point is 65 mm in front of the wires in order to avoid errors caused by line emission from the plasma. For the selection of the starting point, the experimental setup explained in Chapter 5.2 is used. The results are presented in Chapter 6.6 and are discussed in Chapter 7.

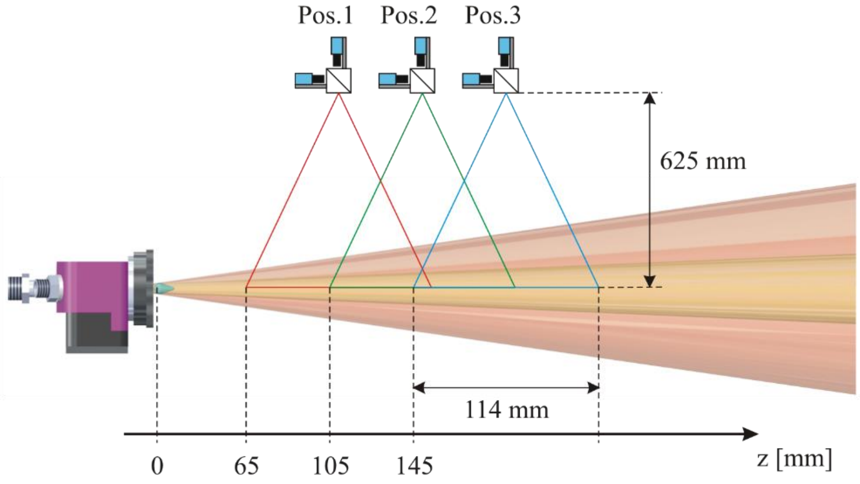

Figure 39: Principle experimental setup for the tomographic measurements. To measure the temperature distribution and the particle oxidation over a wide range of the spray plume the diagnostic is located on three different positions to get three overlapping measuring zones.

3.3.2 Data processing

On the path from the images recorded by the two-color-pyrometer to three dimensional intensity and temperature distributions many different data processing steps are necessary. In Figure 40 an original image of the spray plume acquired by camera 2 with an exposure time of 3.5 s is presented. The wire arc spray process parameters were set to 28.9 V, 4 m/min and 4 bar. Furthermore compressed air was used as atomizing gas. In order to make the image processing steps applied to the original images more visible, the column at $x = 323$ and the row at $z = 180$ are exemplarily highlighted in the diagrams of Figure 41 and Figure 42. Whereby the positon

$x = 323$ is chosen because it is the middle of the spray plume, and $z = 180$ because of the hot pixel that is present in this row.

The first image processing step is the convolution of the original images by a 3×3 median filter [125], in order to remove the hot pixels and to reduce the noise. As it can be seen with the aid of the orange trace in Figure 42, the peak (hot pixel) in the gray signal is successfully removed using the median filter. Another filter that is used to smooth the pictures is a 3×3 mean filter [125]. Due to this filter the processed traces have significantly reduced signal noise and can finally be multiplied pixel per pixel with the corresponding correction factor matrix (see Chapter 2.2.5). The effect of the correction factor matrix is most in evidence comparing the original and the processed curves in Figure 41. The processed trace is amplified from approximately $z = 0$ to 80 and from approximately $z = 240$ to 480, in between the values are scaled down. In the last step a $50\,\text{Pixel}$ wide stripe is added to the upper and the lower border of the original images, whereby the intensity of the pixels in a single row of the stripe is equal to the mean value of the neighboring 10 pixels in the processed image. The extension to a resolution of 740×480 is necessary, in order to be able to choose a region of sufficient range for the tomographic reconstruction.

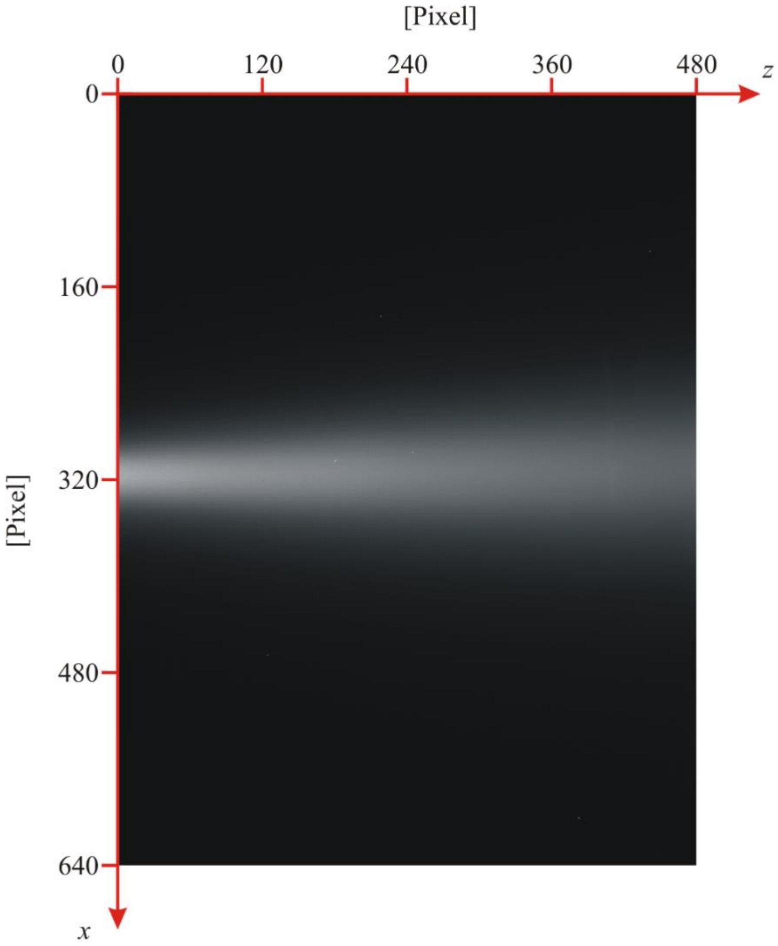

Figure 40: Original image of the spray plume acquired by camera 2 of the two-color-pyrometer with an exposure time of 3.5 s. The process parameters were set to 28.9 V, 4 m/min and 4 bar. Compressed air was used as atomizing gas.

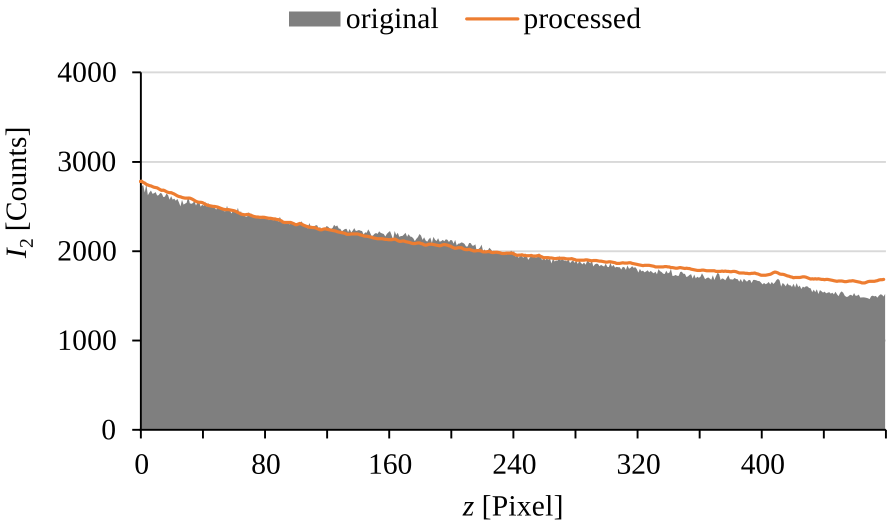

Figure 41: Original (gray) and processed (orange) course of the column positioned at $x = 323$ *in the wire arc spray plume picture presented in Figure 40.*

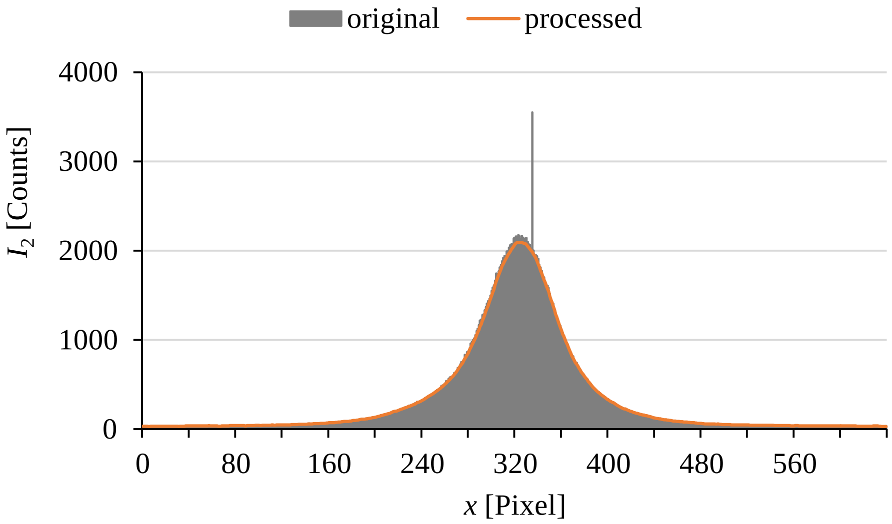

Figure 42: Original (gray) and processed (orange) course of the row positioned at $z = 180$ *in the wire arc spray plume picture presented in Figure 40.*

After applying the before mentioned processing steps to the image series of camera 1 and 2, the resulting data are suitable for the tomographic reconstruction. Since the computation time strongly depends on the edge length n of the cross section (see Equation 3.9), a compromise between a sufficient resolution and an acceptable computation time has to be found. The evaluation of the experimental data showed that a cross section resolution of 180×180 results in a satisfactory calculation time between 1.5 min and 5 min (dependent on the performance of the used computer) for the reconstruction of one cross section. Due to the chosen resolution the processed images of the two-color-pyrometer have to be compressed. Therefore a region of interest with a width of $720\,\text{Pixel}$ is chosen in which $4 \times 4\,\text{Pixel}$ are summarized to one. Subsequently the same rows of every compressed image included in one series are put together in a new picture. An example for such an image is presented on the left side of Figure 43. It contains the projection values in the Cartesian Radon space [116] dependent on the index i and the projection angle ϕ_l. Before the projection values can be used for the tomographic reconstruction additional processing steps have to be applied. At first the projection images are blurred using a 3×3 mean filter, second a correction of the rotation axis is performed [126] and finally the intensities in every row are scaled so that every row total is equal. The last step is necessary because of the sequential acquisition of the images and the spray plume fluctuations that may consequently be recorded.

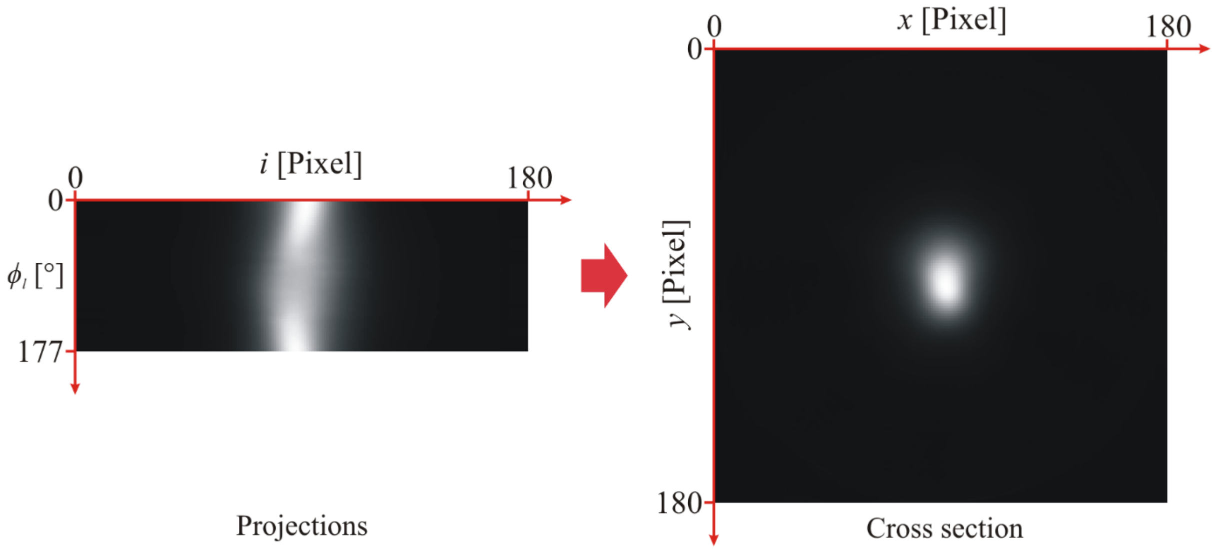

Figure 43: Projection values in the Cartesian Radon space and the corresponding calculated cross section in the Cartesian space. The projections are taken from the same image series as the original picture in Figure 40.

With the projection values and the weights calculated according to [121] all values are available to calculate the cross sections using Equation 3.9. Figure 43 for example shows the cross section resulting from the projection image besides, and Figure 44 shows the development of the intensity I_2 located in the middle of this cross section. It can clearly be seen that the value converges and does not significantly change after the 6th iteration. To guarantee the convergence even in the fringes of the cross section the number of iterations was set to 10. Furthermore the diagram in Figure 44 shows that in the case of this reconstruction the computation lasted approximately 3 min.

Finally with the help of the cross section of camera 2 presented in Figure 43, the corresponding cross section of camera 1 and the calculated quotients (Figure 21), the temperature image can be determined. Therefore the cross section of camera 1 has to be divided pixel per pixel by the cross section of camera 2 and the resulting quotients have to be compared with the calculated ones. In Figure 45 the temperature image is presented, whereby the scale determined experimentally using a ruler is used in order to get the dimensions in mm. The temperature error, that is caused through integrating over many particles (ensemble measurement technique) assuming that all these particles have the same temperature, is according to [127] for temperatures above 2500 K and a standard deviation of 100 K below 1 % and can consequently be neglected.

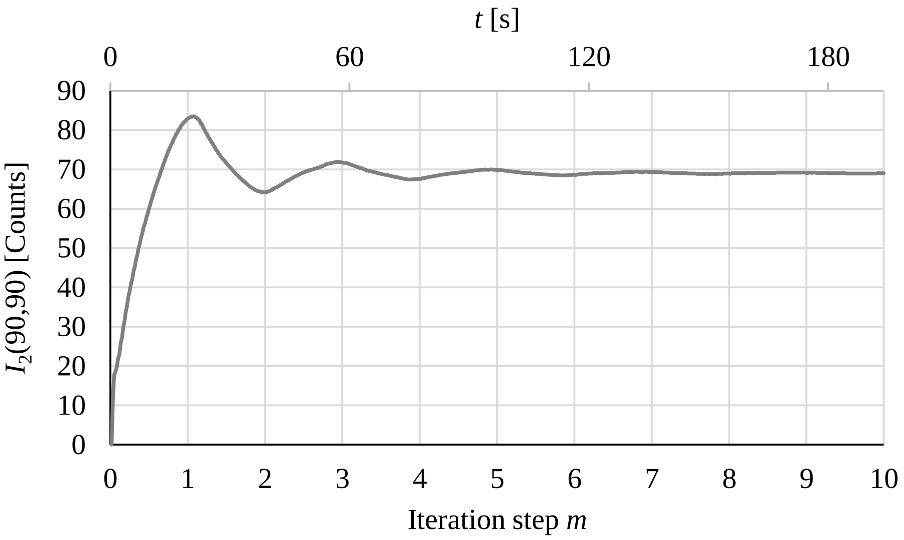

Figure 44: Intensity I_2 *in the middle of the cross section presented in Figure 43 dependent on the iteration step* m.

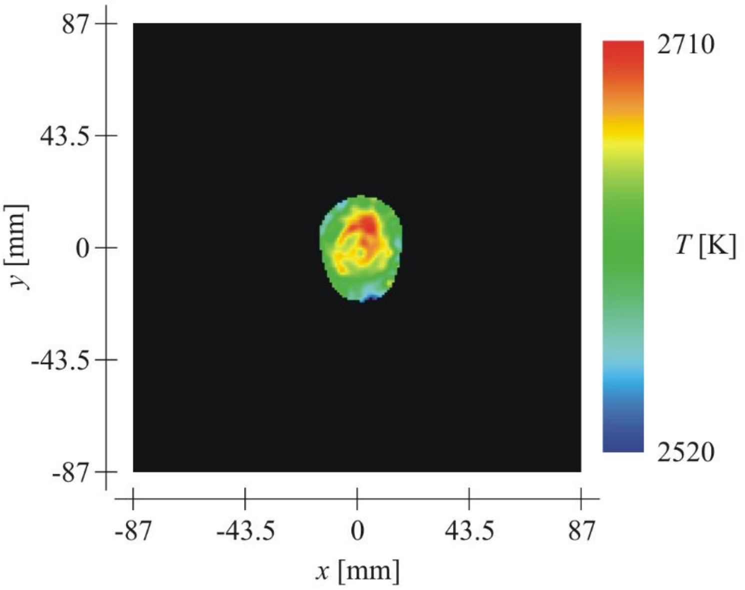

Figure 45: Temperature image calculated with the help of the cross section of camera 2 presented in Figure 43, the corresponding cross section of camera 1 and the calculated quotients shown in the diagram of Figure 21.

To obtain three dimensional intensity and temperature distributions the reconstructed cross sections and the temperature images, respectively, have to be stacked. Further results can be found in Chapter 6.6 and are discussed in Chapter 7.2.

4 In situ particle oxidation measurement

The aim of this work is the development of a diagnostic allowing quantitative conclusions on the particle oxidation along the spraying direction. On the basis of the three dimensional intensity and temperature distributions measured by tomographic pyrometry, the estimation of emissivities depending on the oxidation is performed. In the following sections brief descriptions of the oxidation mechanism of steel and the resulting optical properties are given. And finally within this framework the principle of oxidation measurement is explained.

4.1 Oxidation of metal particles

Since the used feedstock material is mild steel and consists to 97.493 % [91] of iron, it may be justifiable to explain the particle oxidation behavior and the resulting optical properties by means of iron. On the one hand this has the advantage that chemical reactions of materials consisting of only one element are easier to handle and on the other hand that there is a lot of research concerning the high temperature oxidation of pure metals and iron, respectively. As the iron-oxygen phase diagram in Figure 46 [128] shows, iron above 570 °C exposed to oxygen forms a multi-layer oxide scale consisting of FeO (Wustite), Fe_3O_4 (Magnetite) and Fe_2O_3 (Haematite). Since the iron diffusion coefficient of FeO is much larger than of the other oxides [129], the Wustite layer is predominant and much thicker [130].

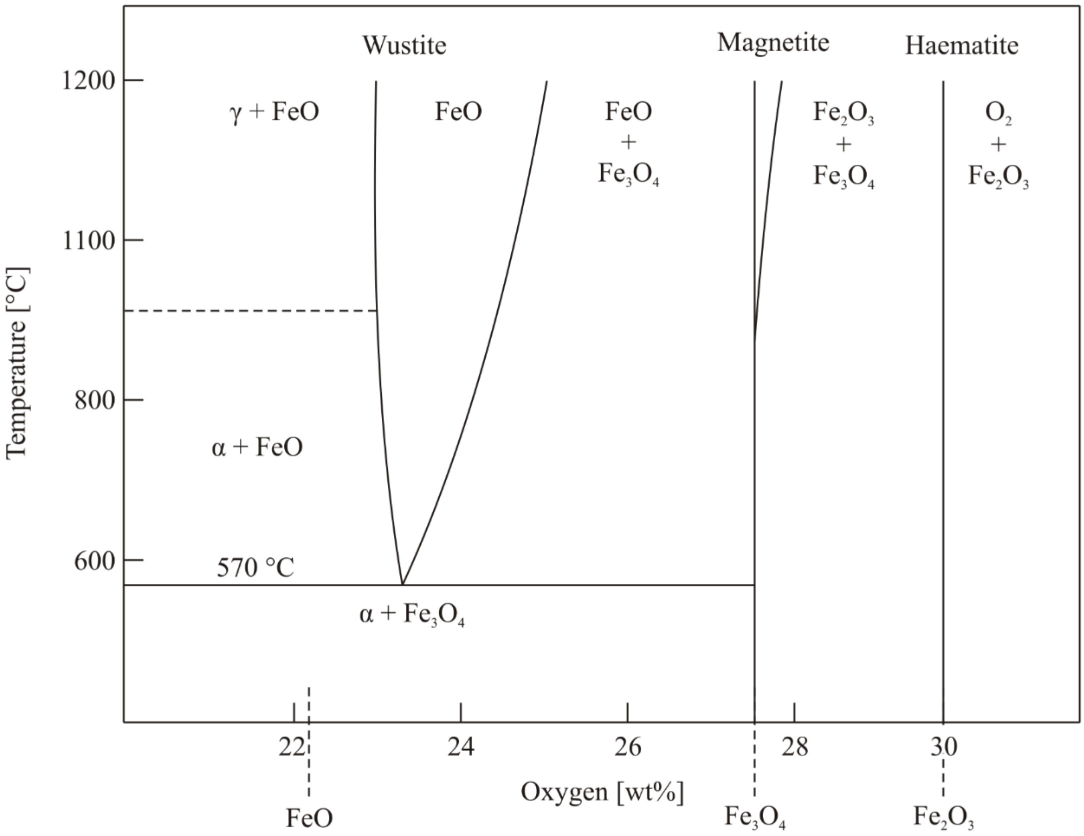

Figure 46: Iron-oxygen phase diagram, showing the different oxide and iron phases dependent on the temperature. Adopted from [128].

The phase diagram shows that this trend increases with increasing temperature. Finally at high temperatures between the melting point and boiling point of iron, as expected at wire arc spraying, the Magnetite and Haematite fractions are assumed to be negligible. Therefore it is considered that the liquid particles only consist of iron and FeO. This kind of simplification has already been used in other research works. Ivarson et al. [131] for example used an oxidation model that only includes iron and FeO in order to explain the striation generation while laser cutting of mild steel. Neiser et al. [73] also postulated that FeO is the major oxide portion occurring in mild steel particles generated by wire HVOF spraying and that the oxide is fully molten due to its low melting point at 1644 K.

As the oxidation measurement technique is based on two-color-pyrometry, only radiation emitted from the particle surfaces is taken into account. If a closed enveloping oxide layer would be formed, this optical measurement method would lead to problems estimating the oxide thickness and the total particle oxide content, respectively. However, Espie et al. [44] and Neiser et al. [73] determined oxide inclusions within iron particles that can be explained by the liquid motion mixing iron and FeO. Consequently there is probably both iron and iron oxide present on the surface and the observation of the radiation emitted from the surface allows conclusions on the total particle oxidation.

In order to be able to estimate the degree of particle oxidation, the emissivity $\varepsilon_{\mathrm{Fe}}$ of liquid iron and the emissivity $\varepsilon_{\mathrm{FeO}}$ of liquid oxidized iron (FeO) have to be known. One widespread technique to determine the emissivity of a material is the fitting of the spectral radiant exitance $M_{\lambda}(\lambda, T)$ (see Equation 2.8) to a measured spectrum, whereby the emissivity can be assumed to be constant [132] or linearly dependent on the wavelength [133]. Another method applied for example by Kobatake et al. [134] uses in addition to the spectrum the material temperature measured by a pyrometer. This technique has the advantage that the wavelength dependence of the emissivity is not specified and can consequently be investigated. Since for emissivity determination defined ambient conditions have to be adhered and the accessibility for the diagnostics to the hot liquid medium has to be guaranteed, experimental setups for such investigations are very complex. For these reasons, in this work emissivities known from literature are used, in order to evaluate the oxidation measurements.

The emissivity of liquid iron above the melting point is well investigated. Some results that are in the wavelength and temperature region of this work are listed in Table 7. Kobatake et al. [134] for example measured a weak negative wavelength and a negligible temperature dependence and give an emissivity of 0.394 at 807 nm for liquid iron. Similar values are postulated by Watanabe et al. [98]. In their work emissivities of 0.38 and 0.37 at 800 nm and 900 nm are measured for liquid iron with a temperature of 1808 K. A research work dealing with mild steel (S235) is presented by Schöpp et al. [132]. Here the measured emissivity exponentially decreases with increasing temperature and finally remains constant at a value of 0.087 above temperatures of 2100 K. Since the mild steel used by Schöpp et al. is more similar to the mild steel used in this work than pure iron (compare Table 8 and Table 10), an emissivity of 0.087 is assumed for the wire arc spray particles that are not oxidized.

The emissivity of oxidized metals in general is higher than the emissivity of pure metals [135]. This predication for example is proved by Muller et al. [133]. In their work they measure the emissivity of laser molten iron in a highly oxidizing environment by means of 2D single-band pyrometry and spectral pyrometry. For oxidized iron they determined an emissivity of approximately 0.7 remaining constant for temperatures above 2100 K.

Apart from the different absolute values, all works listed above measured emissivities that are independent of the temperature in the expected temperature region (>2100 K). Furthermore it is obvious that the emissivity of liquid oxidized iron is significantly higher than the emissivity of liquid pure iron and mild steel, respectively. For these reasons and because of the fact that the two-color-pyrometry measures at two defined wavelengths – consequently wavelength dependence does not matter – the determination of an emissivity increase can be interpreted as material change due to oxidation.

Table 7: Measured emissivities of iron and oxidized iron taken from literature.

Material/phase	Emissivity	Wavelength	Temperature	Reference
Iron/liquid	0.394	807 nm	1600 K to 1950 K	[134]
Iron/liquid	0.38, 0.37	800 nm, 900 nm	1808 K	[98]
S235/liquid	0.087	650 nm to 850 nm	>2100 K	[132]
FeO/liquid	~0.7	500 nm to 700 nm	>2100 K	[133]

Table 8: Chemical analysis of the mild steel “S235” (material reference 1.0038) [136] *used by Schöpp et al.* [132].

Chemical element	C	N	Mn	P	S	Cu
Mass fraction [%]	0.17	0.012	1.4	0.035	0.035	0.55

4.2 Principle of oxidation measurement

As mentioned in the previous chapter the temperature dependence of the spectral emissivity is negligible for the observed materials and temperature regions. Since the two-color-pyrometry works at two defined wavelength bands and enables the temperature determination, emissivity changes that can only accompany with material changes can be measured. For this purpose a simplified model using the results of the tomographic two-color-pyrometry is introduced. Figure 47 for example shows the 3D intensity reconstruction of the wire arc spray plume

(28.9 V, 4 m/min, 4 bar, CA) recorded using camera 1 (800 nm). For every cross section in the *xy*-plane the total measured intensities $I_{1,tot}$ and $I_{2,tot}$ can be calculated with Equation 4.1

$$\begin{aligned} I_{1,tot}(z) &= \sum_{i=1}^{N} A_{\perp,i} \cdot t_{C,i} \cdot I_1(T_i) \\ I_{2,tot}(z) &= \sum_{i=1}^{N} A_{\perp,i} \cdot t_{C,i} \cdot I_2(T_i) \end{aligned} \qquad 4.1$$

whereby $A_{\perp,i}$ is the luminous surface of particle i approximated by Equation 4.2, $t_{C,i}$ is its dwell time in a cross section (see Equation 3.14) and $I_1(T_i)$ and $I_2(T_i)$ are the measured intensities taking the optical sensitivities into account (see Equation 2.26 and 2.27).

$$A_\perp = \pi r_P^2 \qquad 4.2$$

Assuming that all N particles flying through a cross section have the same size, velocity, temperature and emissivity, Equation 4.1 can be transformed to Equation 4.3.

$$\begin{gathered} I_{i,tot}(z) = N \cdot A_\perp \cdot t_C(z) \cdot \varepsilon(z) \cdot K_i \cdot \int_{\lambda_s}^{\lambda_e} q_e(\lambda) \cdot f_i(\lambda) \cdot M_{\lambda s}(\lambda, T_{avg}(z))\, d\lambda \\ \text{with } \lambda_{s/e} = \lambda_{1,2} \mp 2 \cdot FWHM \text{ and for } i = 1,\ 2 \end{gathered} \qquad 4.3$$

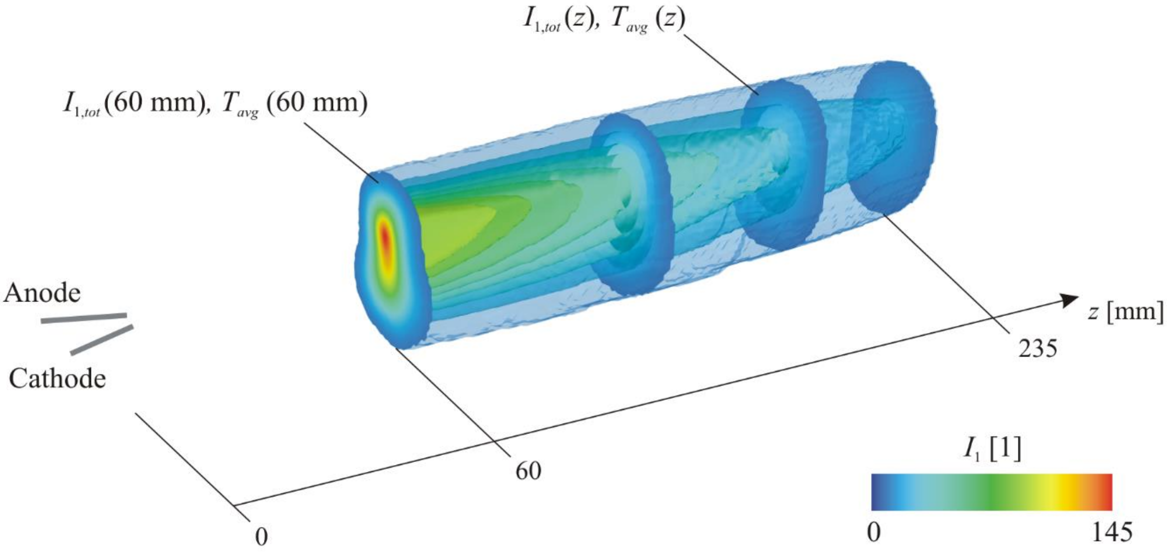

Figure 47: 3D intensity reconstruction of the wire arc spray plume (28.9 V, 4 m/min, 4 bar, compressed air) recorded using camera 1 (800 nm interfernce filter). For every cross section total intensities $I_{1,tot}$ and average temperatures T_{avg} can be calculated.

In addition it is assumed that the particles are not further atomized so that their number N can be calculated using the wire feed rate v_w, the wire radius r_w, the exposure time $t_{\exp}$ of the cameras and the particle radius r_P, whereby both wires have to be taken into account:

$$N = 2 \cdot \frac{v_w \cdot t_{exp} \cdot \pi r_w^2}{\frac{4}{3} \cdot \pi r_P^3} \qquad 4.4$$

Besides the total intensities and the average temperatures measured by means of the tomographic two-color-pyrometry, the particle diameter is measured using a PSI diagnostic (see Chapter 5.3) and the particle velocity is measured using the DPV (see Chapter 5.4). The last missing parameters necessary for the calculation of the emissivities are the calibration factors K_1 and K_2 $\left[1/\mathrm{J}\right]$. These parameters can be estimated by Equation 4.5 using the reference intensities of the calibration lamp measured in Chapter 2.2.5, the edge length $l_C = 0.24$ mm of a pixel in the image plane, the lamp velocity v_{lamp} (see Table 5) and the corresponding reference temperatures (see Table 4). The emissivities $\varepsilon\left(T_{ref}\right)$ of the tungsten calibration lamp are approximated using the values determined by Watanabe et al. [98]. Therefore the mean value between the emissivity at 800 nm and 900 nm is calculated

$$K_i = \frac{I_{ref,i}}{l_C^2 \cdot \frac{l_C}{v_{lamp}} \cdot \varepsilon\left(T_{ref}\right) \cdot \int_{\lambda_s}^{\lambda_e} qe(\lambda) \cdot f_i(\lambda) \cdot M_{\lambda s}\left(\lambda, T_{ref}\right) d\lambda} \qquad \text{for } i = 1, 2 \qquad 4.5$$

The calibration factors for the two different setups (compressed air and nitrogen) and the parameters used for the calculation are listed in Table 9. With the help of K_1 and K_2 finally the material dependent emissivity along the spraying direction z can be determined using Equation 4.6

$$\varepsilon(z) = \frac{I_{i,tot}(z)}{N \cdot A_\perp \cdot t_C(z) \cdot K_i \cdot \int_{\lambda_s}^{\lambda_e} qe(\lambda) \cdot f_i(\lambda) \cdot M_{\lambda s}\left(\lambda, T_{avg}(z)\right) d\lambda} \qquad 4.6$$

$$\text{with } \lambda_{s/e} = \lambda_i \mp FWHM \text{ and for } i = 1,\ 2$$

Table 9: Calibration factors K_1 and K_2 calculated for the compressed air setup (level 4) and the nitrogen setup (level 1). Emissivities of tungsten are calculated according to [98].

$\boldsymbol{T_{ref}}$ **[K]**	$\boldsymbol{\varepsilon_1\left(T_{ref}\right)}$	$\boldsymbol{\varepsilon_2\left(T_{ref}\right)}$	$\boldsymbol{\varepsilon\left(T_{ref}\right)}$	$\boldsymbol{I_{ref,1}}$	$\boldsymbol{I_{ref,2}}$	$\boldsymbol{K_1}$ **[1/J]**	$\boldsymbol{K_2}$ **[1/J]**
2723	0.400187	0.383802	0.3919945	2561	3024	2419670716	13234368881
2190	0.41671	0.383802	0.400256	1560	3260	10811961403	87441550979

5 General experimental settings and pretests

To test the innovative diagnostic presented in this thesis, the wire arc spray process is chosen. In order to evaluate the results of the diagnostic and to prove the boundary conditions, in situ analysis of the particle plume using different diagnostics are done and test coatings are generated. In the following chapter the general experimental settings of the process and the used established diagnostics are presented.

5.1 Wire arc spray system

The used wire arc spray system consist of the Gas Metal Arc Welding (GMAW) power supply “Phoenix” from the company “EWM” and the spray gun “ArcJetOne” from the company “T-Spray”. To be able to use the power source for the wire arc spray process, it is equipped with a second wire feeder. As usual for GMAW the power supply offers a constant voltage with fixed wire feed rate and is direct current operating, whereby one wire serves as cathode and the other one as anode. As described in [137] such a constant voltage supply offers a self-regulating feature that guarantees a constant wire-workpiece distance and wire-wire distance, respectively. In addition the mild steel wire “SW 70S G3” (material reference 1.5125) with a diameter of 1.6 mm from the company “EWM” is used as feedstock. The chemical analysis of the material is listed in Table 10.

Table 10: Chemical analysis of the used mild steel wire “SW 70S G3” (material reference 1.5125) from the company “ewm” [91].

Chemical element	**C**	**Si**	**Mn**	**P**	**S**
Mass fraction [%]	0.08	0.9	1.5	0.015	0.012

To achieve different particle temperatures, sizes and velocities and consequently different particle oxidations, the most influencing parameters are varied. The investigated wire feed rates, voltages, gas types and pressures are listed in Table 11. As already mentioned in Chapter 1.1.1 the wire arc spray process is voltage controlled and the current is proportional to the wire feed rate.

Table 11: Investigated parameters of the wire arc spray process.

Wire feed rate [m/min]	3, 4, 5
Voltage [V]	28.9 V, 33.0 V, 38.8
Gas	Compressed air (CA), Nitrogen (N_2)
Gas pressure [bar]	3, 4, 5
Base parameter	28.9 V, 4 m/min, 4 bar

To be able to estimate the energy input into the wires, the arc voltage $u(t)$ and the arc current $i(t)$ are measured. Since direct current is employed the power P can be calculated as follows:

$$P = \frac{1}{T}\int_{t}^{t+T} u\left(t^*\right)\cdot i\left(t^*\right)dt^* \tag{5.1}$$

The energy input per unit mass H_{mass} is calculated using the electric power P from Equation 5.1, the density of iron ρ_{Fe}, the wire radius r_w and the wire feed rate v_w:

$$H_{mass} = \frac{P}{\pi r_w^2 \cdot v_w \cdot \rho_{Fe}} \tag{5.2}$$

Of course this is only an approximation, since fractions of the electric power are transferred to the environment for example due to the radiation of the arc [138]. However, the values are suitable to allow qualitative interpretations of the tomographic two-color-pyrometry results.

Voltage and current are measured over a period of 2 s with a sampling rate of 50 kHz. To achieve a certain confidence level the tomographic measurements and the voltage and the current measurements are done three times.

5.2 Measurement of the plasma expansion

For the temperature determination based on two-color-pyrometry it is necessary that only continuous radiation from the particles receives the diagnostic. Since process-related an electric arc is struck between the wires and consequently a plasma jet occurs due to the gas flow, there is also line emission. To avoid disturbances of the two-color-pyrometry, the measurements can only take place after the position in spraying direction where the plasma is completely recombined and no line emission appears.

To approximate the plasma expansion in front of the spray gun, the experimental setup shown in Figure 48 is used. It consists of the optical spectrometer “ARYELLE” from the company “LTB” and a collimator that is moved along the spraying direction in 30 mm steps. The collimator collects the parallel light within a measurement channel with a diameter of ~3 mm and couples it into a fiber optic cable connected to the spectrometer.

The “ARYELLE” is a so called echelle spectrometer. This special kind of spectrometer consist of an echelle grating used in high diffraction orders, followed by a prism and a two dimensional detector [139, 140]. Due to this setup it becomes possible to measure a wide spectral range with high resolution [141]. Disadvantageous is the ripple appearance of single orders, due to the blaze function [139]. This behavior is only noticeable when measuring continuous radiation.

Using the measured spectra the point is searched, where the plasma expansion ends and only light emitted from the spray plume can be observed. The results can be seen in Chapter 6.

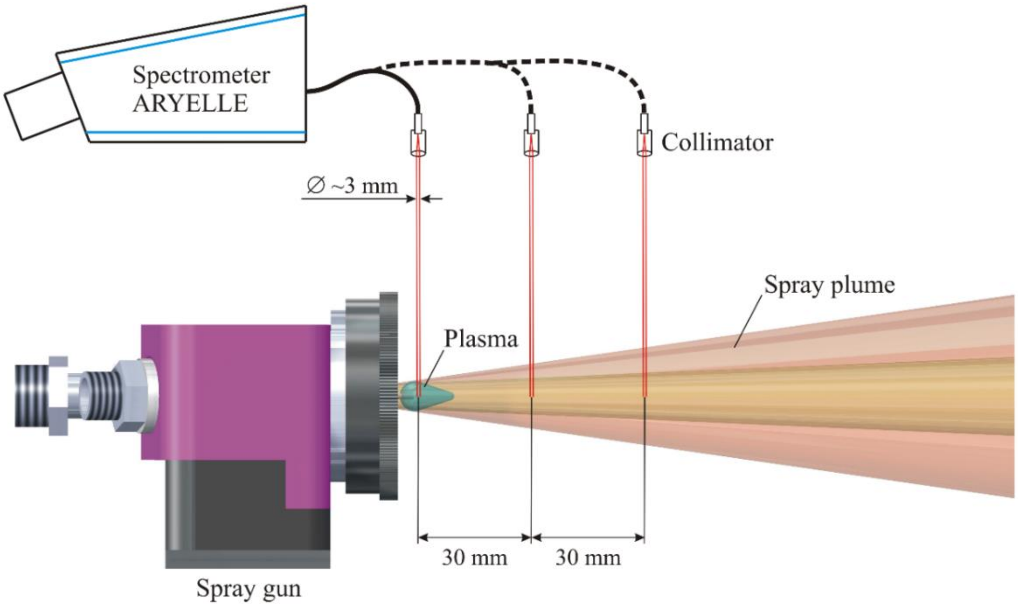

Figure 48: Experimental setup for the approximation of the plasma expansion. The setup consist of the optical spectrometer "ARYELLE" from the company "LTB" and a collimator that is moved along the spraying direction in 30 mm steps.

5.3 Particle Shape Imaging measurements

For the oxidation approximation using the model presented in Chapter 4.2, the particle sizes have to be known. Since the Particle Shape Imaging diagnostic enables the direct measurement of particle sizes, it is used in this work. The experimental setup of the PSI is presented in Figure 49. In contrast to the PSI diagnostics developed in [68, 142], a short arc lamp is used as light source. With the help of two deflection mirrors and two lenses (focal length of 100 mm) two light beams are focused and crossed in order to form the measurement volume. Particles flying through the intersected area shadow the light and are projected onto an image intensifier from different directions. The imaging optic in each optical axis consist of two lenses (focal length of 100 mm) and three deflection mirrors. Its principle optical path without the deflection mirrors is shown in Figure 50. Since the light of the short arc lamp covers the whole visible spectrum, all lenses are achromatic lenses. To be able to restrict the extension of the measurement volume an adjustable aperture is positioned in the image plane of the first lens, which generates a one-to-one projection. By means of the second lens a magnification of approximately six is reached. To realize the resulting long image distance the light paths are deflected to a second plane, in which an image intensifier and a high speed camera are located. As already mentioned in Chapter 1.1.3 the image intensifier ("Quantum Leap" from the company "Stanford Computer Optics") provides short exposure times at sufficient sensitivity in order to avoid motion blur. Its principle setup and function are well described in [143] and are not discussed further in this work. To digitalize the pictures appearing on the phosphor screen of the image intensifier, a high-speed camera equipped with an objective is used, whereby both devices are synchronized via the "exposure out" signal of the camera. In all measurements the exposure time of the image intensifier was set to 500 ns and the framerate of the high-speed camera to 100 fps. Since no particle trigger was used, 15000 images were acquired for each process parameter in order to achieve a statistically sufficient amount of particles. Furthermore, the magnification of the imaging optic was experimentally determined. Therefore, a 1951 USAF resolution target was positioned in the measurement volume and by means of the known group number and element number, a scale of approximately $1.86\,\mu\text{m}/\text{Pixel}$ could be calculated (see Appendix A.3).

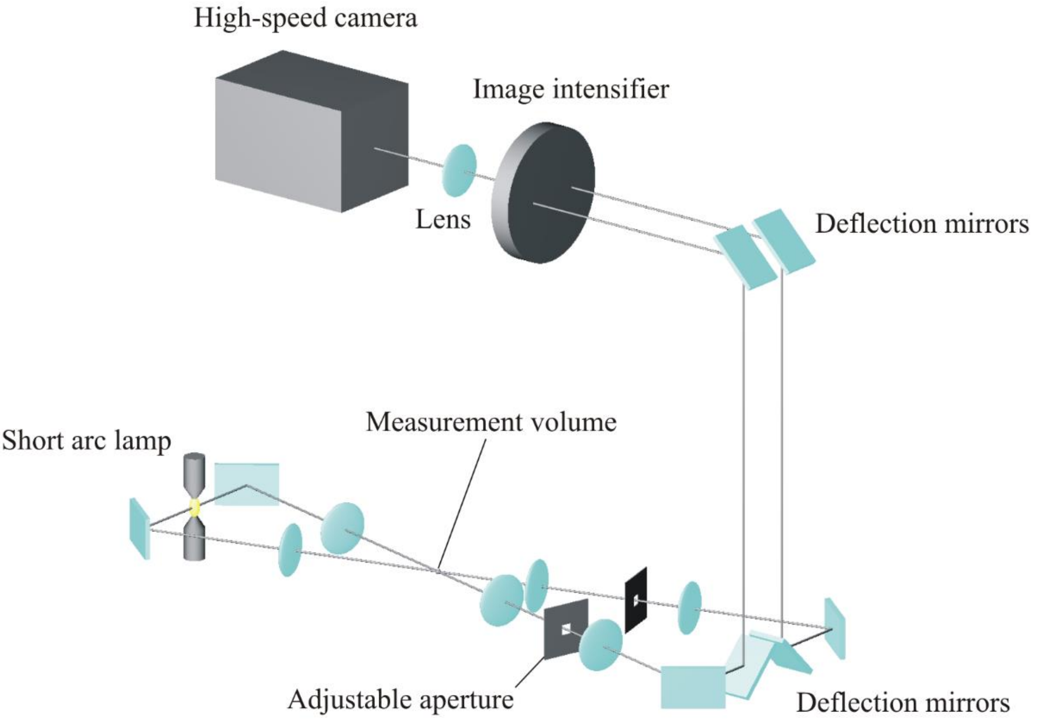

Figure 49: Schematic drawing of the experimental setup used for the PSI measurements. The setup consist of a short arc lamp, an image intensifier, a high-speed camera and diverse optical components like deflection mirrors, lenses and adjustable apertures.

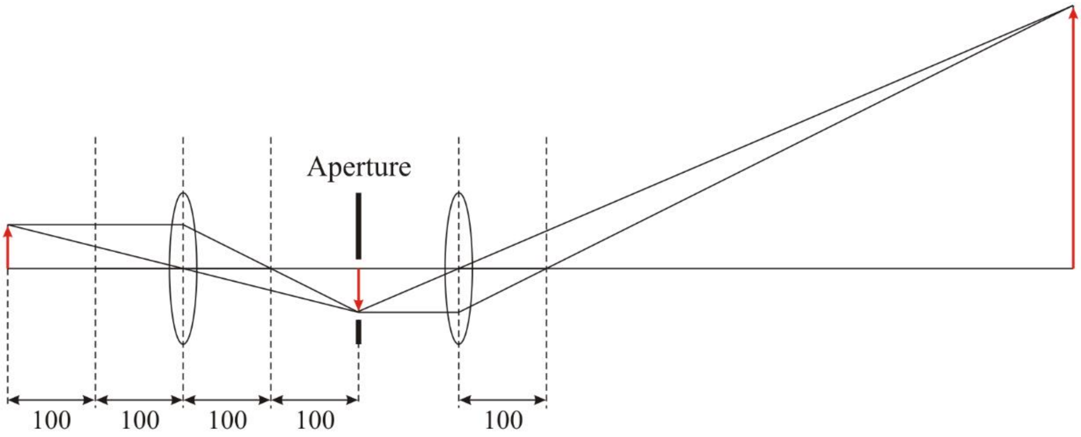

Figure 50: Setup of the imaging optic for each optical axis of the PSI without deflection mirrors. Projects the particles flying through the measurement volume with high magnification (~6) onto the image intensifier.

Figure 51 shows typical original images and processed images of particles flying through the measurement volume of the PSI. Initially all images are processed the same way: a background image is subtracted, the images are binarized using a threshold value and filtered using a median filter, objects are searched and those contacting the frame of the region of interest (ROI) are removed. Through comparing the size of the particles and their position in the ROI, it is proved if both images belong to the same particle and if it is located within the measurement volume, respectively. Since the exposure time of the image intensifier is relatively long, fast particles (Figure 51 below) in contrast to slow particles (Figure 51 above) cause motion blur. Consequently, the determination of the particle diameter has to be performed in two different ways. If the vertical extension of the particles is 1.2 times larger than the horizontal extension, the horizontal extension is used as particle diameter. If this is not the case, an area equal circle is calculated. In addition, it is possible to determine the exact position of the particles within the measurement volume using the relative position of a particle pair to each other and the position within the ROI. Since only particle sizes are needed in this work, the determination of the particle position is not discussed at this point. Figure 52 exemplarily shows particle diameter distributions measured for compressed air at 28.9 V, 4 bar, 3 m/min and 5 m/min, respectively.

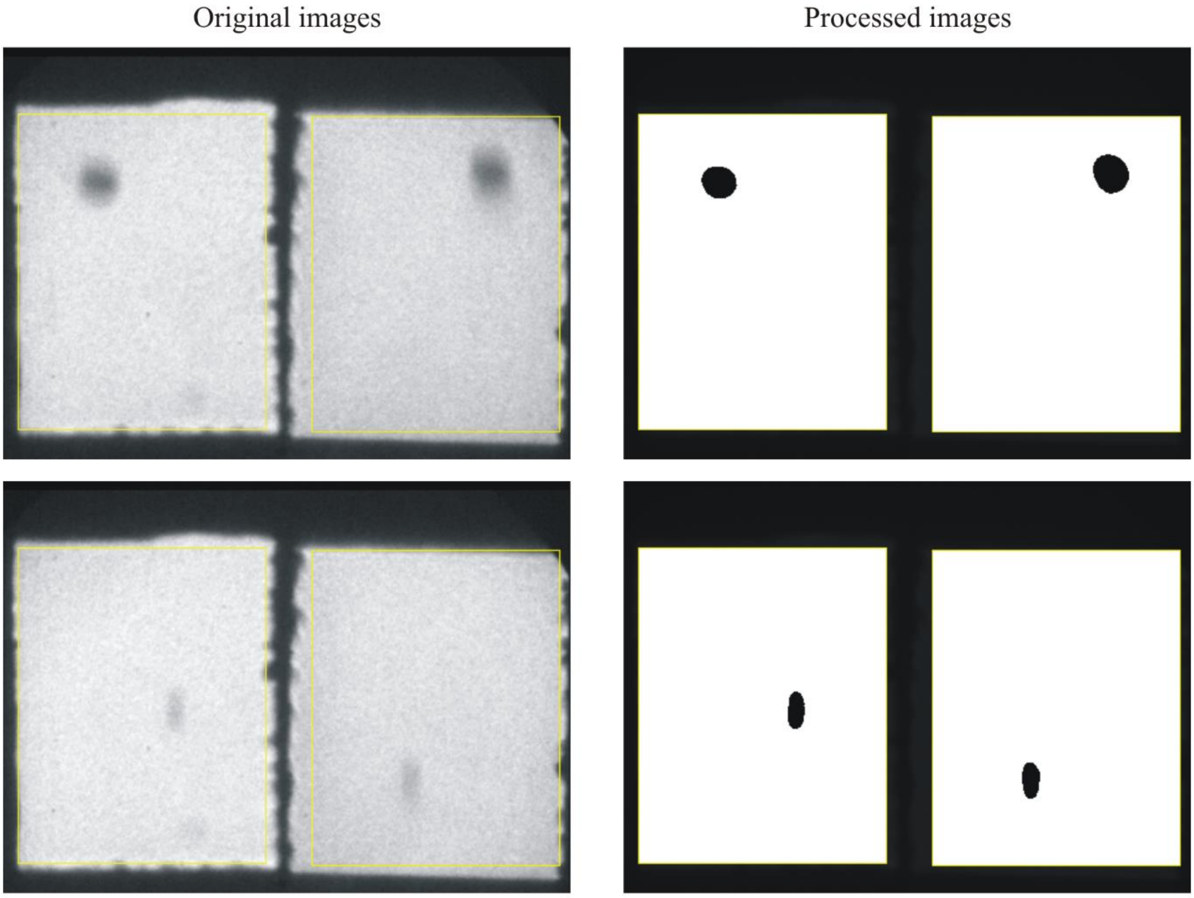

Figure 51: Original images (left) and processed images (right) of particles flying through the measurement volume. The both images above show a slow particle the both images below a fast particle that causes motion blur.

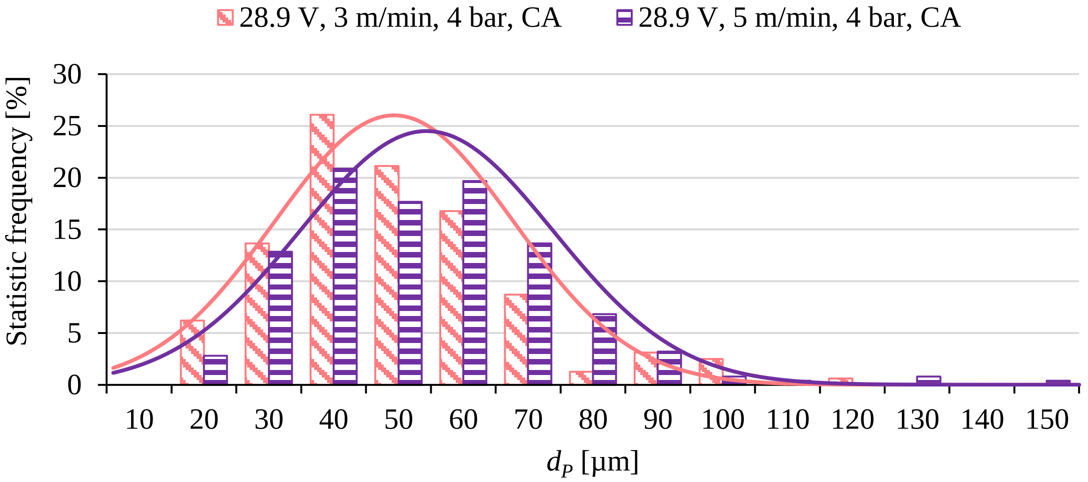

Figure 52: Particle size distributions and corresponding normal distributions measured with the PSI 70 mm away from the spray gun exit. Process parameter were set to 28.9 V, 4 bar, 3 m/min and 5 m/min, respectively. Compressed air was used as atomizing gas.

The particle distribution measured at 3 m/min is based on 161 valid particles determined in the 15000 images, the distribution measured at 5 m/min is based on 249 particles. As it can be seen, the more particles are detected the better the distributions resembles the normal distributions. The measurements for all parameters are performed in the middle of the spray plume 70 mm away from the spray gun exit.

5.4 Laser Doppler Anemometry and DPV measurements

In order to obtain spatially resolved particle rates that are necessary for the estimation of the optical thickness of the wire arc spray plume (see Chapter 3.2), Laser Doppler Anemometry (LDA) measurements are applied. The used LDA system was developed by Mayr [65] and Reusch [66] and its principle function is described in Chapter 1.1.3. An Nd-YAG laser with a wavelength of 532 nm, a beam radius of 1.6 mm and a power of 100 mW is used. The laser is split and the resulting beams are crossed under an angle of 0.8549°, forming an ellipsoid measurement volume with the half-axis $a = 0.16\ \text{mm}$, $b = 5.34\ \text{mm}$ and $c = 0.16\ \text{mm}$.

Figure 53 shows the measuring grid that is scanned with the LDA. It consists of five planes evenly distributed between 70 mm and 210 mm in front of the wire arc gun exit. Each plane includes 9×9 measurement points that are arranged in a square with the edge length of 50 mm. The measurement time at every point is 1 s.

Since the sensitivity of the used LDA system is low for small particles (<35 µm) [64], the diagnostic can be considered to be size selective. Although, invalid bursts cannot be evaluated with respect to the particle velocity, they nevertheless contribute to the particle rate [66]. For this reason only the particle rate results of the LDA are used for the determination of the optical thickness. The particle velocities are measured using the DPV. The principle function of the

DPV is described in Chapter 1.1.3. Its measurement volume is positioned in the center of the spray plume. The first measurement point is located 70 mm in front of the wire arc spray gun exit and the following five measurement points are located downstream with a distance of 35 mm.

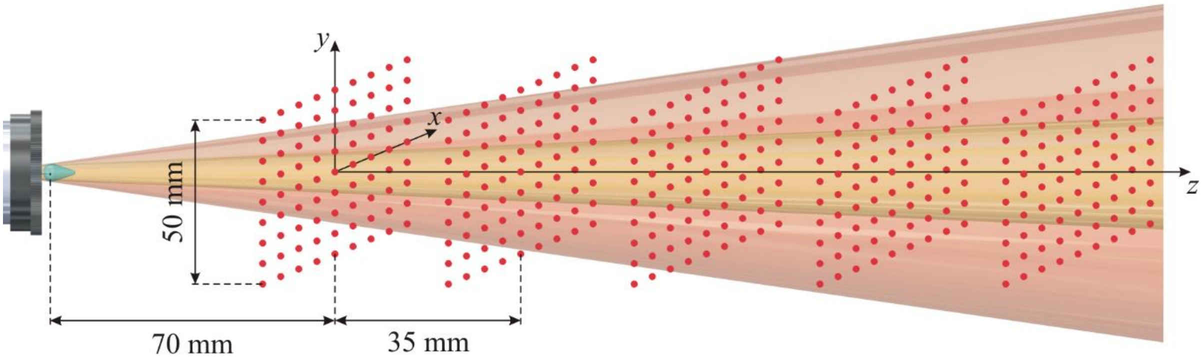

Figure 53: Measuring grid scanned with the Laser Doppler Anemometry. The grid consists of five planes including 9×9 *measurement points.*

The results of the LDA and the DPV are used for the estimation of the optical thickness and the calculation of the material dependent oxidation of the particles. Detailed results are presented in Chapter 6.

5.5 Coating generation and evaluation

In order to be able to validate the tomographic oxidation measurements, test coatings are generated and evaluated. Therefore, copper substrates are coated by moving the spray gun in meandering shape across them (see Figure 54). The procedure is repeated six times and the velocity of the gun is 0.67 m/s. To get several mesh points along the spraying direction the coatings for every parameter set are produced at the distances 65 mm, 105 mm, 145 mm, 185 mm and 225 mm. For one parameter set and one distance always three substrates are coated in order to compensate the rejects due to destruction while generating the cross sections. For the evaluation of the coatings, scanning electron microscope (SEM) photographs (1000 times magnification, 8 bit dynamic range) of the cross sections are used. Figure 55 a) shows a SEM image of a coating produced with a voltage of 33 V, a wire feed rate of 4 m/min and a pressure of 4 bar.

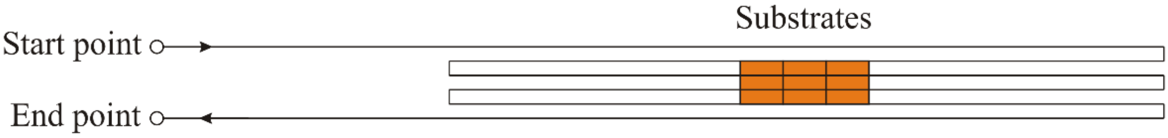

Figure 54: Meander-shaped movement of the spray gun across three copper substrates. The test coatings are generated in order to evaluate the tomographic oxidation measurements.

For the determination of the area fractions of pores, oxides and steel feedstock, several image processing steps are applied. This method is widespread in thermal spraying and is for example described in [72, 144–146]. To separate the different components, their gray scale distribution is analyzed (see Figure 56), whereby pores appear black, oxides dark gray and steel feedstock light gray [72, 144]. The histograms of all cross section images show two maxima, the first one belonging to the light gray steel and the second smaller one belonging to the dark gray oxide. In order to automatize the evaluation process in the first step to every pixel of a SEM photograph an offset is added, so that the first maximum of the histogram lies at a gray scale value of 200. Finally the position of the second maximum is searched and three threshold values are applied to determine the different area fractions:

- Pores: gray scale values between 0 and 126
- Oxides: gray scale values between 126 and the middle of the two maxima
- Steel feedstock: gray scale values between the middle of the two maxima and 255

The threshold value for the pores at 126 is an empirical value that is not very critical, since the contrast between pores and oxides is very high. Figure 56 shows the histogram belonging to the SEM photograph shown in Figure 55. The threshold values for the automatized area fraction determination are marked green.

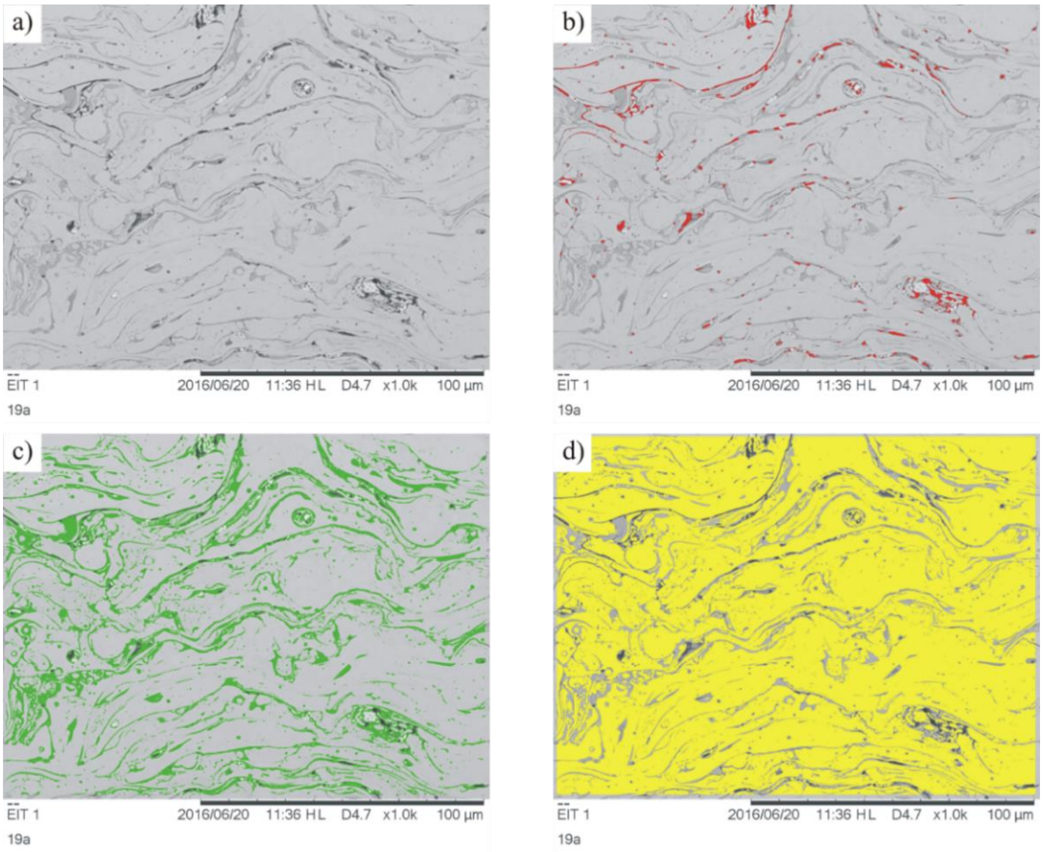

Figure 55: SEM images of a coating cross section produced with 33 V, 4 m/min, 4 bar and CA. a) original image, b) with red marked pores, c) with green marked oxides and d) with yellow marked iron.

To achieve a certain confidence level 16 randomly selected areas (127 µm x 95 µm) are evaluated. In addition the functionality of the image processing method is proved by analyzing selected coatings with the inert gas fusion technique [147] using the oxygen/nitrogen/hydrogen elemental analyzer “TC-436“ from the company “LECO“. For this method the coatings have to be separated from the substrate and grinded to a fine powder. As described in [147] the powder is fused and all elements are transferred from the liquid phase to the gas phase. The oxygen content can finally be detected by infrared spectroscopic investigation of the resulting CO and CO_2, respectively.

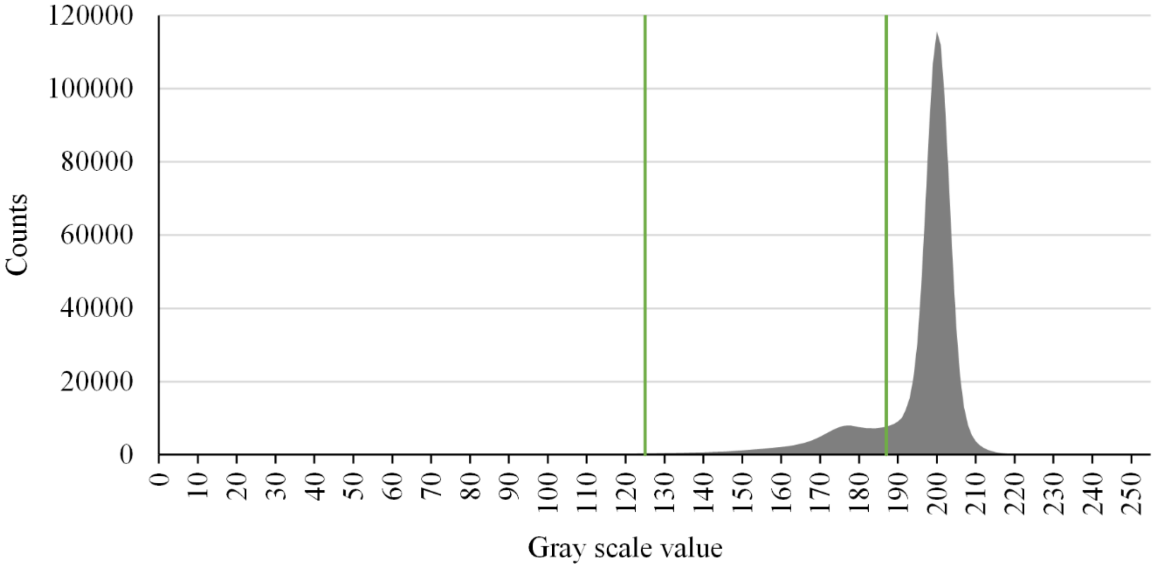

Figure 56: Histogram of the SEM photograph shown in Figure 55. The first maximum at 188 belongs to the dark gray oxide and the second maximum at 200 belongs to the light gray steel (feedstock material). The green lines mark the threshold values for the automatized area fraction determination.

In Figure 57 the two different methods are compared with each other. The diagram on the left side shows oxide area fractions determined by applying the above mentioned image processing steps to SEM photographs of the cross sections. The diagram on the right side shows the oxygen contents determined using the oxygen/nitrogen/hydrogen elemental analyzer. In both cases the coatings were sprayed with three different voltages at three different positions. In addition compressed air was used as atomizing gas, the wire feed rate was set to 4 m/min and the gas pressure was set to 4 bar.

It can be seen that both oxide area fraction and oxygen content increase with increasing distance for all used voltages. Furthermore, no significant trend dependent on the voltage can be observed. Because this is valid for both analyzing systems, the image processing method, that is simpler and available on the institute, seems to be sufficient for the determination of the oxide content.

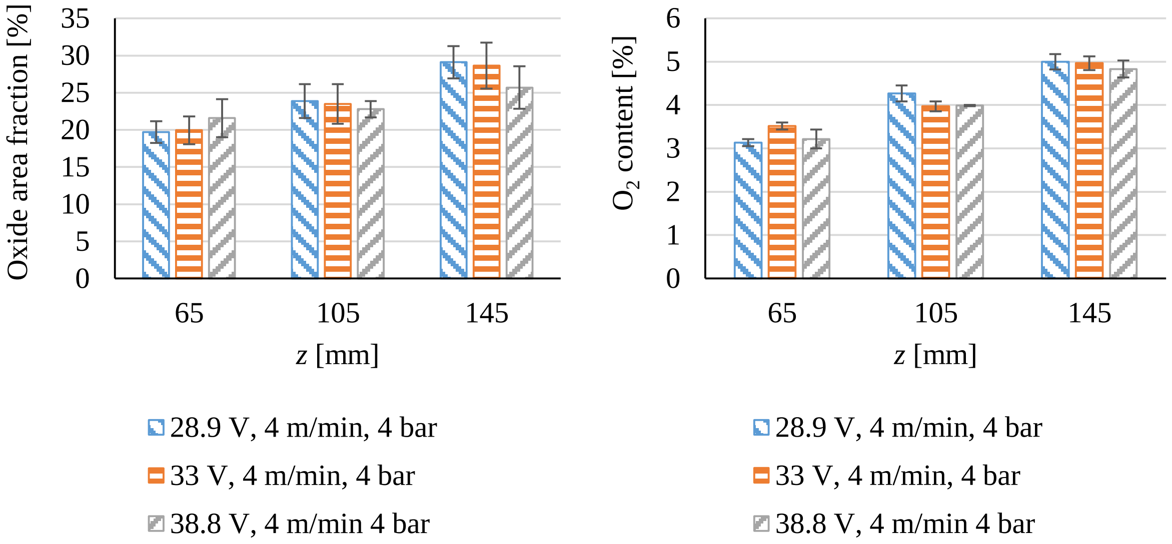

Figure 57: Left: Oxide area fractions determined using SEM photographs of cross sections. Right: Oxygen contents determined using the oxygen/nitrogen/hydrogen elemental analyzer "TC-436". In both cases the coatings are sprayed with three different voltages at three different distances. Compressed air was used as atomizing gas, the wire feed rate was set to 4 m/min and the gas pressure was set to 4 bar.

6 Results

In the following chapter the results of the pretests, the used established diagnostics (PSI, LDA and DPV) and the tomographic two-color-pyrometry are presented. Besides the electrical measurements, the spectroscopic measurements and the approximation of the optical thickness, 3D intensity and temperature reconstructions are presented. Furthermore, the results of the material dependent emissivity calculations, using the measured particle sizes and velocities, are shown.

6.1 Voltage and current measurements

First of all the results of the voltage and current measurements are presented. Typical voltage and current traces are shown in Figure 58. Here the process was operated with 28.9 V, 4 m/min and 4 bar. Compressed air was used as atomizing gas. The voltage trace shows fluctuations between 20 V and 35 V that are typical for the wire arc spray process. They are caused by the length variation of the arc moving in the gap between the wire tips [30]. The uniform voltage fluctuations and the constant current at 170 A is evidence for a good adjusted and stable process. Voltage and current traces for the other parameters are presented in the Appendix A.4.

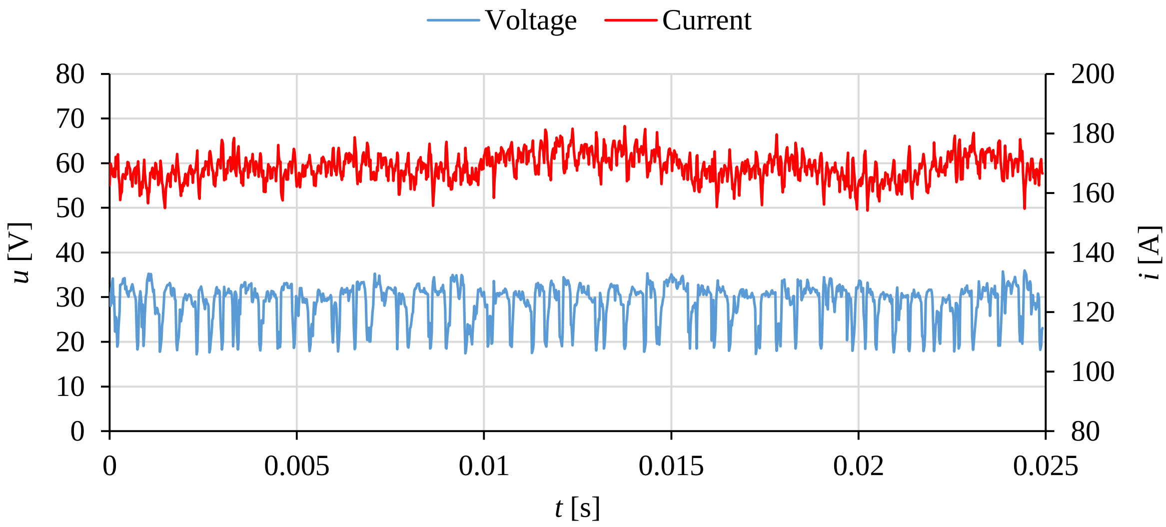

Figure 58: Voltage and current traces of the wire arc spray process operated with 28.9 V, 4 m/min, 4 bar and compressed air (CA).

Using voltage and current traces measured over 2 s and the equations presented in Chapter 5.1, the energy input per mass H_{mass} into the wires can be calculated. Of course this is only an approximation, since fractions of the electric power are transferred to the environment for example due to the radiation of the arc [138]. However, the values are suitable to allow qualitative interpretations of the tomographic two-color-pyrometry results.

The calculated energy inputs for the different parameter variations are presented in Figure 59. As it can be seen on the diagrams a) and b) in Figure 59, there is a linear dependence between the process voltage and the heat input. This connection is valid both for compressed air and nitrogen at a wire feed rate of 4 m/min. Changing the pressure does not affect the energy input per mass. The results presented in Figure 59 c) measured at 28.9 V and 4 m/min show an almost constant heat input of approximately 4750 kJ/g independent of the adjusted pressure. Finally the influence of the wire feed rate is illustrated in Figure 59 d). An increasing wire feed rate at 28.9 V, 4 bar and compressed air leads to a decreasing energy input per mass, whereby the relation seems to be inversely proportional.

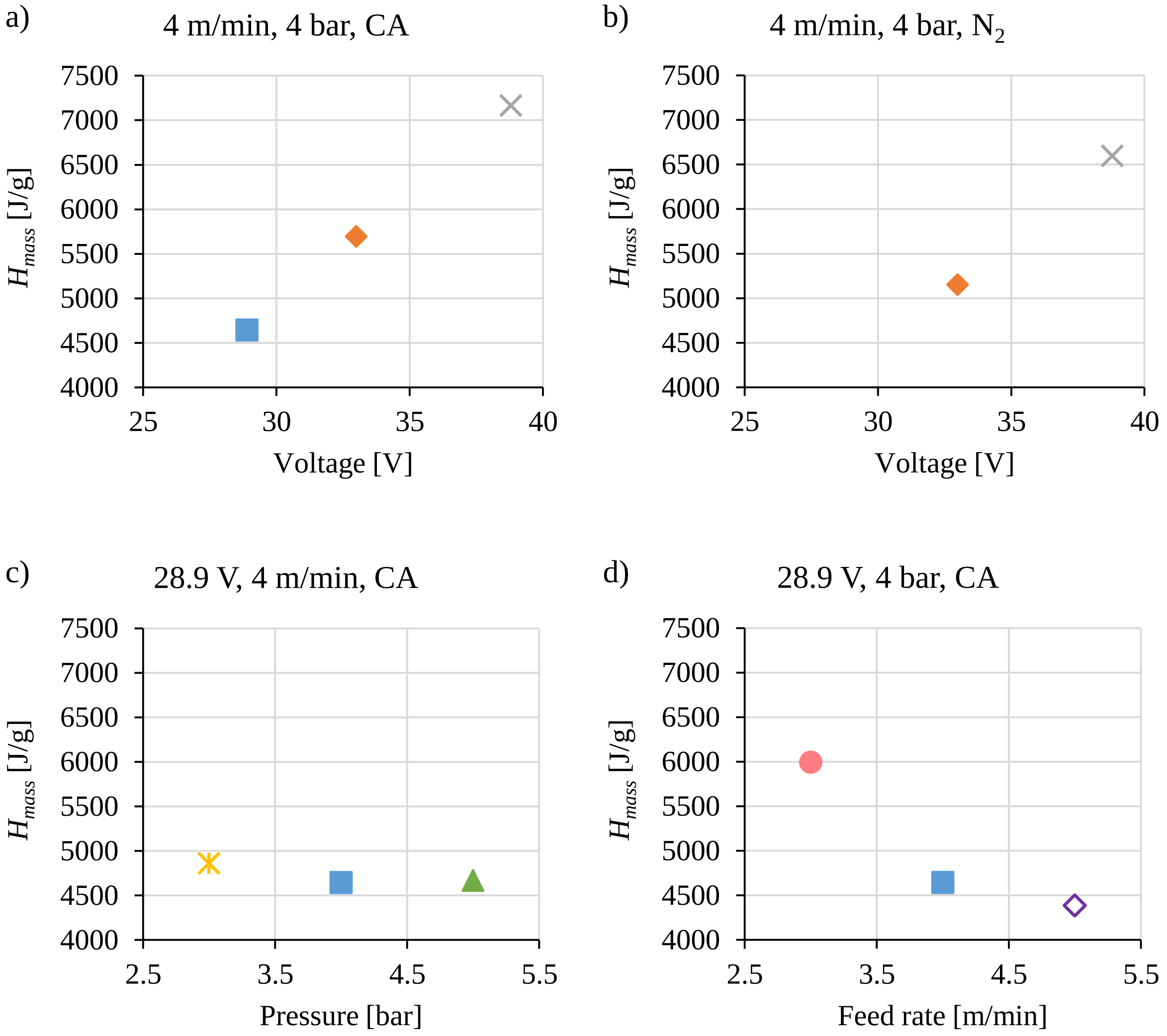

Figure 59: Energy inputs per mass calculated using the equations presented in Chapter 5.1. a) 4 m/min, 4 bar, CA and changing voltage. b) 4 m/min, 4 bar, N_2 and changing voltage. c) 28.9 V, 4 m/min, CA and changing pressure. d) 28.9 V, 4 bar, CA and changing feed rate.

6.2 Plasma expansion

To be sure that the recombination plasma occurring at the wire arc spray gun exit does not affect the measurements with the tomographic two-color-pyrometry, its expansion is investigated by means of spectroscopy. Therefore the spectrum in front of the gun is measured at different positions using the spectrometer "ARYELLE". Since the most electric power is implemented at high voltages and the plasma expansion is considered to be proportional to the arc power, the spectra are measured at 38.8 V, 4 m/min and 4 bar using compressed air as atomizing gas. The diagram in Figure 60 shows the spectra measured at three different positions along the spraying direction. The intensity of the spectrum measured directly at the position of the wire tips (0 mm, primary axis) is two orders of magnitude higher than the spectrum measured 30 mm in front of the tips. Furthermore, it only shows emission lines what in turn is evidence for the presence of plasma. The further away the measurements are performed the lower the amount of line emission gets. At a distance of 30 mm and 60 mm the measurements between 700 nm and 900 nm only show continuous spectra coming from the thermal radiation of the particles. Furthermore, it should be noted that the ripple appearance of the spectra originates from the special setup of the spectrometer (see Chapter 5.2). In conclusion measurements with the tomographic two-color-pyrometry can be applied at a distance of 60 mm without the fear of being disturbed by line emission of the recombination plasma.

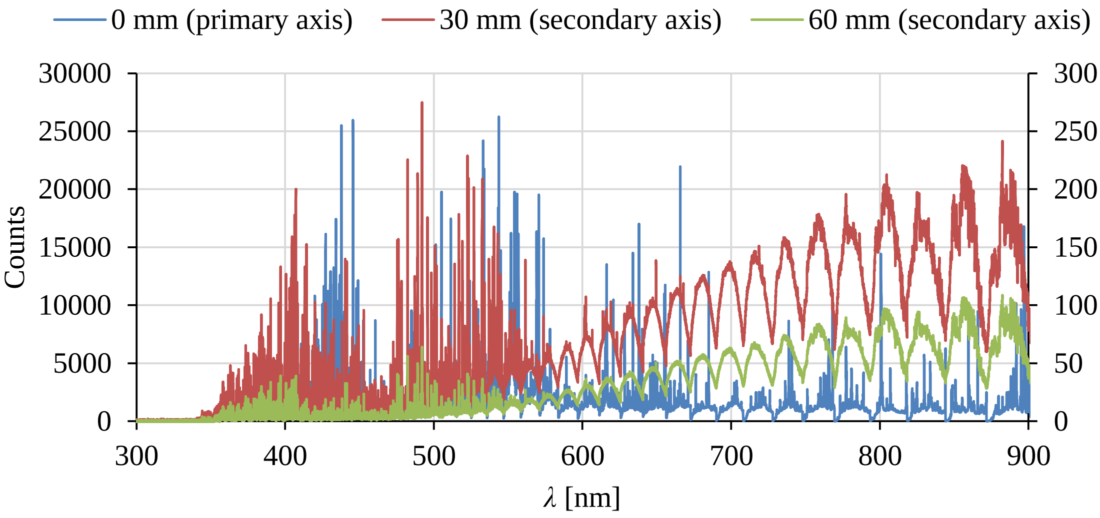

Figure 60: Spectrum of the wire arc spray process measured at different positions in front of the wire tips using the spectrometer "ARYELLE". The blue curve belongs to the primary axis, the red and green curves to the secondary axis. The process parameters were set to 38.8 V, 4 m/min and 4 bar. Compressed air was used as atomizing gas.

6.3 Test coatings

To be able to evaluate the in-flight particle oxidation measurements test coatings are generated for all parameter variations at different positions along the spraying axis. In Figure 61 scanning electron microscope (SEM) photographs of a cross section are exemplarily presented. Both coatings were sprayed 65 mm in front of the spray gun exit with a voltage of 33 V, a feed rate of 4 m/min and a pressure of 4 bar. For the coating on the left side compressed air was used as atomizing gas, for the coating on the right side nitrogen. Both cross sections show the lamellar structure, whereby the oxide content (dark gray) of the compressed air coating is significantly higher than the oxide content of the nitrogen coating. Furthermore, the coating sprayed with nitrogen is more porous. Since only the oxide content is needed in order to evaluate the oxidation measurements of the tomographic two-color-pyrometry, hereinafter only oxide area fraction results determined by the method presented in Chapter 5.5 are presented.

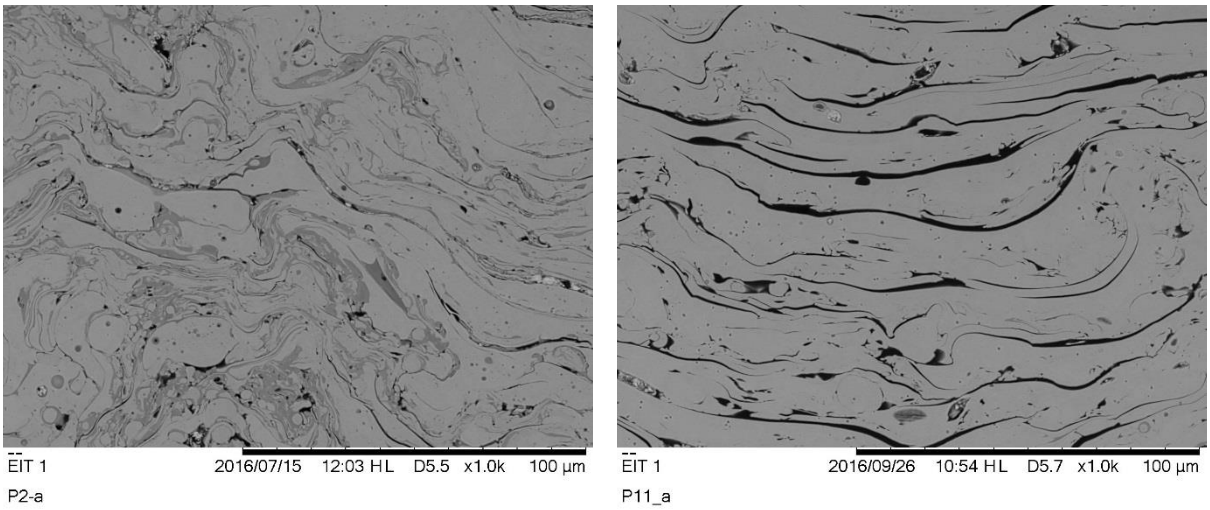

Figure 61: Scanning electron microscope photographs of coating cross sections. The left coating was sprayed with 33 V, 4 m/min, 4 bar and compressed air as atomizing gas. On the right side nitrogen was used instead of CA. Both were sprayed at a distance of 65 mm.

The diagram in Figure 62 shows the oxide area fractions of coatings sprayed at different positions along the *z*-axis for a voltage of 28.9 V, 33 V and 38.8 V. In addition the wire feed rate was set to 4 m/min, the pressure to 4 bar and compressed air was used as atomizing gas. The oxide fractions increase with increasing distance from approximately 20 % to 35 % and no significant trend that is reducible to the voltage change can be seen.

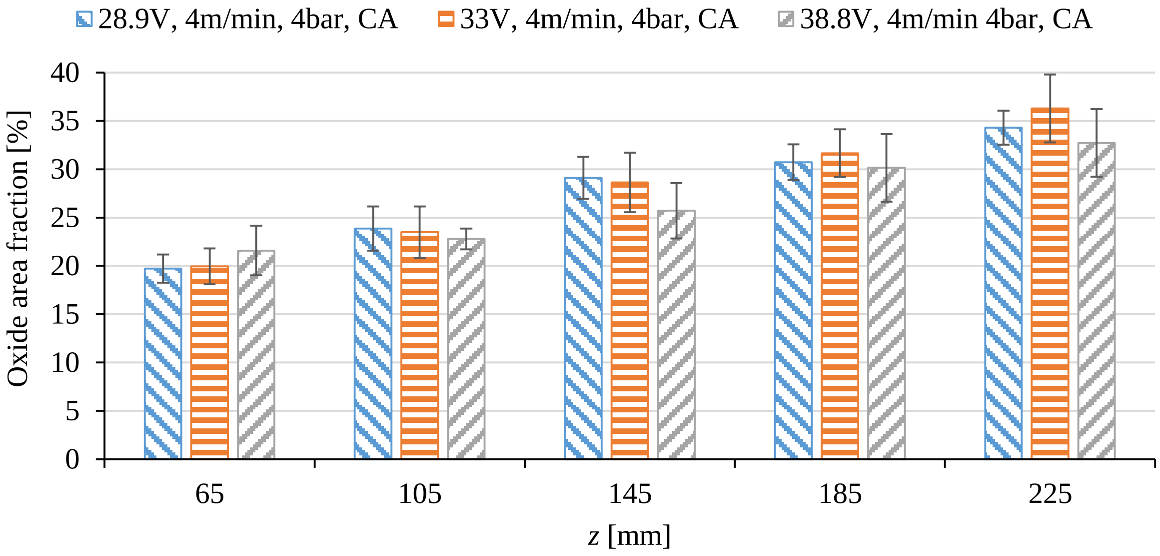

Figure 62: Oxide area fractions dependent on the spraying distance for 28.9 V, 33 V and 38.8 V. The other process parameters were set to 4 m/min and 4 bar. Compressed air was used as atomizing gas.

The influence of the atomizing gas pressure on the oxide content is presented in Figure 63. Here also compressed air was used, the voltage was set to 28.9 V and the wire feed rate to 4 m/min. For all investigated pressures the oxide area fractions increase by approximately 15 % along the observed distance. In addition, a clear trend concerning the influence of the pressure can be observed. The results indicate that the oxide fraction is proportional to the pressure of the atomizing gas.

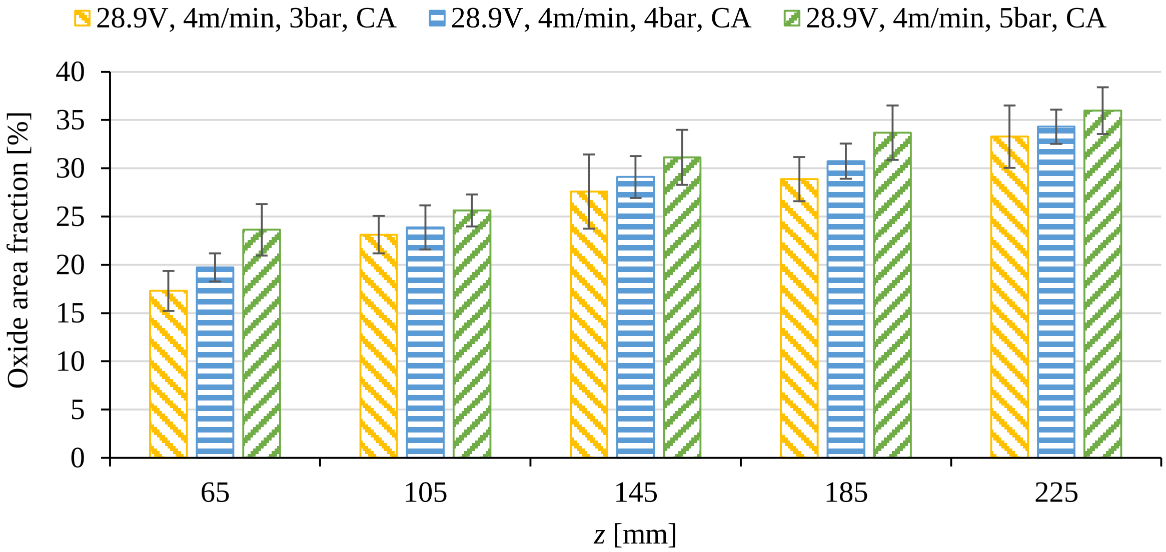

Figure 63: Oxide area fractions dependent on the spraying distance for 3 bar, 4 bar and 5 bar. The other process parameters were set to 28.9 V and 4 m/min. Compressed air was used as atomizing gas.

Figure 64 shows the oxide area fractions for wire feed rates of 3 m/min, 4 m/min and 5 m/min. The other parameters were set to the base values 28.9 V and 4 bar. In addition compressed air was used. As with the changing voltage and the changing pressure the oxide fractions are in the range of 20 % at a distance of 65 mm and in the range of 35 % at a distance of 225 mm. Furthermore, an increasing wire feed rate seems to cause decreasing oxide contents, however this trend remains not very significant from a distance of 145 mm.

As it can be seen by means of the diagram in Figure 65 using nitrogen as atomizing gas substantially influences the amount of oxides in the coatings. Compared to coatings sprayed with compressed air the oxide area fractions are lower by more than a factor of two. Unfortunately the influence of the voltage cannot be determined, since the measurements with 28.9 V could not be performed at 185 mm and 225 mm due to an unstable process. However, it seems that the influence of the voltage increases with increasing distance. At 65 mm, 105 mm and 145 mm the oxide area fractions for the different voltages are almost equal. At a distance of 185 mm and 225 mm the amount of oxide at 38.8 V is significantly higher compared to 33 V.

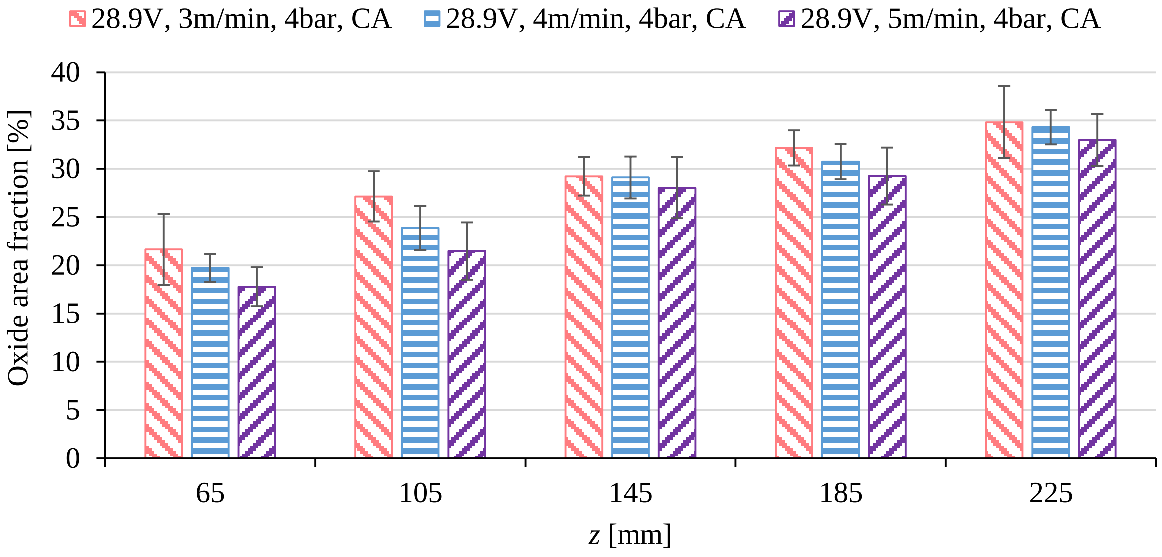

Figure 64: Oxide area fractions dependent on the spraying distance for 3 m/min, 4 m/min and 5 m/min. The other process parameters were set to 28.9 V and 4 bar. Compressed air was used as atomizing gas.

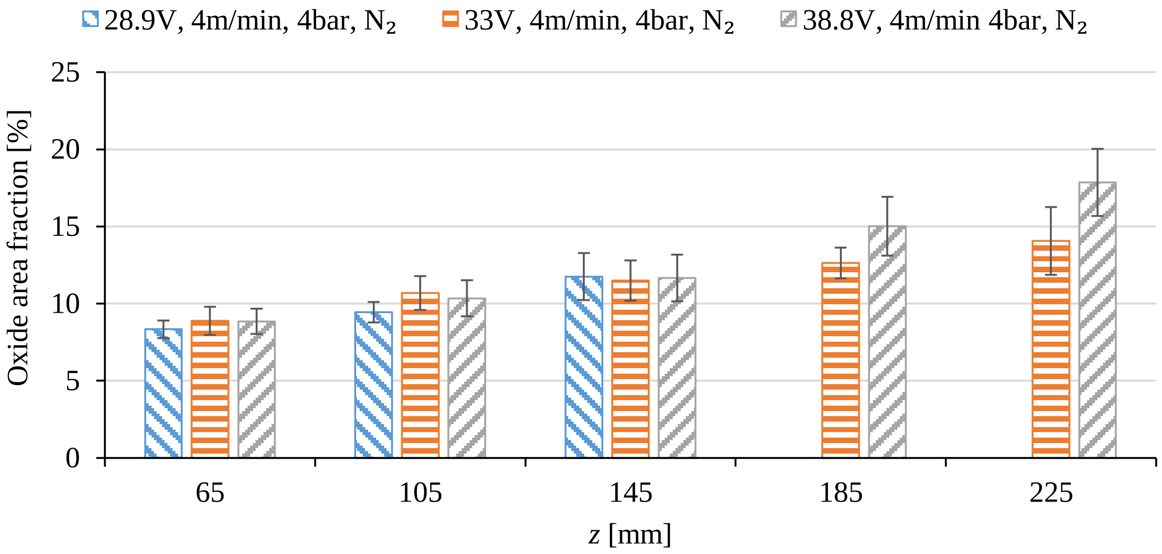

Figure 65: Oxide area fractions dependent on the spraying distance for 28.9 V, 33 V and 38.8 V. The other process parameters were set to 4 m/min and 4 bar. Nitrogen was used as atomizing gas.

6.4 Particle size, rate and velocity

In this chapter the results of the PSI, the LDA and the DPV measurements are presented. The determined particle sizes, rates and velocities are used in the next two chapters in order to approximate the optical thickness of the wire arc spray plume and to calculate the material dependent emissivity of the particles.

Since for all following calculations mean values of the particle radii are used, no further particle size distributions are presented. The diagrams in Figure 66 show the mean particle sizes for the different investigated parameter combinations. Diagram a) illustrates the influence of the voltage, whereby compressed air was used, the feed rate was set to 4 m/min and the pressure to 4 bar. As it can be seen, the particle radius slightly increases from approximately 22 µm at 28.9 V to 22.9 µm at 33 V. Increasing the voltage to 38.8 V leads to an increased radius of ~25 µm. Using nitrogen as atomizing gas apparently does not affect the particle size. The particle radius at 33 V, 4 m/min and 4 bar is almost equal for compressed air and nitrogen. The measurements with nitrogen again could not be performed at all three voltage parameters, since the process was unstable and the PSI had to be protected from unmolten wire pieces. The influence of the pressure is presented in diagram c). Between 3 bar and 4 bar the mean particle radius slightly decreases, whereas at a pressure of 5 bar the radius strongly decreases to ~20 µm.

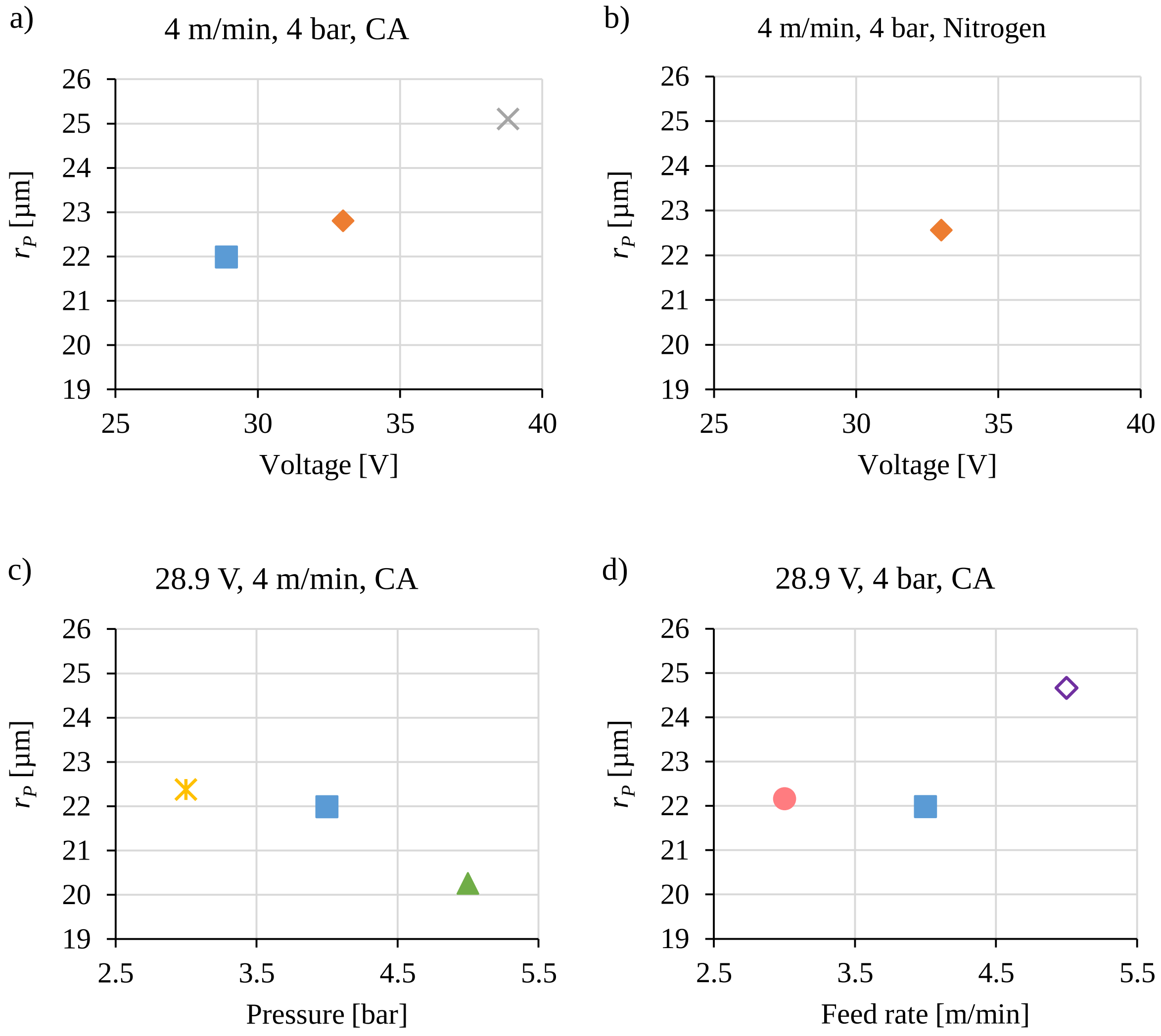

Figure 66: Particle radii measured with the Particle Shape Imaging diagnostic. a) 4 m/min, 4 bar, CA and changing voltage. b) 4 m/min, 4 bar, N_2 and changing voltage. c) 28.9 V, 4 m/min, CA and changing pressure. d) 28.9 V, 4 bar, CA and changing feed rate.

Diagram d) in Figure 66 shows the mean particle radii for a wire feed rate of 3 m/min, 4 m/min and 5 m/min. The voltage was set to 28.9 V and the pressure to 4 bar. In addition compressed air was used as atomizing gas. The results indicate that there is no clear trend between the wire feed rate and the mean particle size. From 3 m/min to 4 m/min the radius slightly decreases, whereas at 5 m/min the size in turn strongly declines to approximately 24.7 µm

To be able to estimate the optical thickness, particle rates were measured using the LDA. In the following, for reasons of simplicity only 2D particle rate distributions in the *xy*-plane, 70 mm in front of the wire arc spray gun exit are presented. The images in Figure 67 show the spatial resolved particle rates measured at 28.9 V, 33 V and 38.8 V. The other parameters in turn were set to the base parameters and compressed air was used as atomizing gas. Besides the oval appearance of the spray plume cross sections, it can be observed that with increasing voltage the wire arc spray plume spreads. Furthermore the maximum particle rate in the middle increases from 28.9 V to 33 V, whereas from 33 V to 38.8 V it decreases again.

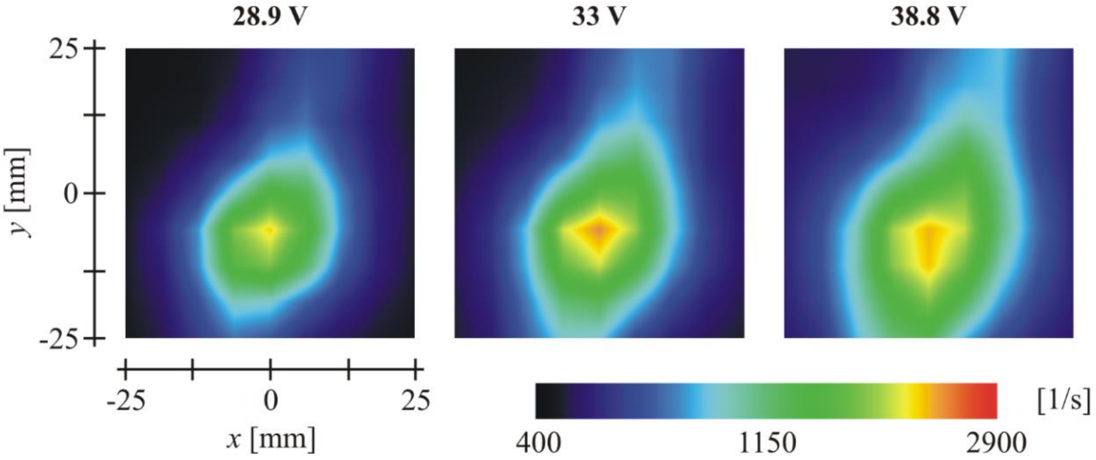

Figure 67: Particle rates for a changing voltage measured with the LDA in the xy-plane at z=70 mm. The other parameters were set to 4 m/min, 4bar and compressed air was used.

As can be seen in Figure 68, through increasing the gas pressure the spray plume gets constricted and the maximum particle rate in the middle increases. In addition the oval form of the cross section turns to a more round appearance. Besides the usage of compressed air, the other parameters for these measurements were set to 4 m/min and 4 bar.

The influence of the wire feed rate is illustrated in Figure 69. With increasing wire feed rate the maximum and the total particle rates increase. Furthermore the shape of the cross sections again gets more round with increasing wire feed rate.

Using nitrogen instead of compressed air leads to lower particle rates and a round appearance of the spray plume in the *xy*-plane. The corresponding 2D particle rates for 33 V and 38.8 V are presented in Figure 70. The pressure was set to 4 bar, the feed rate to 4 m/min. For reasons of comparability the space resolved particle distribution for compressed air measured at 33 V, 4 m/min and 4 bar is shown on the right side of Figure 70.

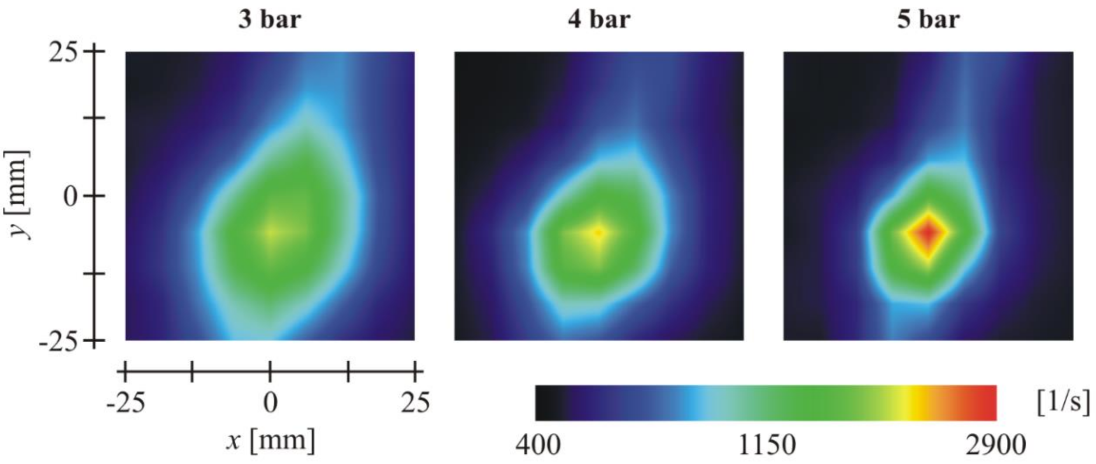

Figure 68: Particle rates for a changing pressure measured with the LDA in the xy-plane at z=70 mm. The other parameters were set to 28.9 V, 4 m/min and compressed air was used.

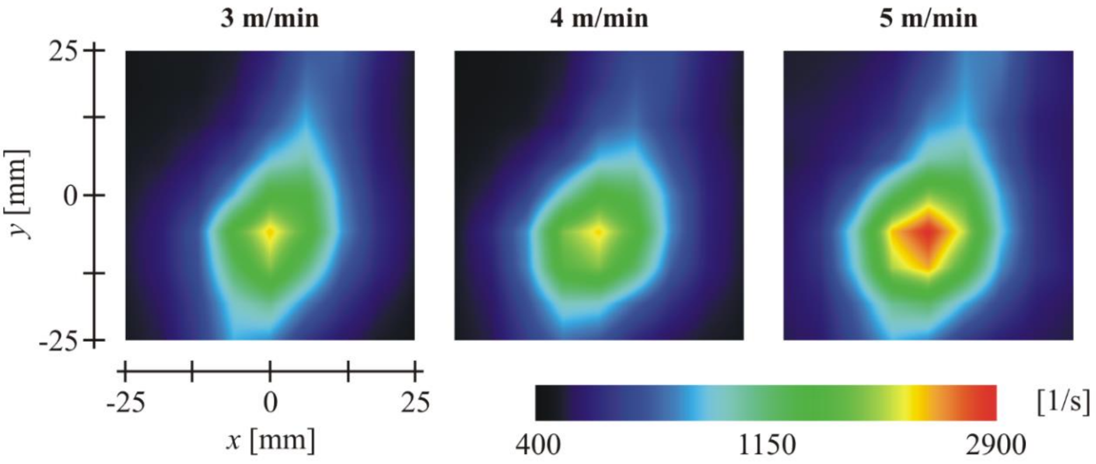

Figure 69: Particle rates for a changing wire feed rate measured with the LDA in the xy-plane at z=70 mm. The other parameters were set to 28.9 V, 4 bar and compressed air was used.

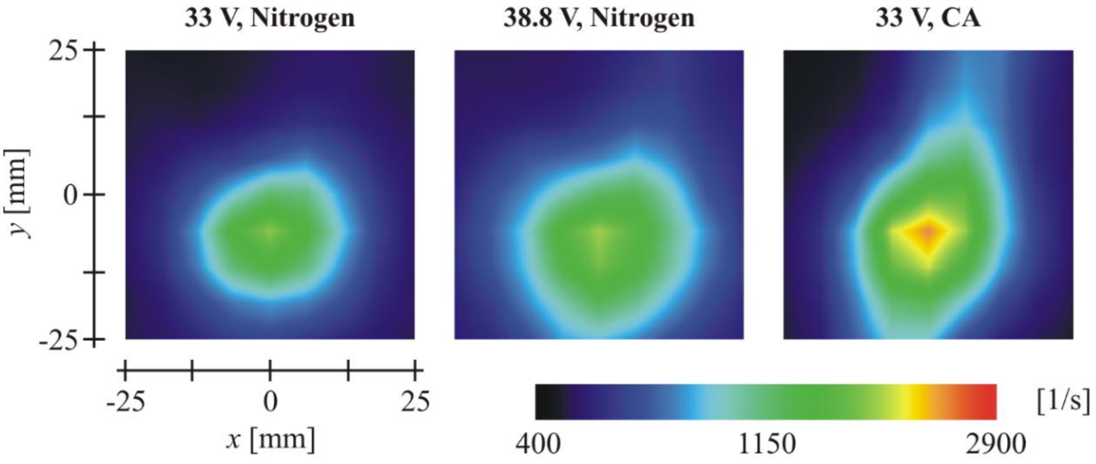

Figure 70: Particle rates for a changing voltage and nitrogen measured with the LDA in the xy-plane at z=70 mm. The other parameters were set to 4 m/min and 4 bar. For comparison the particle rate distribution for compressed air and 33 V is illustrated on the right side.

The particle velocities measured with the DPV are necessary both for the optical thickness calculations and for the particle emissivity determinations. To minimize the experimental efforts the particle velocities are only measured in the middle of the spray plume on six points along the spraying axis. Finally the particle velocity $v_{P,z}$ dependent on the *z*-coordinate is approximated by fitting a polynomial of third order to the measurement points.

The diagram in Figure 71 shows the particle velocities depending on the *z*-coordinate for a changing voltage. The wire feed rate was set to 4 m/min and the pressure to 4 bar. In addition compressed air was used as atomizing gas. As it can be seen, at the beginning the velocities increase and finally from $z \approx 130\ \mathrm{mm}$ decrease. Furthermore at the beginning at $z = 70\ \mathrm{mm}$ the velocities are separated from each other by about 5 m/s, whereby the velocity increases with decreasing voltage. However, at the end the velocities are closer to each other and the influence of the voltage is maintained when the measured value for 28.9 V at 190 mm is considered as outlier. The polynomial fits for a voltage of 33 V and a voltage of 38.8 V have satisfactory coefficients of determination above 0.99. At 28.9 V the coefficient is only 0.97 due to the outlier at $z = 190\mathrm{mm}$.

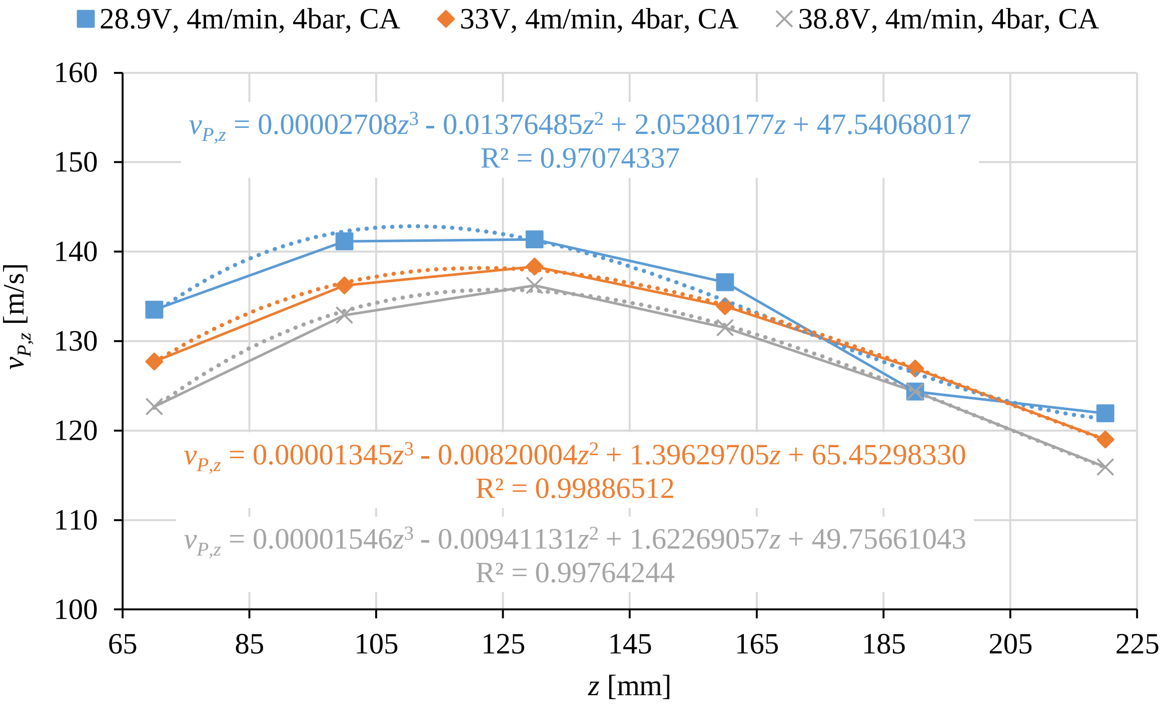

Figure 71: Particle velocities depending on the z-coordinate for a changing voltage and the corresponding third order polynomial fits with its coefficients of determination. The other parameters were set to 4 m/min, 4 bar and compressed air was used.

How the diagram in Figure 72 shows, the influence of the atomizing gas pressure on the particle velocity is significant. The velocity using 4 bar is over the whole observed distance approximately 15 to 20 m/s higher than at a pressure of 3 bar. The difference between 4 bar and 5 bar increases from ~8 m/s at 65 mm to almost 15 m/s at 220 mm. As with the changing voltage the velocities for all pressures increase from 70 mm to 130 mm and subsequently decrease. The coefficients of determination of the polynomial fits are sufficiently high both for a pressure of 3 bar and 5 bar ($R^2 > 0.99$).

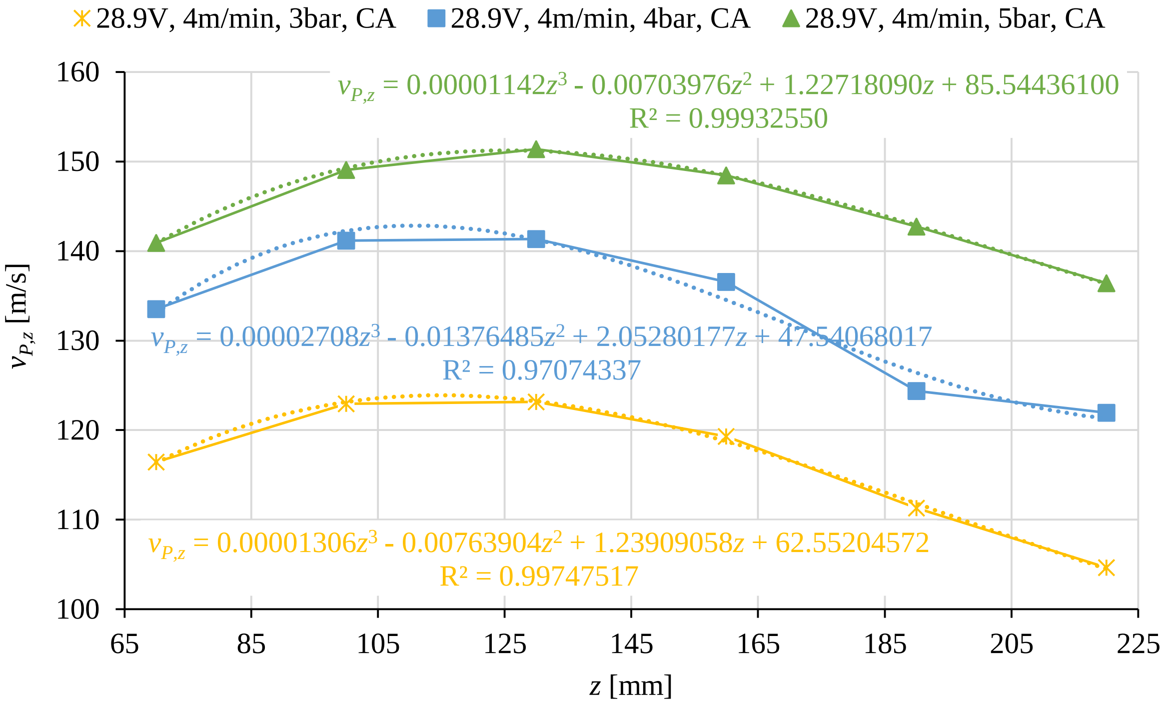

Figure 72: Particle velocities depending on the z-coordinate for a changing pressure and the corresponding third order polynomial fits with its coefficients of determination. The other parameters were set to 28.9 V, 4 m/min and compressed air was used.

The particle velocities depending on z for different wire feed rates are present in Figure 73. Besides the usage of compressed air the voltage was set to 28.9 V and the pressure to 4 bar. As with the other parameters, first of all the particles are accelerated and above $z \approx 130$ mm slowed down. A significant velocity difference between 3 m/min, 4 m/min and 5 m/min can only be found in the first half of the observed spray plume part. 70 mm away from the spray gun exit the velocities measured at 3 m/min are approximately 5 m/s higher than at a wire feed rate of 5 m/min. The velocities measured at 4 m/min are in turn 5 m/s higher than the velocities measured at 4 m/min. The further away the measurements were performed the smaller the velocity difference between the three feed rates gets. Consequently there seems to be no direct proportional relation between the wire feed rate and the particle velocity.

The influence of nitrogen and a changing voltage is illustrated by means of the diagram in Figure 74. As it can be seen the velocities are lower in contrast to the velocities measured using compressed air (see Figure 71) at the same parameters (4 m/min and 4 bar). Furthermore only a small acceleration (33 V) and almost no acceleration (38.8 V), respectively can be observed. The velocity difference between 33 V and 38.8 V increases from 0 m/s at 70 mm to approximately 5 m/s at 220 mm.

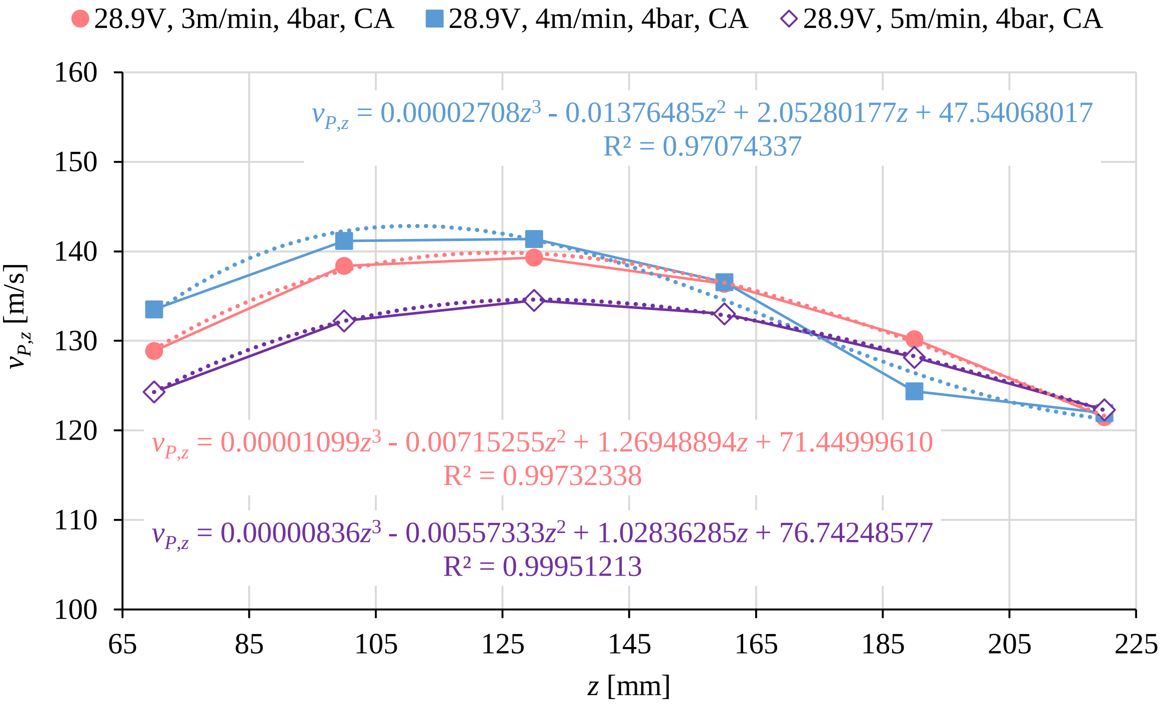

Figure 73: Particle velocities depending on the z-coordinate for a changing wire feed rate and the corresponding third order polynomial fits with its coefficients of determination. The other parameters were set to 28.9 V, 4 bar and compressed air was used.

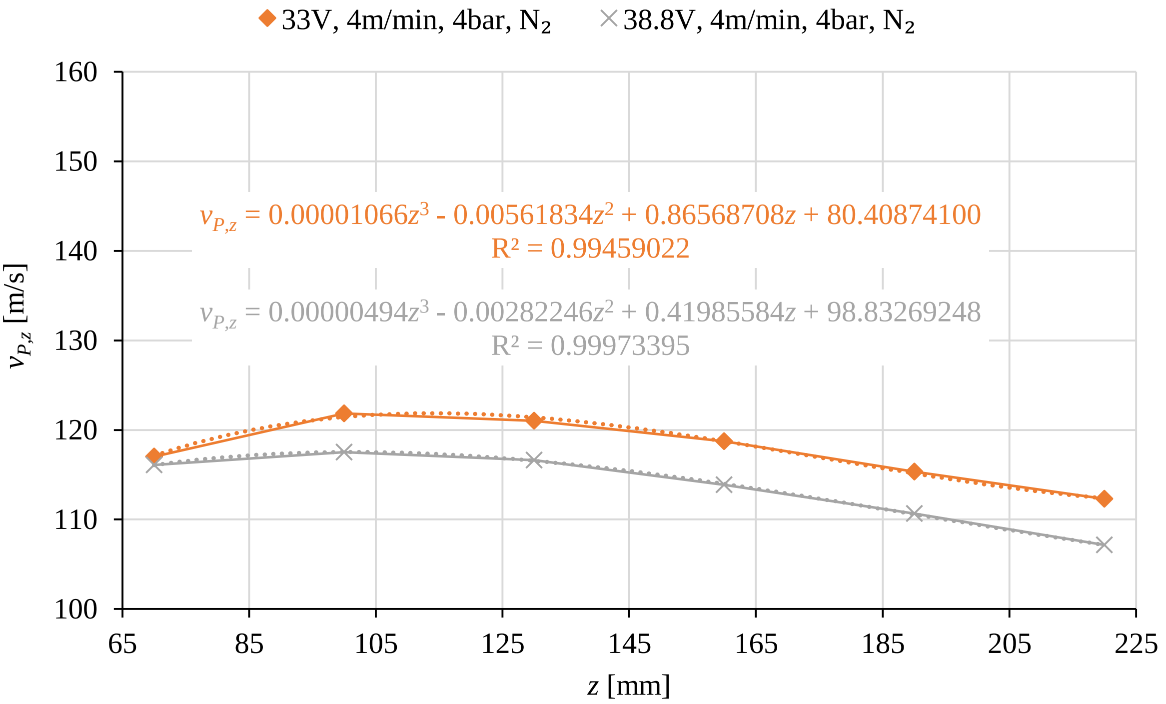

Figure 74: Particle velocities depending on the z-coordinate for a changing voltage and the corresponding third order polynomial fits with its coefficients of determination. The other parameters were set to 4 m/min, 4 bar and nitrogen was used.

6.5 Optical thickness of the spray plume

For the determination of the optical thickness the 2D particle rate distributions measured with the LDA are used (see Chapter 6.4). The example in Figure 75 shows such spatially resolved particle rates in the *xy*-plane including nine observation channels located in 5 mm steps along the *x*-axis. By means of these channels the optical thickness, depending on the distance to the middle of the spray plume, is calculated using the algorithm presented in Chapter 3.2. Since the variation of the optical thickness depending on the *z*-coordinate is negligible, only the LDA results at $z = 70\,\mathrm{mm}$ are shown in the following. Furthermore the evaluation of only one observation direction is sufficient, since the spray plume is almost rotationally symmetric.

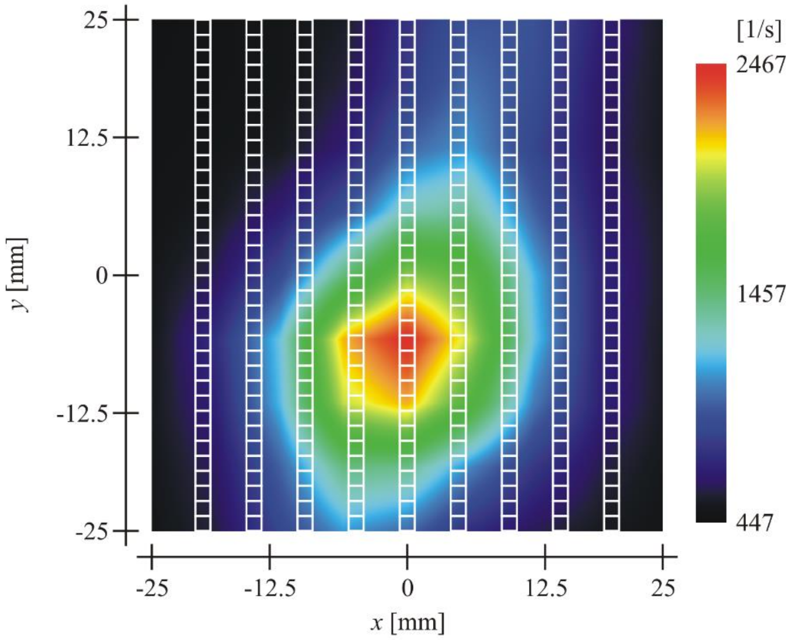

Figure 75: Example for a spatially resolved particle rate distribution measured with the LDA including the nine observation channels used for the optical thickness determination.

The diagram in Figure 76 shows the optical thickness depending on *x* for a changing voltage. The other parameters again are set to the base parameters, 4 m/min and 4 bar. In addition compressed air was used as atomizing gas. The optical thickness curves for all three voltages resemble a Gaussian distribution, whereby the maxima are located at $x = 0\,\mathrm{mm}$. Furthermore, increasing the voltage leads to an increasing optical thickness. The highest optical thickness of 0.045 is reached for a voltage of 38.8 V.

The results for a changing pressure, 28.9 V, 4 m/min and compressed air are presented in Figure 77. Again the curves are similar to Gaussian distributions and the maxima belong to the channel passing through the middle of spray plume. Increasing the pressure results in a decreasing optical thickness. The maximum value was determined for a pressure of 3 bar and is $\tau = 0.035$.

The influence of the wire feed rate on the optical thickness is shown by means of the diagram in Figure 78. The other parameters again were set to the base parameters. All three curves show the typical Gaussian form with the maxima at $x = 0\ \mathrm{mm}$. No significant trend concerning the feed rate can be recognized, since the values for 3 m/min and 4 m/min are almost equal and the values for 5 m/min are higher.

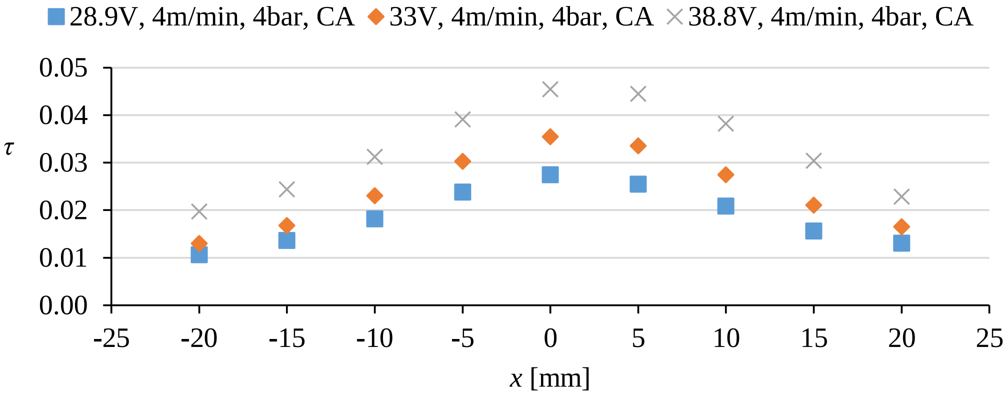

Figure 76: Optical thickness at $z = 70$ mm dependent on the x-coordinate for a changing voltage. The other parameters were set to the base parameters (4 m/min, 4 bar, CA).

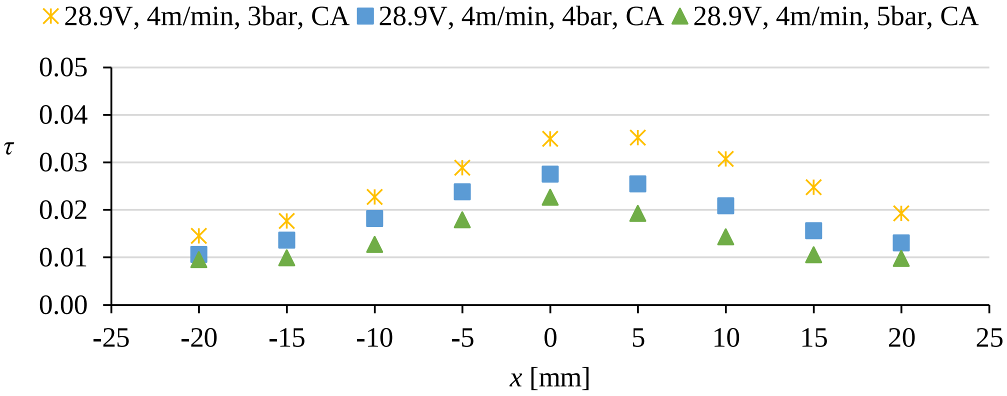

Figure 77: Optical thickness at $z = 70$ mm dependent on the x coordinate for a changing pressure. The other parameters were set to the base parameters (28.9 V, 4 m/min, CA).

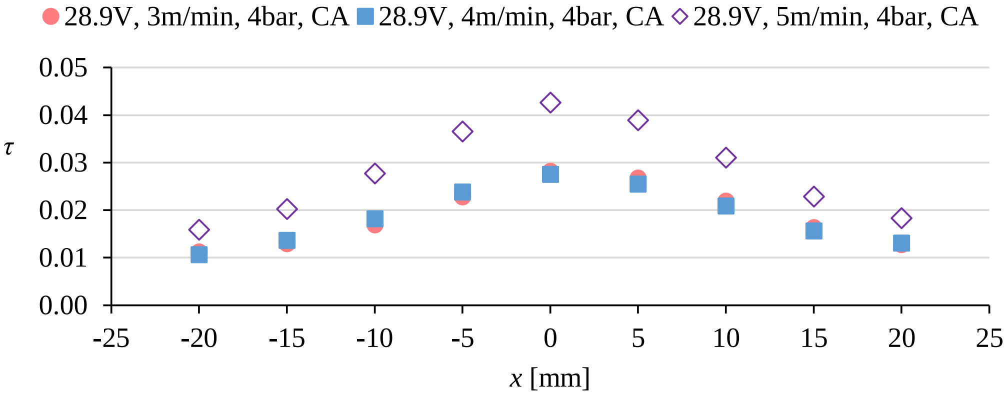

Figure 78: Optical thickness at $z = 70$ mm dependent on the x coordinate for a changing wire feed rate. The other parameters were set to the base parameters (28.9 V, 4 bar, CA).

Using nitrogen instead of compressed air does not significantly affect the optical thickness. The curve calculated for 33 V, 4 m/min and 4 bar is presented in Figure 79. It resembles a Gaussian distribution, whereby the maximum value of 0.027 is located at $x = 0\ \mathrm{mm}$.

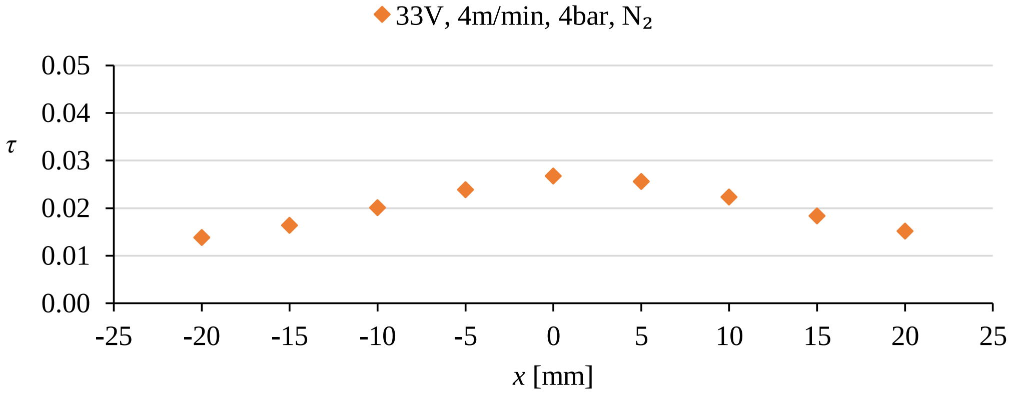

Figure 79: Optical thickness at $z = 70\ \mathrm{mm}$ *dependent on the x-coordinate for nitrogen, 33 V, 4 m/min and 4 bar.*

6.6 Tomographic measurements

Important results that can be achieved with the tomographic two-color-pyrometry are the three-dimensional intensity reconstructions. Since the intensities according to Equation 4.3 depend on the particle rate, velocity, size, temperature and emissivity, the 3D reconstructions only allow qualitative conclusions. For reasons of clarity in the following only the reconstructions for camera 1 (800 nm) are presented. They are made up of the single measurements at the three positions shown in Figure 39 and are presented using eight isosurfaces and a filled contour grid plane located at $z = 60\ \mathrm{mm}$.

For the 3D intensity distribution shown in Figure 80 the process was operated at the base parameters. The shape of the spray plume resembles an oval cylinder with a slightly downwards pronounced bulge. The maximum intensity was measured in the middle of the spray plume at $z = 60\ \mathrm{mm}$. Furthermore the extension of the outer isosurface is over the whole measured distance almost constant. How the reconstruction in Figure 81 shows, increasing the voltage to 33 V leads to a much more pronounced bulge, whereby the maximum at $z = 60\ \mathrm{mm}$ increases and shifts upwards. The effect on the shape of the spray plume for a further increase of the voltage to 38.8 V is presented in Figure 82. The widening of the bulge proceeds and a second lower maximum appears below the first one, whereby the larger upper maximum is again smaller than the maximum measured at 33 V. Finally it seems that increasing the voltage leads to the splitting of the spray plume into an upper and a bottom part merging with increasing distance to the wire arc gun exit.

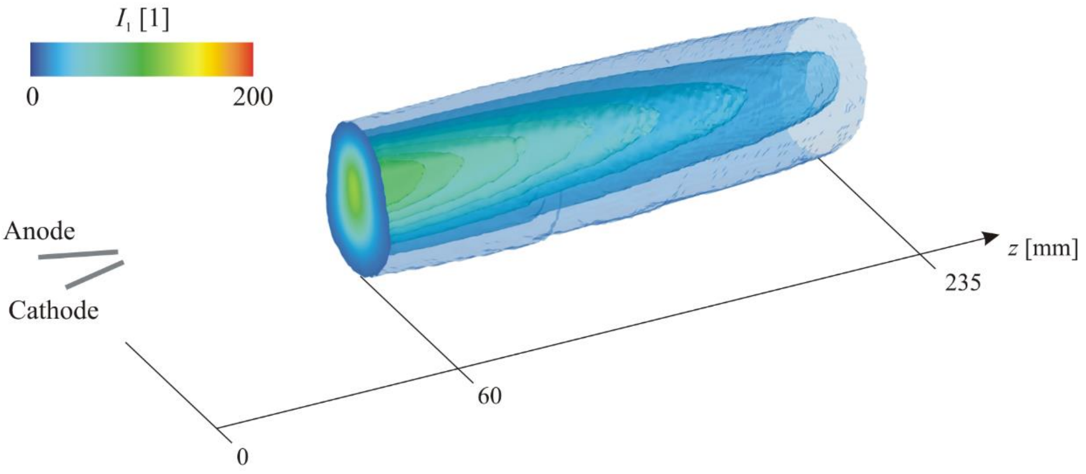

*Figure 80: 3D intensity reconstruction measured with camera 1 (800 nm) at **28.9 V**, **4 m/min**, **4 bar** and compressed air as atomizing gas.*

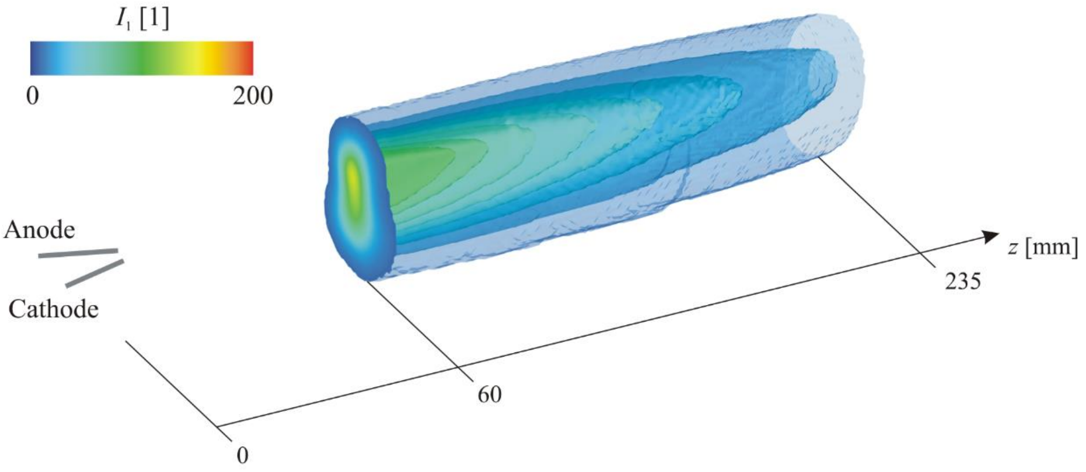

*Figure 81: 3D intensity reconstruction measured with camera 1 (800 nm) at **33 V**, 4 m/min, 4 bar and compressed air as atomizing gas.*

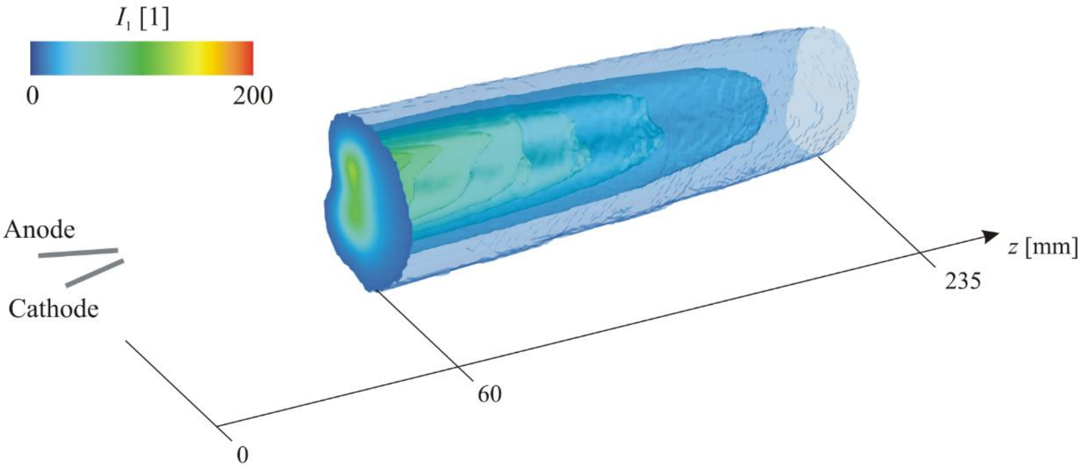

*Figure 82: 3D intensity reconstruction measured with camera 1 (800 nm) at **38.8 V**, 4 m/min, 4 bar and compressed air as atomizing gas.*

Hereafter the influence of the atomizing gas pressure is presented. Figure 83 shows the 3D reconstruction of the spray plume for a pressure of 3 bar, Figure 84 the 3D reconstruction of the spray plume for a pressure of 5 bar. For both measurements the wire feed rate was set to 4 m/min and the voltage to 28.9 V. Furthermore compressed air was used as gas. It can be seen that the expansion of the spray plume in radial direction increases with decreasing pressure, consequently the maximum at 3 bar ($I_{1,\max} = 104$) is much smaller than maximum at 5 bar ($I_{1,\max} = 199$). In summary it can be said that increasing the pressure leads to the constriction of the spray plume.

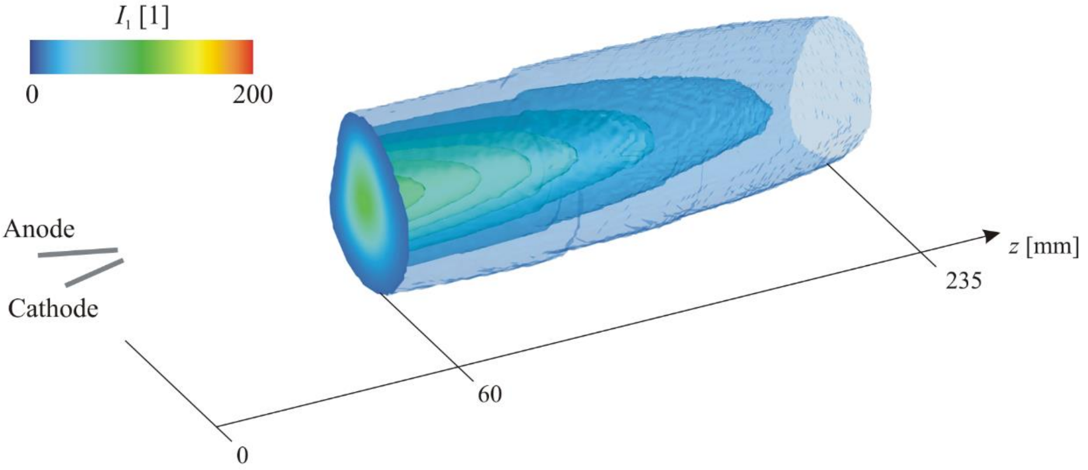

Figure 83: 3D intensity reconstruction measured with camera 1 (800 nm) at 28.9 V, 4 m/min, ***3 bar*** *and compressed air as atomizing gas.*

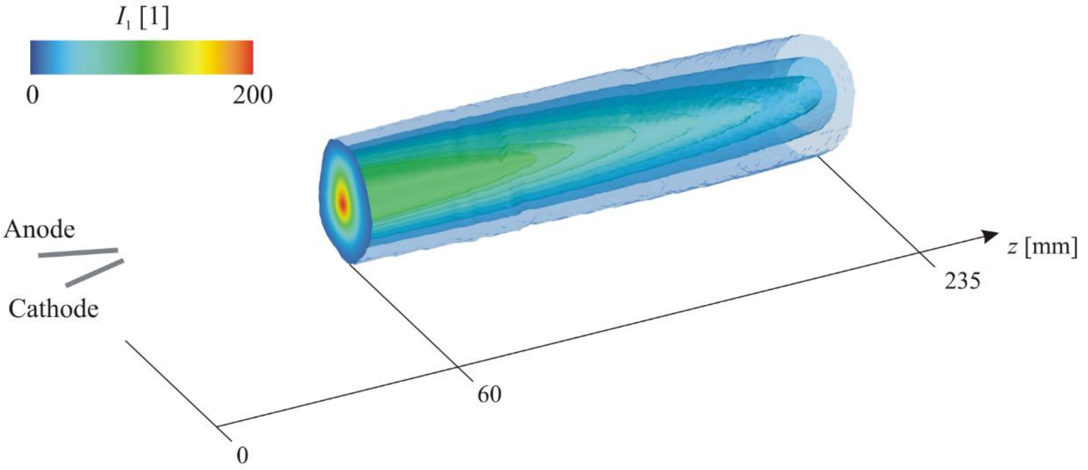

Figure 84: 3D intensity reconstruction measured with camera 1 (800 nm) at 28.9 V, 4 m/min, ***5 bar*** *and compressed air as atomizing gas.*

For the 3D intensity distributions presented in Figure 85 and Figure 86 the process was operated with 3 m/min and 5 m/min, respectively. The other parameters again were set to the base parameters. Comparing the results measured at 3 m/min, 4 m/min (see Figure 80) and 5 m/min it is noticeable that the form at $z = 60\ \mathrm{mm}$ does not significantly change. All in all it remains oval with a slightly downwards pronounced bulge. However, the expansion of the isosurfaces increases with increasing wire feed rate, what also becomes apparent on the rising maxima.

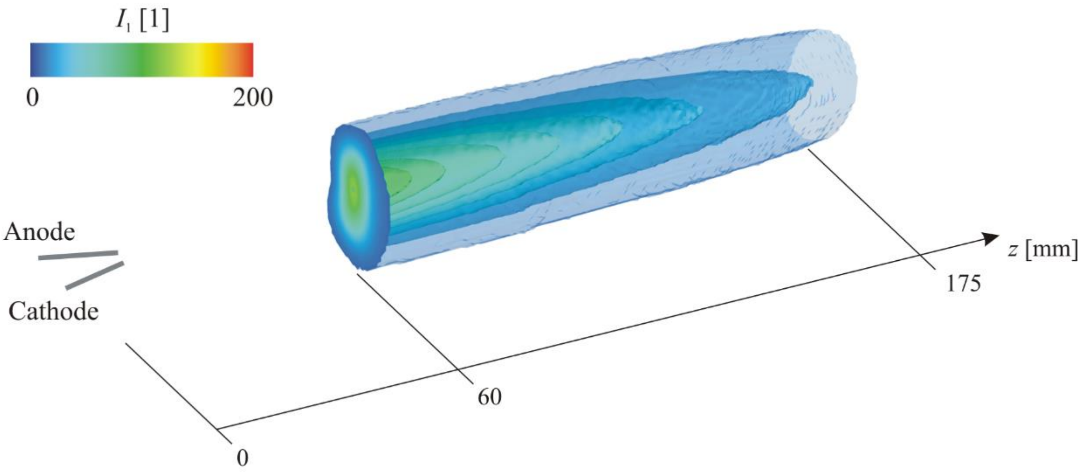

Figure 85: 3D intensity reconstruction measured with camera 1 (800 nm) at 28.9 V, ***3 m/min****,*
4 bar and compressed air as atomizing gas.

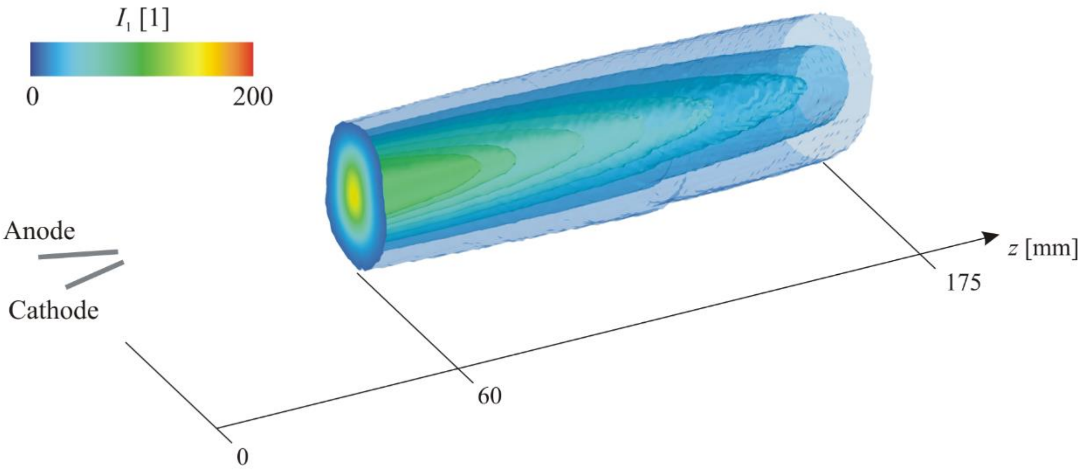

Figure 86: 3D intensity reconstruction measured with camera 1 (800 nm) at 28.9 V, ***5 m/min****,*
4 bar and compressed air as atomizing gas.

Using nitrogen instead of compressed air strongly affects the shape of the wire arc spray plume. In Figure 87 and Figure 88 the 3D reconstructions for nitrogen measured at a voltage of 33 V and 38.8 V are presented. Here the bulge is very pronounced and the extension of the isosurfaces in spraying direction is comparatively low. In contrary to compressed air, increasing the voltage causes a shift of the maximum at $z = 60\,\mathrm{mm}$ downwards. Comparing the reconstructions for compressed air and for nitrogen it has to be taken into a count that the maximum of the legend has been changed from 200 to 40.

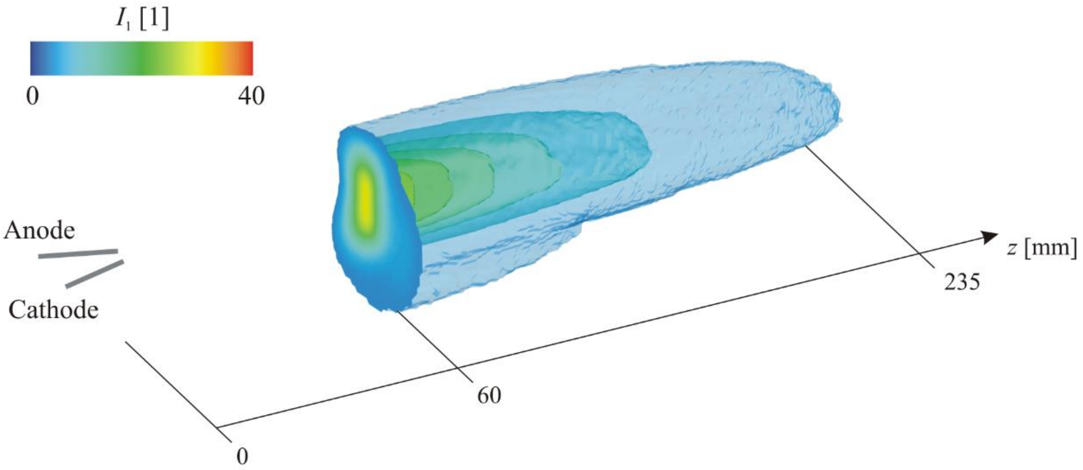

Figure 87: 3D intensity reconstruction measured with camera 1 (800 nm) at ***33 V****, 4 m/min, 4 bar and* ***nitrogen*** *as atomizing gas.*

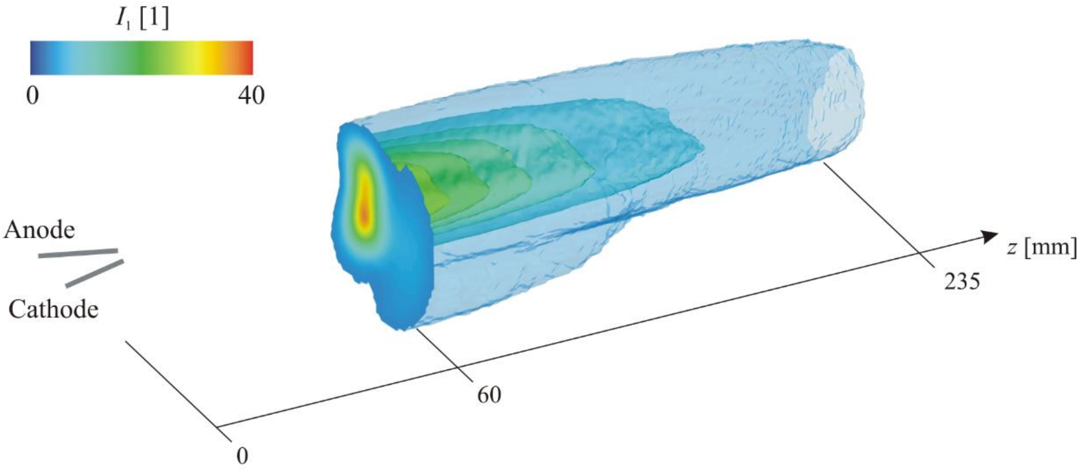

Figure 88: 3D intensity reconstruction measured with camera 1 (800 nm) at ***38.8 V****, 4 m/min, 4 bar and* ***nitrogen*** *as atomizing gas.*

Besides the 3D intensity reconstructions 3D temperature distributions are calculated. A typical temperature cross section measured in the *yz*-plane of the spray plume at $x = 0\ \mathrm{mm}$ for the base parameters is presented in Figure 89. Here the temperatures range from 2500 K to 2860 K, whereby the standard deviation is small. Due to these small temperature differences and the inhomogeneity of the distributions, the 3D presentation of the temperature reconstructions is not very informative. For these reasons only temperature cross sections in the *xy*-plane at $z = 70\ \mathrm{mm}$ are exemplarily shown. These 2D temperature images are in turn used in order to calculate the average particle temperatures along the spraying direction necessary for the material dependent emissivity determination.

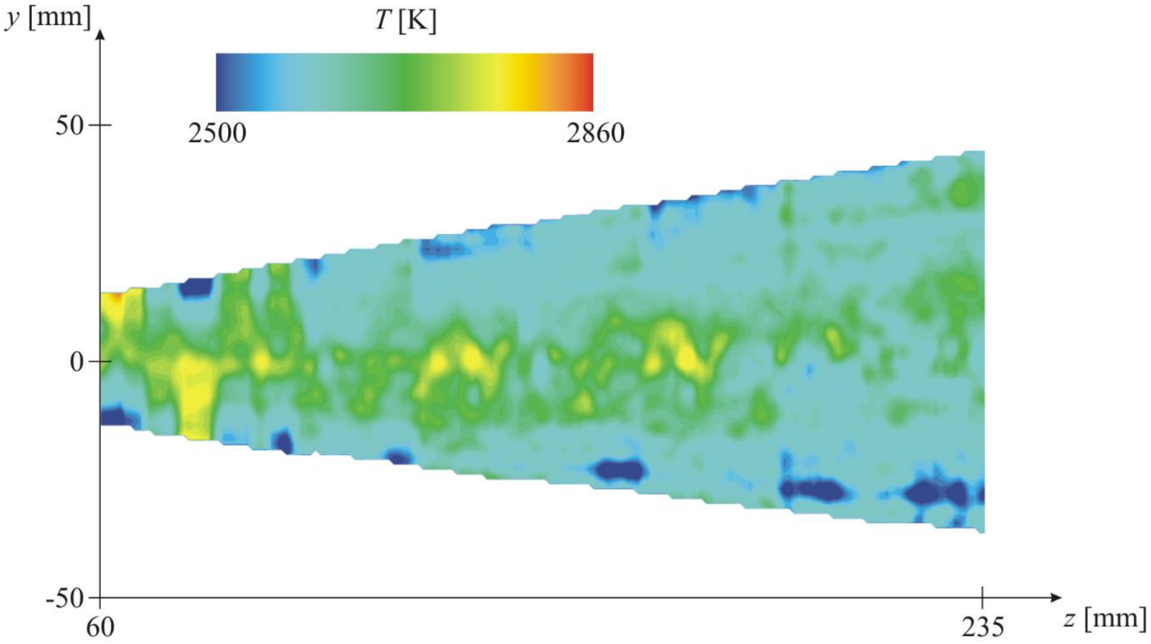

Figure 89: Temperature cross sections of the spray plume measured in the yz-plane at $x = 0\ mm$ *for the base parameters 28.9 V, 4m/min, 4 bar and CA as gas.*

The temperature cross sections for 28.9 V, 33 V and 38.8 V are presented in Figure 90. It can be seen that increasing the voltage leads to an increase of the particle temperature. The average temperature is 2663 K for a voltage of 28.9 V, 2736 K for a voltage of 33 V and 2821 K for a voltage of 38.8 V.

Figure 91 shows the 2D temperature images at $z = 70\ \mathrm{mm}$ for a changing pressure and the base parameters (4 m/min, 4 bar and CA). To highlight the influence of the changed parameter on the temperature, different temperature regions for the legend are chosen. Thus it becomes clear that with increasing pressure the temperatures decrease, whereby the difference between the average temperatures at 3 bar ($T_{avg} = 2676\ \mathrm{K}$) and 5 bar ($T_{avg} = 2631\ \mathrm{K}$) is rather low.

As the images in Figure 92 show the particle temperatures also decrease with increasing wire feed rate. With an average temperature of 2703 K at 3 m/min and an average temperature of 2598 K the effect again is very marked.

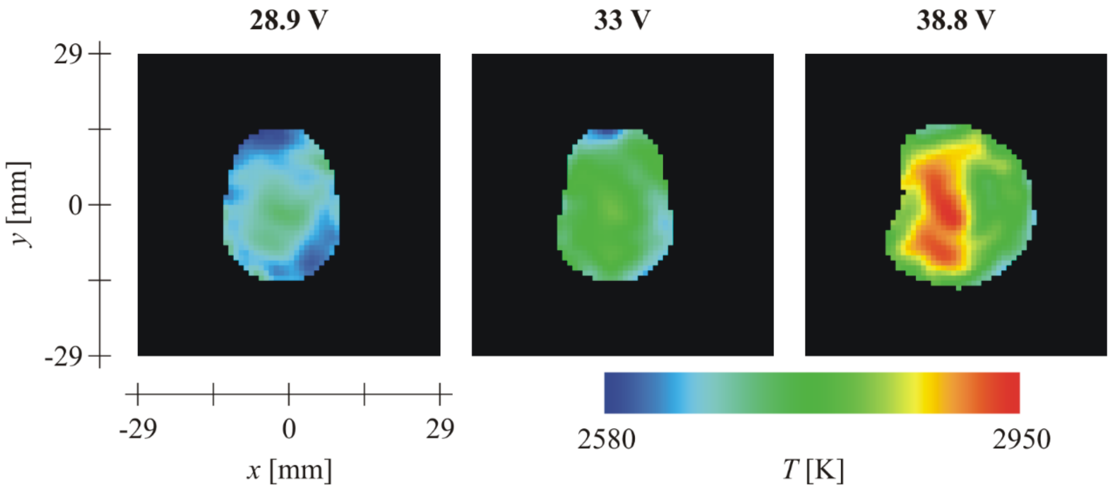

Figure 90: Temperature cross sections of the spray plume measured in the xy-plane at $z = 70$ mm for a changing voltage and the base parameters 4m/min, 4 bar and CA as gas.

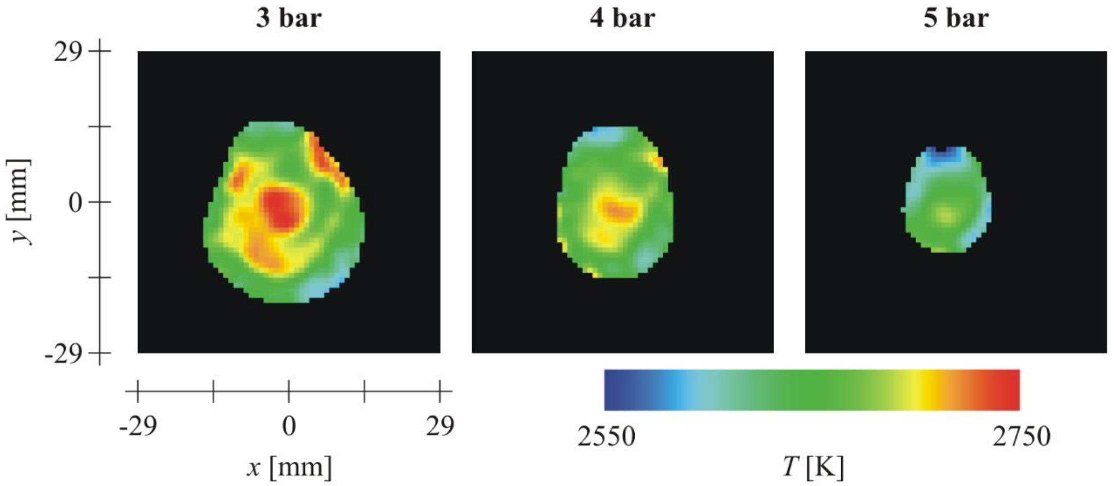

Figure 91: Temperature cross sections of the spray plume measured in the xy-plane at $z = 70$ mm for a changing pressure and the base parameters 28.9 V, 4m/min and CA as gas.

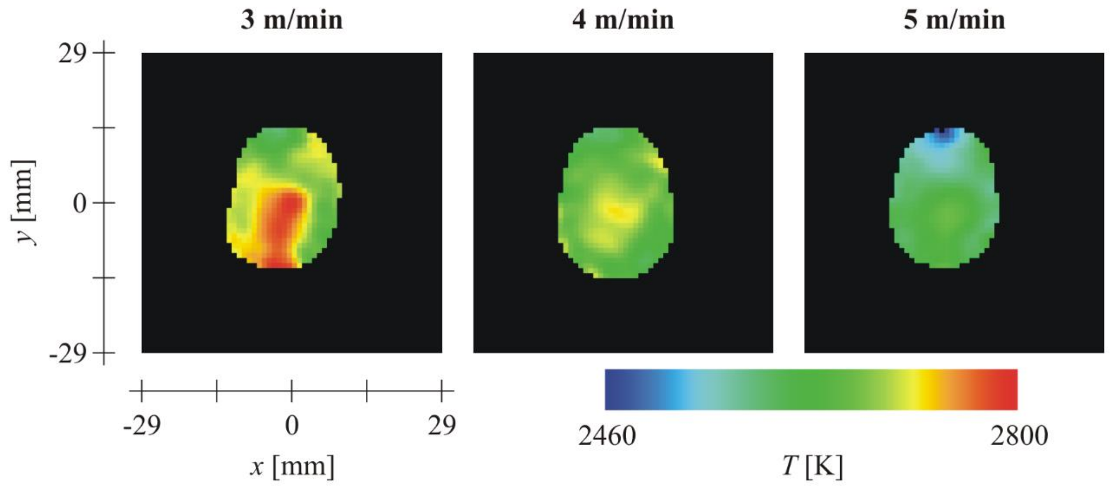

Figure 92: Temperature cross sections of the spray plume measured in the xy-plane at $z = 70$ mm for a changing feed rate and the base parameters 29.9 V, 4 bar and CA as gas.

Using nitrogen as atomizing gas instead of compressed air leads to lower particle temperatures. The average temperatures of the distributions presented in Figure 93 are 2592 K for 33 V and 2722 K for 38.8 V. The trend of increasing particle temperatures with increasing voltage remains unchanged using nitrogen.

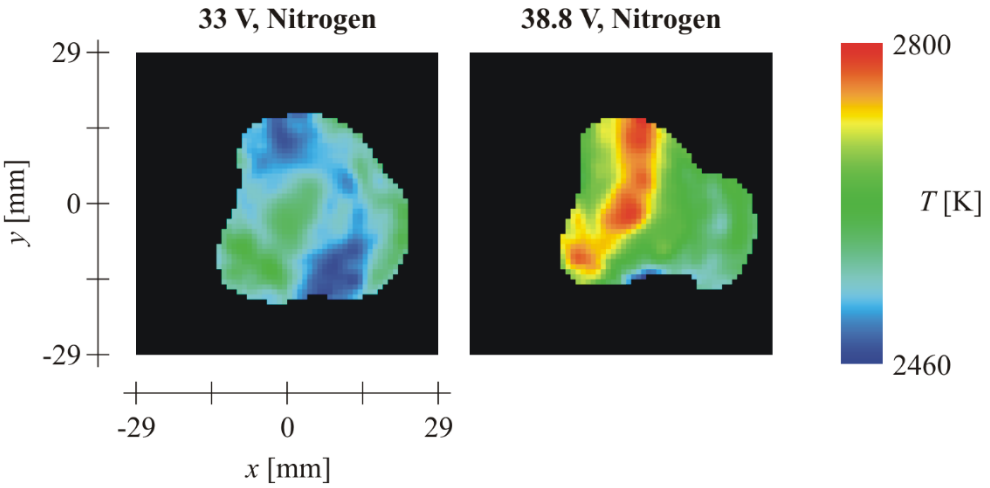

Figure 93: Temperature cross sections measured in the xy-plane at $z = 70$ *mm for nitrogen and a changing voltage. The feed rate was set to 4 m/min, the pressure to 4 bar.*

As already mentioned in Chapter 4.2, for the calculation of the material dependent emissivities some assumptions have to be made. First of all, it has to be assumed that all particles in the whole measurement volume have the same particle size and are consequently not further atomized. The used particle radii r_P measured with the PSI in the middle of the spray plume at $z = 70\ \mathrm{mm}$ and the from this calculated numbers of particles N (see Equation 4.4) are listed in Table 12.

Table 12: Particle radii for the different parameter sets measured using the PSI and the corresponding numbers of particles (see Equation 4.4) necessary for the emissivity calculations. The wire radius for all measurements was 0.8 mm.

Parameter set	v_w [m/min]	t_{exp} [s]	r_P [µm]	N
28.9 V, 4 m/min, 4 bar, CA	4	3.5	22.0	18410455
33 V, 4 m/min, 4 bar, CA	4	3.5	22.8	18410455
38.8 V, 4 m/min, 4 bar, CA	4	3.5	25.1	14336000
28.9 V, 4 m/min, 3 bar, CA	4	3.5	22.4	21036814
28.9 V, 4 m/min, 5 bar, CA	4	3.5	20.3	28000000
28.9 V, 3 m/min, 4 bar, CA	3	3.5	22.2	15777611
28.9 V, 5 m/min, 4 bar, CA	5	3.5	24.7	17920000
33 V, 4 m/min, 4 bar, Nitrogen	4	2.4	22.6	12624312

The second assumption is that the velocity of the particles only depends on the *z*-coordinate and is constant in the whole *xy*-plane. The particle velocity for a single cross section can finally be approximated using the polynomial fits of third order determined in Chapter 6.4.

Furthermore, the total intensities of a cross section and the average temperatures have to be calculated using the 3D intensity and temperature distributions. Since the tomographic two-color-pyrometry measurements are applied at three overlapping positions (see Chapter 3.3.1, Figure 39) the results initially have to be merged. Figure 94 for example shows the average temperatures measured for the base parameters at the three overlapping measurement positions that are shown in Figure 39. The single values along the *z*-axis are determined by calculating the mean values of the corresponding 2D temperature distributions. Examples for such temperature images can be seen in Figure 89 to Figure 93. To obtain a continuous temperature curve, the mean values in the overlapping regions are calculated and the resulting curve is smoothed over 20 neighboring values (see Figure 95). The same procedure is applied to the total intensities, which are determined through summing over all intensities of a cross section. The example in Figure 96 shows the total intensities measured with camera 1 at the three overlapping positions. The parameters in turn were set to the base parameters 28.9 V, 4 m/min, 4 bar and compressed air. The resulting smoothed continuous intensity curve is illustrated in Figure 97.

Finally the smoothed average intensity curves, the smoothed temperature curves, the particle velocities measured with the DPV and the particle radii measured with the PSI are used in order to calculate the material dependent emissivities by means of Equation 4.6.

For reasons of clarity, the raw data of all other parameter sets are not shown. In the following only the average temperature and emissivity curves calculated using the respective three measurements are presented, whereby the error bars represent the standard deviation.

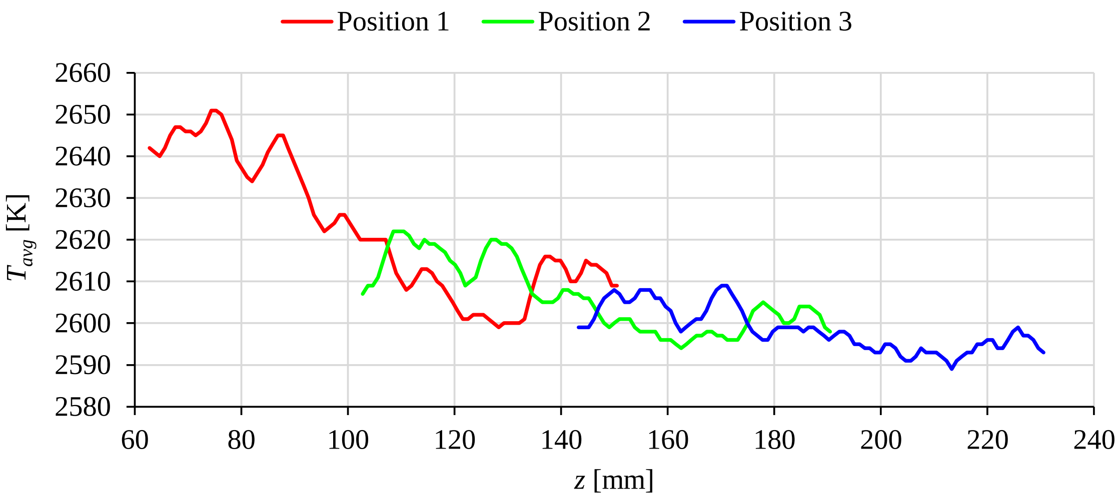

Figure 94: Average particle temperatures measured at three overlapping positions (see Figure 39). The parameters were set to the base parameters 28.9 V, 4 m/min, 4 bar and CA.

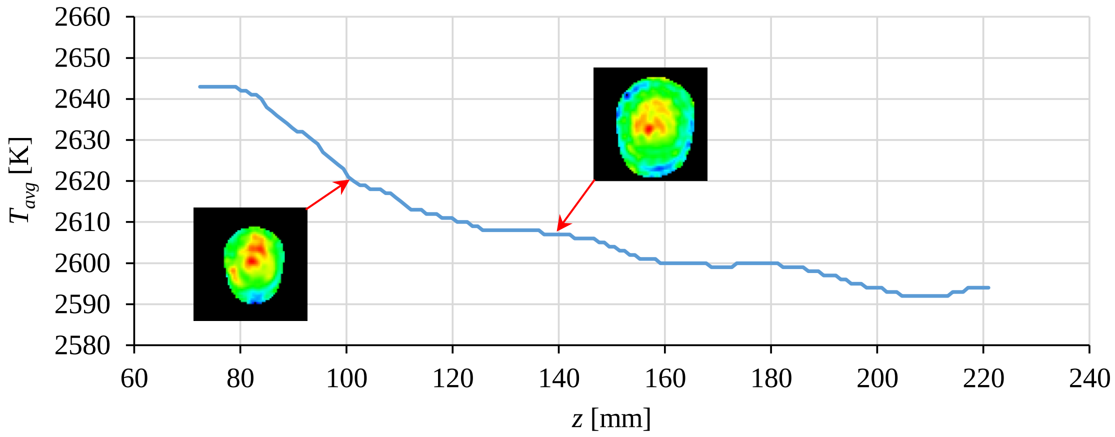

Figure 95: Average particle temperatures determined by calculating the mean values in the overlapping regions of the curves in Figure 94 and subsequent smoothing over 20 values.

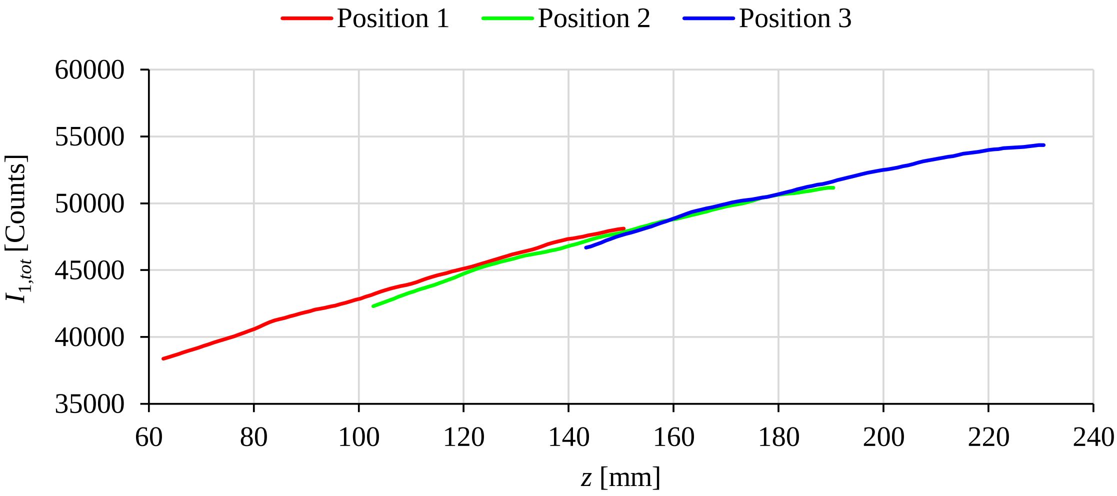

Figure 96: Total intensities measured with camera 1 at three overlapping positions (see Figure 39). The parameters were set to the base parameters 28.9 V, 4 m/min, 4 bar and CA.

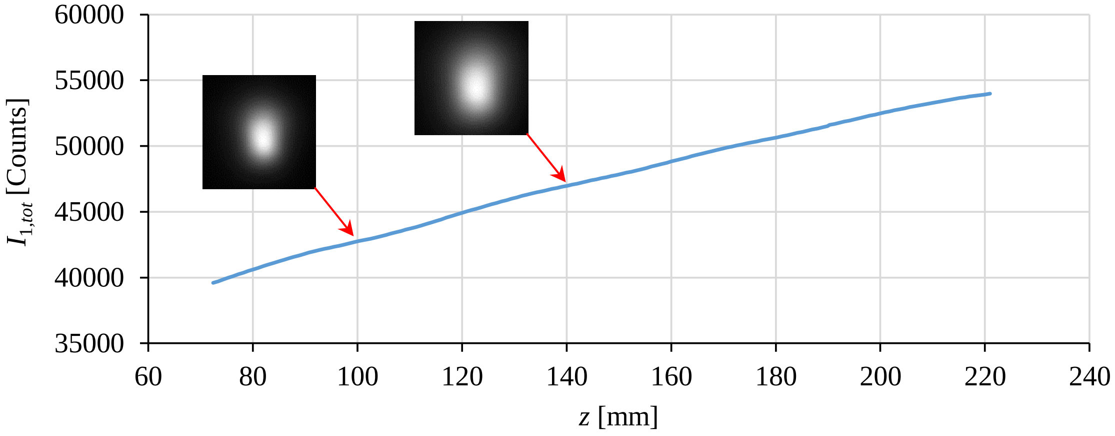

Figure 97: Total intensities determined by calculating the mean values in the overlapping regions of the curves in Figure 96 and subsequent smoothing over 20 values.

The diagram in Figure 98 shows the average temperature curves dependent on the *z*-coordinate for compressed air and three different voltages. The remaining process parameters were set to 4 m/min and 4 bar. Initially at $z = 70\ \mathrm{mm}$ the temperature for 28.9 V is 2650 K. Along the observed distance it decreases by 50 K. The average temperatures measured for 33 V are greater than the temperatures measured at 28.9 V, at the beginning by 75 K at the end by 50 K. The highest temperatures are reached for 38.8 V. Here the temperatures decrease from approximately 2810 K to approximately 2660 K. To conclude, it can be noted that on the one hand the average temperatures decrease with increasing distance to the spray gun and on the other hand the temperatures increase with increasing process voltage.

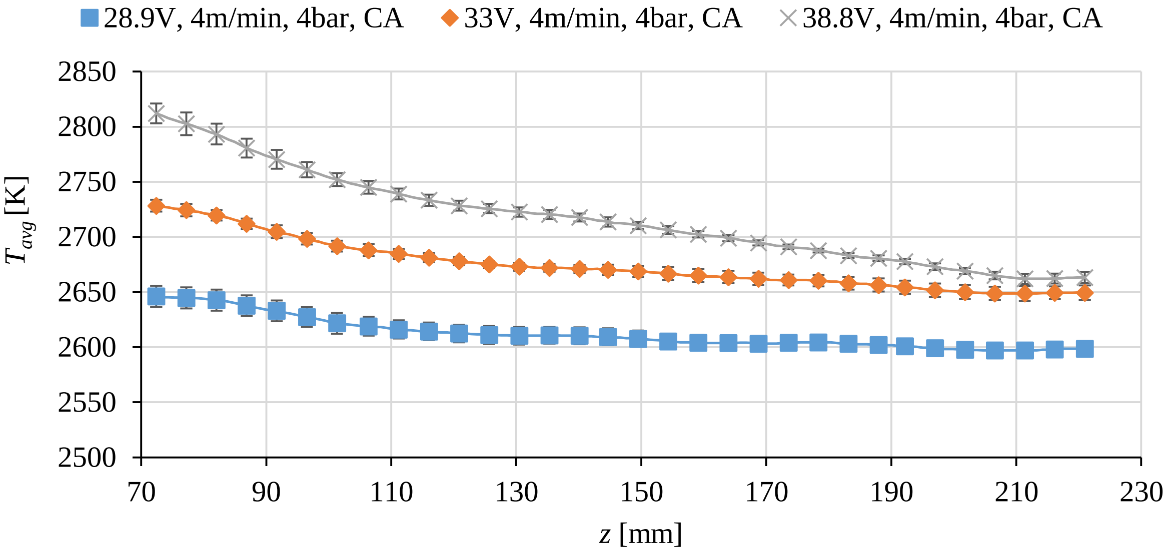

Figure 98: Average particle temperatures dependent on the z-coordinate for compressed air and a changing voltage. The remaining process parameters were set to 4 m/min and 4 bar.

The influence of the atomizing gas pressure is illustrated by means of the diagram in Figure 99. At the first measurement point the difference between the average temperatures is approximately 25 K, whereby increasing the pressure leads to decreasing temperatures. Furthermore, all three temperature curves drop and are finally almost equal at $z = 225\ \mathrm{mm}$.

The average temperature curves measured for a wire feed rate of 3 m/min, 4 m/min and 5 m/min are presented in Figure 100. Besides compressed air the base parameters were used in order to operate the wire arc spray process. As it can be seen, with increasing wire feed rate the average particle temperature decreases. All three curves again decline along the spraying direction, whereby the temperature drop from ~2710 K to ~2640 K measured for 3 m/min is greatest.

Figure 101 shows the average temperature curves measured when operating the process with nitrogen instead of compressed air. Since the measurements using nitrogen could only be performed one times, no error bars are included. It becomes clear that the temperatures for nitrogen are lower than for compressed air (see Figure 98). At 33 V the difference is approximately 150 K, at 38.8 V it is approximately 85 K. The relation between the temperature and the voltage remains, just like the relation between the temperature and the distance to the spray gun exit.

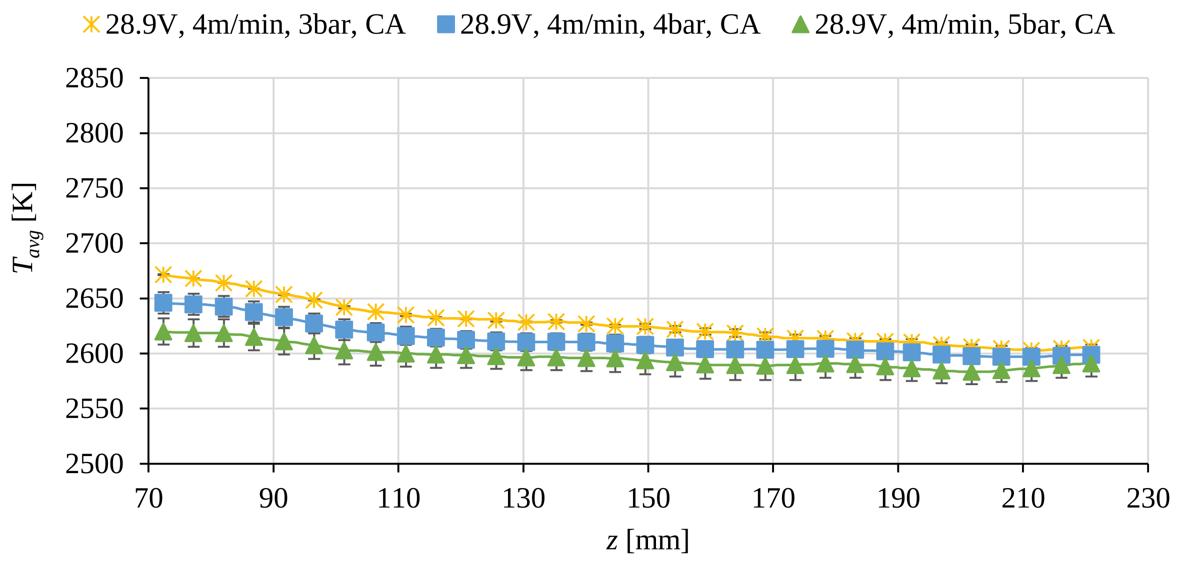

Figure 99: Average particle temperatures dependent on the z-coordinate for compressed air and a changing pressure. The remaining process parameters were set to 28.9 V and 4 m/min.

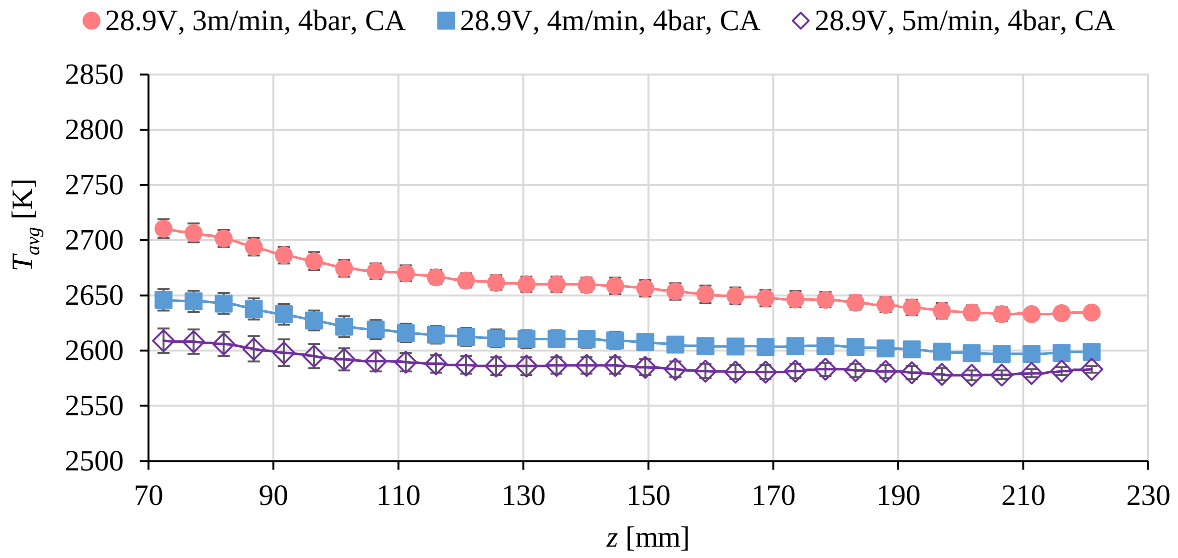

Figure 100: Average particle temperatures dependent on the z-coordinate for compressed air and a changing feed rate. The remaining process parameters were set to 28.9 V and 4 bar.

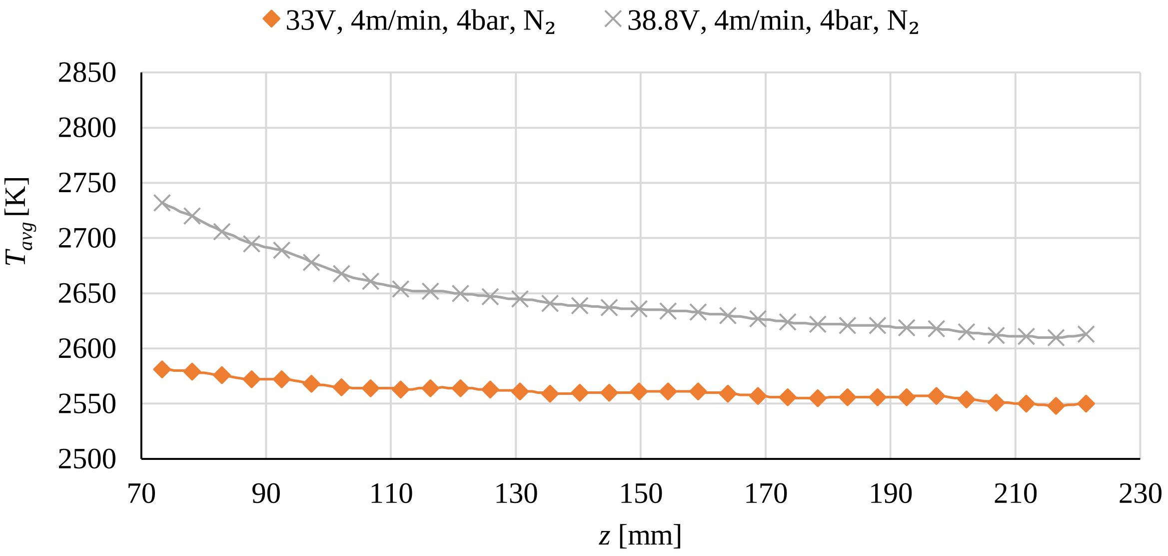

Figure 101: Average particle temperatures dependent on the z-coordinate for nitrogen and a changing voltage. The remaining process parameters were set to 4 m/min and 4 bar.

Finally the emissivities along the spraying direction can be calculated using the results presented in Chapter 6.4 and Chapter 6.5. The emissivity curves do not include error bars, since the standard deviations of the tomographic and pyrometry results are too small to be seen. The diagram in Figure 102 shows the emissivities for compressed air and a changing voltage. The remaining parameters were set to the standard parameters 4 m/min and 4 bar. Independent of the voltage, the emissivities increase from $z = 70$ mm to $z = 170$ mm by approximately 0.8 and subsequently remain almost constant. Furthermore the emissivities measured for 28.9 V are slightly higher than the emissivities measured at 33 V and 38.8 V.

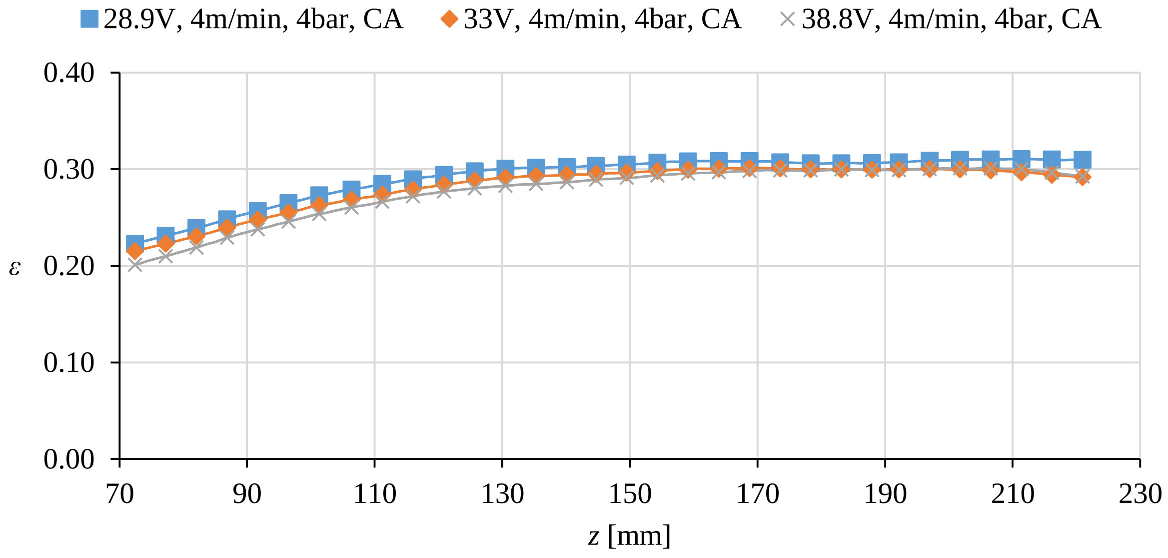

Figure 102: Average particle emissivities dependent on the z-coordinate for compressed air and a changing voltage. The remaining process parameters were set to 4 m/min and 4 bar.

The influence of the pressure on the emissivities is presented by means of the diagram in Figure 103. The process again was operated using the base parameters. It can be seen, that the trends of the calculated emissivities are comparable with the results measured for a changing voltage, whereby the rise for 5 bar is more linear. In addition the emissivities measured for 5 bar are smaller than the emissivities measured for 3 bar and 4 bar.

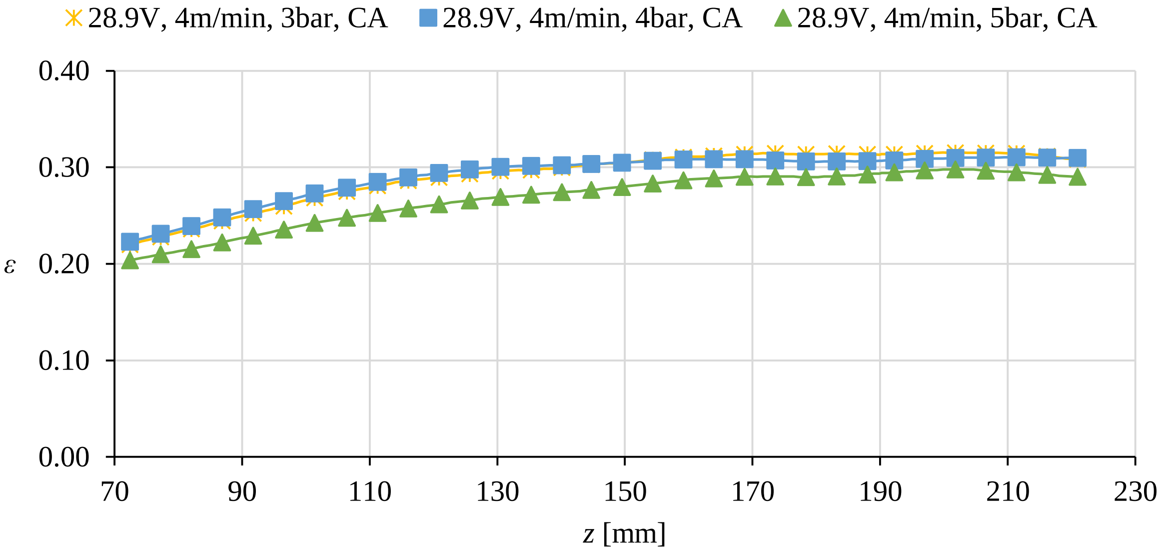

Figure 103: Average particle emissivities dependent on the z-coordinate for compressed air and a changing pressure. The remaining process parameters were set to 28.9 V and 4 m/min.

As the diagram in Figure 104 indicates, changing the feed rate obviously does not significantly affect the particle emissivities. Again a rise of approximately 0.8 can be observed, whereby the increase in the first two thirds is substantially higher than in the last third.

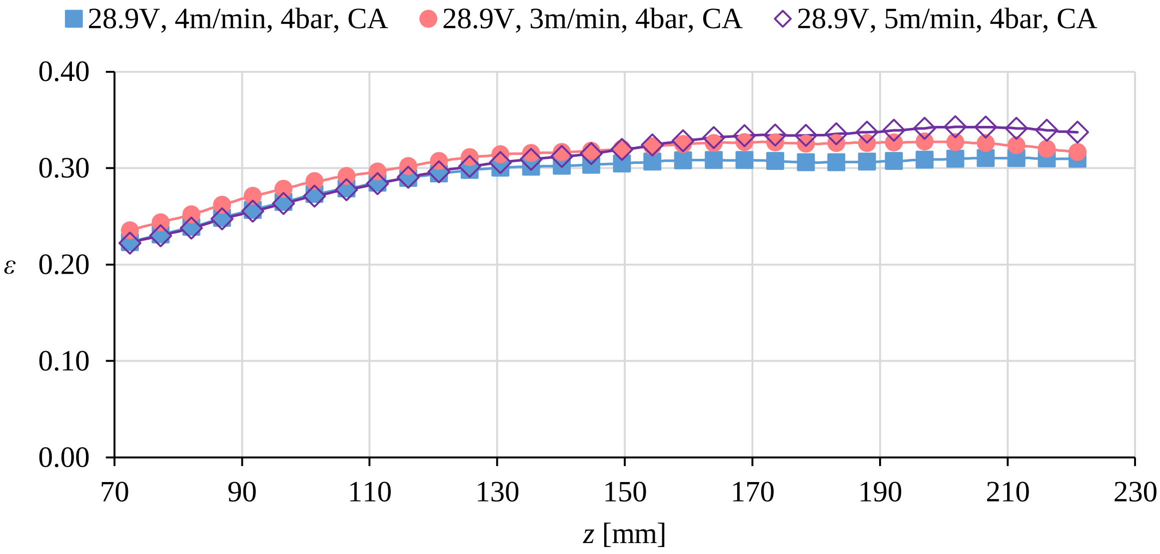

Figure 104: Average particle emissivities dependent on the z coordinate for compressed air and a changing feed rate. The remaining process parameters were set to 28.9 V and 4 bar.

The emissivities, measured using nitrogen as atomizing gas, are illustrated in Figure 105. Due to the missing particle sizes for 38.8 V, the emissivity calculations could only be performed for a voltage of 33 V, a feed rate of 4 m/min and a pressure of 4 bar. Comparing the emissivities for compressed air measured at 33 V (see Figure 102) with the trace in Figure 105, it is noticeable that the values for nitrogen are half the size than the values for compressed air. Furthermore the emissivities for nitrogen only increase by 0.3 along the observed distance, whereby the rise is nearly linear.

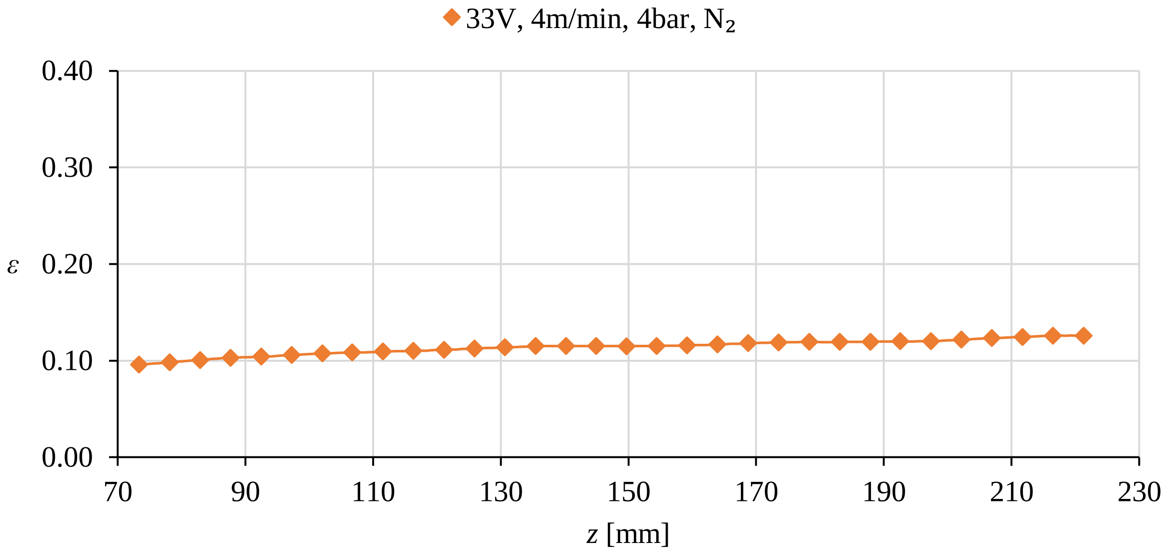

Figure 105: Average particle emissivities dependent on the z-coordinate for nitrogen, 33 V, 4 m/min and 4 bar.

Finally it can be concluded that the emissivities for all parameters increase with increasing distance to the wire tips. The only significant emissivity difference concerning the process parameter variation could be determined using nitrogen instead of compressed air as atomizing gas. A further discussion of the measured results and the derived physical quantities is performed in the next chapter.

7 Discussion

To be able to estimate possible error sources of the in-flight oxidation determination all single measurement results that contribute to the model have to be verified. According to Equation 4.6 the particle sizes, the particle velocities and the particle temperatures are among other things necessary for the calculation of the emissivity. Furthermore the tomographic two-color-pyrometry results including the temperature and emissivity measurements are discussed.

7.1 Particle size and velocity measurements

The particle sizes are measured by means of PSI (see Chapter 5.3 and Chapter 6.4), whereby the measurement volume is located in the middle of the spray plume 70 mm in front of the wire tips. Since it is difficult to find values for the particle size in literature that are measured using the same nozzle geometry, the same feedstock and the same process parameters, the accuracy of the PSI results can only qualitatively be evaluated. First of all the influence of the process voltage on the particle size is discussed. As shown in Figure 66 and listed in Table 12, for 28.9 V a mean particle radius of 22 µm and for 33 V a mean particle radius of 22.8 µm was measured, whereas for 38.8 V the radius increases to 25 µm. According to Kelkar et al. [148] the size of droplets detached from the cathode depends on the electromagnetic pinch effect (first term on the left hand side of Equation 7.1), the aerodynamic drag (second term), the weight force (third term) and the surface tension (right hand side).

$$\frac{\mu_0}{4\pi}\left(\frac{a}{b}\right)^4 I^2 + \frac{1}{2}C_d\rho_g v_{rel}^2 A_{drop}\cos\left(\frac{\theta}{2}\right) + \frac{4}{3}\pi a^3\rho g = \pi a\sigma \tag{7.1}$$

a: radius of the spherical droplet
b: radius of the wire
C_d: drag coefficient
ρ_g, ρ: density of the atomizing gas and the wire, respectively
v_{rel}: relative velocity between the gas and the droplet
A_{drop}: cross section area of the droplet
θ: angle between the wires
σ: surface tension

Because on the anode in contrast to the cathode long non current-carrying sheets are formed, the size of the anode particles is only influenced by the gas flow and the surface tension (Equation 7.2).

$$\frac{1}{2}C_d\rho_g v_{rel}^2 A_{drop} = \sigma l_{drop} \tag{7.2}$$

Since with increasing voltage the heat input (see Figure 59) and consequently the particle temperatures (see Figure 98) increase, the temperature dependent surface tension that keeps liquid material attached decreases [149]. Furthermore, the current rises with increasing voltage leading to an increase of the electromagnetic force. To conclude, these two effects should cause smaller particles and consequently, the increase of the particle radius from 22 µm for 28.9 V to 25 µm for 38.8 V can only be explained with changed flow conditions. How the typical high speed images of the wire arc spray process illustrated in Figure 106 show, there are significant detachment differences between operating the process with 28.9 V and operating the process with 38.8 V. At 28.9 V the particle replacement is concentrated between the two tips, whereas the replacement at 38.8 V is shifted outwards. Since the flow velocity probably decreases with increasing distance to the spraying axis, the atomization of the detached particles decreases for higher voltages and consequently the discrepancy between Kelkar's model and the measured particle sizes can be explained.

The influence of the pressure on the particle size seems to be easier to explain. Using again the model of Kelkar et al., it is obvious that with increasing gas flow and consistent other process parameters the particle size decreases. This trend was for example measured by Liao et al. [36] using copper as anode wire and steel as cathode wire and vice versa in order to be able to separate the collected anode and cathode particles with the help of a magnet. The size distributions, determined using a particle size analyzer, show both for steel particles detached from the anode and the steel particles detached from the cathode a decreasing particle size for an increasing pressure. For 2.8 bar they measured a mean anode particle diameter of 52 µm and a mean cathode particle diameter of 44 µm, for a pressure of 4.9 bar 39 µm and 28 µm The other process parameters used by Liao (200 A, 30 V) are comparable to the base parameters. In this work for 3 bar an average particle diameter of 44.8 µm was determined, for 4 bar a diameter of 44 µm and for 5 bar a mean particle diameter of 40.6 µm. Consequently the trend of decreasing particle sizes with increasing pressure could be confirmed.

In the case of a changing wire feed rate, the different influences on the particle size are more complex to explain. On the one hand the flow keeps constant and on the other hand the amount of material to be fused, the current and the voltage (see Appendix A.4) change with changing

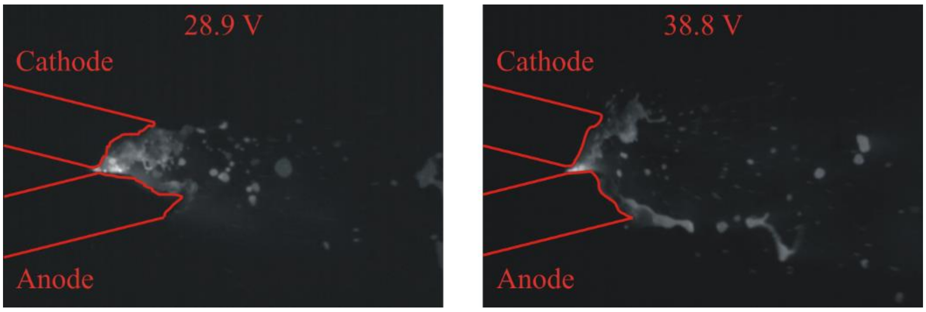

Figure 106: High speed images of the wire arc spray process acquired for 28.9 V and 38.8 V. The other parameters were set to the base parameters and compressed air was used as gas.

feed rate. Based on the velocity measurements presented in Figure 73, the mean particle radius for 4 bar should be smaller than the radii measured for 3 bar and 5 bar, whereby the values for 3 bar in turn should be between 4 bar and 5 bar. Looking at diagram d) in Figure 66 this trend can be confirmed, although the difference between the mean particle radii measured for 3 m/min and 4 m/min might be too low.

For the usage of nitrogen as gas, a voltage of 33 V, a feed rate of 4 m/min and a pressure of 4 bar the measured mean particle radius is 22.6 µm. This value is almost equal to the radius measured using compressed air and the same parameters (22.8 µm). Since nitrogen causes a higher surface tension than oxygen [150] the detached particles should be larger. Another indicator therefore are again the velocity measurements (Figure 74). For a voltage of 33 V the velocities using nitrogen are approximately 10 m/s lower than the velocities measured using compressed air. The too small average particle radius for nitrogen may be caused by the image processing steps applied to the PSI images. Since it is more likely that great particles touch the fringe of the region of interest and therefore are ignored, they are underrepresented what in turn is more pronounced for using nitrogen as atomizing gas.

In summary, the mean particle radii for all investigated parameters are between 20.3 µm and 25.1 µm (compare Table 12). Due to this small variation and the all in all accordance of the velocity trends and the particle sizes trends, the measured mean particle radii are suitable for the emissivity calculations.

The measured particle velocities again can only qualitatively be evaluated, because no particle velocity investigations using the same arc spray gun and consequently the same nozzle configuration could be found in literature. Comparable measurements are performed by Newbery et al. [33] using laser two-focus velocimetry (L2F). Results of their work are presented in Figure 107. The velocities were measured in the middle of the spray plume at a voltage of 34 V, a feed rate of 1 g/s (≙ 3.8 m/min) and a pressure of 2.8 bar. As atomizing gas compressed air was used. Since the influence of the voltage on the particle velocity is less than the influence of the pressure, the most comparable parameters of this work are 28.9 V, 4 m/min and 3 bar (also presented in Figure 107). The velocities measured by Newbery slightly increase from 104 m/s at 70 mm to 109 m/s at 120 mm and subsequently decrease to 103 m/s at 200 mm. Responsible for the lower velocities may be the higher voltage and the lower pressure. The increasing and subsequently decreasing particle velocitiy along the spraying direction is also observed by Hale et al. [32] for spraying aluminum and Tillmann et al. [151] for spraying massive steel wires. The simulations and the measurements of Prehm [152] show that the gas velocity steadily declines with increasing distance to the wire tips and consequently the detached particles are accelerated until they reach the gas velocity and are subsequently slowed down.

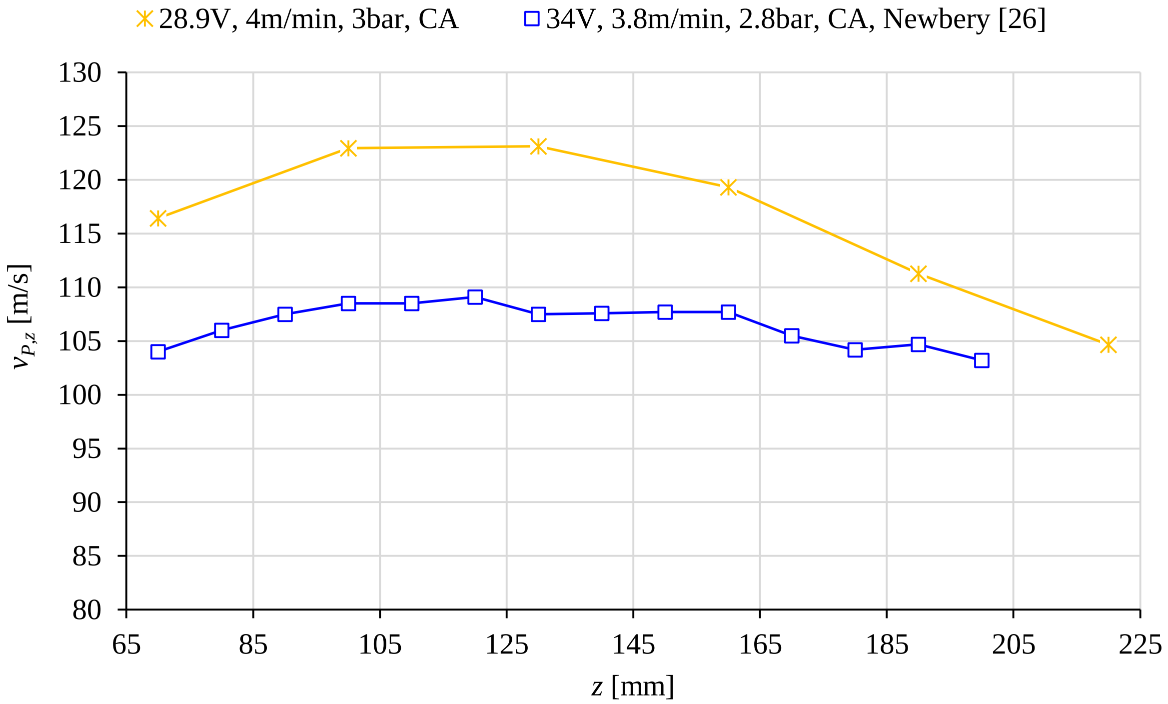

Figure 107: Particle velocities depending on z measured in the middle of spray plume. The yellow curve shows results of this work (28.9 V, 4 m/min, 3 bar, CA). The blue curve shows results measured by Newbery et al. [33] *using L2F (34 V, 3.8 m/min, 2.8 bar, CA).*

The proportional relation between the gas pressure and the particle velocity measured in this work is also observed by Newbery et al. [33], Gedzevicius et al. [153] and Hale et al. [32]. Furthermore, according to [154] small particles better track the flow than great particles and consequently the particle velocities and the particle sizes are linked indirect proportional. The velocity trends for a changing voltage and a changing wire feed rate correlate with the measured particle sizes, except at using nitrogen instead of compressed air.

7.2 Tomographic two-color-pyrometry measurements

Since the tomographic two-color-pyrometry measurement technique is an innovative approach that is not known from literature so far, the discussion of the feasibility is very important. To ensure that tomographic measurements can be applied to the wire arc spray plume, different conditions have to be fulfilled. As already mentioned in Chapter 3.1 the observed measurement object has to be luminous and optically thin in order to be able to do emission tomography. The requirement of a luminous object that can be observed with a normal CCD-camera is given, since the atomized feedstock particles are very hot (>2400 K) and therefore the emitted thermal radiation is according to Wien's displacement law (see Chapter 2.1) in the visible spectral region. In contrast the property “optically thin” is not fulfilled at first glance, because the particles are opaque and consequently only the radiation emitted from the surface can be detected. Remedy for this problem is provided by not observing single particles but an ensemble of particles. By integrating over a long time (>1 s) it should be guaranteed that a sufficient number of particles flies through every point of the measurement volume so that the acquired smooth 2D images reflect statistical particle distributions. The preconditions for this are a stationary and an optically thin spray plume, whereby the property optically thin ensures that the radiation of almost all particles receives the detector without being shaded by other particles. The stability of the wire arc spray process can be proved by the voltage and current measurements. As Figure 122 to Figure 129 in the Appendix A.4 show, the voltage and current traces do not show any short circuits or other long-lasting disturbances. All current and voltage fluctuations take place in a period of less than 5 ms and are consequently averaged over the integration time. The optical thickness of the spray plume is determined through using the LDA, PSI and DPV measurements as input for the model developed in Chapter 3.2. Since the calculated optical thickness for all used parameters is below 0.05 (see Chapter 6.5), the condition optically thin ($\tau \ll 1$ [119, 120]) is fulfilled in any case.

Besides this theoretical considerations, the 3D reconstructions itself are evidence for an optically thin spray plume, since they do not show any artifacts caused by too high optical thickness. Looking for example at the computerized tomography (CT) used in medicine, an object that is not optically thin for the X-Ray radiation is given by metal. If there is metal in the body of a patient e.g. in the form of solid amalgam tooth fillings, so called strike artifacts can be seen in the reconstructions [116]. An example for such an erroneous CT image is presented on the left side of Figure 108. For comparison on the right side a reconstructed cross section of the spray plume that does not show any artifacts is illustrated.

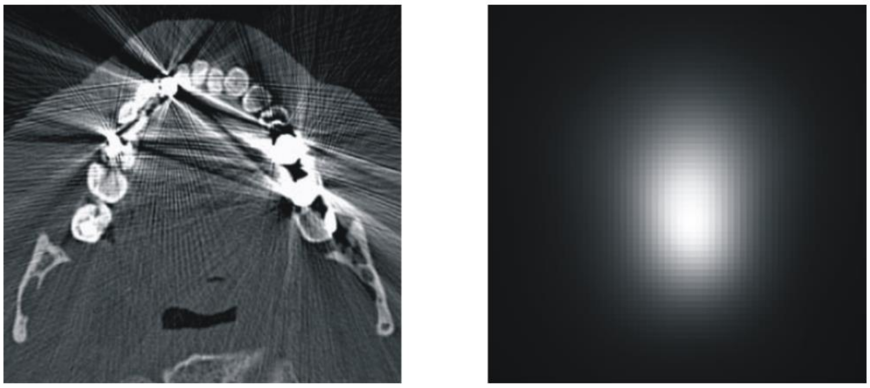

Figure 108: Left: CT image of the tooth region showing strike artifacts caused by solid amalgam fillings (adopted from [116]*). Right: cross section of the reconstructed spray plume without any artifacts.*

To conclude, the wire arc spray plume is suitable for tomographic investigations, whereby it has to be noted that only the radiation emitted from the surface can be reconstructed and hence only surface temperatures can be determined.

The structure of the 3D intensity reconstructions (Figure 80 to Figure 88) presented in the previous chapter depends according to Equation 4.3 on the particle size, velocity rate, temperature and emissivity. Because of the interdependence of all these different parameters the 3D reconstructions only allow qualitative conclusions. Thus for example the intensity distributions for a changing pressure show a strong constriction of the spray plume with increasing pressure, which in turn is confirmed by the LDA results presented in Figure 68. Consequently, the intensity distributions for a changing pressure seem to be strongly connected to the spatial resolved particle rates. Also in the case of a changing wire feed rate the reconstructed intensities seem to be proportional to the particle rate, since both the rates measured with the LDA (see Figure 69) and the intensities measured with the tomography strongly increase with increasing feed rate. Finally it can be stated that the tomographic 3D intensity reconstruction is a useful tool in order to visualize the expansion of the spray plume.

More interesting is the processing of the obtained intensity data. By voxel vice dividing of the two intensity distributions measured with the two-color-pyrometry and comparing the results with calculated quotients, spatial resolved temperature distributions can be determined (see Chapter 3.3.2). As already mentioned, the 3D visualization of the temperature distributions is not very informative, because the deviation of the temperatures is low and the distributions are not very homogenous (compare Figure 89). However, the cross sections in the *xy*-plane are suitable to show the general influence of the different parameters on the particle temperature. Furthermore, the cross sections are used in order to calculate the average temperatures along the spraying direction that in turn are necessary for the emissivity calculation.

Looking at the average temperatures determined for a changing voltage (see Figure 98), it is obvious that increasing the voltage leads to an increasing particle temperature. The reason for this behavior is the heat input that according to Figure 59 a) declines proportional to the rising voltage. After the heated and molten particles are detached they are atomized and are exposed to various influences. On the one hand they are heated due to exothermic oxidation [33, 72] and on the other hand they are cooled down due to convection and radiation losses [32, 34]. As the temperature traces for all three voltages decrease with increasing distance to the wire tips, the heat loses due to convection and radiation generally seem to be higher than the heating due to oxidation. It can be noted that the temperature drop for high initial temperatures is greater than for low temperatures. Responsible therefore may be the higher heat transfer caused by the higher difference temperature.

The influence of the gas pressure on the average particle temperature is according to Figure 99 not significant. Increasing the pressure from 3 bar to 5 bar causes a temperature difference of approximately 50 K at a distance of 70 mm. The reason for this temperature difference may be on the one hand the decreasing gas temperatures for an increasing pressure and on the other hand the decreasing particle sizes for an increasing pressure leading to a larger effective surface and consequently to more heat losses due to radiation an convection. The heat input for the three investigated pressures is according to Figure 59 c) almost constant. A small temperature drop along the spraying direction can be observed again.

To explain the influence of the wire feed rate on the average particle temperature again the calculated heat inputs per mass can be used. Figure 59 d) shows an indirect proportional relation between the feed rate and the heat input. This connection can also be found at the measured average temperatures (see Figure 100).

Using nitrogen instead of compressed air strongly affects the average particle temperatures. Comparing the traces for nitrogen in Figure 101 with the traces for compressed air in Figure 98, it can be seen that the temperatures using nitrogen are ~150 K lower for 33 V and ~80 K lower for 38.8 V. A possible explanation therefore are, besides the lower oxidation using nitrogen [33, 72], the differences in heat input. The results presented in Figure 59 show that the heat input for nitrogen at 33 V is approximately 10 % lower than the heat input for compressed air at 33 V and that the input for nitrogen at 38.8 V is approximately 8 % lower than the heat input for compressed air at 38.8 V. Responsible for the lower electric energy input are the higher dissociation energy and ionization energy of nitrogen compared to oxygen [155] leading to a higher electrical resistance of the arc and consequently to a lower current at the same voltage.

To be able to estimate if the measured average temperatures are in a plausible range, the results have to be compared with data from literature. The measured particle temperatures are again most likely comparable with the results obtained by Newbery et al. [33]. The temperature determination in their work is performed using a two-color pyrometer that is calibrated with the help of a tungsten ribbon standard. They measured the temperature along the spraying direction for a voltage of 34 V, a feed rate of 3.8 m/min and pressure of 2.8 bar. Compressed air was used as atomizing gas. Because the voltage is the most temperature influencing parameter, the parameters used in this work that should cause the most comparable temperatures are a voltage of 33 V, a feed rate of 4 m/min and a pressure of 4 bar. The results measured in this work and the results measured by Newbery et al. are presented in Figure 109. The temperatures from Newbery et al. decrease from 2638 K at 70 mm to 2539 K at 200 mm and are approximately 100 K lower than the temperatures measured in this work. Since the voltage used by Newbery et al. is higher and the feed rate and the pressure are lower, the measured temperatures should according to the above discussed trends actually be higher. As Newbery et al. mention, responsible for the too low temperatures is the underestimation up to 250 K caused by the assumption that the steel particles have the same emissivity ratio as tungsten at the two widely separated filter wavelengths (950 nm and 1350 nm). Taking this underestimation into account the temperatures of Newbery et al. are above the temperatures measured in this work and therefore would better match to the discussed tendencies.

All in all it can be noted that the measured particle temperatures are in good agreement with literature and that the determined trends fit well together with the current and voltage measurements. Finally, the tomographic two-color-pyrometry is a suitable diagnostic allowing average particle temperature determination along the spraying direction without the need of scanning the whole spray plume.

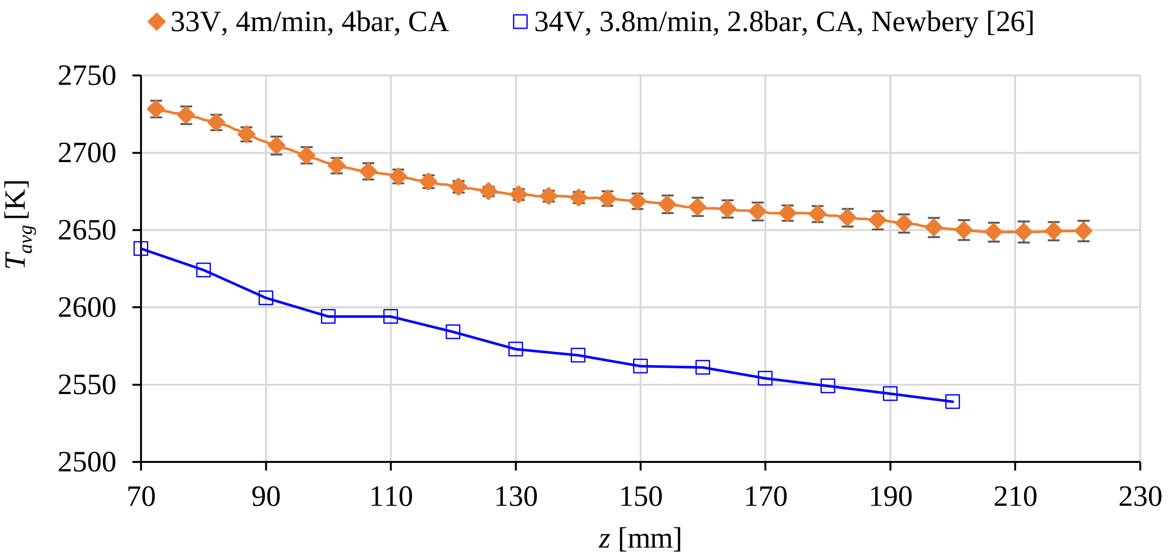

Figure 109: Particle temperatures depending on z measured in the middle of spray plume. The orange curve shows results of this work. The blue curve shows results measured by Newbery et al. [33] *using a two-color pyrometer.*

Besides the application of the tomographic measurement technique on the wire arc spray plume, the in-flight determination of material depended emissivities is the innovative approach of this work. Using the model presented in Chapter 4 and the tomographic two-color-pyrometry, the PSI and the DPV results as input, the average particle emissivities can be calculated. Since all emissivities measured at a wavelength of 800 nm (see Figure 102 to Figure 105) are between 0.1 and 0.35, the emissivity of liquid S235 above 2100 K ($\varepsilon_{\mathrm{S235}} = 0.087$ compare Table 7) measured by Schöpp et al. [132] seems to be the most suitable value for the iron based feedstock material used in this work. Furthermore for the emissivity of liquid FeO ($\varepsilon_{\mathrm{FeO}} = 0.7$ compare Table 7) the value of Muller et al. [133] has to be used to discuss the results, because no other values could be found in literature for temperatures above 2100 K.

Assuming that the unoxidized material and the dominating oxide FeO are mixed continuously and thus the surface is measure for the degree of oxidation of the whole particle, the in-flight oxide content depending on *z* can be estimated by Equation 7.3.

$$C_{ox}(z) = \frac{\varepsilon(z) - \varepsilon_{\mathrm{S235}}}{\varepsilon_{\mathrm{FeO}} - \varepsilon_{\mathrm{S235}}} \cdot 100\,\% \qquad 7.3$$

To be able to evaluate the in-flight oxide content, it is assumed that the oxide area fractions presented in Chapter 6.3 represent the absolute oxide content of the test coatings and that these oxides are only caused by particle in-flight oxidation and not by the post-oxidation of the splat surfaces. This assumption may be justified, since the wire arc spray process is a process with high deposition rates leading to short times between the impingement of two consecutive particles. Furthermore, the dwell time of the particles in the gas stream is compared to other thermal spray process (e.g. HVOF) long [43], whereby the degree of in-flight oxidation is high.

The diagrams in Figure 110 to Figure 113 show the comparison of the test coating oxide contents and the particle oxide contents for the different investigated parameter sets. With compressed air as atomizing gas, the measured particle oxide contents tend to be higher than the oxide contents determined for the test coatings. Furthermore in contrast to the coating oxide contents, the particle oxide contents do not linearly increase, but slowly go into saturation. Both observations are evidence that the feedstock material and the oxides do not continuously mix. Instead, it is assumed that the oxidation on the particle surfaces initially progresses fast and subsides with increasing oxide shell. Nevertheless, the relative increase of the particle oxide contents along the observed distance is in good agreement with the increase of the oxide contents of the test coatings. However, it is not possible to measure the trend of the changing parameters. For example, the proportional relations between the pressure and the oxide content and the feed rate and the oxide content cannot be found in the in-flight oxidation measurements.

As Figure 113 shows, the particle oxide contents calculated for nitrogen as atomizing gas are significantly smaller than the corresponding test coating oxide contents. Responsible therefore is most probably the too low particle size measured with the PSI (see discussion in Chapter 7.1). Through inserting Equation 4.4 into Equation 4.6 it can be seen that the emissivity and consequently the particle oxide content are direct proportional to the particle radius. To clarify the influence of the particle size, the particle oxide content trace calculated for a 45 % increased particle radius is presented in Figure 113. Apart from that, both the slope of the original particle oxide contents and the slope of the modified particle oxide contents are in good agreement with the slope of the coating oxide contents. Due to the significant lower degree of oxidation no saturation can be observed.

To conclude, the tomographic two-color-pyrometry in combination with particle size and velocity measurements offers the possibility of in-flight oxidation measurements. The results are in good agreement with the oxide contents of sprayed coatings. To obtain more precise results it may be necessary to perform spatial resolved particle size and velocity measurements along the spraying direction.

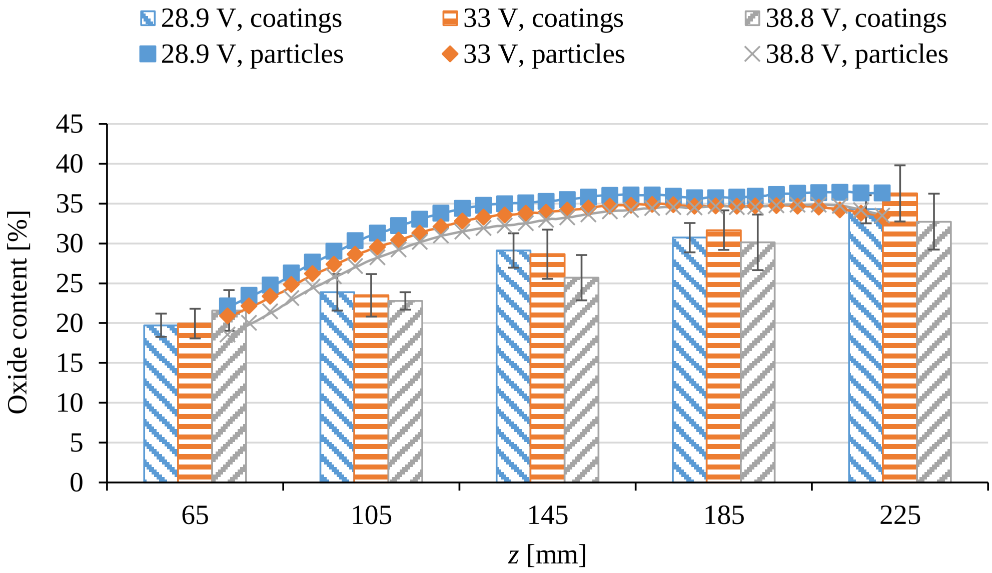

Figure 110: Comparison of test coating oxide contents and in-flight measured particle oxide contents. The process was operated with CA, 4 m/min, 4 bar and three different voltages.

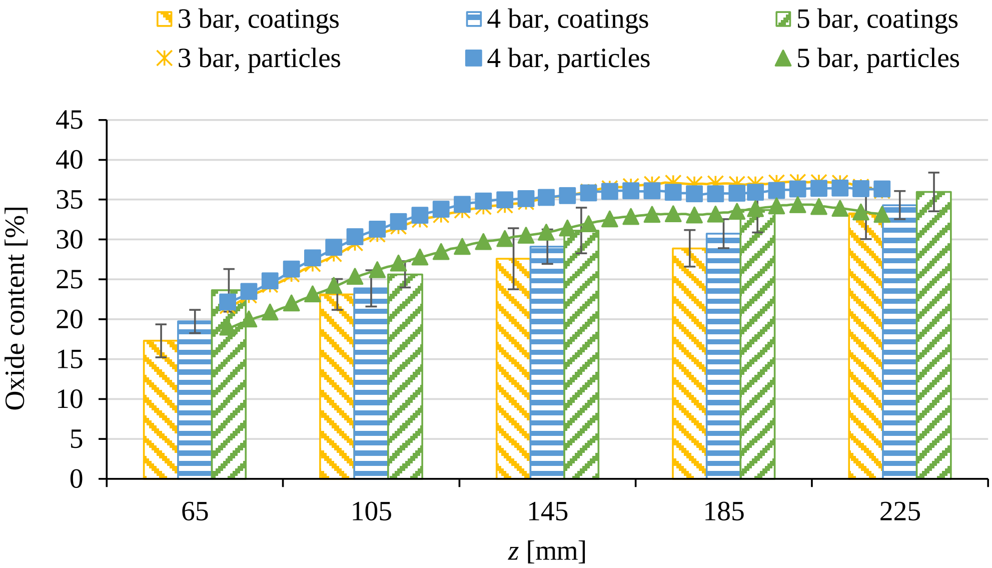

Figure 111: Comparison of test coating oxide contents and in-flight measured particle oxide contents. The process was operated with CA, 28.9 V, 4 m/min and three different pressures.

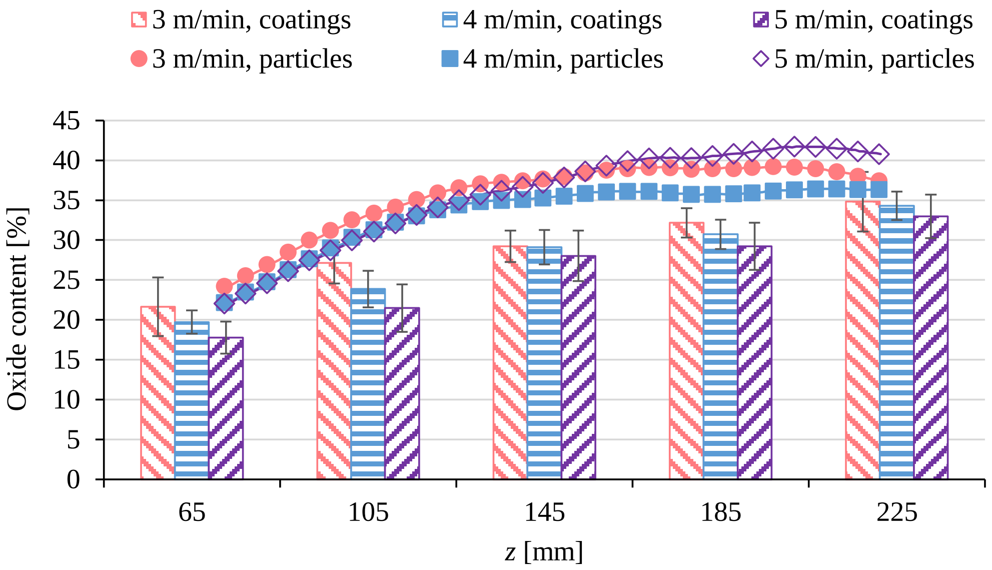

Figure 112 Comparison of test coating oxide contents and in-flight measured particle oxide contents. The process was operated with CA, 28.9 V, 4 bar and three different wire feed rates.

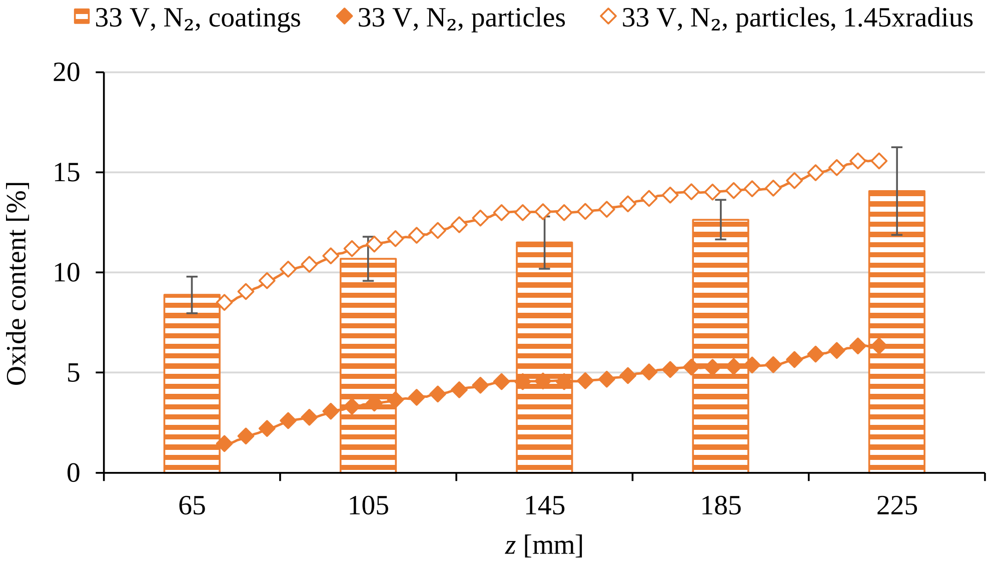

Figure 113: Comparison of test coating oxide contents and in flight measured particle oxide contents. In addition the particle oxide contents calculated for a particle radius 1.45 times higher than the measured one are presented. The process was operated with nitrogen, 33 V, 4 m/min and 4 bar.

8 Conclusion

Thermal spraying is the generic term for processes that provide a high amount of energy in order to melt and atomize feedstock material that is finally accelerate towards a substrate to be coated. Due to the broad available power range, a great variety of feedstock materials and their combinations can be used to improve the surface properties of the base material. Decisive for the quality of a coating are the proper selection of materials and gases as well as a conscientious substrate preparation. Important parameters that cannot be proved beforehand and that may change during the coating process are the properties of the atomized particles. The velocity, the size, the temperature and the rate influence for example the adhesion to the substrate, the cohesion between the splats or the hardness of the coating. A key factor that is strongly connected to the before-mentioned coating properties is the oxide content, whereby a high amount of oxides depending on the requirements on the coating can both be desirable or undesirable. The oxide content in turn strongly depends on the in-flight oxidation of the particles and consequently on their temperature, size and velocity. For the measurement of these properties many diagnostics for industry and for research purpose are available and known. However, the determination of the particle in-flight oxidation based on these diagnostics and their results can only be done qualitatively, since the influence of the used process gases and the surrounding environment is not taken into account. For these reasons the approach of this work is the development of a thermal spraying diagnostic allowing quantitative conclusions on the in-flight particle oxidation.

The innovative diagnostic combines two-color-pyrometry with tomographic recording and evaluation techniques. Observing the spray plume at two different wavelength bands from different directions enables the determination of three dimensional intensity and temperature distributions. The measured total intensity along the spraying direction depends on the particle rate, velocity, size, temperature and emissivity. Since the emissivities for the used feedstock material and the resulting oxides are known form literature and the temperature and the intensities are measured using the tomographic two-color-pyrometry, it is possible to determine the in-flight particle oxide content. Whereby the velocities and sizes have to be measured using the established diagnostics DPV and PSI.

The two-color-pyrometry setup consist of a beam splitter and two CCD-cameras with different interference filters in front. All components are chosen in a way that the error due the assumption of gray body behavior and the error caused by measurement uncertainties are low. Furthermore, for every pixel of the cameras a calibration factor is determined using a moving tungsten calibration lamp, whose temperature is spectroscopically measured.

The two-color-pyrometry module is moved around the spray plume and acquires images in defined angle steps with a long exposure time (>1 s). By applying the so called algebraic reconstruction technique on the raw data three dimensional intensity distributions for the two used wavelength regions are processed, that in turn are used in order to calculate three dimensional temperature distributions. Based on these results and the particle velocity and size measurements, a model is developed allowing the calculation of the material dependent emissivity. Finally feedstock and oxide emissivities known from literature are used in order to calculate the particle in-flight oxide content.

To prove the feasibility of applying the tomography on the spray plume of the wire arc spray process, different conditions have to be fulfilled. Since the spray plume consist of fast moving liquid steel droplets that are opaque, the exposure time of the camera has to be long enough to guarantee a sufficient amount of particles on every position of the measurement volume. Applying this statistical method, it has to be ensured that the spray plume is optically thin and that consequently the radiation of almost all particles is received by the detector. For the determination of the optical thickness, a model was developed that needs the particle rates (LDA measurements), velocities (DPV measurements) and sizes (PSI measurements) as input. The results of the model show that the wire arc spray plume is optically thin for all investigated parameters.

In order to evaluate the measured particle in-flight oxidation, test coatings are generated at different positions along the spraying direction and oxide contents are determined by means of scanning electron microscope photographs of cross sections. These coating oxide contents are in good agreement with the measured particle in-flight oxide contents and are evidence for the principle function of tomographic two-color-pyrometry. Especially the differences between using nitrogen as atomizing gas instead of compressed air are significant. Unfortunately the differences caused by changing process parameters like the gas pressure or the wire feed rate could not be detected.

To achieve more detailed results the particle velocity and size measurements should be performed spatial resolved. Furthermore it would be useful to integrate the particle velocity and size diagnostic into the tomographic two-color-pyrometry in order to reduce the experimental effort and the measurement time. This could be achieved by mounting a sensor head using the two-slit-method of the DPV on the two-color-pyrometer.

In summary, the tomographic two-color-pyrometry developed in this work proves the ability of performing tomographic measurements on the spray plume of a wire arc spray process and provides first results for the quantitative determination of particle in-flight oxidation.

9 References

[1] H. Kagermann, W.-D. Lukas, and W. Wahlster, “Industrie 4.0: Mit dem Internet der Dinge auf dem Weg zur 4. industriellen Revolution,” *VDI nachrichten*, vol. 13, 2011.

[2] A. Roth, *Einführung und Umsetzung von Industrie 4.0: Grundlagen, Vorgehensmodell und Use Cases aus der Praxis*: Springer Berlin Heidelberg, 2016.

[3] H. Böhme, *Industry 4.0 at the starting gates.* Available: http://dw.com/p/1F7KS.

[4] K. Hartz-Behrend, J. Schaup, J. Zierhut, and J. Schein, “Controlling the Twin Wire Arc Spray Process Using Artificial Neural Networks (ANN),” *Journal of thermal spray technology*, vol. 25, no. 1-2, pp. 21–27, 2016.

[5] D. Bémer *et al*, “Ultrafine particles emitted by flame and electric arc guns for thermal spraying of metals,” (eng), *The Annals of occupational hygiene*, vol. 54, no. 6, pp. 607–614, 2010.

[6] J. Schein, "Head-mounted display for the use in thermal spraying.", personal communication, Dec. 2016.

[7] *Thermisches Spritzen - Begriffe, Einteilung*, DIN EN 657:2005-06.

[8] P. Fauchais, J. Heberlein, and M. Boulos, *Thermal Spray Fundamentals: From Powder to Part*: Springer US, 2014.

[9] P. Fauchais, A. Vardelle, and B. Dussoubs, “Quo vadis thermal spraying?,” *Journal of thermal spray technology*, vol. 10, no. 1, pp. 44–66, 2001.

[10] L. Pawlowski, *The Science and Engineering of Thermal Spray Coatings*: Wiley, 2008.

[11] Oerlikon Metco, “Einführung Thermisches Spritzen,” Jul. 2016.

[12] B. Gérard, “Application of thermal spraying in the automobile industry,” *Surface and Coatings Technology*, vol. 201, no. 5, pp. 2028–2031, 2006.

[13] K. Bobzin *et al*, “Thermal spraying of cylinder bores with the Plasma Transferred Wire Arc process,” *Surface and Coatings Technology*, vol. 202, no. 18, pp. 4438–4443, 2008.

[14] G. Darut, H. Liao, C. Coddet, J. M. Bordes, and M. Diaby, “Steel coating application for engine block bores by Plasma Transferred Wire Arc spraying process,” *Surface and Coatings Technology*, vol. 268, pp. 115–122, 2015.

[15] S. Uozato, K. Nakata, and M. Ushio, “Evaluation of ferrous powder thermal spray coatings on diesel engine cylinder bores,” *Surface and Coatings Technology*, vol. 200, no. 7, pp. 2580–2586, 2005.

[16] ASM International, J.R. Davis & Associates, *Handbook of thermal spray technology*. Materials Park, OH: ASM International, 2004.

[17] J. Ružbarský and A. Panda, *Plasma and Thermal Spraying*: Springer International Publishing, 2016.

[18] H. Assadi, F. Gärtner, T. Stoltenhoff, and H. Kreye, “Bonding mechanism in cold gas spraying,” *Acta Materialia*, vol. 51, no. 15, pp. 4379–4394, 2003.

[19] T. Stoltenhoff, H. Kreye, and H. J. Richter, “An analysis of the cold spray process and its coatings,” *Journal of thermal spray technology*, vol. 11, no. 4, pp. 542–550, 2002.

[20] S. Siegmann and C. Abert, “100 years of thermal spray: About the inventor Max Ulrich Schoop,” *Proceedings of the fifth workshop RIPT (Les Rencontres Internationales sur la Projection Thermique)*, vol. 220, pp. 3–13, 2013.

[21] Oerlikon Metco, “Hochgeschwindigkeits-Flammspritzen (HVOF),”

[22] B. Irving, R. Knight, and R. W. Smith, “The HVOF process-The hottest topic in the thermal spray industry,” *Welding Journal*, vol. 72, pp. 25–30, 1993.

[23] J. L Marqués, G. Forster, and J. Schein, “Multi-electrode plasma torches: motivation for development and current state-of-the-art,” *The Open Plasma Physics Journal*, vol. 2, no. 1, 2009.

[24] J. Schein, J. Zierhut, M. Dzulko, G. Forster, and K. D. Landes, “Improved Plasma Spray Torch Stability Through Multi-Electrode Design,” *Contributions to Plasma Physics*, vol. 47, no. 7, pp. 498–504, 2007.

[25] K. D. Landes, "Plasma spray apparatus for spraying powdery or gaseous material" US5225652 A, 1993

[26] P. Haslbeck, “Entwicklung eines Dreikathoden-Plasmaspritzbrenners unter Anwendung adaptierter plasmadiagnostischer Methoden,” Ph.D. Thesis, Universität der Bundeswehr München, Neubiberg, 1995.

[27] M. Dzulko, “Entwicklung des Mehranoden DC-Plasmagenerators „Delta Gun“,” Ph.D. Thesis, Universität der Bundeswehr München, Neubiberg, 2007.

[28] T. Schläfer, A. Wank, C. Schmengler, and K. Müller-Roden, “PENTA: A novel high spray rate APS gun,” in *Thermal Spray: Proceedings of the International Thermal Spray Conference*, 2017.

[29] H.-D. Steffens, Z. Babiak, and M. Wewel, “Recent developments in arc spraying,” *IEEE Transactions on Plasma Science*, vol. 18, no. 6, pp. 974–979, 1990.

[30] N. A. Hussary and J. V. Heberlein, “Atomization and particle-jet interactions in the wire-arc spraying process,” *Journal of thermal spray technology*, vol. 10, no. 4, pp. 604–610, 2001.

[31] N. A. Hussary and J. V. Heberlein, “Effect of system parameters on metal breakup and particle formation in the wire arc spray process,” *Journal of thermal spray technology,* vol. 16, no. 1, pp. 140–152, 2007.

[32] D. L. Hale, W. D. Swank, and D. C. Haggard, “In-flight particle measurements of twin wire electric arc sprayed aluminum,” *Journal of thermal spray technology,* vol. 7, no. 1, pp. 58–63, 1998.

[33] A. P. Newbery, P. S. Grant, and R. A. Neiser, “The velocity and temperature of steel droplets during electric arc spraying,” *Surface and Coatings Technology*, vol. 195, no. 1, pp. 91–101, 2005.

[34] A. Pourmousa, J. Mostaghimi, A. Abedini, and S. Chandra, “Particle size distribution in a wire-arc spraying system,” *Journal of thermal spray technology,* vol. 14, no. 4, pp. 502–510, 2005.

[35] T. Watanabe, T. Sato, and A. Nezu, “Electrode phenomena investigation of wire arc spraying for preparation of Ti-Al intermetallic compounds,” *Thin Solid Films*, vol. 407, no. 1, pp. 98–103, 2002.

[36] H. L. Liao, Y. L. Zhu, R. Bolot, C. Coddet, and S. N. Ma, “Size distribution of particles from individual wires and the effects of nozzle geometry in twin wire arc spraying,” *Surface and Coatings Technology,* vol. 200, no. 7, pp. 2123–2130, 2005.

[37] A. Atzberger *et al,* “Thermische Plasmen: Einfluss der Strommodulation und der verwendeten Prozessgase auf den Lichtbogendrahtspritzprozess,” *Thermal Spray Bulletin*, vol. 68, no. 2, pp. 114–121, 2016.

[38] P. Fauchais, “Understanding plasma spraying,” *Journal of Physics D: Applied Physics*, vol. 37, no. 9, pp. R86, 2004.

[39] J. Kotz, P. Treichel, and J. Townsend, *Chemistry and Chemical Reactivity*: Cengage Learning, 2008.

[40] C. Law, *Combustion Physics*: Cambridge University Press, 2010.

[41] D. B. Wilson, T. A. Steinberg, and J. M. Stoltzfus, “Thermodynamics and kinetics of burning iron,” in *Flammability and Sensitivity of Materials in Oxygen-Enriched Atmospheres: Eighth Volume*: ASTM International, 1997.

[42] D. Young, *High Temperature Oxidation and Corrosion of Metals*: Elsevier Science, 2016.

[43] S. Deshpande, S. Sampath, and H. Zhang, “Mechanisms of oxidation and its role in microstructural evolution of metallic thermal spray coatings—Case study for Ni–Al,” *Surface and Coatings Technology*, vol. 200, no. 18–19, pp. 5395–5406, 2006.

[44] G. Espie *et al*, “In-flight oxidation of iron particles sprayed using gas and water stabilized plasma torch,” *Surface and Coatings Technology*, vol. 195, no. 1, pp. 17–28, 2005.

[45] V. V. Sobolev and J. M. Guilemany, “Effect of oxidation on droplet flattening and splat-substrate interaction in thermal spraying,” *Journal of thermal spray technology*, vol. 8, no. 4, pp. 523–530, 1999.

[46] S. Sampath and X. Jiang, “Splat formation and microstructure development during plasma spraying: deposition temperature effects,” *Materials Science and Engineering: A*, vol. 304, pp. 144–150, 2001.

[47] C.-J. Li and W.-Y. Li, “Effect of sprayed powder particle size on the oxidation behavior of MCrAlY materials during high velocity oxygen-fuel deposition,” *Surface and Coatings Technology*, vol. 162, no. 1, pp. 31–41, 2003.

[48] M.-M. Matz and M. Aumiller, “Practical Comparison of Cylindrical Nozzle and De Laval Nozzle for Wire Arc Spraying,” *J Therm Spray Tech*, vol. 23, no. 8, pp. 1470–1477, 2014.

[49] E. Hämäläinen *et al*, “Imaging Diagnostics in Thermal Spraying-SprayWatch System,” in *Thermal spray surface engineering via applied research: Proceedings of the 1st International Thermal Spray Conference, 8-11 May, 2000, Montréal, Québec, Canada*, Materials Park, OH: ASM International, 2000.

[50] F. Raletz, G. Ezo’o, M. Vardelle, and M. Ducos, “Characterization of cold-sprayed nickel-base coatings,” in *Thermal spray: Advances in technology and application: proceedings of the International Thermal Spray Conference*, Materials Park, OH: ASM International, 2004.

[51] S. Yoon, C. Lee, H. Choi, and H. Jo, “Kinetic spraying deposition behavior of bulk amorphous NiTiZrSiSn feedstock,” *Materials Science and Engineering: A*, vol. 415, no. 1–2, pp. 45–52, 2006.

[52] J. Vattulainen, E. Hämäläinen, R. Hernberg, P. Vuoristo, and T. Mäntylä, “Novel method for in-flight particle temperature and velocity measurements in plasma spraying using a single CCD camera,” *Journal of thermal spray technology*, vol. 10, no. 1, pp. 94–104, 2001.

[53] S. Kirner, G. Forster, and J. Schein, “Tomographic Particle Localization and Velocity Measurement,” *Journal of thermal spray technology*, 2014.

[54] M. Krauss, D. Bergmann, U. Fritsching, and K. Bauckhage, “In-situ particle temperature, velocity and size measurements in the spray forming process,” *Materials Science and Engineering: A*, vol. 326, no. 1, pp. 154–164, 2002.

[55] G. Mauer, R. Vaßen, and D. Stöver, “Comparison and Applications of DPV-2000 and Accuraspray-g3 Diagnostic Systems,” *J Therm Spray Tech*, vol. 16, no. 3, pp. 414–424, 2007.

[56] C. Moreau, J.-F. Bisson, R. S. Lima, and B. R. Marple, “Diagnostics for advanced materials processing by plasma spraying,” *Pure and Applied Chemistry*, vol. 77, no. 2, pp. 443–462, 2005.

[57] Tecnar Automation Ltd, “DPV EVOLUTION: Product Manual, Edition 1,” 2012.

[58] J. Zierhut, “Entwicklung von Diagnostikverfahren zur Optimierung von Plasmaspritzsystemen,” Ph.D. Thesis, Institut für Plasmatechnik und Mathematik, Universität der Bundeswehr München, Neubiberg, 2000.

[59] J. Zierhut, K. D. Landes, W. Krommer, and P. Heinrich, “Particle Flux Imaging(PFI) in-situ diagnostics for thermal coating process,” in *Thermal Spray: Surface Engineering via Applied Research : Proceedings of the 1st International Thermal Spray Conference*, Materials Park, OH: ASM International, 2000, pp. 63–66.

[60] F.-W. Bach *et al*, “Particle image velocimetry in thermal spraying,” *2nd International Conference on Spray Deposition and Melt Atomization and the 5th International Conference on Spray Forming*, vol. 383, no. 1, pp. 146–152, 2004.

[61] G. E. Elsinga, B. Wieneke, F. Scarano, and A. Schröder, “Tomographic 3D-PIV and applications,” in *Particle image velocimetry*: Springer, 2007, pp. 103–125.

[62] C. Baukal, *Industrial Combustion Testing*: CRC Press, 2010.

[63] C. Tropea, A. Yarin, and J. Foss, *Springer Handbook of Experimental Fluid Mechanics*: Springer, 2007.

[64] G. Mauer *et al*, “Investigation and Comparison of In-Flight Particle Velocity During the Plasma-Spray Process as Measured by Laser Doppler Anemometry and DPV-2000,” *J Therm Spray Tech*, vol. 22, no. 6, pp. 892–900, 2013.

[65] W. Mayr, “Bestimmung der lokalen Geschwindigkeits- und Grössenverteilungen von Partikeln im Plasmastrahl mittels Laser-Doppler-Anemometrie,” Ph.D. Thesis, Fachbereich Elektrotechnik, Hochschule der Bundeswehr München, Neubiberg, 1983.

[66] A. Reusch, “Die Entwicklung eines Laser-Doppler-Meßsystems und seine Anwendung bei Verfahren des thermischen Beschichtens,” Ph.D. Thesis, Institut für Plasmatechnik und Mathematik, Universität der Bundeswehr München, Neubiberg, 1995.

[67] P. Lehmann, *In-process Laser-Messmethoden auf der Grundlage der Fourieranalyse*: expert-Verlag, 2003.

[68] T. Streibl, “Entwicklung eines bildgebenden Partikeldiagnostikverfahrens zur Untersuchung Thermischer Spritzprozesse,” Ph.D. Thesis, Institut für Plasmatechnik und Mathematik, Universität der Bundeswehr München, Neubiberg, 2002.

[69] S. Zimmermann, “Particle Shape Imaging (PSI) – eine innovative Methode der Partikeldiagnostik bei thermischen Beschichtungsverfahren,” Ph.D. Thesis, Institut für Plasmatechnik und Mathematik, Universität der Bundeswehr München, Neubiberg, 2007.

[70] T. Streibl, K. D. Landes, and G. Forster, “PSI: new diagnostics for the determination of particle size and shape in thermal spray processes,” in *Thermal Spray: Surface Engineering via Applied Research : Proceedings of the 1st International Thermal Spray Conference*, Materials Park, OH: ASM International, 2000, pp. 67–70.

[71] J. R. Fincke, W. D. Swank, and C. L. Jeffery, “Simultaneous Measurement of Particle Size, Velocity, and Temperature in Thermal Plasmas,” *Plasma Science, IEEE Transactions on*, vol. 18, no. 6, pp. 948–957, 1990.

[72] A. P. Newbery and P. S. Grant, “Oxidation during electric arc spray forming of steel,” *Journal of materials processing technology*, vol. 178, no. 1, pp. 259–269, 2006.

[73] R. A. Neiser, M. F. Smith, and R. C. Dykhuizen, “Oxidation in wire HVOF-sprayed steel,” *Journal of thermal spray technology*, vol. 7, no. 4, pp. 537–545, 1998.

[74] K. Voleník, V. Novák, J. Dubský, P. Chráska, and K. Neufuss, “Properties of alloy steel coatings oxidized during plasma spraying,” *Materials Science and Engineering: A*, vol. 234–236, pp. 493–496, 1997.

[75] J. Hlína and J. Šonský, “Time-resolved tomographic measurements of temperatures in a thermal plasma jet,” *Journal of Physics D: Applied Physics*, vol. 43, no. 5, p. 55202, 2010.

[76] K. D. Landes, G. Forste, J. Zierhut, M. Dzulko, and D. Hawley, “Computer tomography of plasma jets–applied on a TRIPLEX II torch,” in *Thermal spray: Advances in technology and application: proceedings of the International Thermal Spray Conference*, Materials Park, OH: ASM International, 2004.

[77] G. Kirchhoff, “Ueber das Verhältniss zwischen dem Emissionsvermögen und dem Absorptionsvermögen der Körper für Wärme und Licht,” *Ann. Phys. Chem*, vol. 185, no. 2, pp. 275–301, 1860.

[78] J. Stefan, *Über die Beziehung zwischen der Wärmestrahlung und der Temperatur*. Wien, vol. 79.

[79] L. Boltzmann, “Ableitung des Stefan'schen Gesetzes, betreffend die Abhängigkeit der Wärmestrahlung von der Temperatur aus der electromagnetischen Lichttheorie,” *Ann. Phys*, vol. 258, no. 6, pp. 291–294, 1884.

[80] W. Wien, “Ueber die Energievertheilung im Emissionsspectrum eines schwarzen Körpers,” *Annalen der Physik*, vol. 294, no. 8, pp. 662–669, 1896.

[81] M. Ambaum, *Thermal Physics of the Atmosphere*: Wiley, 2010.

[82] M. Planck, “Ueber das Gesetz der Energieverteilung im Normalspectrum,” *Ann. Phys*, vol. 309, no. 3, pp. 553–563, 1901.

[83] J. Vincent, S. Hodges, J. Vampola, M. Stegall, and G. Pierce, *Fundamentals of Infrared and Visible Detector Operation and Testing*: Wiley, 2015.

[84] H. Tränkler and G. Fischerauer, *Das Ingenieurwissen: Messtechnik*: Springer Berlin Heidelberg, 2014.

[85] J. Howell, M. Menguc, and R. Siegel, *Thermal Radiation Heat Transfer, 6th Edition*: CRC Press, 2015.

[86] M. Kaviany, *Principles of Heat Transfer*: Wiley, 2002.

[87] R. Bentley, *Handbook of Temperature Measurement: Volume 1, Temperature and Humidity Measurement*: Springer, 1998.

[88] S. Kirner, G. Forster, and J. Schein, “Influence of the Surface Structure on the Anode Boundary of High Current Moving Arcs in Atmosphere,” *Plasma chemistry and plasma processing*, vol. 36, no. 1, pp. 169–183, 2016.

[89] PCO AG, *pixelfly: high performance digital 12 bit CCD camera system.* Available: http://www.pco.de/fileadmin/user_upload/db/products/datasheet/pixelfly_20090505_02.pdf.

[90] G. R. Gathers, “Error analysis of a ratio pyrometer by numerical simulation,” Lawrence Livermore National Lab, CA (USA), Jan. 1990.

[91] ewm, “Schweißzusatzwerkstoffe: Handbuch,” 2016.

[92] G. Krauss, *Steels: Processing, Structure, and Performance, Second Edition*: A S M International, 2015.

[93] R. Ross, *Metallic Materials Specification Handbook*: Springer US, 2013.

[94] Edmund optics, *Coating Curve, 800nm CWL, 10nm FWHM, 25mm Mounted Diameter.* Available: http://www.edmundoptics.de/optics/optical-filters/bandpass-filters/traditional-coated-700-999nm-bandpass-interference-filters/65724/.

[95] Edmund optics, *Coating Curve, 900nm CWL, 10nm FWHM, 25mm Mounted Diameter.* Available: http://www.edmundoptics.de/optics/optical-filters/bandpass-filters/traditional-coated-700-999nm-bandpass-interference-filters/67857/.

[96] J. Thevenet, M. Siroux, and B. Desmet, “Measurements of brake disc surface temperature and emissivity by two-color pyrometry,” *Applied Thermal Engineering*, vol. 30, no. 6, pp. 753–759, 2010.

[97] E. C. Pyatt, “Some consideration of the errors of brightness and two-colour types of spectral radiation pyrometer,” *British Journal of Applied Physics*, vol. 5, no. 7, p. 264, 1954.

[98] H. Watanabe, M. Susa, H. Fukuyama, and K. Nagata, “Phase (liquid/solid) dependence of the normal spectral emissivity for iron, cobalt, and nickel at melting points,” *International journal of thermophysics*, vol. 24, no. 2, pp. 473–488, 2003.

[99] H. Friedrich and F. Pietschmann, *Numerische Methoden: ein Lehr- und Übungsbuch*: De Gruyter, 2010.

[100] T. Peifer and P. Profos, *Handbuch der industriellen Messtechnik*: Oldenbourg Industrieverlag, 2008.

[101] Qioptiq Photonics GmbH u. Co. KG, *Dünne Schichten – Datenblatt: ARB 2 NIR – Breitband-Antireflex-Coating*. Available: https://www.qioptiq-shop.com/out/Graphics/en/00109153_0.pdf.

[102] S. Battiato, A. Bruna, G. Messina, and G. Puglisi, *Image Processing for Embedded Devices*: Bentham Science Publishers, 2010.

[103] K. Kraus, *Photogrammetry: Geometry from Images and Laser Scans*: Bod Third Party Titles, 2007.

[104] M. Katz, *Introduction to Geometrical Optics*: World Scientific, 2002.

[105] J. Watson and O. Zielinski, *Subsea Optics and Imaging*: Elsevier Science, 2013.

[106] L. Stroebel, *View Camera Technique*: Taylor & Francis, 1999.

[107] G. Meurant, *Physical Optics and Light Measurements*: Elsevier Science, 1989.

[108] Qioptiq Photonics GmbH u. Co. KG, *LINOS Produkte: News & Highlights 2011*. Available: http://www.qioptiq.com/company-brochures.html.

[109] T. Vialar, *Handbook of mathematics*: Books on Demand, 2015.

[110] V. D. Dmitriev and G. K. Kholopov, “Spectral emissivity of a tungsten strip in the visible and near infrared,” *J Appl Spectrosc*, vol. 6, no. 4, pp. 283–286, 1967.

[111] R. D. Larrabee, “The spectral emissivity and optical properties of tungsten,” Technical report 328, Research Laboratory of Electronics, Massachusetts Institute of Technology, Massachusetts, 1957.

[112] M. I. A. Lourakis, “A brief description of the Levenberg-Marquardt algorithm implemented by levmar,” Institute of Computer Science, Foundation for Research and Technology - Hellas (FORTH), Heraklion, Crete, GREECE, 2005.

[113] J. Li, *Optical Delay Interferometers and Their Application for Self-coherent Detection*: KIT Scientific Publishing, 2013.

[114] M. Burke, *Image Acquisition: Handbook of machine vision engineering*: Springer Netherlands, 2012.

[115] T. Matsuyama, S. Nobuhara, T. Takai, and T. Tung, *3D Video and Its Applications*: Springer London, 2012.

[116] T. M. Buzug, *Computed tomography: From photon statistics to modern cone-beam CT*. Berlin: Springer, 2008.

[117] A. Ramm and A. Katsevich, *The Radon Transform and Local Tomography*: Taylor & Francis, 1996.

[118] J. Radon, “Über die Bestimmung von Funktionen durch ihre Integralwerte längs gewisser Mannigfaltigkeiten,” *Berichte über die Verhandlungen der Königlich Sächsischen Gesellschaft der Wissenschaften zu Leipzig. Mathematisch-Physische Klasse,* no. 69, pp. 262–277, 1917.

[119] A. Fridman, *Plasma Chemistry*: Cambridge University Press, 2008.

[120] A. Fridman and L. Kennedy, *Plasma Physics and Engineering*: Taylor & Francis, 2004.

[121] A. Bappert, “Tomographische Bildverarbeitung zur lokalen Bestimmung der Emissionskoeffizienten von Plasmastrahlen,” Diplomarbeit, Institut für Grundgebiete der Elektrotechnik, Universität der Bundeswehr München, Neubiberg, 1995.

[122] S. Kaczmarz, “Angenäherte auflösung von systemen linearer gleichungen,” *Bulletin International de l’Academie Polonaise des Sciences et des Lettres*, vol. 35, pp. 355–357, 1937.

[123] G. T. Herman, *Image reconstruction from projections: The fundamentals of computerized tomography*. San Francisco: Academic Press, 1980.

[124] H. Karttunen, P. Kröger, H. Oja, M. Poutanen, and K. Donner, *Fundamental Astronomy*: Springer Berlin Heidelberg, 2007.

[125] *Digital Image Processing*: Tata McGraw Hill Education, 2011.

[126] S. Kirner, “Bestimmung lokaler Gleichgewichts-Temperaturen thermischer Plasmen mittels tomografischer Emissionsspektroskopie,” Diplomarbeit, Lehrstuhl für Messsystem- und Sensortechnik, Technische Universität München, München, 2010.

[127] J. Fincke, D. Haggard, and W. Swank, “Particle temperature measurement in the thermal spray process,” *Journal of thermal spray technology*, vol. 10, no. 2, pp. 255–266, 2001.

[128] N. Birks, G. Meier, and F. Pettit, *Introduction to the High Temperature Oxidation of Metals*: Cambridge University Press, 2006.

[129] D. J. Young, *High temperature oxidation and corrosion of metals*: Elsevier, 2008.

[130] A. Khanna, *Introduction to High Temperature Oxidation and Corrosion*: ASM International, 2002.

[131] A. Ivarson, J. Powell, J. Kamalu, and C. Magnusson, “The oxidation dynamics of laser cutting of mild steel and the generation of striations on the cut edge,” *Journal of materials processing technology*, vol. 40, no. 3-4, pp. 359–374, 1994.

[132] H. Schöpp *et al*, “Temperature and emissivity determination of liquid steel S235,” *Journal of Physics D: Applied Physics*, vol. 45, no. 23, p. 235203, 2012.

[133] M. Muller, R. Fabbro, H. El-Rabii, and K. Hirano, “Temperature measurement of laser heated metals in highly oxidizing environment using 2D single-band and spectral pyrometry,” *Journal of laser applications*, vol. 24, no. 2, p. 22006, 2012.

[134] H. Kobatake, H. Khosroabadi, and H. Fukuyama, “Normal spectral emissivity measurement of liquid iron and nickel using electromagnetic levitation in direct current magnetic field,” *Metallurgical and Materials Transactions A*, vol. 43, no. 7, pp. 2466–2472, 2012.

[135] T. Burakowski and T. Wierzchon, *Surface Engineering of Metals: Principles, Equipment, Technologies*: CRC Press, 1998.

[136] Salzgitter Flachstahl, “S235JR,” 2010.

[137] S. Ozcelik, K. Moore, and D. Naidu, *Modeling, Sensing and Control of Gas Metal Arc Welding*: Elsevier Science, 2003.

[138] J. Hu and H.-L. Tsai, “Heat and mass transfer in gas metal arc welding. Part I: The arc,” *International journal of heat and mass transfer*, vol. 50, no. 5, pp. 833–846, 2007.

[139] Lasertechnik Berlin, “Manual ARYELLE - Spectrograph Series,” 2009.

[140] R. Neuhauser, *Anwendungen der laserinduzierten Plasmaspektroskopie (LIPS) in der industriellen Überwachung von Schwermetall-Aerosolemissionen*: Utz, Wiss, 1999.

[141] E. Loewen and E. Popov, *Diffraction Gratings and Applications*: Taylor & Francis, 1997.

[142] S. Zimmermann and K. Landes, “A particle image shape imaging (PSI) investigation of particles in a plasma jet,” *2nd International Conference on Spray Deposition and*

Melt Atomization and the 5th International Conference on Spray Forming, vol. 383, no. 1, pp. 153–157, 2004.

[143] Stanford Computer Optics, “Quantum Leap: The image intensifier module for continuous or gated operation providing high speed shutter,” 2014.

[144] S. Hoile, T. Rayment, P. S. Grant, and A. D. Roche, “Oxide formation in the sprayform tool process,” *Materials Science and Engineering: A*, vol. 383, no. 1, pp. 50–57, 2004.

[145] G. Jandin, H. Liao, Z. Q. Feng, and C. Coddet, “Correlations between operating conditions, microstructure and mechanical properties of twin wire arc sprayed steel coatings,” *Materials Science and Engineering: A*, vol. 349, no. 1, pp. 298–305, 2003.

[146] M. P. Planche, H. Liao, and C. Coddet, “Relationships between in-flight particle characteristics and coating microstructure with a twin wire arc spray process and different working conditions,” *Surface and Coatings Technology*, vol. 182, no. 2–3, pp. 215–226, 2004.

[147] B. Böhme, *Neue Präparationswege für intermetallische Verbindungen*: Logos, 2010.

[148] M. Kelkar and J. Heberlein, “Wire-arc spray modeling,” *Plasma chemistry and plasma processing*, vol. 22, no. 1, pp. 1–25, 2002.

[149] B. J. Keene, “Review of data for the surface tension of pure metals,” *International Materials Reviews*, vol. 38, no. 4, pp. 157–192, 2013.

[150] U. Dilthey, *Schweißtechnische Fertigungsverfahren: Schweiß- und Schneidtechnologien*: Springer Berlin Heidelberg, 2013.

[151] W. Tillmann, E. Vogli, and M. Abdulgader, “Asymmetric melting behavior in twin wire arc spraying with cored wires,” *Journal of thermal spray technology*, vol. 17, no. 5-6, pp. 974–982, 2008.

[152] J. Prehm, “Modellierung thermisch-physikalischer Vorgänge beim Thermischen Spritzen,” Ph.D. Thesis, Fakultät für Maschinenbau, Gottfried Wilhelm Leibniz Universität Hannover, Hannover, 2014.

[153] I. Gedzevicius and A. V. Valiulis, “Analysis of wire arc spraying process variables on coatings properties,” *Journal of materials processing technology*, vol. 175, no. 1, pp. 206–211, 2006.

[154] Z. Zhengji, *LDA Application Methods: Laser Doppler Anemometry for Fluid Dynamics*: Springer Berlin Heidelberg, 2010.

[155] J. Huheey *et al*, *Anorganische Chemie: Prinzipien von Struktur und Reaktivität*: De Gruyter, 2014.

A Appendix

A.1 Two-color-pyrometry

Derivation of the measurement error E_{GB} (Equation A.2) caused by the gray body assumption. For the calculation of the temperature the Wien approximation is used (Equation A.1).

$$T = \frac{C_2\left(\frac{1}{\lambda_2} - \frac{1}{\lambda 1}\right)}{\ln\left(\frac{M_{\lambda s,1}}{M_{\lambda s,2}} \cdot \frac{\varepsilon_2}{\varepsilon_1} \cdot \frac{\lambda_1^5}{\lambda_2^5}\right)} \tag{A.1}$$

$$E_{GB} = \frac{T_{real} - T_{measured}}{T_{measured}} =$$

$$= \frac{C_2\left(\frac{1}{\lambda_2} - \frac{1}{\lambda 1}\right) \cdot \ln\left(\frac{\varepsilon_2}{\varepsilon_1}\frac{M_{\lambda s,1}}{M_{\lambda s,2}}\left(\frac{\lambda_1}{\lambda_2}\right)^5\right)^{-1} - C_2\left(\frac{1}{\lambda_2} - \frac{1}{\lambda 1}\right) \cdot \ln\left(\frac{M_{\lambda s,1}}{M_{\lambda s,2}}\left(\frac{\lambda_1}{\lambda_2}\right)^5\right)^{-1}}{C_2\left(\frac{1}{\lambda_2} - \frac{1}{\lambda 1}\right) \cdot \ln\left(\frac{M_{\lambda s,1}}{M_{\lambda s,2}}\left(\frac{\lambda_1}{\lambda_2}\right)^5\right)^{-1}} =$$

$$= \frac{C_2\left(\frac{1}{\lambda_2} - \frac{1}{\lambda 1}\right) \cdot \left(\ln\left(\frac{\varepsilon_2}{\varepsilon_1}\right) + \ln\left(\frac{M_{\lambda s,1}}{M_{\lambda s,2}}\left(\frac{\lambda_1}{\lambda_2}\right)^5\right)\right)^{-1} - C_2\left(\frac{1}{\lambda_2} - \frac{1}{\lambda_1}\right) \cdot \ln\left(\frac{M_{\lambda s,1}}{M_{\lambda s,2}}\left(\frac{\lambda_1}{\lambda_2}\right)^5\right)^{-1}}{C_2\left(\frac{1}{\lambda_2} - \frac{1}{\lambda 1}\right) \cdot \ln\left(\frac{M_{\lambda s,1}}{M_{\lambda s,2}}\left(\frac{\lambda_1}{\lambda_2}\right)^5\right)^{-1}} =$$

$$= \frac{C_2\left(\frac{1}{\lambda_2} - \frac{1}{\lambda 1}\right) - C_2\left(\frac{1}{\lambda_2} - \frac{1}{\lambda 1}\right) \cdot \ln\left(\frac{\varepsilon_2}{\varepsilon_1}\right) \cdot \ln\left(\frac{M_{\lambda s,1}}{M_{\lambda s,2}}\left(\frac{\lambda_1}{\lambda_2}\right)^5\right)^{-1} - C_2\left(\frac{1}{\lambda_2} - \frac{1}{\lambda 1}\right)}{C_2\left(\frac{1}{\lambda_2} - \frac{1}{\lambda 1}\right) \cdot \ln\left(\frac{\varepsilon_2}{\varepsilon_1}\frac{M_{\lambda s,1}}{M_{\lambda s,2}}\left(\frac{\lambda_1}{\lambda_2}\right)^5\right) \cdot \ln\left(\frac{M_{\lambda s,1}}{M_{\lambda s,2}}\left(\frac{\lambda_1}{\lambda_2}\right)^5\right)^{-1}} =$$

$$= \frac{T_{real} \cdot \ln\left(\frac{\varepsilon(\lambda_1, T_{real})}{\varepsilon(\lambda_2, T_{real})}\right)}{C_2 \cdot \left(\frac{1}{\lambda_1} - \frac{1}{\lambda_2}\right)} \tag{A.2}$$

Derivation of the temperature uncertainty (Equation A.4) caused by measurement errors. Again for the calculation of the temperature the Wien approximation is used (Equation A.3), whereby the spectral radiant exitance is replaced by the measured intensities I_1 and I_2.

$$T=\frac{C_2\left(\frac{1}{\lambda_2}-\frac{1}{\lambda_1}\right)}{\ln\left(\frac{I_1}{I_2}\cdot\frac{\lambda_1^5}{\lambda_2^5}\right)} \tag{A.3}$$

$$\Delta T=\frac{\delta T}{\delta I_1}\Delta I_1+\frac{\delta T}{\delta I_2}\Delta I_2=$$

$$=\frac{-C_2\left(\frac{1}{\lambda_2}-\frac{1}{\lambda_1}\right)\cdot\frac{I_2}{I_1}\cdot\frac{\lambda_2^5}{\lambda_1^5}\cdot\frac{1}{I_2}\cdot\frac{\lambda_1^5}{\lambda_2^5}}{\left(\ln\left(\frac{I_1}{I_2}\cdot\frac{\lambda_1^5}{\lambda_2^5}\right)\right)^2}\cdot\Delta I_1+\frac{-C_2\left(\frac{1}{\lambda_2}-\frac{1}{\lambda_1}\right)\cdot\frac{I_2}{I_1}\cdot\frac{\lambda_2^5}{\lambda_1^5}\cdot\left(-\frac{1}{I_2^2}\right)\cdot I_1\cdot\frac{\lambda_1^5}{\lambda_2^5}}{\left(\ln\left(\frac{I_1}{I_2}\cdot\frac{\lambda_1^5}{\lambda_2^5}\right)\right)^2}\cdot\Delta I_2=$$

$$=\frac{-T\cdot\frac{1}{I_1}}{\ln\left(\frac{I_1}{I_2}\cdot\frac{\lambda_1^5}{\lambda_2^5}\right)}\cdot\Delta I_1+\frac{T\cdot\frac{1}{I_2}}{\ln\left(\frac{I_1}{I_2}\cdot\frac{\lambda_1^5}{\lambda_2^5}\right)}\cdot\Delta I_2 \quad\Bigg|\quad \cdot\frac{C_2\left(\frac{1}{\lambda_2}-\frac{1}{\lambda_1}\right)}{C_2\left(\frac{1}{\lambda_2}-\frac{1}{\lambda_1}\right)} \tag{A.4}$$

$$\Rightarrow\quad \frac{\Delta T}{T}=\frac{T\lambda_1\lambda_2}{C_2\left(\lambda_2-\lambda_1\right)}\cdot\frac{\Delta I_1}{I_1}+\frac{T\lambda_1\lambda_2}{C_2\left(\lambda_1-\lambda_2\right)}\cdot\frac{\Delta I_2}{I_2}$$

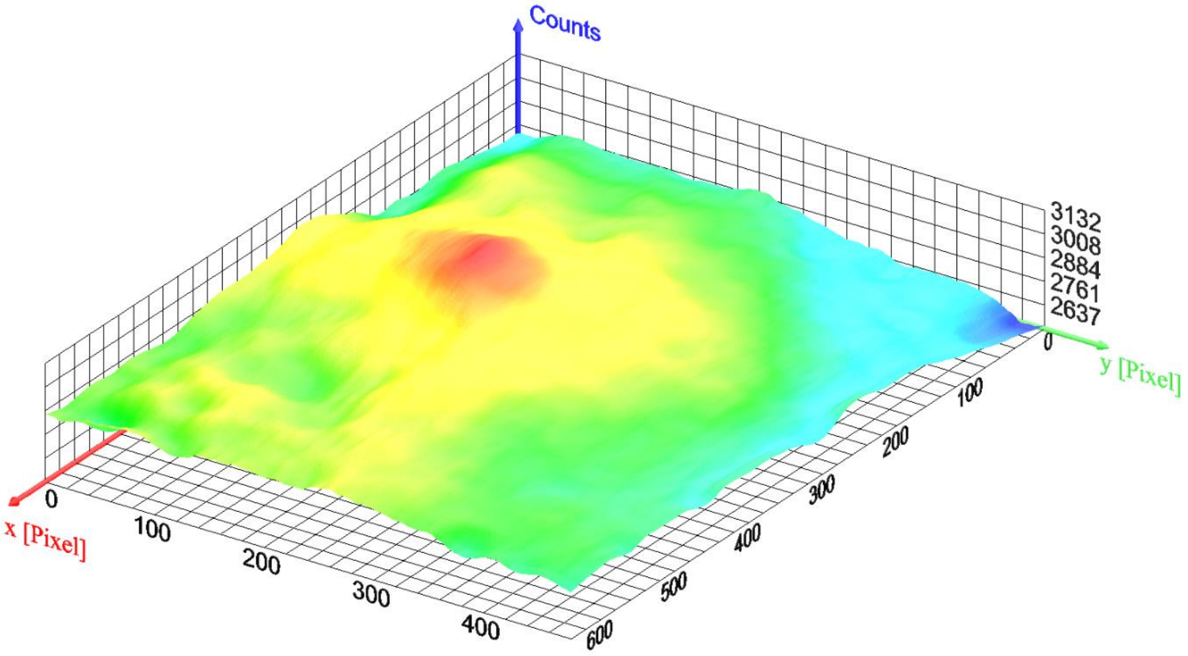

Figure 114: Intensities camera 2, compressed air.

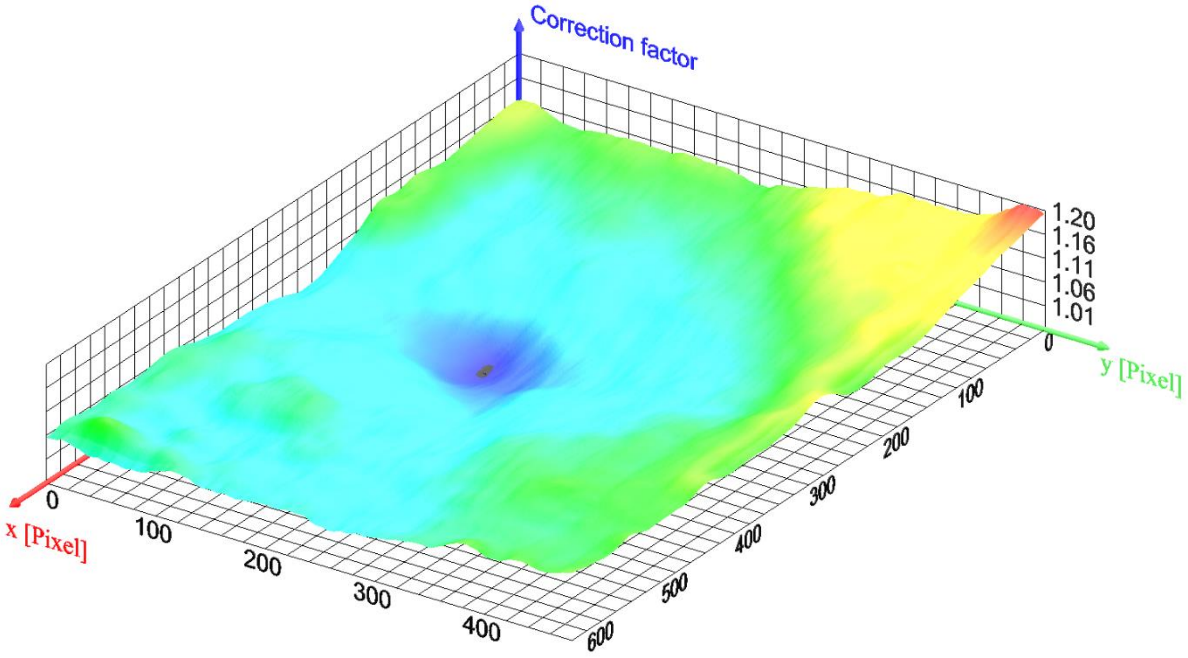

Figure 115: Correction factors camera 2, compressed air.

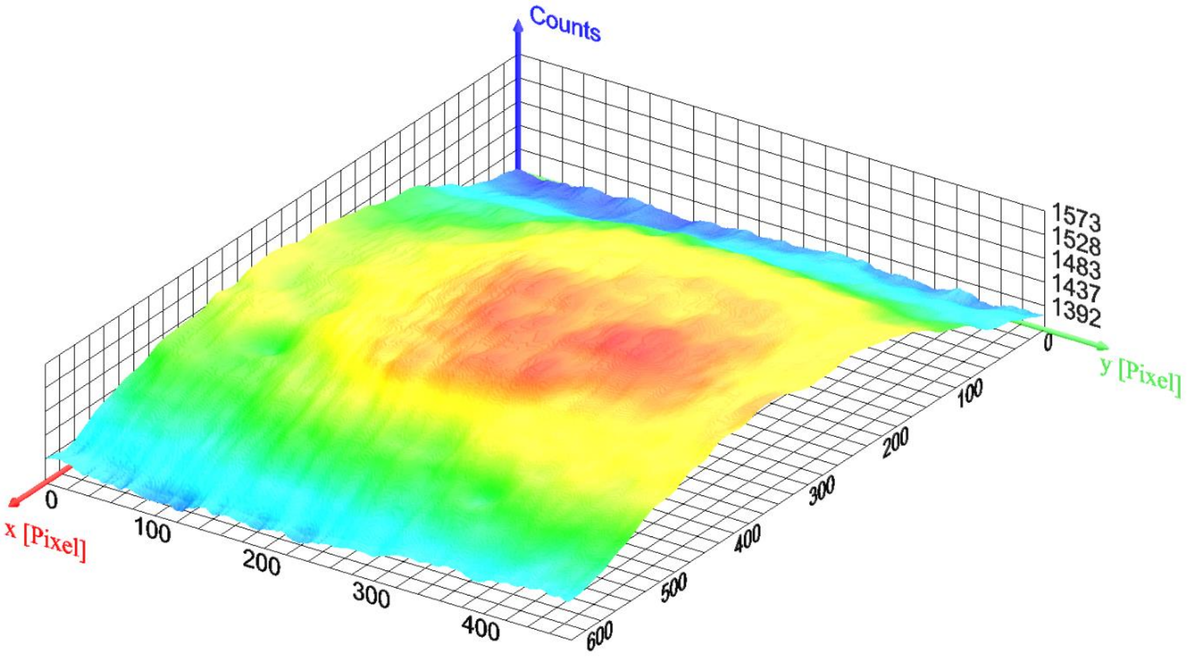

Figure 116: Intensities camera 1, nitrogen.

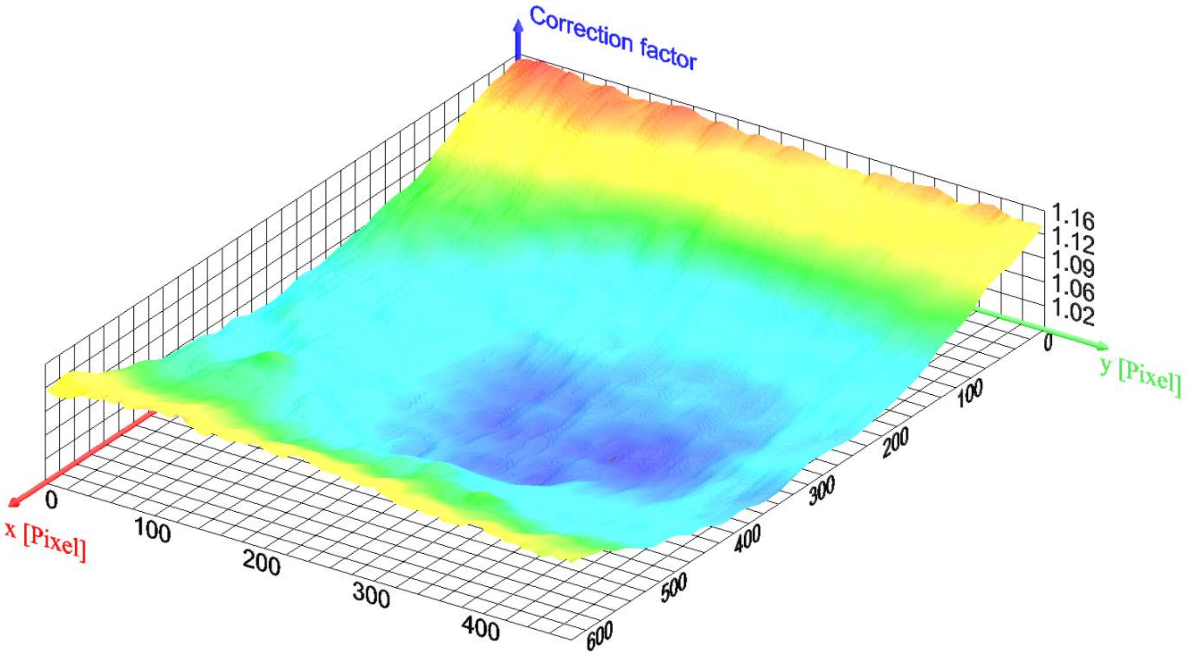

Figure 117: Correction factors camera 1, nitrogen.

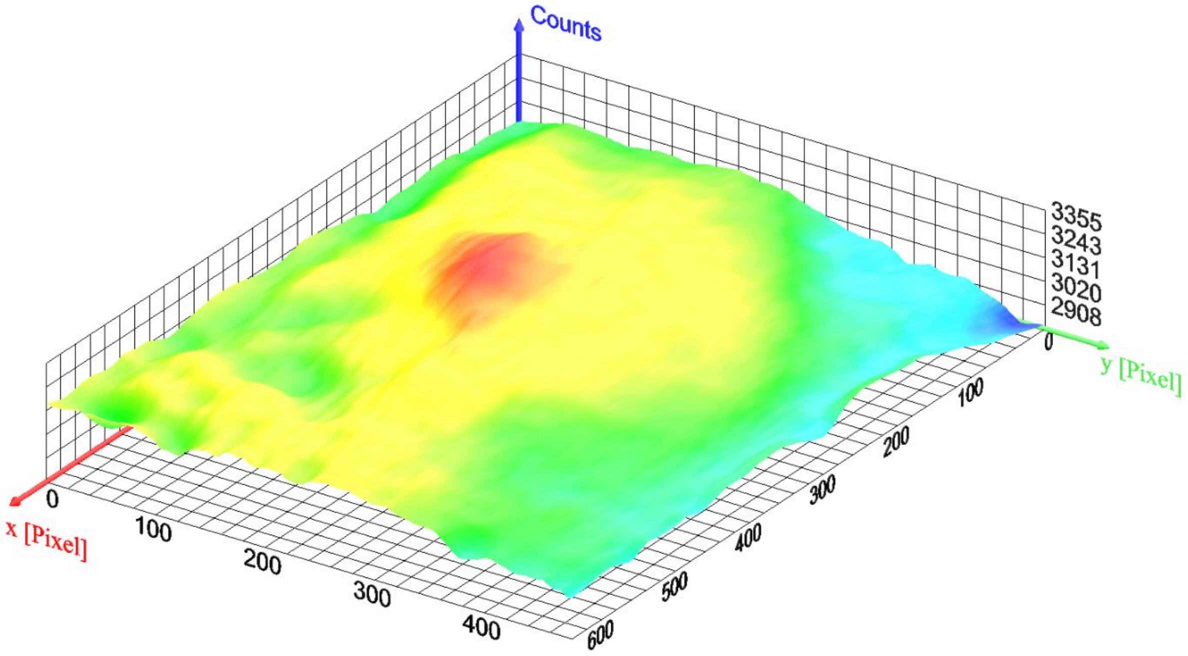

Figure 118: Intensities camera 2, nitrogen.

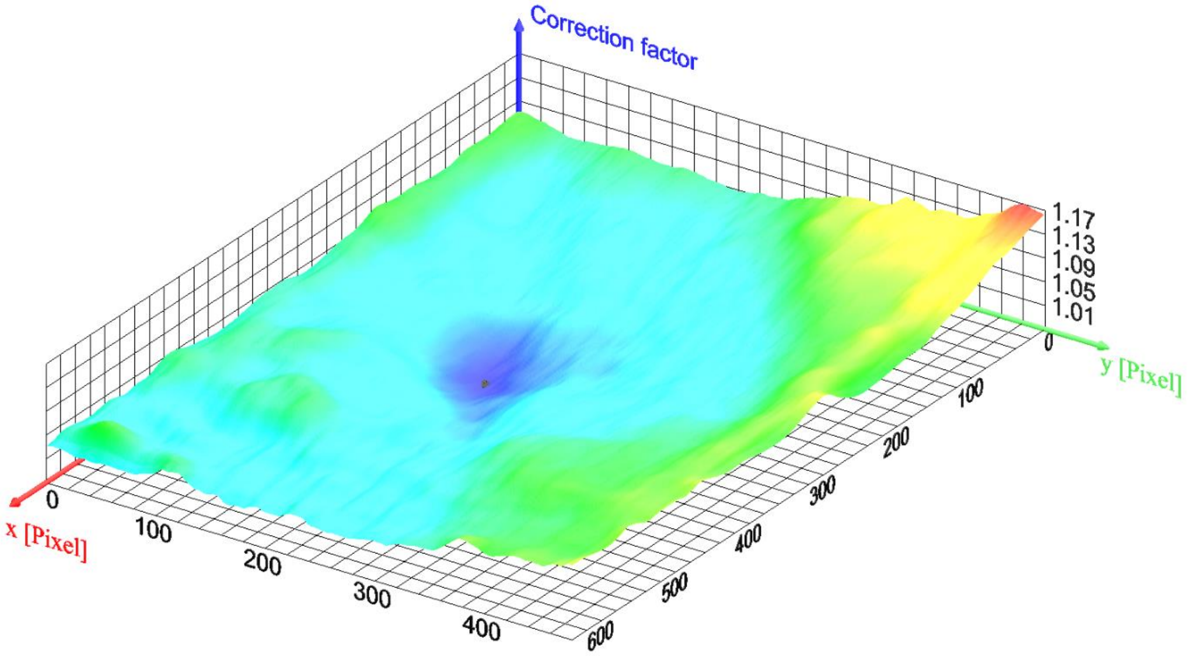

Figure 119: Correction factors camera 2, nitrogen.

A.2 Tomographic measurement of the temperature distribution

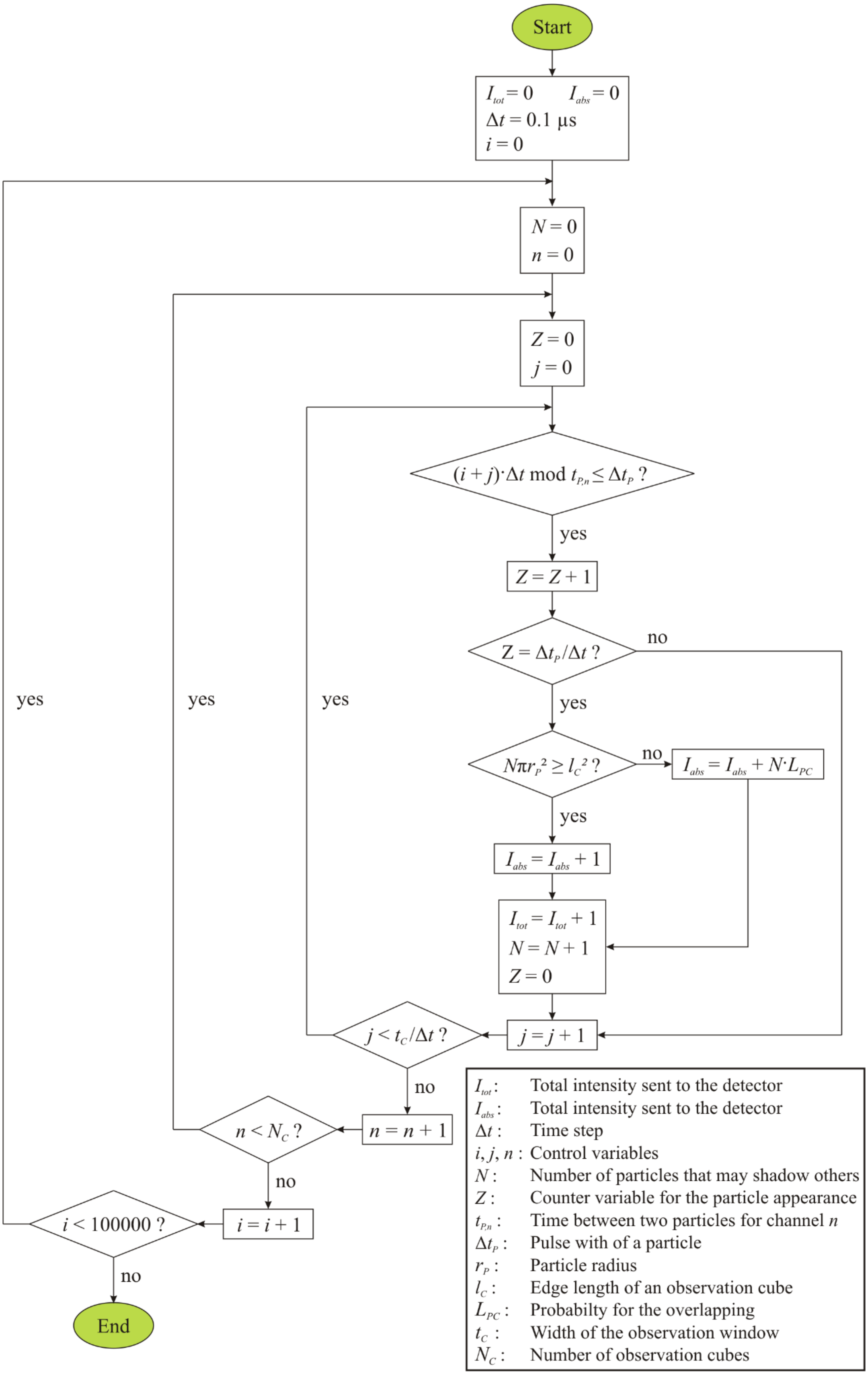

I_{tot} :	Total intensity sent to the detector
I_{abs} :	Total intensity sent to the detector
Δt :	Time step
i, j, n :	Control variables
N :	Number of particles that may shadow others
Z :	Counter variable for the particle appearance
$t_{P,n}$:	Time between two particles for channel n
Δt_P :	Pulse with of a particle
r_P :	Particle radius
l_C :	Edge length of an observation cube
L_{PC} :	Probabilty for the overlapping
t_C :	Width of the observation window
N_C :	Number of observation cubes

Figure 120: Program flow chart for the determination of the total intensity I_{tot} *sent to the detector and the absorbed intensity* I_{abs}.

A.3 General experimental settings and pretests

Equations (A.5 and A.6) for the calculation of the PSI scale using group number 5, element 1 of the 1951 USAF resolution target (see Figure 121).

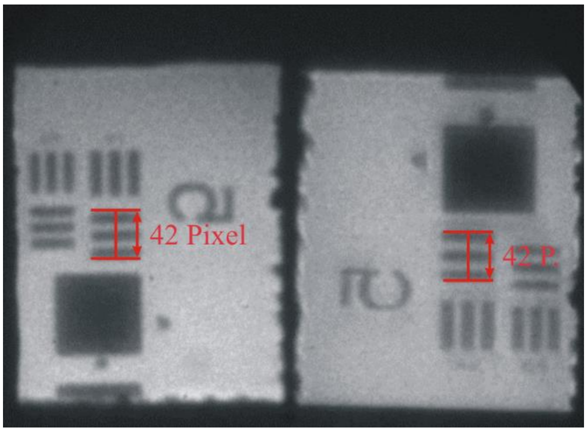

Figure 121: Image of the 1951 USAF resolution target acquired by the PSI-diagnostic.

$$\text{Group number 5, element 1: } \frac{32\ \text{Line pairs}}{\text{mm}} \tag{A.5}$$

$$S = \frac{2.5\ \text{Line pairs}}{32\ \text{Line pairs}} \cdot \frac{1000\ \mu\text{m}}{42\ \text{Pixel}} = 1.86\ \frac{\mu\text{m}}{\text{Pixel}} \tag{A.6}$$

A.4 Results

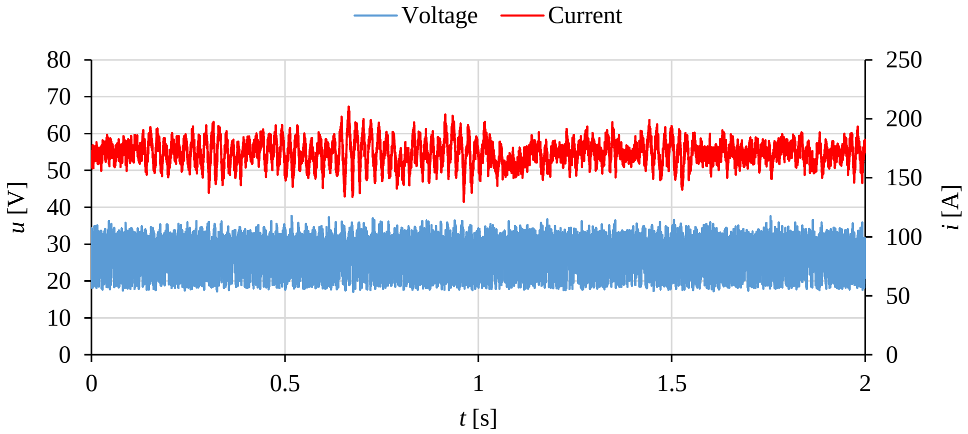

Figure 122: Voltage and current traces of the wire arc spray process operated with ***28.9 V****,* ***4 m/min****,* ***4 bar*** and ***compressed air (CA)****.*

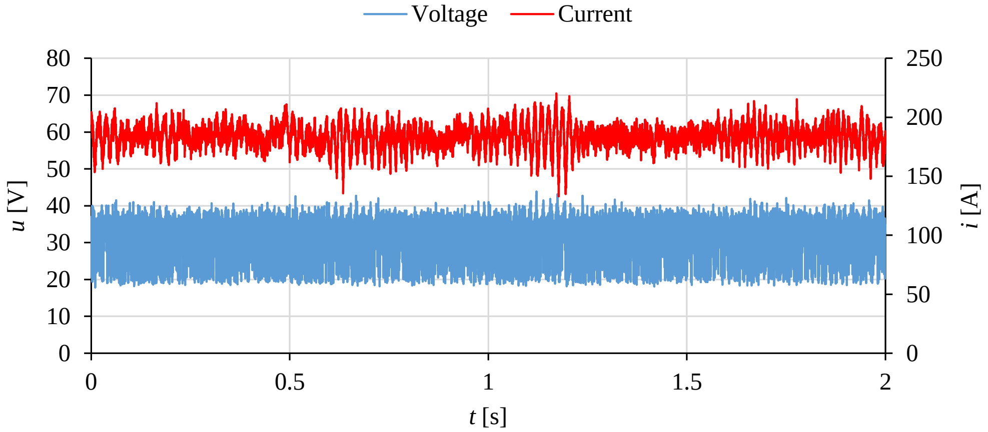

Figure 123: Voltage and current traces of the wire arc spray process operated with ***33 V****, 4 m/min, 4 bar and compressed air (CA).*

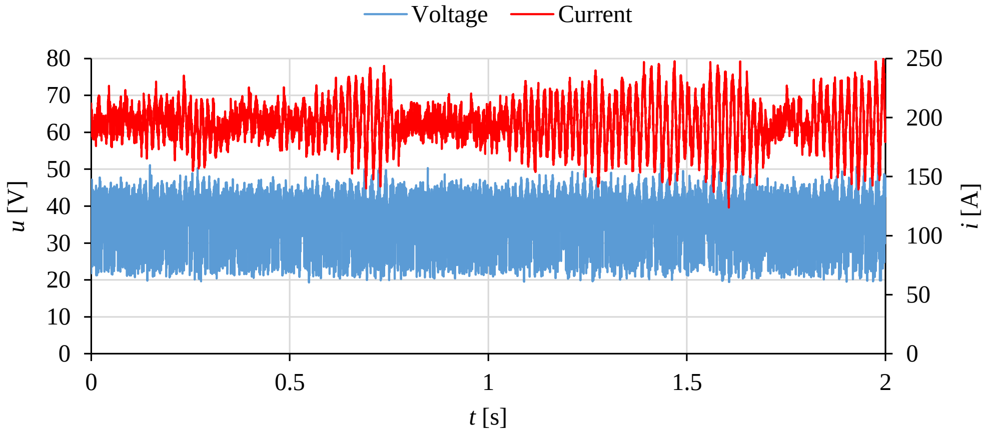

Figure 124: Voltage and current traces of the wire arc spray process operated with ***38.8 V****, 4 m/min, 4 bar and compressed air (CA).*

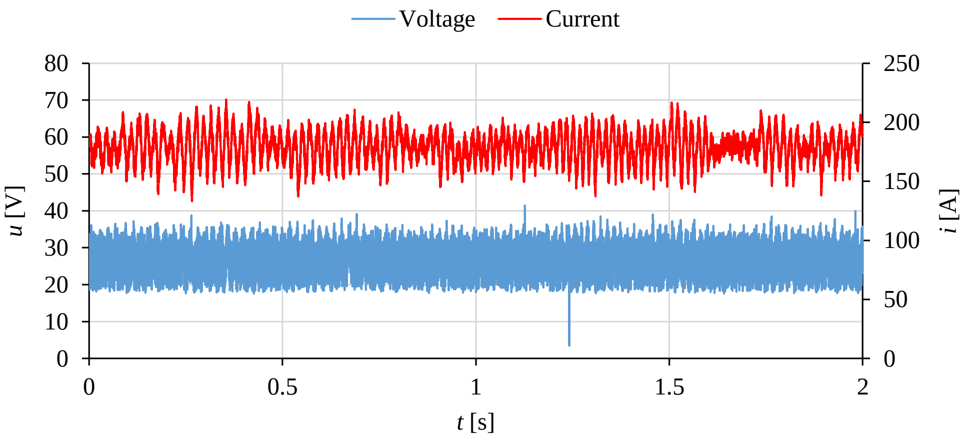

*Figure 125: Voltage and current traces of the wire arc spray process operated with 28.9 V, 4 m/min, **3 bar** and compressed air (CA).*

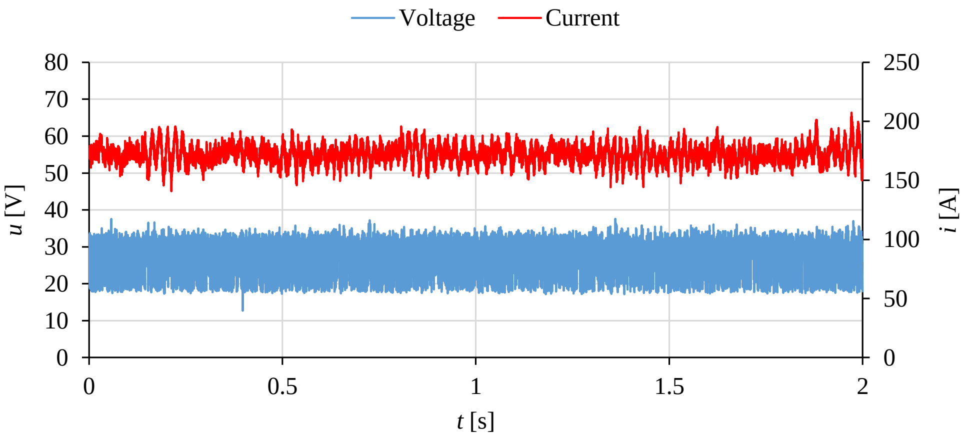

*Figure 126: Voltage and current traces of the wire arc spray process operated with 28.9 V, 4 m/min, **5 bar** and compressed air (CA).*

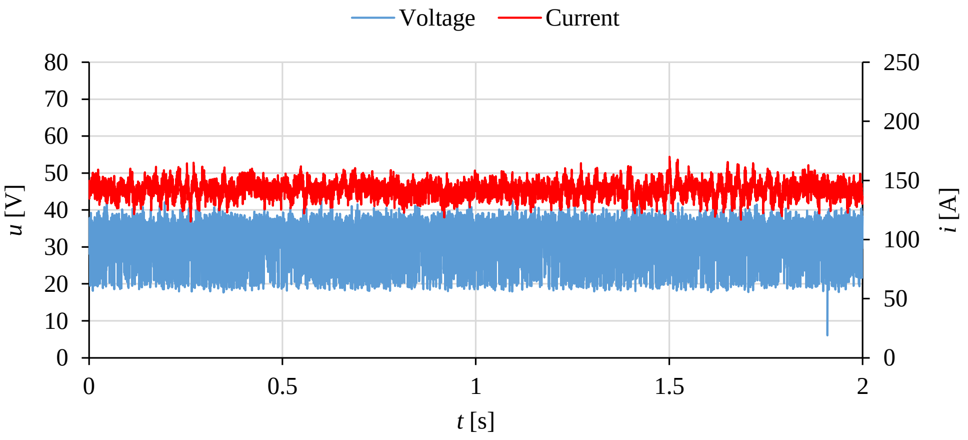

*Figure 127: Voltage and current traces of the wire arc spray process operated with 28.9 V, **3 m/min**, 4 bar and compressed air (CA).*

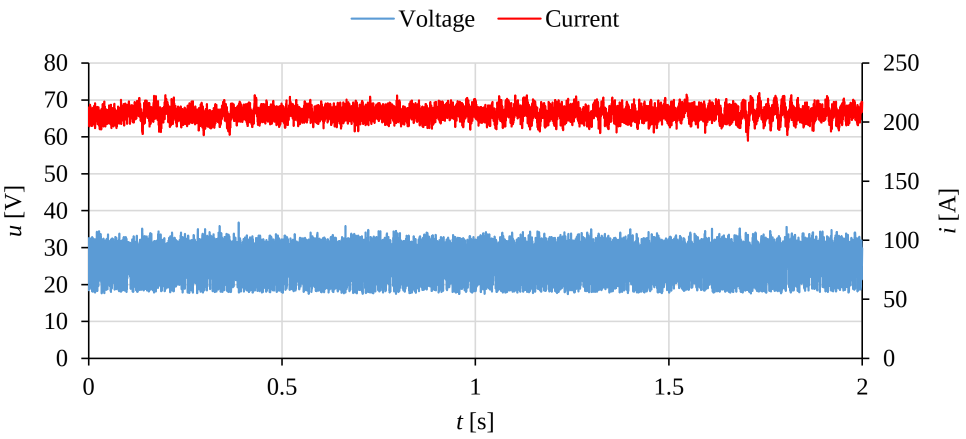

Figure 128: Voltage and current traces of the wire arc spray process operated with 28.9 V, ***5 m/min****, 4 bar and compressed air (CA).*

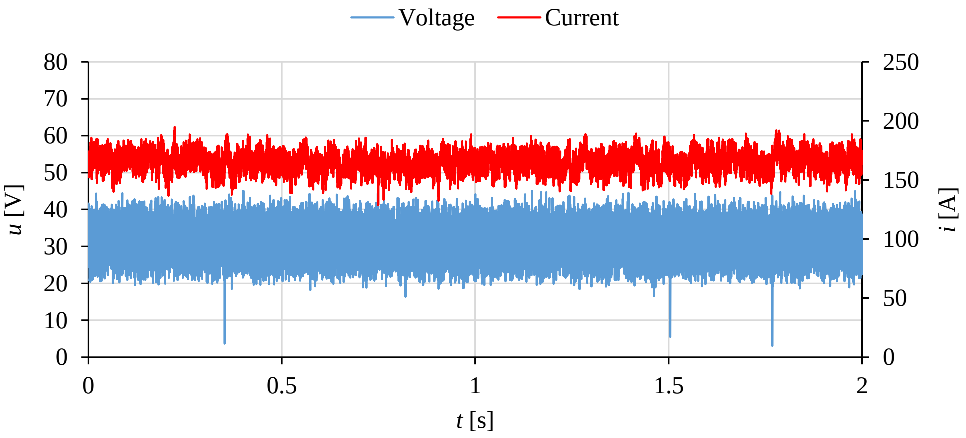

Figure 129: Voltage and current traces of the wire arc spray process operated with ***33 V****, 4 m/min, 4 bar and* ***nitrogen****.*

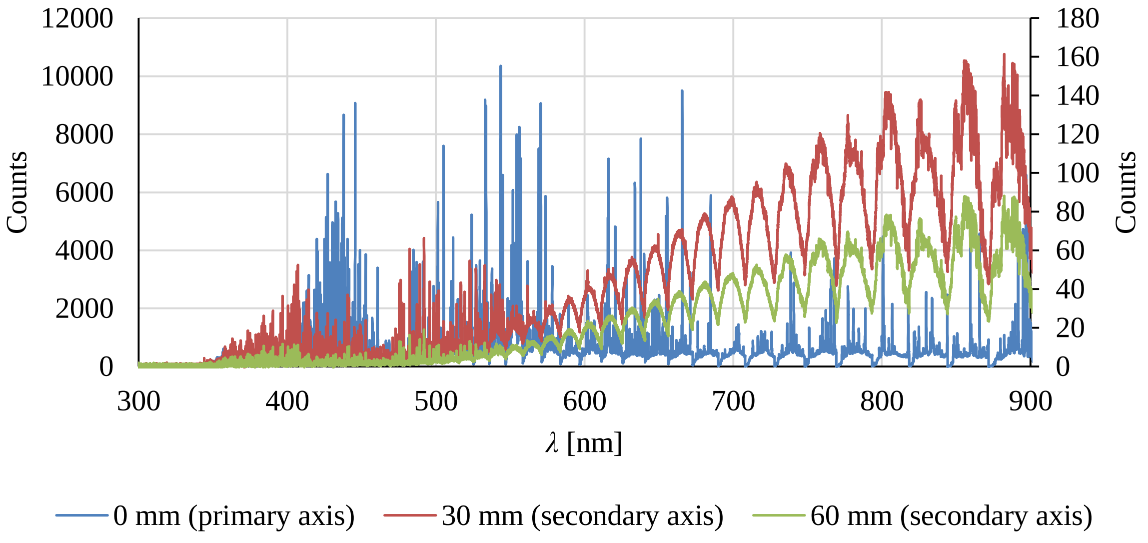

ffk

Figure 130: Spectrum of the wire arc spray process measured at different positions in front of the wire tips using the spectrometer "ARYELLE". The blue curve belongs to the primary axis, the red and green curves to the secondary axis. The process parameters were set to 28.9 V, 4 m/min and 4 bar. Compressed air was used as atomizing gas.

A.5 Nomenclature

Acronyms

HVOF	High Velocity Oxygen Fuel
PFI	Particle Flux Imaging
PIV	Particle Image Velocimetry
LDA	Laser Doppler Anemometry
L2F	Laser-Two-Focus
PDA	Phase Doppler Anemometry
PSI	Particle Shape Imaging
FWHM	Full Width at Half Maximum
DOF	Depth of Field
CoC	Circle of Confusion
LM	Levenberg-Marquardt
CT	Computed tomography
GMAW	Gas Metal Arc Welding
ROI	Region of Interest
CA	Compressed Air

Constants

R	Gas constant	(83144598 kg m^{2} s^{-2} mol^{-1} K^{-1})
c	Speed of light	(299272458 m s^{-1})
σ	Stefan-Boltzmann-constant	(5.6704·10^{-8} W m^{-2} K^{-4})
h	Planck’s constant	(6.6260·10^{-34} J s)
k	Boltzmann constant	(1.3806·10^{-23} J K^{-1})
ρ_{Fe}	Density of iron	(7.874 g cm^{-3})

Symbols

k	Rate of a chemical reaction	
E_a	Activation energy	(kJ mol^{-1})
T	Temperature	(K)

A	Frequency factor or surface area	(Hz, m^2)
Θ	Angle	(°)
f_P	Doppler frequency	(Hz)
$\vec{v}_P$	Particle velocity	(m s^{-1})
f_L	Laser frequency	(Hz)
λ_L	Laser wavelength	(nm)
$\vec{k}$	Wave vector	
f_{PM}	Doppler shifted frequency	(Hz)
f_D	Doppler-difference frequency	(Hz)
x, y, z	Cartesian coordinates	(m or Pixel)
dn/dt	Particle rate	(s^{-1})
ρ	Reflectivity	
α	Absorptivity	
τ	Transmissivity	
ε	Emissivity	
P	Power	(W)
λ	wavelength	(nm)
$M_{\lambda s}$	Spectral exitance	(W m^{-3})
C_1	First radiation constant	(J m^2 s^{-1})
C_2	Second radiation constant	(m K^{-1})
M_λ	Spectral radiant exitance	(W m^{-3})
λ_1, λ_2	Peak intensity wavelengths	(nm)
Q	Calculated two-color-pyrometry quotient	
Q_m	Measured two-color-pyrometry quotient	
q_e	Quantum efficiency	
f_1, f_2	Transmission curves of interference filters	
E_{GB}	Measurement error	
I, I_1, I_2	Measured or calculated intensities	
W	Width of the object plane	(mm)
H	Height of the object plane	(mm)

DOF	Depth of field	(mm)
D_N, D_F	Nera and far DOF limits	(mm)
s_o	Object distance	(mm)
f	Focal length	(mm)
N	f-Number or number of measurements	
d_c	Diameter of the CoC	(µm)
w	Width of the CCD sensor	(Pixel)
h	Height of the CCD sensor	(Pixel)
G	Dimension of an object	(mm)
s_i	Image distance	(mm)
B	Dimension of an image	(mm)
B_N, B_F	Dimension of blurred images in the near and far DOF	(mm)
x_N	Distance	(mm)
K_1, K_2	Calibration factors	(m^2 W^{-1})
K	Quotient of the calibration factors	
$\Delta\lambda$	Wavelength step	(nm)
k_0	Proportional factor	(m^3 W^{-1})
H_T	Proportional factor	(m^3 W^{-1})
R	Sum of square residuals	
$\boldsymbol{p}$	Paramter vector	
$\boldsymbol{J}$	Jacobi matrix	
i	Control variable	
$\delta_{\boldsymbol{p}}$	Correction vector	
μ	Damping term	
$\boldsymbol{E}$	Identity matrix	
ε	Error vector	
$\boldsymbol{N}, \boldsymbol{F}$	Auxiliary matrices	
T_{ref}	Reference temperature	(K)
v_L	Calibration lamp velocity	(cm min^{-1})

$t_E, t_{\exp}$	Exposure time	(s)
$I_{ref,1}, I_{ref,2}$	Average reference values	
p	Projection value	
ϕ	Projection angle	(°)
$L_{\phi,i}$	Integration direction	
$f(x,y)$	2D intensity distribution	
$\Delta\phi$	Angle step	(°)
k	Number of projections directions	
n	Edge length of a cross section	(Pixel)
N	Number of cells in a cross section	
M	Number of projections	
$w_{i,j}$	Weight of projection i and cell j	
$\vec{p}$	Projection vector	
$\vec{f}$	Intensity vector	
W	Weight matrix	
m	Iteration step	
τ	Optical thickness	
I_{tot}	Source intensity	
I_{rec}	Received intensity	
dN_n/dt	Particle rate flying through channel n	(s^{-1})
$t_{P,n}$	Time between following particles	(s)
r_P	Particle radius	(µm)
$v_{P,x}, v_{P,y}, v_{P,z}$	Particle velocity components	(m/s)
Δt_P	Particle time pulse	(s)
l_C	Channel cube edge length	(m)
t_C	Particle duration of stay in a cube	(s)
Δt	Time step	(s)
I_{abs}	Absorbed intensity	
L_{PC}	Particle overlapping probability	
I_0	Intensity emitted by one particle	

ε_{Fe}	Emissivity of liquid iron	
ε_{FeO}	Emissivity of liquid oxidized iron	
$I_{1,tot}, I_{2,tot}$	Total measured intensities from particles flying through a cross section	
$A_{\perp,i}$	Luminous area of particle number i	(m^2)
N	Number of particles flying through a cross section	
T_{avg}	Average temperature	(K)
v_w	Wire federate	(m min^{-1})
r_w	Wire radius	(mm)
K_1, K_2	Calibration factors	(J^{-1})
u	Voltage	(V)
i	Electric current	(A)
T	Time period	(s)
H_{mass}	Energy input per unit mass	(J/g)
C_{ox}	In-flight oxide content of the particles	